CFD STUDY OF COMPLEX CIRCULATING FLUIDIZED BED SYSTEMS

Author:
Li, Shuyue

Publication Date:
2021

DOI:
https://doi.org/10.26190/unsworks/1619

CFD STUDY OF COMPLEX CIRCULATING FLUIDIZED BED SYSTEMS

by

Shuyue Li

A thesis submitted in fulfilment of the requirements for the degree of Doctor of Philosophy

School of Chemical Engineering

The University of New South Wales

Sydney, Australia

April 2021

Thesis/Dissertation Sheet

Surname/Family Name	:	Li
Given Name/s	:	Shuyue
Abbreviation for degree as give in the University calendar	:	PhD
Faculty	:	Faculty of Engineering
School	:	School of Chemical Engineering
Thesis Title	:	CFD STUDY OF COMPLEX CIRCULATING FLUIDIZED BED SYSTEMS

Abstract 350 words maximum: (PLEASE TYPE)

Circulating fluidized bed (CFB) has been widely applied to many chemical engineering processes. Although significant developments have been made in understanding the performance using the complex CFB technology during the last decades, the detailed inner information cannot be obtained by experiments because of complicated flow pattern in the system and backward measuring equipment. Numerical simulation has become the primary method to accelerate the development of complex CFB technology, reduce the cost of design and operating time, as well as reduce the technical risks. This thesis aims to provide more detailed in-furnace phenomena of complex CFB systems, including the hydrodynamic behaviours and chemical reactions based on the numerical simulation method. The promising chemical looping combustion (CLC) technology, as an example of complex CFB systems, will be focused on in this thesis. Meanwhile, the non-uniformity phenomenon in complex CFB units is comprehensively investigated in two symmetrical CFB configurations connected in parallel and series. Sequentially, an integrated method to dynamically combine CFD modelling and the process simulation is developed as a solution to improve the CFB performance. Specifically, it covers the following five aspects:

1. The hydrodynamic characteristics in a full-loop dual CFB CLC unit are comprehensively investigated based on the Eulerian multi-fluid model to give more detailed information about the flow behaviours.
2. The hydrodynamic characteristics in a unique counter-current moving bed full-loop CLC unit are comprehensively investigated based on the Eulerian multi-fluid model to study the unique configuration and in-furnace fluidization.
3. The reaction characteristics in the unique counter-current moving bed full-loop CLC unit are firstly attempt based on the hybrid Eulerian- Eulerian-Lagrangian model to study the in-furnace reaction details.
4. The non-uniformity characteristics of the multiphase flow in two complex CFB units connected in parallel and series, respectively, are studied based on the Eulerian multi-fluid model.
5. A novel direct integrated method to dynamically combine CFD modelling and the process simulation is developed. A case study of real-time regulation of boundary and operating conditions of reactors in complex CFBs is realized.

These studies contribute to the deep understanding and further optimization of complex CFB systems.

Dedicated to my family

Originality Statement

"I hereby declare that this submission is my own work and to the best of my knowledge it contains no materials previously published or written by another person, or substantial proportions of material which have been accepted for the award of any other degree or diploma at UNSW or any other educational institution, except where due acknowledgment is made in the thesis. Any contribution made to the research by others, with whom I have worked at UNSW or elsewhere, is explicitly acknowledged in the thesis. I also declare that the intellectual content of this thesis is the product of my own work, except to the extent that assistance from others in the project's design and conception or in style, presentation and linguistic expression is acknowledged."

Signed.....

Date……

INCLUSION OF PUBLICATIONS STATEMENT

UNSW is supportive of candidates publishing their research results during their candidature as detailed in the UNSW Thesis Examination Procedure.

Publications can be used in their thesis in lieu of a Chapter if:

- The student contributed greater than 50% of the content in the publication and is the "primary author", ie. the student was responsible primarily for the planning, execution and preparation of the work for publication
- The student has approval to include the publication in their thesis in lieu of a Chapter from their supervisor and Postgraduate Coordinator.
- The publication is not subject to any obligations or contractual agreements with a third party that would constrain its inclusion in the thesis

Please indicate whether this thesis contains published material or not.

☐ This thesis contains no publications, either published or submitted for publication

☒ Some of the work described in this thesis has been published and it has been documented in the relevant Chapters with acknowledgement

☐ This thesis has publications (either published or submitted for publication) incorporated into it in lieu of a chapter and the details are presented below

CANDIDATE'S DECLARATION

I declare that:

- I have complied with the Thesis Examination Procedure
- where I have used a publication in lieu of a Chapter, the listed publication(s) below meet(s) the requirements to be included in the thesis.

Name	**Signature**	**Date (dd/mm/yy)**

Copyright Statement

Authenticity Statement

"I certify that the Library deposit digital copy is a direct equivalent of the final officially approved version of my thesis. No emendation of content has occurred, and if there are any minor variations in formatting, they are the result of the conversion to digital format."

Signed .....

Date……

Abstract

Circulating fluidized beds (CFBs) have been widely applied to many chemical engineering processes, due to its good gas-solid mixing, wide fuel flexibility, and excellent heat and mass transfer performance. Although significant developments have been made in understanding the performance using the complex CFB technology during the last decades, the detailed inner information cannot be obtained by experiments because of complicated flow pattern in the system and backward measuring equipment. The present knowledge, understanding, and experience of the complex CFB systems mainly come from a limited number of research groups operating small CFB plants. Meantime, the lab- or pilot-scale results cannot safely be translated to an industrial scale, the performance of the actual industrial CFB unit is still uncertain. With the development of computer technology and parallel computing, numerical simulation has become the primary method to accelerate the growth of complex CFB technology, reduce the cost of design and operating time, and reduce the technical risks. However, present simulations are still very limited for the full-loop CFB system, especially in some complex configurations with reactions taking place. Among various CFB chemical engineering systems, the chemical looping combustion (CLC) system is regarded as one of the most promising clean combustion technologies because of the inherent CO_2 separation. Therefore, the CLC technology, as an example of a complex CFB system, will be focused on in this thesis. Meantime, the simulation work of the hydrodynamic and reaction behaviours of the counter-current moving-bed CDCL process has not been done yet, and details of the flow and chemical reactions have not been revealed and fully understood.

Besides, the non-uniformity phenomena of gas-solid distribution in symmetrical dual CFB systems have not been comprehensively investigated yet. For non-identical CFB configurations, the effect of gas-solid non-uniformity on the system stability will intensify. Therefore, it is vital to get a deep understanding of the non-uniformity phenomenon. Moreover, most CFD simulations on complex CFB systems only reveal

microscale phenomena based on separate reactor components. The boundary and operating conditions are fixed during the simulation process without considering the external adjustment and environment change. For fulfilling the knowledge gap, an integrated online regulation method is firstly established to realize the collaborative simulation of the transient CFD model and process control algorithm based on Ansys-Fluent and MATLAB platforms. This thesis aims to provide more detailed in-furnace phenomena of complex CFB units, including the hydrodynamic behaviours and chemical reactions based on the numerical simulation method. Meanwhile, the optimization of boundary conditions and the model set is thoroughly investigated in these CFBs. Specifically, it covers the following six aspects:

1. In chapter 3, a multi-fluid model based on the Eulerian-Eulerian framework is used to study the gas-solid hydrodynamics, such as solid distribution, particle motion and solid velocity, in a three-dimensional (3D) CLC unit with the configuration of dual circulating fluidized bed (DCFB). The influence of four different drag force models, including two classic models, i.e., Gidaspow, EMMS drag model and two recent drag models, i.e., Rong and Tang drag model, on hydrodynamics in DCFB are assessed. Numerical results show that the characteristics of solid distribution and velocity in different sections are distinct. For qualitative analysis, all the drag models can predict a reasonable radial solid distribution and pressure distribution. However, only the EMMS, Rong and Tang drag model can capture the phenomenon of dense solid concentration in the low part. For quantitative analysis, the solid circulating rate predicted by the EMMS drag model is the closest to the experimental value, while the Gidaspow drag model shows the most significant deviation. The overall assessments confirm that the drag model selection significantly influences the simulations of gas-solid flow in DCFBs. This study sheds lights on the design and optimization of fluidized bed apparatuses.

2. In chapter 4, a multi-fluid model based on the Eulerian-Eulerian framework is used to study the gas-solid hydrodynamics in a unique moving-bed Coal-Direct Chemical Looping (CDCL) unit. In the CDCL process, iron-based oxygen carriers belong to Geldart D particles are used. Such a system has been seldom studied. In particular, the study of this part is divided into two steps: firstly, a TFM method with the kinetic theory of granular flow (KTGF) is adopted for describing the gas-solid flows in a bottom-enlarged air reactor of this CDCL process. The model is qualitatively and quantitatively validated. The simulation results indicate that the oxygen carrier particles show a slugging flow pattern in the bottom section of the air reactor, an anti-core-annulus structure in the riser and a periodic fluctuation in the whole air reactor. The effects of several variables on the gas-solid flow in the air reactor of CDCL unit are also studied, including gas velocity, specularity coefficient and different drag models. The simulation results indicate that the higher gas inlet velocity can increase the pressure drop over the air reactor and significantly influence solid allocation in the bottom regime and the riser. Specularity coefficient of zero and Syamlal-O'Brien drag model give the closest mass flow rate by comparing with experimental values, indicating that they are suitable for the three-dimensional air reactor modelling. This model provides a cost-effective tool for better understanding of gas-solid flows of Geldart D particle in the air reactor of CDCL systems. Then, the validated model settings are applied to build the 3D full-loop moving-bed CDCL unit. Unique fluidization states are predicted in different domains of the full-loop system by simulation results. And the influences of several boundary conditions on the solid circulation rate and pressure distribution are investigated. Compared with the DCFB CLC unit, the pressure drop in this moving bed CDCL unit is small which means that the system is more stable. Results show that the solid flux through the L-valve is not affected when the combustor gas velocity increases from 1.6 m/s to 1.8 m/s. The solid circulation rate is controlled by the flow rate of aeration gas on the standpipe of

L-valve, which is consistent with the experimental measurements. The hydrodynamic behaviours of the unique CDCL unit can be well understood by simulation.

3. In chapter 5, a multi-fluid model based on the hybrid of Eulerian-Eulerian-Lagrangian framework is used to study the reactive flow characteristics in a unique counter-current moving-bed CDCL unit, where the unit has been introduced in chapter 4. In the CDCL process, iron-based oxygen carriers belong to Geldart D particles are used. The reaction characteristics in such a system have been seldom studied. The gas mixture and dense oxygen carrier phase are treated as the continuum with the two-fluid model (TFM) and the dilute coal powder as the discrete element with the Discrete Particle Model (DPM). Multiple homogenous and heterogeneous reactions are considered, including redox reactions of the oxygen carrier, devolatilization, moisture release and char gasification of coal particles, and water-gas shift reaction. The simulation results show good agreement with the experimental data. Transport characteristics of discrete coal powder in the reducer under cold and hot conditions are compared to explain the mechanism of the mixing and separation behaviours between the oxygen carrier and coal in the system. A severe gas leakage phenomenon is captured by simulations. Meantime, the cause and optimization suggestion of gas leakage is given. The distribution of gas-solid species and reaction rates are shown to explore the reaction characteristics of this system. This work provides a deep understanding of this moving bed CDCL unit and can be used as a tool for further designing and optimizing similar CLC processes.

4. In chapter 6, the non-uniformities of symmetrical CFBs with two different configurations are comprehensively studied. In section 1, the maldistribution phenomenon of complex symmetrical CFB units with parallel cyclones is deeply

investigated by using the Eulerian multi-fluid model. Simulation results verify the maldistribution phenomena in parallel symmetrical CFB units, and the model settings are validated by experimental data. The maldistribution phenomena are discussed and evaluated in terms of bed inventory evolution and gas-solid distribution in symmetrical parts. The effects of key operating parameters, including total bed inventory, gas aeration rate, and wall roughness on maldistribution degree are then studied. Simulation results show that the maldistribution degree between the two symmetrical parts increases with the increase of total bed inventory and gas aeration rate. And through the analysis of pressure fluctuation, the instability of the system is aggravated. However, wall roughness does not show a clear influence and tendency. Conclusions in this chapter provide an insightful understanding of non-uniformity and help further optimize symmetrical complex CFB systems with parallel configuration. In section 2, the non-uniformity of complex symmetrical CFB units with series configuration is deeply investigated by using the Eulerian multi-fluid model. It is known that chemical looping combustion (CLC) units are connected in series. In recent years, many CLC units are established based on the symmetrical dual circulating fluidized bed (DCFB) where the air reactor (AR) and fuel reactor (FR) have identical configurations. The flow pattern may be highly non-uniform in these identical symmetrical paths, compromising the stability. In this chapter, the non-uniformity in a symmetrical CLC apparatus is studied by setting identical boundary conditions. First, the typical non-uniformity phenomenon is evaluated through bed inventory evolution and gas-solid distribution in symmetrical parts. The effects of key operating parameters, including total bed inventory, gas aeration rate, and wall roughness on non-uniformity degree are then studied. The simulating results show that the non-uniformity degree between the two symmetrical parts increases with the increase of total bed inventory and gas aeration rate. And through the *R*/*S* analysis, results indicate the degree of non-

uniformity will be intensified in the predictable short-term future with the increase of total bed inventory and gas aeration rate. However, wall roughness does not show a clear influence and tendency. This work provides an insightful understanding of non-uniformity and will help further optimize symmetrical CLC systems.

5. Complex CFB units in industries require continuous monitoring and effective control to maintain product specifications and meet safety criteria. In chapter 7, an integrated simulation method is firstly established by combining the CFD model and process simulation based on Ansys-Fluent and MATLAB platforms. An example is conducted based on this method to reduce the degree of maldistribution in one symmetrical DRCFB system, studied in chapter 6, through online regulation of L-valve aeration rate and the better operating performance coupling with the process controller is discussed. This work provides a new solution to test and optimize practical industrial CFB processes in economical and safe manners.

Acknowledgments

Throughout the writing of this dissertation, I have received a great deal of support and assistance.

I would first like to thank my supervisor, Associate professor Yansong Shen. I appreciate all his contributions of time, ideas, and funding to make my PhD experience productive and stimulating. His excellent quality of thinking and planning for his research work is contagious and motivational for me, even during tough times in the PhD pursuit. I am also thankful for the excellent example he has provided as a successful researcher and supervisor.

I am extremely grateful to postdoc Yuting Zhuo and Shuai Wang for their guidance and support throughout my PhD candidature for the continuous interest, encouragement, and guidance during this study which I greatly appreciate.

The group has been a source of friendships as well as useful advice and collaboration. My appreciation also extends to my colleagues: Dr. Jiaxin Cui, Dr. Yiran Liu, Dr. Xiaobing Yu, Dr. Yuanhe Yue, Dr. Shuang Song, Dr. Xin Jin, Dr. Zhouzun Xie, Dr. XiaoYing Wong, Dr. Ziguang Zhao and Dr. Xinxin Tang. I am also deeply grateful to Dr. Tianyu Wang and Dr. Chenxi Zhang.

Last but not least, I would like to acknowledge with my deepest gratitude, the support and love of my boyfriend, Dr. Xin Jin, during my undergraduate, postgraduate and doctoral years. I also firmly believe that you are the love companion of my life.

List of Publications

Paper 1: S. Li, Y. Shen, Multi-fluid modelling of hydrodynamics in a dual circulating fluidized bed, Adv. Powder Technol. 31. 7 (2020) 2778-279.

Paper 2: S. Li, Y. Shen, Numerical study of gas-solid flow behaviors in the air reactor of coal-direct chemical looping combustion with Geldart D particles, Powder Technol. 361 (2020) 74–86.

Paper 3: S. Li, Y. Shen, CFD investigation of maldistribution in a full-loop circulating fluidized bed with double parallel cyclones, Powder Technol. 381 (2020) 665-684.

Paper 4: S. Li, Y. Shen, CFD study of non-uniformity of gas-solid flow through a chemical looping combustion system with symmetrical series loops. Powder Technol. (2021)

Paper 5: S. Li, Y. Shen, Online regulation of maldistribution in a full-loop CFB by combining CFD and Process Simulation. (Under revision)

Paper 6: S. Li, Y. Shen, Three-dimensional transient modeling of an iron-based coal direct chemical looping combustion process. (Under revision)

Paper 7: S. Li, Y. Shen, Numerical simulation of the coal-direct chemical looping combustion process. (under revision)

Paper 8: C. Zhang, S. Li, Z. Wang, Y. Shen, F. Wei, Model and experimental study of relationship between solid fraction and back-mixing in a fluidized bed, Powder Technol. 363 (2020) 146–151.

Nomenclature

$\vec{u}$	Velocity (m/s)
t	Time (s)
p	Pressure (Pa)
$\vec{g}$	Gravitational acceleration (m/s^2)
$\bar{\bar{I}}$	Unit tensor
G_k	Generation of turbulence kinetic energy due to the mean velocity gradients
e	Restitution coefficient for the particle-particle collision
d_p	Particle diameter (m)
g_0	Radial distribution function
I_{2D}	Second invariant of the deviatoric stress tensor.
C_D	Drag coefficient
Re_s	Particle Reynolds number
H_D	Heterogeneous index calculated by EMMS drag model
F_0	Non-dimensional drag force
Re_T	Reynolds number based on the granular temperature
e_{sw}	Restitution coefficient of particles
A	Constant in Syamlal–O′Brien drag model
B	Constant in Syamlal–O′Brien drag model
$v_{r,s}$	Terminal solid velocity(m/s)
m_r	Mass in the right external loops (kg)
m_l	Mass in the left external loops (kg)
U_f	Superficial gas inlet velocity (m/s)
M_t	Total bed inventory (kg)
Y_i	Mass fraction of the ith species
$\dot{m}$	Mass transfer rate (kg/m^3·s)
S	Mass source term owing to mass transfer (kg/m^3·s)
$\vec{F}_{td,g}$	Drag force on the discrete particle by gas (N)
h	Convective heat transfer coefficient (W·/m^2·s)
Q	Intensity of heat exchange (W/m^3)

A_p	Surface area of single coal particle (m^2)
T	Temperature (K)
T_∞	Local temperature of continuous phase (K)
f_h	Heat absorb fraction
H_{reac}	Heat released by surface reaction (J)
Nu_s	Nusselt number
k	Thermal conductivity (W/m·K)
Pr	Prandtl number
C	Concentration
k_i	Reaction rate constant (kg/(m^2·Pa·s))
A_i	Pre-exponential factor of the rate constant
E_i	Activation energy (J/kmol)
R	Constant of the ideal gases (J/kmol·K)
X	Oxidation degree

Greek Symbols

α	Volume fraction
ρ	Density (kg/m^3)
$\bar{\bar{\tau}}$	Stress tensor (Pa)
β	Interphase momentum transfer coefficient (kg/m^3·s)
β_0	Interphase momentum exchange coefficient derived from Wen and Yu (kg/m^3·s)
μ	Dynamic viscosity (Pa s)
λ_s	Solid bulk viscosity (Pa s)
σ_k	turbulent Prandtl numbers for k
ε	Dissipation rate of turbulent kinetic energy (kg/(m s^3))
κ	Turbulent kinetic energy (m^2/s^2)
$\prod_k$	Turbulence exchange terms between the gas and solid phases
σ_ε	Turbulent Prandtl numbers for ε
C_1	Constant in turbulence model
C_2	Constant in turbulence model
$\prod_\varepsilon$	Turbulence exchange terms between the gas and solid phases

γ_{Θ_s}	Collisional dissipation rate of the granular fluctuating energy (kg/(m·s^3))
Θ_s	Granular temperature (m^2/s^2)
$\alpha_{s,max}$	Solids volume fraction at maximum packing state
μ_s	Particle shear viscosity (kg/(m·s))
$\mu_{s,col}$	Collisional viscosity(kg/(m·s))
$\mu_{s.kin}$	Kinetic viscosity (kg/(m·s))
$\mu_{s.fr}$	Frictional viscosity (kg/m·s)
Φ	Angle of internal friction (°)
ψ	Specularity coefficient
λ	Thermal conductivity (W/m·K)
$\bar{\bar{\tau}}$	

Subscripts

g	Gas phase
s	Solid phase
p	Discrete particle phase
rad	Radiation
$H_2o, gasi$	Steam gasification
$co_2, gasi$	CO_2 gasification
$\mathrm{CH_4}, \mathrm{reduc}$	CH_4 reduction
$H_2, reduc$	H_2 reduction
$CO, reduc$	CO reduction
oxi	Oxidation
wgs	Water-gas shift reaction

Abbreviations

CFB	Circulating fluidized bed
CLC	Chemical looping combustion
TFM	Two-fluid model
3D	Three-dimensional
DCFB	Dual circulating fluidized bed
EMMS	Energy-minimisation multi-scale
CDCL	Coal-Direct Chemical Looping

DPM	Discrete Particle Model
CCS	Carbon Capture and Storage
FR	Fuel reactor
AR	Air reactor
CFD	Computational fluid dynamics
iG-CLC	In-situ Gasification Chemical-Looping Combustion
CLOU	Chemical-Looping with Oxygen Uncoupled
CUT	Chalmers University of Technology
SU	Southeast University
ICB-CSIC	Instituto de Carboquímica
HUST	Huazhong University of Science and Technology
OSU	Ohio State University
KTGF	Kinetic theory of granular flow
DEM	Discrete Element Methods
CSD	Cluster structure-dependent drag
2D	Two-dimensional
BFB	Bubbling fluidized bed
SFB	Spouted fluidized bed
SCR	Solids circulation rate
NETL	National Energy Technology Laboratory
CPFD	Computational Particle Fluid Dynamics
MPPIC	Multi-Phase Particle-In-Cell
DNS	Direct Numerical Simulation
LBM	Lattice-Boltzmann method
IBM	Immersed Boundary Method
QUICK	Quadratic Upwind Interpolation of Convective Kinematics
SIMPLE	Semi-Implicit Method for Pressure Linked Equations
PUReIBM	Particle-resolved Uncontaminated fluid Reconcilable Immersed Boundary Method
DRCFB	Dual side refeed circulating fluidized bed
Dev	Relative deviation of bed inventory
IGCC	Integrated coal gasification combined cycle
ANN	Artificial neural network

UDF	User-defined function
AI	Artificial Intelligence
FLC	Fuzzy logic control
aaS	ANSYS Fluent as a Server

List of Figures

List of Tables

Contents

CHAPTER.1 Introduction

In this chapter, the application of CFB technology in energy production is briefly introduced firstly. During energy conversion, greenhouse gas emissions make a severe impact on the environment. The process optimization and efficiency improvement of the CFB power plant becomes a primary task. The background of promising CLC process, as an example of complex CFB systems, is reviewed. The scope and objective of the present work are outlined. The structure of the thesis is presented.

1.1 Background and motivation

The circulating fluidized bed (CFB) has been widely applied to various thermal power processes, including the combustion [1–3], gasification [4,5], pyrolysis [6,7] of various gas and solid fuels, which benefits gas-solid contact, bed-to-wall heat transfer, catalyst regeneration, and reaction selectivity. In the past several decades, the CFB configuration has come to prominence in terms of major applications of energy production. Optimizing the design and operation of the corresponding CFB system is the key factor to improve productivity and efficiency, as well as reduce energy loss and exhaust emissions for various thermal power plants.

Over the past decades, carbon dioxide emission has caused the increasing concentration of greenhouse gases in the atmosphere and contributed to many irreversible severe environmental and health issues, such as the atmospheric warming, sea-level rise and so on [8]. The average temperature of the earth has been estimated to increase around 1.6 degrees over the past century. Therefore, reducing the emission of CO_2 has become an urgent task currently. Among variable emission sources, the release of CO_2 from fossil fuel combustion in the large industrial CFB power plant is the essential source. However, after the industrial revolution, global energy demand is rapidly expanding. As the world's primary energy source, fossil fuel is estimated to account for almost 80% of global energy production at the current stage. In the meantime, renewable energy sources, such as the biomass, municipal waste, wind and solar [2], have seen rapid growth but have not yet replaced the traditional fossil fuels entirely in the current energy market because of a higher handling cost. There are still many difficulties in developing nuclear energy like the lack of waste management, hazard issues, and public objects [9]. Therefore, the continued dependence on fossil fuels for energy supply in the long-term future is inevitable. As a result, a considerable amount of CO_2 will continue to be generated in the foreseeable future. The reduction of CO_2 release from the combustion of fossil fuels is a primary task.

To reduce CO_2 emissions, Carbon Capture and Storage (CCS) technology has drawn more and more attention, which is an economically attractive method of reducing greenhouse gases emissions from the combustion of fossil fuels [10]. Currently, there are three primary methods to capture CO_2: (i) pre-combustion, which is a technique to remove the carbon from the fuel before it is burnt, based on fuel gasification; (ii) oxy-fuel combustion, which uses oxygen-enriched gas mixture instead of air; and (iii) post-combustion, in which the CO_2 is separated from the flue gases using suitable methods [11]. However, the main issue in these processes is the relatively low overall efficiency, and as a consequence, a large proportion of the produced energy is consumed by CO_2 separation and compression. Varying with different units, the contribution of CO_2 capture to the overall CCS cost could be as high as 75% [12]. Therefore, current research activities include developing "breakthrough technologies"; lower-cost capture systems with smaller energy penalties.

In recent decades, chemical looping combustion (CLC) technology has been regarded as the latest and most promising combustion technology due to its unique property [13]. In conventional combustion processes, the fuel usually mixes with air or high concentration oxygen in the combustor to produce heat and energy. A massive volume of exhaust gas exits from the combustor outlet, consisting of primarily carbon dioxide, steam and nitrogen. Separating CO_2 from the exhaust gas requires considerable energy and extra costs. However, for CLC technology, CO_2 separation can be easily achieved because the fuel is isolated from the air during the operation process. The net chemical reaction and energy release of the CLC process are identical to that of the conventional combustion of fossil fuels without the extra CCS cost, where only a small amount of energy is spent on solid circulation (0.3% of the total energy released) [14].

A typical CLC system has a CFB configuration consisting of two interconnected fluidized bed reactors, a fuel reactor (FR) and an air reactor (AR), as illustrated in Fig 1.1. The solid oxygen carrier, generally a metal oxide, is usually applied in a chemical looping

combustion process to transfer oxygen from the gaseous oxygen source of the air to the fuel, effectively avoiding gaseous direct contact oxygen fuel decrease the energy penalty of separation.

In the FR, the fuel is injected into the reactor and releases the volatile matter under the high temperature. Then, the raw oxygen carrier is reduced by various volatile gas species, and it generally can be simplified in R(1-1) - R(1-3):

$$C_xH_y + xMeO_a \rightarrow xCO + \frac{y}{2}H_2 + xMeO_{a-1} \quad \text{R(1-1)}$$

$$CO + MeO_a \leftrightarrow CO_2 + MeO_{a-1} \quad \text{R(1-2)}$$

$$H_2 + MeO_a \leftrightarrow H_2O + MeO_{a-1} \quad \text{R(1-3)}$$

R(1-1)-R(1-3) are usually endothermic reactions ($\Delta H > 0$); however, it can be either exothermic or endothermic depending on the choice of metal oxide and the fuel used. In the AR, the oxygen carrier is oxidized by the oxygen in the air to regenerate the oxygen carrier, depicted by R(1-4).

$$\frac{1}{2}O_2 + MeO_{a-1} \leftrightarrow MeO_a \quad \text{R(1-4)}$$

R(1-4) is highly exothermic. The net reaction of an entire cycle is simply a conventional combustion reaction. After oxidation in the AR, the regenerated oxygen carrier will be transported back to the FR by other accessories, such as the cyclone and downcomer. Thus, a circulation loop is formed between the AR and FR, as shown in Fig 1.1.

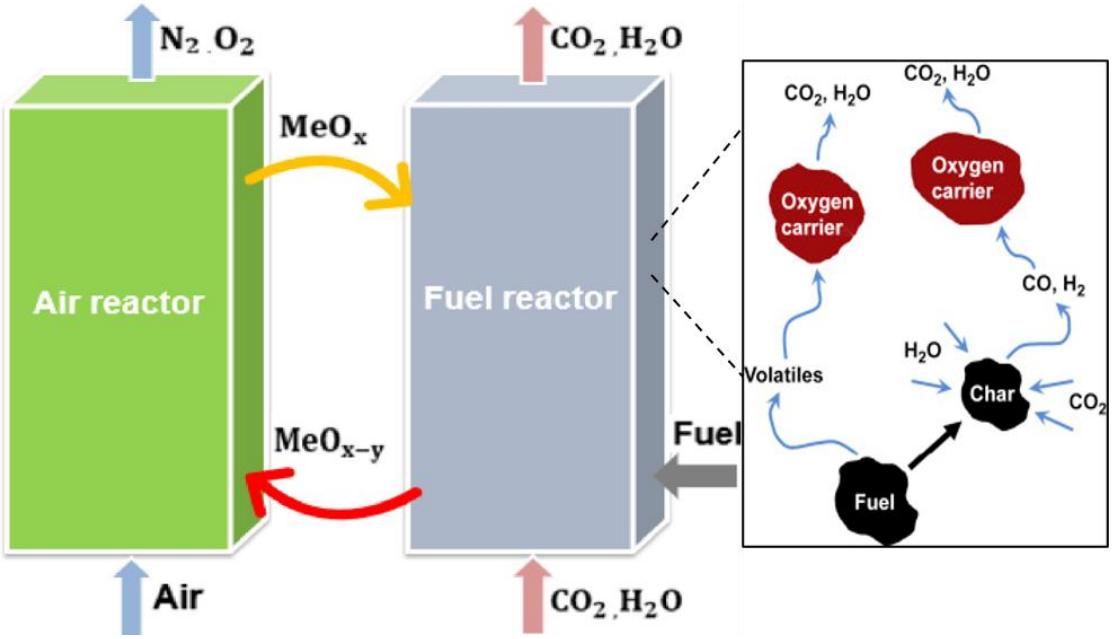

Fig 1.1. Schematic diagram of the CLC process.

Although significant developments have been made in fossil fuel combustion using the CLC technology during the last decades, the detailed inner information cannot be obtained by experiments because of complicated flow patterns in the system and poor measuring equipment. The present knowledge, understanding, and experience of the CLC process mainly come from a limited number of research groups operating small CLC plants. Besides, because the lab- or pilot-scale experimental experience cannot safely be translated to an industrial scale, the performance of the actual industrial CLC unit is still uncertain. Having a deep understanding of the dynamic characteristic and reaction performance is essential for optimal design and scale-up of the CLC system. With the development of computer technology and parallel computing, numerical simulation has become the primary method to accelerate the improvement of the CLC technology, reduce the cost of design and operating time, as well as reduce the technical risks.

1.2 Objectives

This study aims to unveil the hydrodynamic and thermodynamic characteristics of complex CFB systems, mainly taking the CLC processes as the example, and optimize the design and operating conditions by simulating the transient flow pattern, heat transfer and reactions based on the multi-fluid mathematical model. Meanwhile, the characteristics of non-uniformity phenomena in different complex CFB systems, which seriously affects the stability of the CFB system, is revealed in detail by simulation. The simulation results in this thesis bridge the data gaps missed in the bench-scale and pilot-scale experiments and provide guidance for industrial units. For optimizing the performance and improving the stability of complex CFB systems, an integrated method is proposed to realize an online regulation by coupling CFD modelling and process simulation. The following points summarise the critical objectives of mathematical model study:

1. To investigate the hydrodynamic characteristics in a full-loop dual CLC unit based on the Eulerian multi-fluid model to give more detailed information about the flow behaviours.
2. To investigate the hydrodynamic characteristics in a unique moving bed full-loop CDCL unit based on the Eulerian multi-fluid model to study the unique configuration and multiple fluidization states.
3. To investigate the reaction characteristics in the unique counter-current moving bed full-loop CDCL unit based on the hybrid Eulerian-Eulerian-Lagrangian model.
4. To investigate the non-uniformity characteristics of the gas-solid distribution in a complex DCFB unit with parallel configuration based on the Eulerian multi-fluid model. The influences of several parameters on the degree of non-uniformity are investigated.

5. To investigate the non-uniformity characteristics of the gas-solid distribution in a complex DCFB unit with the series configuration based on the Eulerian multi-fluid model. The influences of several parameters on the degree of non-uniformity are investigated.
6. To develop a novel integrated method to dynamically coupling the CFD modelling and the process simulation and realize the online regulation of boundary and operating conditions in complex CFB systems. This method is a solution to adjust the CFB issue during operating and further improve production efficiency.

1.3 Thesis structure

Based on the objectives of this work, the rest of the thesis is organized as follows:

Chapter 2 firstly presents a brief introduction about the basics and characteristics of the CFB technology, and the applications of various CFB chemical engineering processes are summarised. Then, the CLC process, as one of the most advanced and concerned CFB technologies, is focused on in this chapter. The developments about the CLC process, including the experimental and numerical studies for different units, are reviewed in detail.

In Chapter 3, a multi-fluid model based on the Eulerian-Eulerian framework is used to study the gas-solid hydrodynamics in a full-loop DCFB CLC unit. The multiple fluidization states are predicted by simulation results. The influence of two classical and two recent drag force models on gas-solid hydrodynamics in DCFB are assessed by comparing with the experimental data.

In Chapter 4, a multi-fluid model based on the Eulerian-Eulerian framework is used to study the gas-solid hydrodynamics in a full-loop moving-bed CDCL unit. In this chapter, the study is divided into two steps: Firstly, a 3D CFD model is used to investigate the

gas-solid flow in the air reactor of a CDCL unit used in this chapter. The unique fluidization state of Geldart type D particle is detailed studied. The effects of several variables in terms of the operation condition and model selections on the gas-solid flow in the air reactor are also explored, including gas velocity, specularity coefficient and different drag models. The model is qualitatively and quantitatively validated. Secondly, the validated model settings are applied to build the 3D full-loop moving-bed CDCL unit. Unique fluidization states are predicted in different domains by simulation results and are consistent with the actual experiments. And the influence of several boundary conditions on the solid circulation rate and pressure distribution are investigated. Also, the dominant factor of solid circulation rate is obtained by simulation results.

In Chapter 5, a multi-fluid model based on the hybrid of Eulerian-Eulerian-Lagrangian framework is used to study the reactive flow characteristics in a unique counter-current moving-bed CDCL unit. In the CDCL process, iron-based oxygen carriers, which belong to Geldart D particles, are used. The reaction characteristics in such a system have been seldom studied. The gas mixture and dense oxygen carrier phase are treated as the continuum with the two-fluid model (TFM) and the dilute coal powder as the discrete element with the Discrete Particle Model (DPM). Multiple homogenous and heterogeneous reactions are considered, including the redox reaction of the oxygen carrier, devolatilization, moisture release and char gasification of coal particles. Transport characteristics of discrete coal powder in the reducer under cold and hot conditions are compared to explain the mechanism of the mixing and separation behaviours between the oxygen carrier and coal in the system. A severe gas leakage phenomenon is captured by simulations, and the cause and optimization suggestion of the gas leakage are discussed in this section. The distribution of gas-solid species and reaction rates are shown to explore the reaction characteristics of this system. This work provides a deep understanding of this unique counter-current moving bed CDCL unit and can be used as a tool for further designing and optimizing similar CLC processes.

In Chapter 6 and 7, the non-uniformity characteristics of complex symmetrical DCFB units are deeply investigated in both parallel and series connection configurations using the Eulerian multi-fluid model. The non-uniformity phenomena in two symmetrical DCFB units are all verified by simulation, and the model set is validated by experimental data. The non-uniformity phenomena are discussed and evaluated in terms of bed inventory evolution and gas-solid distribution in symmetrical parts. The effects of critical operating parameters, including total bed inventory, gas aeration rate, and wall roughness on non-uniformity degree are then studied. This chapter provides an insight understanding of non-uniformity phenomena in complex CFB systems and reminds researchers to pay attention to the impact of this inevitable phenomena in the future study.

In Chapter 8, an integrated method is firstly established by combining the CFD modelling and process simulation dynamically. For illustrating the feasibility of this method, a collaborative simulation is conducted to reduce the degree of maldistribution in one symmetrical DRCFB system, which has been investigated in chapter 6, through online regulation of L-valve aeration rate based on Ansys-Fluent and MATLAB. The better operating performance after coupling with the process controller is obtained. This work provides a new method to test and optimize practical industrial CFB processes. More in-depth research can be carried out based on the work of this chapter.

Chapter 9 concludes the results and contribution of the research on the numerical simulation of complex CFB systems. Future works for future developments and the optimization of CFB related upgrading and application are presented.

To help better overview of the thesis structure, Fig 1.2 shows the diagram of the thesis structure.

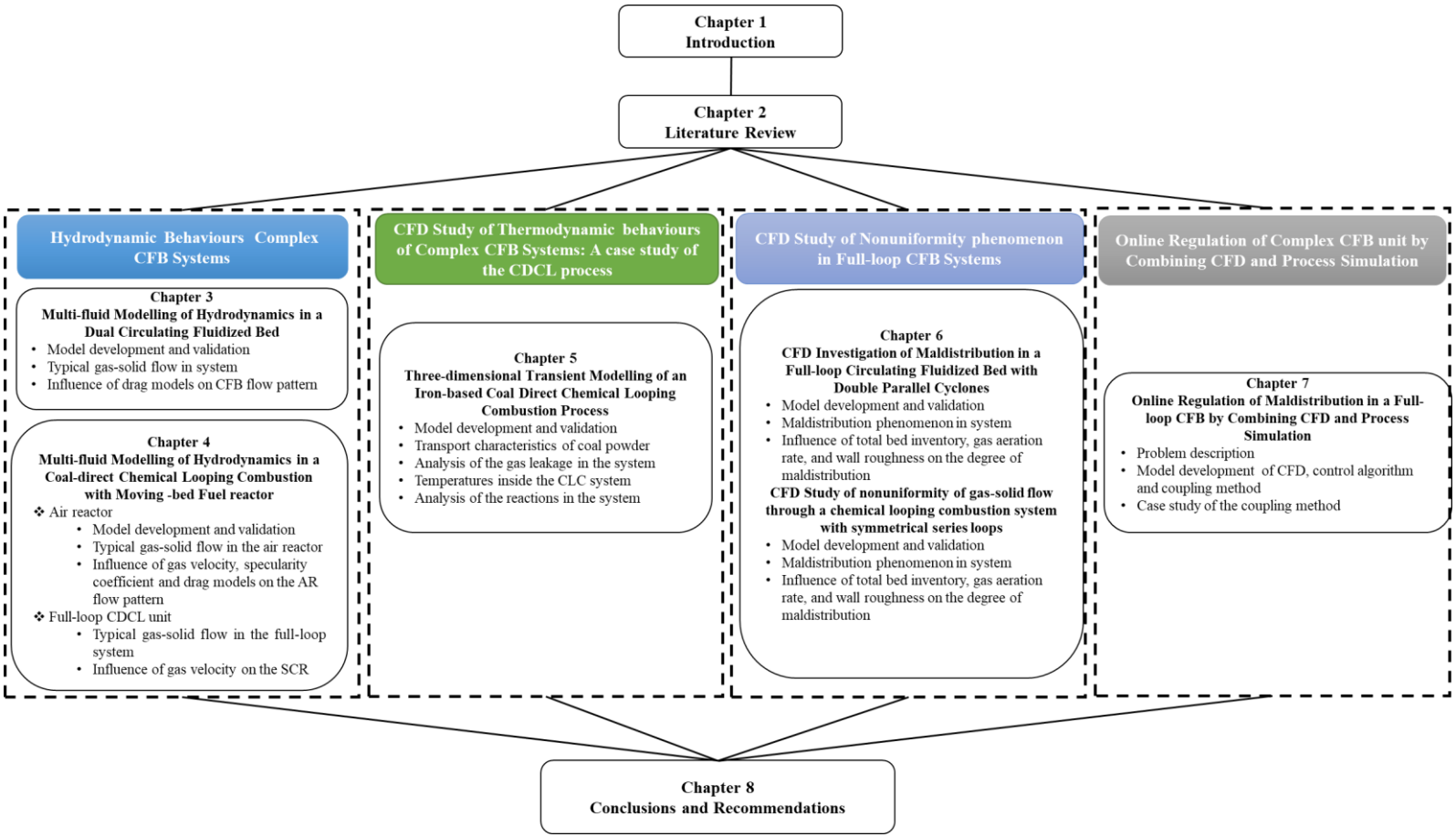

Fig 1.2. Thesis structure.

CHAPTER.2 Literature Review

In this chapter, firstly, the basics and characteristics of CFB technology are introduced, and the applications of CFB technology in the actual industrial processes are briefly summarised. Sequentially, the basics of the CLC process with the solid fuel, as an example of advanced complex CFB systems, are introduced, and the experiments and simulations of the chemical looping combustion technology are reviewed. Besides, the summary and gap of current research work are discussed.

2.1. Basics of the circulating fluidized bed

The CFB unit has been widely applied to various chemical engineering processes, including coal and biomass gasification/combustion [1–3], catalytic cracking [15,16] and Fischer–Tropsch synthesis [17,18], which benefits gas-solid contact, bed-to-wall heat transfer, catalyst regeneration, and reaction selectivity. A typical CFB unit generally consists of a riser (usually operates in fast fluidization regime) as the main reactor, one or several cyclone separators where coarser particles are captured from the product gas and returned to the bottom of the riser through a standpipe and an air-driven loop seal, as shown in Fig 2-1(a). To meet the demand of the processes that need distinct reactive environments, the dual reactor circulating fluidized bed (DCFB) technology is developed for some complex chemical engineering processes. As depicted in Fig. 2-1(b), there are two reactors in the CFB system to form a solid circulating loop, where the solid material is mainly a catalyst, reactant or thermal energy carrier. Depending on relative pressures, a DCFB can have an additional solid recycle valve between the two reactors. In Table 2-1, key features that distinguish CFB reactors from other typical fluidized bed reactors can be compared definitely.

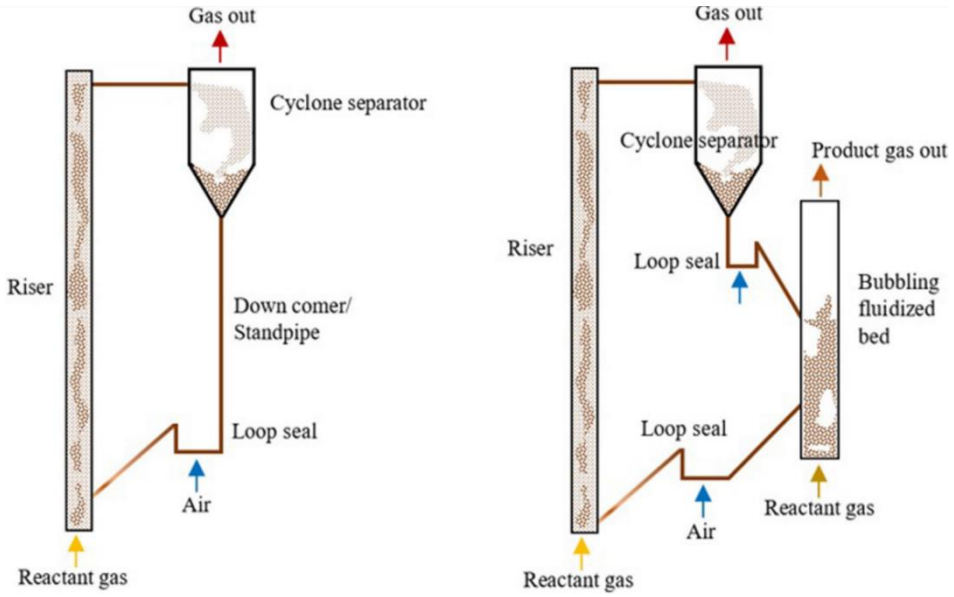

(a) (b)

Fig 2.1. Typical CFB configurations.

Table 2-1 Key features that distinguish CFB reactors from other typical fluidized bed reactors [19].

	Low-velocity fluidized bed reactors	**Circulating fluidized bed**	**Dilute-phase transport reactors**
Operation	Particles spend substantial time (minutes or hours) in the main reactor vessel. Occasional excursions occur through cyclone and standpipe.	Particles repeatedly pass through the recirculating system; residence time in the main vessel for each circuit is counted in seconds.	Once-through system
Fluidization regime	Bubbling, slugging or turbulent fluidization, with a distinct upper interface	Usually fast fluidization, though the bottom of the reactor may correspond to turbulent fluidization conditions or even bubbling	Dilute transport conditions
Range of superficial gas velocity	Below generally, 2m/s	Usually, 3 to 16 m/s	Usually, 15 to 20 m/s
Mean particle size	0.03 to 3 mm	Usually, 0.05 to 0.5 mm	Typically, 0.02 to 0.08 mm
Solid circulating flux	Low, generally 0.1 to 5 kg/m^2s	Substantial, e.g., 15 to 1000kg/ m^2s	Up to 20 kg/ m^2s
Void	Typically, 0.6 to 0.8 in bed. Much higher in freeboard above the bed	Typically, 0.8 to 0.98 averaged over the riser	Generally, >0.99
Gas mixing	Substantial axial dispersion; complex two-phase behaviour	Some gas downflow near walls typically results in intermediate gas mixing	Very little axial dispersion

2.2. Advantages and disadvantages of the circulating fluidized bed

CFB reactors (such as combustor, gasifier and pyrolizer) have many unique features that make them more attractive than other solid fuel power plants. These advantages include the following:

- Fuel flexibility is a major attractive property of CFB reactors, especially in the current market, where the price and availability of fuels fluctuate widely.

- The conversion efficiency of a CFB reactor is higher than that of a bubbling fluidized bed (BFB) reactor. Several features contribute to the high conversion efficiency of CFBs including better gas-solid mixing, higher burning rate and continuous recirculation of hot unburnt carbon particles to the furnace's base.

- Sulphur capture in a CFB is more efficient than that in the BFB reactor. A typical CFB reactor unit can capture nearly 90% of the SO_2 with only 1.5–2.5 times the stoichiometric amount of sorbent, while a BFB reactor may require 2.5–3.5 or more for the 90 % capture.

- The emission of nitrogen oxides in a CFB unit is lower than that in other typical fluidized bed reactors. It is a direct result of low combustion temperature and staged combustion air supply.

- A high heat-release rate per unit furnace cross section is a significant advantage of the CFB boiler. A BFB boiler requires a furnace grate area 2–3 times larger than a CFB boiler for a given thermal output.

- The fuel feed system is simplified in a CFB boiler due to its relatively fewer feed points. It requires less grate area for a given thermal output. Furthermore, good mixing and the extended combustion zone allow one feed point to serve a grate area much larger (>10 m^2/feed) than that in other typical fluidized bed reactors.

- A high fluidizing velocity and easy control of heat absorption allow the quick response of CFB boilers to varying loads.

Disadvantages of the CFB reactor are:

- They require significant heights for sufficient gas residence time because of their high gas velocities.
- The higher gas velocities can cause more tube erosion and solids attrition.
- A slightly higher emission of carbon monoxide and minimal decrease in combustion efficiency
- The level of automation control is required to be higher. Compared with conventional fluidized bed reactor, CFB reactor automatic control requirements than the same level of the fluidized bed furnace.

To sum up, due to a series of advantages of CFB reactors, it is crucial and necessary to improve the CFB performance by further optimization of the design and operation condition and reduce the effect of CFB disadvantages. Many efforts have been made in the practical industry and academic research.

2.3. Applications of the circulating fluidized bed system

The unique characteristics and advantages of CFB reactors have attracted much attention, resulting in broad applications in many chemical engineering processes. Several typical CFB applications in the actual industrial processes are briefly introduced in this section.

2.3.1 CFB combustion process

The CFB technology was first used for the coal combustion process because of its unique ability to handle low-quality, high-sulphur coals. This technology has been a commercial topper for over the last 60 years. Principles and applications for the operation of large scale CFB units are numerous and widespread. So far, approximate 8000 CFB combustors, most burning coals, have been put in industrial processes worldwide.

Fig 2.2 shows a typical example of a modern CFB combustion industrial process. During the CFB combustion process, raw coal particles are fluidized by high-velocity air at the bottom region. Therefore, sufficient mixing and heat transfer between solid fuel and gas can be achieved. The fluidized solid fuel burns in a relatively low-temperature

environment and generates a large amount of heat. The low in-furnace temperature limits the formation of nitrogen oxides during the combustion process whilst the limestone can be used to absorb SO_2 formed during the combustion process. The heat generated from the combustion process boils the water into high-energy steam in the water tubes, which can be used to drive a steam turbine for power generation. The cyclone separator is used to separate the entrained ash and unburnt coal particles from the flue gas and return them to the combustor's bottom.

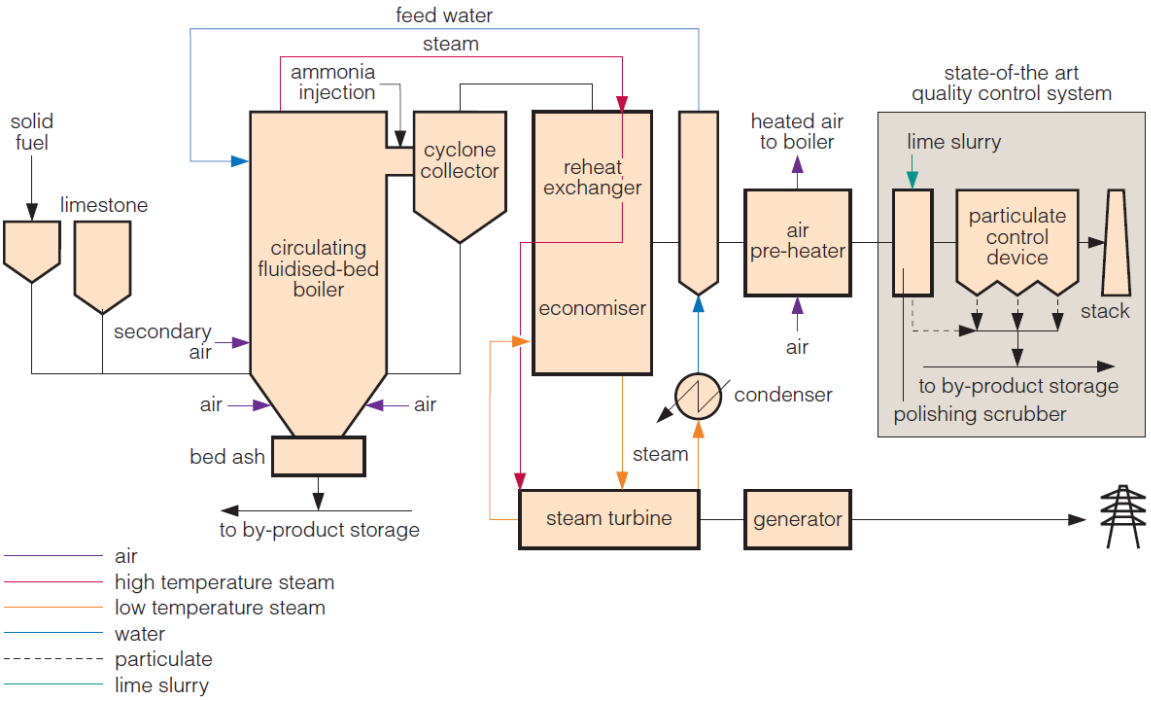

Fig 2.2. A CFB combustion power generation plant.

2.3.2 CFB fluid catalytic cracking process

Due to the increasing demand for refinery products combined with the decreasing quality of crude oils and tighter product specifications of environmental constraints, the fluid catalytic cracking (FCC) unit plays a vital role in the economy of a modern refinery industry, as the primary conversion process of crude oil to lighter products [20]. FCC can process a wide range of feedstocks and is suitable to operate in unique campaigns that may soon include coprocessing renewable feedstocks [21–23]. Up to date. More than 400 FCC units are operated around the global [24].

A series of complex reactions occur when a large gas oil molecule contacts the FCC catalyst. The whole process can be divided into three steps: reaction, product separation, and regeneration. A typical layout of the FCC process is shown in Fig 2.3. In this cyclic process, gas oils from vacuum distillation towers and residues from atmospheric distillation towers are converted into lighter products. One of the desired products is cracked naphtha, the major constituent of the gasoline pool [19]. Operating conditions comprise high reaction temperatures in the range of 750-800 K and pressures close to atmospheric conditions. Lifting productivity, increasing energy efficiency, and minimizing operating costs are also future objects to FCC units' profitability.

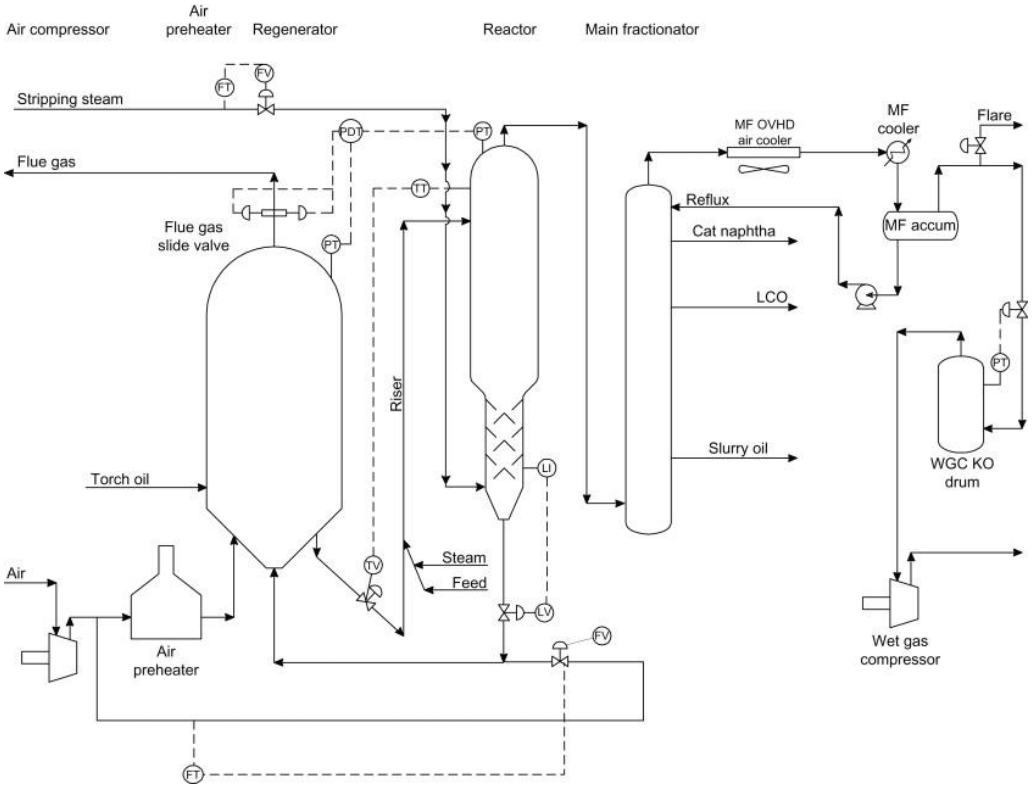

Fig 2.3. A CFB FCC process flow diagram.

2.3.3 CFB gasification process

Typical coal gasification involves converting coal particles and air (or high-purity oxygen) into a series of gaseous products, mainly including CO, H_2, CO_2, H_2O, CH_4 and N_2, and mineral residues. Gasification is an efficient way to improve the solid fuel quality by converting it into a gas fuel. The typical gasification process, as shown in Fig 2.4, can be

divided into the several steps. Firstly, the moisture in the solid feedstock is released at a temperature which is strongly relevant to the pressure inside the furnace. Then, the multiple organic components in the solid fuel decompose to the oxygen-deprived atmosphere at elevated temperatures (600–900 K) [25]. This results in the release of light gases (volatile matter) and high molecular-weight hydrocarbons (tar) and the formation of a carbonized residue (char). Sequentially, the volatile matter species and some of the char react with oxygen in the air or high purity oxygen to form CO_2, CO and H_2O, and produces heat for the subsequent gasification reactions. Finally, the remaining char residue reacts with CO_2 and H_2O in the furnace to produce the syngas with a high CO and H_2 content.

Currently, a number of large-scale CFB plants are being built or commissioned to prove the good performance of gasification technology. For example, gasification can be combined with power generation using IGCC power plants to efficiently and cleanly generate energy. Large energy companies, such as Shell, GE, ConocoPhillips, and Siemens, have built many IGCC facilities around the world [26]. Compared with incineration and combustion of the solid fuel, the utilization of syngas produces less solid waste and emits fewer harmful gases into the atmosphere [27]. Besides, the gasification process installs small, low-cost, efficient reactors to reduce storage and transport costs.

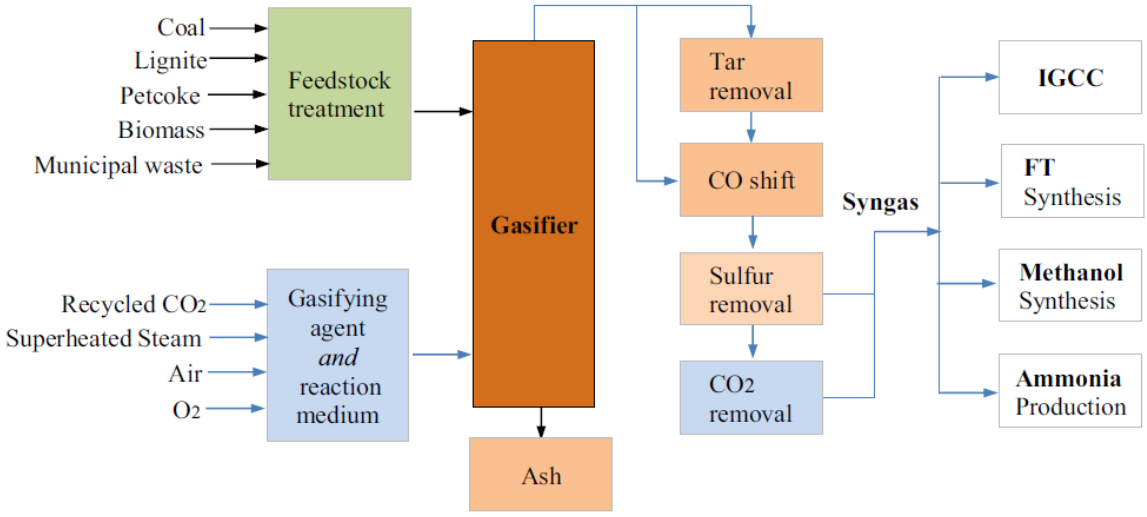

Fig 2.4. A CFB gasification power generation plant.

2.3.4 CFB pyrolysis process

Pyrolysis technology is an old power technology and has been applied for thousands of years. The pyrolysis process directly gives high yields of liquids of up to 75 wt.%, which can be directly used in a variety of applications [7] or used as an efficient energy carrier. In the last 30 years, the fast pyrolysis at moderate temperatures of around 500 °C and very short reaction times of up to 2 s has attracted the considerable interest from the industry [6].

Coal pyrolysis is a thermal decomposition process occurring in the absence of O_2 environment. It mainly can be divided into three operating environments: (1) lower reaction temperatures and longer vapour residence times are beneficial for the production of charcoal, (2) moderate temperatures and short vapour residence time are optimum for producing liquid products, and (3) high temperatures and longer residence times improve the solid fuel conversion. Three types of products are always produced simultaneously, but the proportions can be varied over a wide range by adjustment of the process parameters. The CFB pyrolizer can lead to higher char contents in the collected bio-oil unless more extensive char removal is included because the residence time of the char particles is almost the same as the vapours in the system, and the attrition of char particles is more severe due to the higher gas velocities. A typical layout of CFB pyrolysis process is shown in Fig 2.5. Although the hydrodynamics of CFB pyrolizer are more complex, this technology has been widely used at very high throughputs in the petroleum and petrochemical industry.

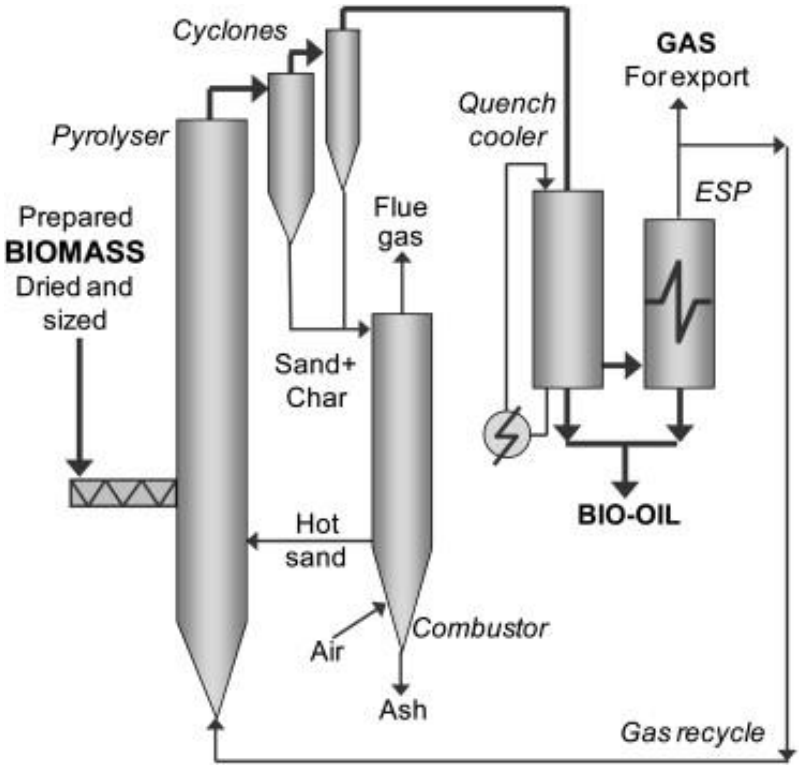

Fig 2.5. A CFB pyrolysis power generation plant.

To sum up, the CFB is an advanced reactor configuration for many chemical engineering processes and has been widely applied in current industrial processes. CLC technology is a promising combustion technology among various chemical engineering processes and has been a hot concern in recent years due to its excellent performance. Meantime, all the CLC processes are made up of a complex CFB configuration. In this thesis, the CLC process is taken as the main example to study both hydrodynamic and thermodynamic behaviours of complex CFB system.

2.4. Basics of the CLC process with solid fuel

Solid fuels have been widely used in the CLC systems, such as coal, petroleum coke, solid wastes or biomass, which are considerably more abundant and less expensive than natural gas. Comparing with the gaseous fuel, the CLC process with solid fuels is more complicated because of the heterogeneous material and multiple organic matters (carbon, hydrogen, oxygen, nitrogen, and sulphur) and mineral matter (ash, subsequent to combustion and gasification). In most CLC units with the solid fuel, the solid feedstock is directly fed into the FR and mixed with the oxygen carrier material. The combustion of solid fuels using chemical looping technology has been commonly performed using

two different approaches. One approach is the in-situ Gasification Chemical-Looping Combustion (iG-CLC), where the gasification of the solid fuel takes place in-situ by fluidization agent after injection into the FR. The other approach is the so-called Chemical-Looping with Oxygen Uncoupled (CLOU) process, where the solid fuel is burned with gaseous oxygen released by the oxygen carrier in the FR. The detailed reaction processes are described below.

2.4.1 In-situ Gasification Chemical-Looping Combustion (iG-CLC)

The iG-CLC concept (Fig 2.6), has been widely used in many CLC units due to the potential to obtain higher power efficiencies and lower costs than other evaluated technologies [28].

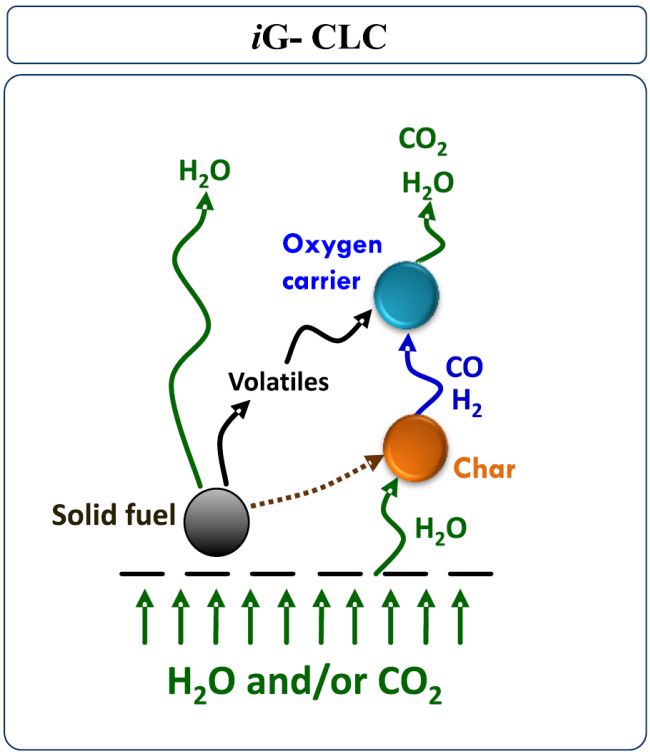

Fig 2.6. Scheme of the iG-CLC process for solid fuel combustion.

In this approach, the solid fuel particles are fed into the hot FR and mixed with a large amount of oxygen carrier particles. With the increase of temperature, the devolatilization of raw coal takes place first, releasing the volatile matter (R(2-1)):

$$Coal \rightarrow Volatile\ matter + Char \qquad \text{R(2-1)}$$

Subsequently, char is generated and continues to flow in the FR under the action of various forces (gravity, drag, lift and so on). The solid-solid reaction between char and oxygen carrier can take place if a close contact between solid particles is ensured. However, this interaction is not relevant for most of FRs in CLC units where the gas-solid contact is dominant contact mode. Therefore, steam or carbon dioxide is supplied as fluidization agent to promote char gasification reaction and release of gasification products (H_2/CO) (R(2-2), R(2-3)).

$$Char + H_2O \rightarrow H_2 + CO \qquad \text{R(2-2)}$$

$$Char + CO_2 \rightarrow 2CO \qquad \text{R(2-3)}$$

Next, the oxygen-carrier is reduced by volatiles and gasification products in the FR (R(2-4), R(2-5), R(2-6))

$$C_xH_y + xMeO_a \rightarrow xCO + \frac{y}{2}H_2 + xMeO_{a-1} \qquad \text{R(2-4)}$$

$$CO + MeO_a \leftrightarrow CO_2 + MeO_{a-1} \qquad \text{R(2-5)}$$

$$H_2 + MeO_a \leftrightarrow H_2O + MeO_{a-1} \qquad \text{R(2-6)}$$

The reduced oxygen carrier then is transported to the AR and is oxidized by the air to regenerate the new oxygen carrier, depicted by R(2-7).

$$\frac{1}{2}O_2 + MeO_{a-1} \leftrightarrow MeO_a \qquad \text{R(2-7)}$$

Among these reactions, the gasification step of the char is the limiting step in the coal conversion in the FR.

2.4.2 Chemical-Looping with Oxygen Uncoupling (CLOU)

Due to the slow char gasification rate in the iG-CLC process, another approach is newly proposed in recent years, called the Chemical-Looping with Oxygen Uncoupling (CLOU) process. The implementation of the CLOU process is based on the special property of an oxygen-carrier which can release gaseous oxygen directly to the FR and the solid fuel can be burnt by gaseous oxygen (Fig. 2.7). In this way, the limited gasification rate in the iG-CLC is avoided and a much faster solid conversion is obtained. Moreover, it has been proven that less amount of the oxygen carrier is consumed in the CLOU system, which is beneficial to reduce the reactor size and operation costs.

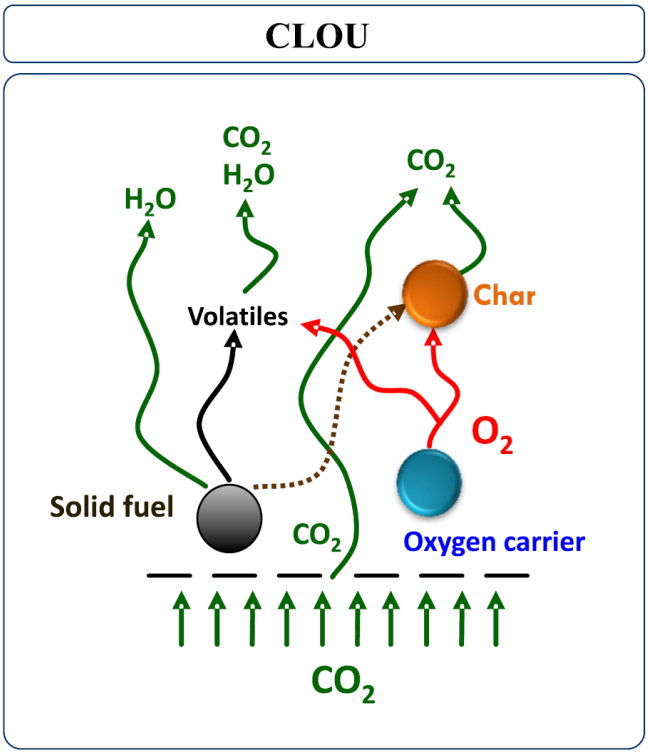

Fig 2.7. **Schematic** of the CLOU process for solid fuel combustion.

In this method, the oxygen carrier particle releases the gaseous oxygen through R(2-8) first:

$$MeO_a \leftrightarrow MeO_{a-1} + \frac{1}{2}O_2 \qquad \text{R(2-8)}$$

Then, the solid fuel reacts with the gaseous oxygen directly, as the conventional combustion process, and produces the CO_2 and steam:

$$C_xH_y + (x + \frac{y}{4})O_2 \rightarrow xCO_2 + \frac{y}{2}H_2O \qquad \text{R(2-9)}$$

Finally, same as the R(2-7), the reduced oxygen carrier is transported to the AR where it reacts with the gaseous oxygen in the combustion air.

Many advantages of the CLOU process have been proposed by comparing with the iG-CLC process. Due to the unique characteristics of the oxygen carrier material, the experience in operating the CLOU process to burn solid fuels is still very limited.

2.5. Status development of chemical looping combustion units

The 10 kWh CLC unit with solid fuel at the Chalmers University of Technology (CUT) designed by Berguerand and Lyngfelt (2008) [29] is the first successful attempt to realize the 22 h continuous operation. In the last decade, many CLC plants have been built and tested worldwide. Many researchers have carried out amounts bench-scale or pilot-scale experiments to explore the characteristics of flow, heat transfer, and mass transfer inside various CLC units. By 2020, there are 22 testing CLC plants worldwide burning solid fuels, ranging from 0.5 kWh to 4 MWh. The total operational time has exceeded 4000 h for over 100 experiments. Many researchers have conducted fundamental experiments to find out optimum operating conditions of industrial units. The typical CLC units will be described in the following sections. For understanding the development of multiple CLC

processes clearly, several representative CLC processes with different configurations in different research groups are introduced.

2.5.1 Chalmers University of Technology (CUT, Sweden)

The first attempt of 10 kWh CLC system with solid fuels was started in 2008 by Berguerand and Lyngfelt at CUT [29]. They tested the combustion of bituminous coal and petcoke in a 10 kWh experimental rig for solid fuels. The significant changes to adapt CLC to solid fuels were related to the fuel-reactor design and the type of oxygen-carrier. This plant comprised two interconnected fluidized bed as an oxidizer (AR) and reducer (FR), as shown in Fig 2.8. The reducer consisted of three chambers: a bubbling fluidized bed (BFB) where coal particles were devolatilized and gasified at a low-velocity condition, a carbon stripper where oxygen carrier particles and unburnt coal particles can be separated, and a high-velocity domain where char can be conveyed back to the reducer via a small cyclone separator. The oxidizer was a riser reactor to regenerate oxygen carrier and entrain particles back to the reducer. Different solid fuels: bituminous coal, petroleum coke and wood char had been successfully tested in this unit by mainly using Fe-based oxygen carriers. Meantime, the performances of several different oxygen carriers were also tested by experiments, such as manganese ore and ilmenite based on this unit. Many operational parameters variations, such as particle circulation, fluidizing velocities, fuel load and fuel reactor temperature were tested, and the influence on the operation performance include CO_2 capture, solid fuel and gas conversions from the fuel reactor were discussed.

Although some significant practical problems were observed during experiments, such as fuel feeding and gas analysis, this first continuous test provided proof of concept for chemical-looping combustion of solid fuels. Relevant experimental experiences for the 10 kWh CLC unit at CUT can be found in Table 2-2.

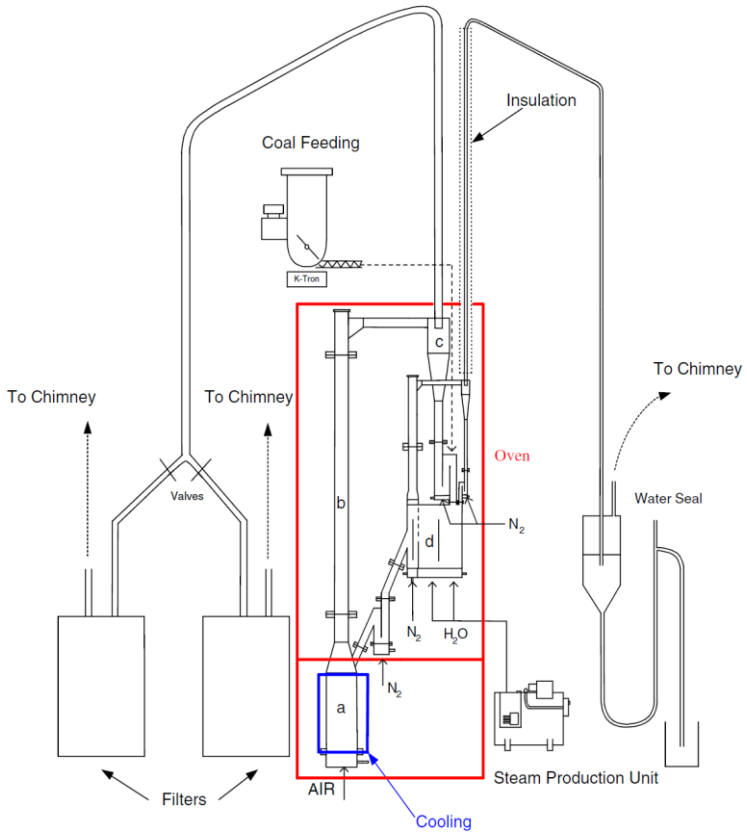

Fig 2.8. Sketch of 10 kWh CLC system at CUT: air reactor (a), riser (b), air reactor cyclone (c), and fuel reactor (d) [29].

Table 2-2 Experiments of 10 kWh CLC unit at CUT.

Operator	Total operation	Solid fuel	Oxygen carrier	Process	Year
CUT, Sweden [29,30]	22h (coal) 11h (Petcoke)	Coal/Petcoke	Ilmenite	iG-CLC	2008
CUT, Sweden [31]	44h	Petcoke	Ilmenite	iG-CLC	2009
CUT, Sweden [32]	-	Petcoke	CuO	CLOU	2009
CUT, Sweden [33]	4h (mixture) 4h ($FeTiO_3$)	Petcoke	Lime+ ilmenite	iG-CLC	2011
CUT, Sweden [34]	28.5h (Ilmenite) 10.5h (Mn ore)	Coal/Petcoke	Ilmenite Manganese ore	iG-CLC	2012
CUT, Sweden [35]	9.2h (Mn ore) 6h (Mn ore + lime)	Petcoke	Manganese ore Manganese ore+ lime	iG-CLC	2013

CUT, Sweden [36]	29h	Petcoke/Wood char	Calcium Manganate	CLOU	2014
CUT, Sweden [37]	16h (Mangagran) 14.6h (Sinfin) 11.5h (Mesa)	Petcoke/Wood char	Mangagran Sinfin Mesa	iG-CLC	2016
CUT, Sweden [38]	32h	Wood char/Coal Petcoke/Lignite	Manganese-silicon-titanium	iG-CLC	2018
CUT, Sweden [39]	-	Biomass	Ilmenite	iG-CLC	2020

Lyngfelt et al. [40,41] built a 100 kWh CLC experimental unit for solid fuels in 2012. This unit contained two interconnected circulating fluidized beds, as shown in Fig 2.9. There was also one crucial component called carbon stripper, which had four chambers for high-efficiency separation of char particles. The FR was 5 m high with an inner diameter of 0.154 m, and the AR was 4 m tall with a riser having the same size as the fuel reactor and an expanded bottom section with a diameter of 0.4 m. Firstly, the oxygen carrier particles were entrained by the high-velocity gas introduced from the bottom of the AR (riser). A reasonable solid circulation rate can be obtained by adjusting the inlet gas velocity of AR and FR. The oxygen carrier used was ilmenite, an iron-titanium oxide. Coal was fed directly into a loop seal, leading to the fuel reactor, through a set of screws. All parts of the unit were fluidized with steam, except for the air reactor, which was fluidized with air, and the loop seal with the fuel insertion, which was fluidized with nitrogen. Gas conversion, solid fuel conversion and carbon capture efficiency were discussed under different operating conditions. Through a series of experimental studies, the operation had been proven stable and the CO_2 capture efficiency was high. These works showed the first extended operation of chemical looping combustion with solid fuels in the 100 kWh scales. The operational experience gave a strong indication that the process is viable. Relevant experimental experiences for the 100 kWh CLC unit at CUT can be found in Table 2-3.

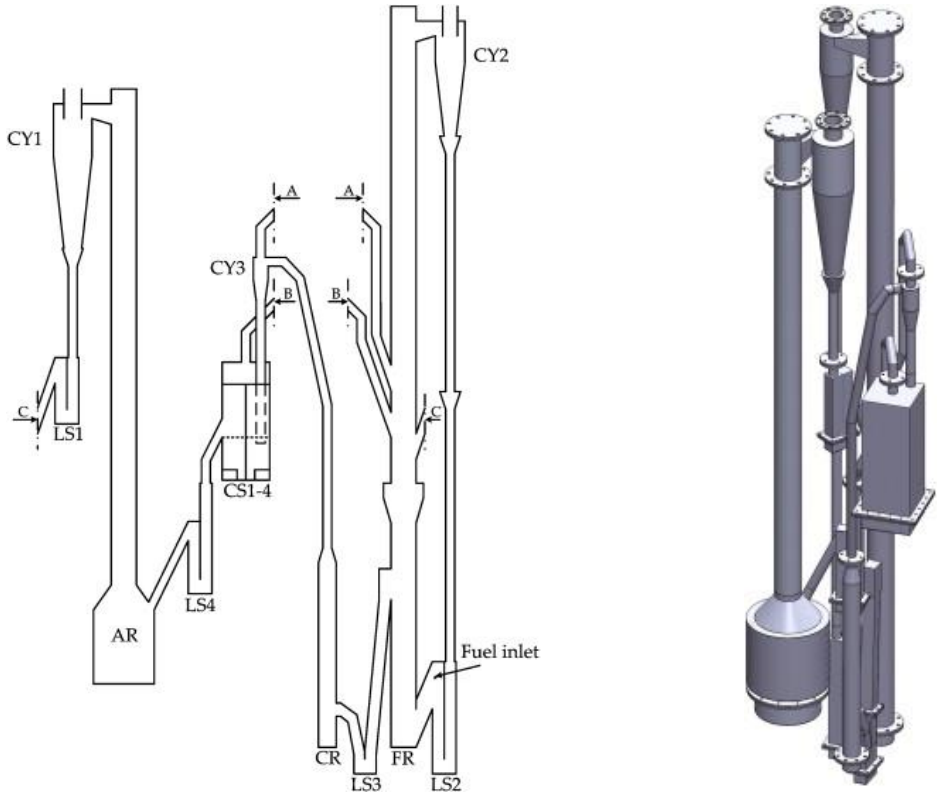

Fig 2.9. A 2D and 3D sketch of the 100 kWh unit at CUT [40,41].

.

Table 2-3 Experiments of 100 kWh CLC unit at CUT

Operator	Total operation time	Solid fuel	Oxygen carrier	Process	Year
CUT, Sweden [40,41]	10h (cold) 70min (hot)	Coal	Ilmenite	iG-CLC	2012
CUT, Sweden [42]	20h	Coal	ilmenite	iG-CLC	2013
CUT, Sweden [43]	8 ~32min	Coal Petcoke	Ilmenite	iG-CLC	2014
CUT, Sweden [44]	31h (wood char) 3.5h (coal)	Wood char Coal	Ilmenite	iG-CLC	2014
CUT, Sweden [45]	12h	Coal	Ilmenite	iG-CLC	2014
CUT, Sweden [46]	18h	Wood char Coal	Ilmenite+ Manganese ore	iG-CLC	2016
CUT, Sweden [47]	51.5h	Wood char Coal Petcoke	Sinaus	iG-CLC	2017

CUT, Sweden [48]	18.6h	Biomass	calcium manganite + ilmenite	iG-CLC	2019

2.5.2 Southeast University (SU, China)

The research group of Professor Shen at Southeast University (SU) has built and tested two CLC units for 1 and 10 kWh, respectively. These two units have a similar configuration for the AR using a riser and fuel reactor using a spouted bed, as shown in Fig 2.10. These two units have been successfully tested using coal and biomass as solid fuels and Fe-based with Ni-based oxygen carriers.

In 2009, a 1 kWh CLC process for coal using interconnected fluidized beds was proposed at SU, China. It is composed of a high-velocity fluidized bed as AR, a cyclone, and a spout-fluid bed as FR. The AR is connected to the spout-fluid bed through a cyclone. There are two reduction paths in the FR, direct reduction of oxygen carrier by coal and indirect reduction by the syngas of coal gasification. The AR is a circular column of 20 mm in inner diameter and 1600 mm in height. The FR is a rectangular bed, with a cross section of 50×30 mm^2, and a height of 1000 mm. The loop-seal connects the FR with the AR, and it is a rectangular bed with a cross section of 34×30 mm^2, and a height of 370 mm. For improving the coal conversion efficiency, a spout-fluid bed is adopted for the FR instead of a BFB, because of strong solids mixing and long residence time of coal particles in the spout-fluid bed. Relevant experimental experiences of the 1 kWh CLC unit at SU can be found in Table 2-4.

In the same year, a 10 kWh CLC process for biomass was conducted in a continuous interconnected fluidized bed. It has a similar configuration with the 1 kWh one, which is composed of a fast fluidized bed as AR, a cyclone and a spouted bed as FR. The inner diameter of AR is 50 mm, and the height is 2000 mm with a perforated plate as the air distribution. The cross section of the FR is 230 ×40 $mm^{2,}$ and the height is 1500 mm. The inner seal with a cross area of 23 × 40 mm^2 allows particles movement from the reaction chamber to the AR and prevents the bypassing of the flue gas from the AR to the FR. Relevant experimental experiences can be found in Table 2-5.

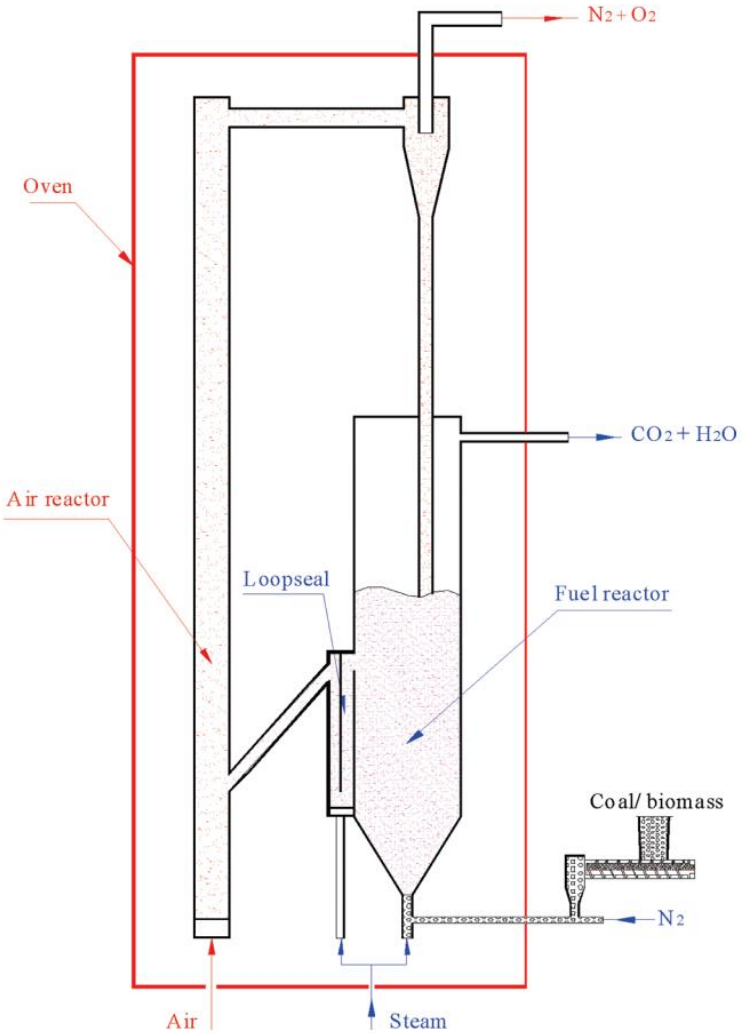

Fig 2.10. Sketch of 1 kWh and 10 kWh CLC system at SU [49][50].

Table 2-4 Experiments of 1 kWh CLC unit at SU.

Operator	Total operation time	Solid fuel	Oxygen carrier	Process	Year
SU, China [49]	-	Coal	NiO	IG-CLC	2009
SU, China [51]	30h	Coal	NiO/Al_2O_3	IG-CLC	2010
SU, China [52]	-	Coal/Biomass	Iron ore	IG-CLC	2011
SU, China [53]	-	Coal	NiO/Al_2O_3	IG-CLC	2012
SU, China [54]	20h	Coal	Natural hematite	IG-CLC	2013
SU, China [55]	2h	Coal	K_2CO_3-modified iron ore	IG-CLC	2014
SU, China [56]	-	Coal	Iron ore	IG-CLC	2015
SU, China [57]	5h	Coal	CaO-modified iron ore	IG-CLC	2015
SU, China [58]	10h	Coal	Natural hematite	IG-CLC	2015
SU, China [59]	5h	Sewage sludge/Coal	Natural hematite	IG-CLC	2016
SU, China [60]	-	Sewage sludge	Iron ore	IG-CLC	2019

Table 2-5 Experiments of 10 kWh CLC unit at SU.

Operator	Total operation time	Solid fuel	Oxygen carrier	Process	Year
SU, China [50]	30h	Biomass	Iron oxide	IG-CLC	2009
SU, China [61]	100 h	Coal	NiO/Al_2O_3	IG-CLC	2009

2.5.3 Instituto de Carboquímica (ICB-CSIC, Spain)

The research group from the Consejo Superior de Investigacions Cientificas (ICB-CSIC) had successfully run two CLC units with lab- and pilot scales. These two CLC units can be operated both in iG-CLC and CLOU modes. The first experimental continuous CLC unit (nominal power 0.5 kWh in iG-CLC and 1.5 kWh in CLOU) [62] was shown in Fig 2.11. It was composed of two interconnected fluidized-bed reactors as the AR and FR, respectively. Two reactors were connected by a loop seal and a riser was used for solids transport from the AR to the FR, a cyclone and a solids valve were adopted to control the solids circulation flow rate in the system.

The AR consisted of a bottom BFB with 80 mm of inner diameter and 100 mm height and followed by a riser with 30 mm diameter. The FR consisted of a BFB with 50 mm diameter and 200 mm height. Another 50 kWh CLC unit [63] for solid fuels was performed in 2014. The unit also can be operated both in iG-CLC and CLOU modes, with the power of 20 kWh for iG-CLC and 50 kWh for CLOU process. It was composed of two interconnected circulating fluidized beds as the AR and FR. a carbon stripper was contained to improve the carbon capture efficiency. The AR consisted of a bottom BFB with 30 cm of inner diameter and followed by a riser with 10.2 cm diameter. The total height of the AR was 4.80 m. The FR consisted of a BFB with 11.2 cm diameter and followed by a riser with 8.1 cm diameter and the total height was 4.15 m. Extensive experiments were performed using two CLC units to test different materials of the oxygen carrier, solid fuel types and methods to limit pollutant emissions. Relevant experimental experiences for the CLC processes at ICB-CSIC can be found in Table 2-6 and Table 2-7.

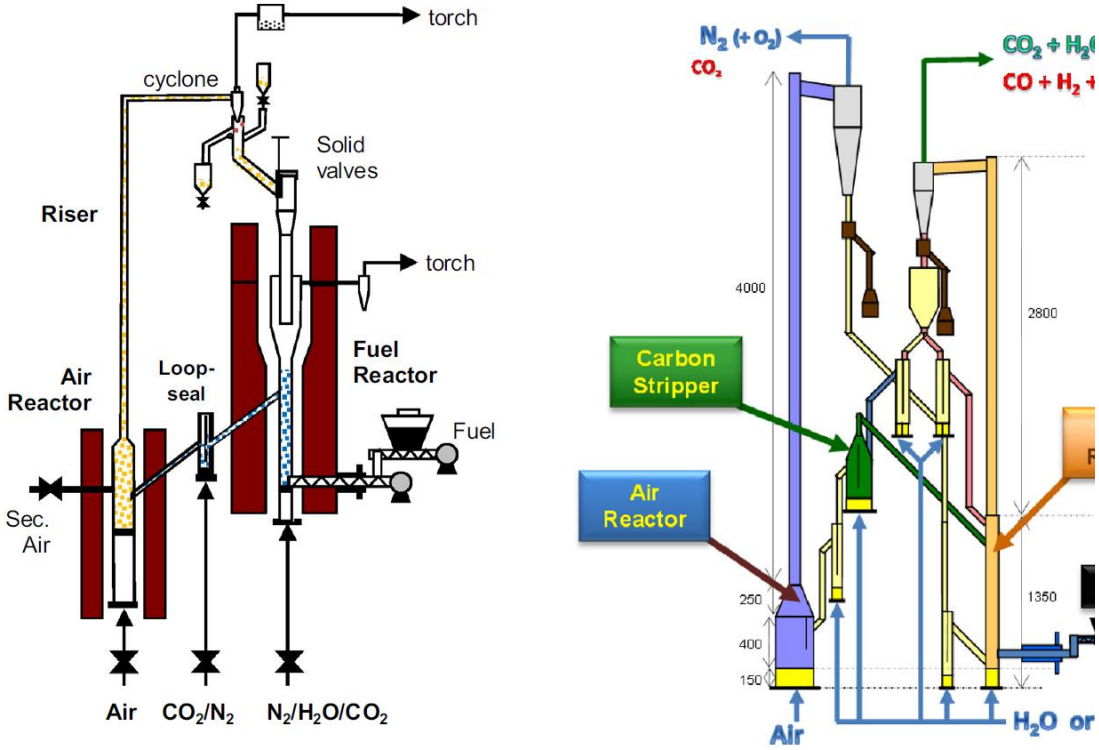

(a) (b)

Fig 2.11. Sketch of lab-scale [62] and pilot-scale [63] CLC system at ICB-CSI.

Table 2-6 Experiments of 1.5 kWh CLC unit at ICB-CSIC

Operator	Total operation time	Solid fuel	Oxygen carrier	Process	Year
ICB-CSIC [62]	43h	Coal	Fe_2TiO_5, Fe_2O_3, TiO_2	iG-CLC	2011
ICB-CSIC [64]	35h	Coal	$FeTiO_3$	iG-CLC	2011
ICB-CSIC [65]	30h	Coal	CuO, $MgAl_2O_4$	CLOU	2012
ICB-CSIC [66]	-	Coal	$FeTiO_3$	iG-CLC	2012
ICB-CSIC [67]	-	Coal	Cu60MgAl	CLOU	2013
ICB-CSIC [68]	-	Coal	Fe_2O_3, β-Al_2O_3 Cu60MgAl	iG-CLC CLOU	2013
ICB-CSIC [69]	40h	Coal	Fe_2O_3, β-Al_2O_3	iG-CLC	2013
ICB-CSIC [70]	78h	Pine sawdust	Fe_2O_3	iG-CLC	2013
ICB-CSIC [71]	15h	Lignite	CuO, $MgAl_2O_4$	CLOU	2014

ICB-CSIC [72]	55h	Coal	Fe_2TiO_5, Fe_2O_3	iG-CLC	2014
ICB-CSIC [73]	50h	Coal	Fe_2O_3	iG-CLC	2014
ICB-CSIC [74]	10h	Pine wood	Cu60AlMg	CLOU	2014
ICB-CSIC [75]	35h	Lignite	Cu50Fe, MgAl	CLOU	2016
ICB-CSIC [76]	78h (iG-CLC) 12h (CLOU)	Pine sawdust	Fe_2O_3, Cu60MgAl	iG-CLC CLOU	2016
ICB-CSIC [77]	100h (Fe_2TiO_5) 210h (Fe_2O_3) 120h (CuO) 16h ($Cu_{1.5}Mn_{1.5}O_4$) 10h ($(Mn_{0.66}Fe_{0.34})_2O_3$)	Coal	Fe_2TiO_5, Fe_2O_3, CuO, $Cu_{1.5}Mn_{1.5}O_4$, $(Mn_{0.66}Fe_{0.34})_2O_3$	iG-CLC CLOU	2017

		Pine sawdust			
ICB-CSIC [78]	70h	Olive stones	Fe_2O_3	iG-CLC	2017
		Almond shells			
ICB-CSIC [79]	62h	Coal	$Cu_{1.5}Mn_{1.5}O_4$, Mn_3O_4	CLOU	2017
		Pine sawdust			
ICB-CSIC [80]	40h	Olive stones	Fe_2O_3	CLOU	2018
		Almond shells			
		Pine sawdust			
ICB-CSIC [81]	10h (Cu60MgAl) 65h (Cu34Mn66)	Olive stones	Cu60MgAl Cu34Mn66	CLOU	2018
		Almond shells			
ICB-CSIC [82]	50h	Coal	$Cu_{1.5}Mn_{1.5}O_4$	CLOU	2018
ICB-CSIC [83]	10h	Coal	$(Mn_{0.77}Fe_{0.23})_2O_3$	IG-CLC	2018

		Pine sawdust			
ICB-CSIC [84]	65h	Olive stones	$Cu_{1.5}Mn_{1.5}O_4$, Mn_3O_4	CLOU	2018
		Almond shells			
ICB-CSIC [85]	-	Coal	Mn_2O_3- Fe_2O_3	IG-CLC	2018
	15.4h (Pine sawdust)	Pine sawdust		IG-CLC	
ICB-CSIC [86]	16.9h (Olive stones)	Olive stones	Cu34Mn66-GR		2019
	22h (Almond shells)	Almond shells		CLOU	
		Pine sawdust			
ICB-CSIC [87]	65h	Olive stones	Cu60MgAl/Cu34Mn66	CLOU	2019
		Almond shells			

		Pine sawdust			
ICB-CSIC [88]	160h	Olive stones	Mn_3O_4/Fe_2O_3	IG-CLC	2020
		Almond shells			
ICB-CSIC [89]	75h	Coal	$(Mn_{0.66}Fe_{0.34})_2O_3 \cdot (TiO_2)_{0.15}$	CLOU	2020
ICB-CSIC [90]	38h	Pine wood	Fe_2O_3/Al_2O_3	IG-CLC	2020
ICB-CSIC [91]	55h	Pine wood	Ilmenite	IG-CLC	2020

Table 2-7 Experiments of 50 kWh CLC unit at ICB-CSIC

Operator	Total operation time	Solid fuel	Oxygen carrier	Process	Year
ICB-CSIC [63]	-	Coal	Ilmenite (iG-CLC) CuO, $MgAl_2O_4$ (CLOU)	IG-CLC	2014
ICB-CSIC [92]	-	Coal	Ilmenite (iG-CLC) CuO, $MgAl_2O_4$ (CLOU)	iG-CLC CLOU	2015
ICB-CSIC [93]	50h	Coal	Fe_2TiO_5, Fe_2O_3, TiO_2	iG-CLC	2016
ICB-CSIC [77]	100h	Coal	Fe_2TiO_5	iG-CLC	2017
ICB-CSIC [94]	-	Coal	ilmenite/ iron-ore	IG-CLC	2020

2.5.4 Huazhong University of Science and Technology (HUST, China)

The exploration of CLC technology at Huazhong University of Science & Technology (HUST) has experienced rapid improvement in the past 10 years, under the guidance of Prof. Zhao. A 5 kWh lab-scale [95] and 50 kWh pilot-scale [96] CLC units were developed at HUST.

For the 5 kWh lab-scale CLC unit (Fig 2.12), a bottom BFB and upper fast fluidized bed were connected to realise the function of the FR. The BFB provided enough residence time of fuel, whilst the fast fluidisation bed provided fast transportation of oxygen carrier. The AR is in the turbulent fluidisation state during the operation. Based on the operational experience attained in the 5 kWh CLC reactor with coal, a 50 kWh CLC reactor was developed in 2018. The 50 kWh unit was similar to the configuration of the 5 kWh CLC plant (Fig 2.13), but a carbon stripper was added after the FR to enhance residual char the conversion. In recent years, a series of experimental tests were conducted to investigate the performance of the two CLC reactors at HUST under different operational parameters. Over 300 h of continuous operation experience of HUST CLC units contributes to the demonstration of this technique.

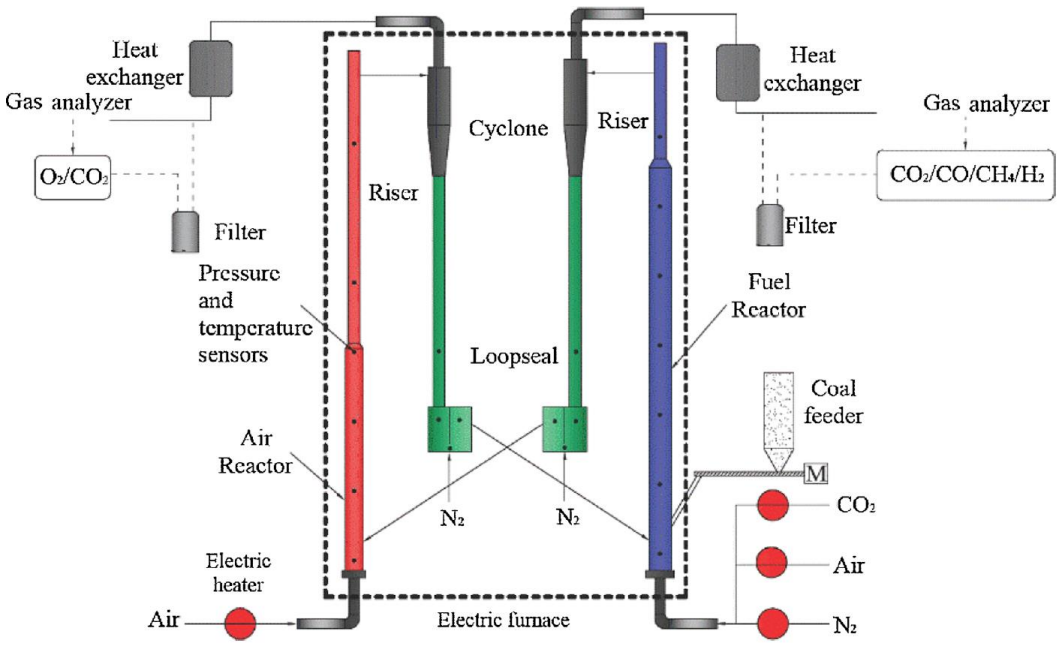

Fig 2.12. A sketch of 5 kWh CLC system at HUST [95].

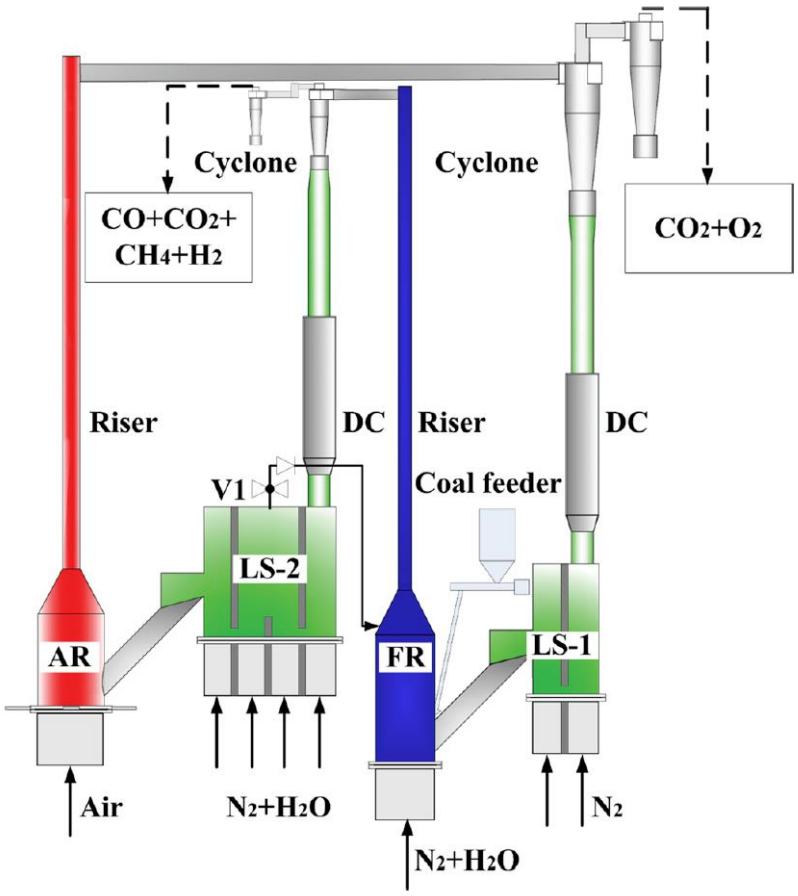

Fig 2.13. A sketch of 50 kWh CLC system at HUST [96].

2.5.5 Ohio State University (OSU)

At Ohio State University (OSU), a 25 kWh pilot-scale Coal-Direct Chemical Looping (CDCL) plant has been built for electric power generation with the characteristic of inherent CO_2 capture [97–101]. The schematic geometry of the 25 kWh CDCL sub-pilot system constructed at OSU is shown in Fig. 2.14(a). It can be seen that the CDCL unit consists of two main reactors, a combustor (or AR) and a reducer (or FR), and these two reactors were connected by a cyclone and a non-mechanical L-valve to form a circulation loop. The FR in this CDCL unit adopted a counter-current moving bed design where the solid oxygen carriers moved down by virtue of gravity in a dense phase. In contrast, gases, such as the fuel gasification enhancer (CO_2 or steam) as well as the gasification products, move upward, counter-current to the solids flow direction. The gas-solid counter-current moving bed provides many advantages over a fluidized bed such as greater control of the fuel residence time and conversion as well as of the oxygen carrier conversions. The reduced oxygen carrier particles exit the reducer through a non-mechanical L-valve and

flow into the combustor reactor. The role of the non-mechanical L-valve is to regulate the oxygen carrier circulation rate while providing the gas sealing between the combustor and the reducer. In the fluidized combustor reactor, the reduced iron particles are regenerated with air at high temperatures. The oxygen carrier particles reaching above the freeboard region of the combustor reactor become entrained into the riser section and pass through a cyclone to replenish the oxygen carrier at the top of the reducer reactor. The total height of the system is 5 m.

The oxygen carrier size used in the OSU CDCL process is unique compared to the other chemical looping process mentioned previously as the fluidized bed reducer design performs better with smaller oxygen carrier particle sizes. The moving bed reducer design can operate with a larger oxygen carrier particle size (1.5–5 mm), an order of magnitude greater than coal fly ash, which allows for in situ ash removal with the reducer gas outlet stream. The notable size difference between the oxygen carrier particle and coal/ash particle aids in the solid-solid separation. In the reducer, the solid fuel particles are injected at the middle of the reducer. Then, the oxygen carriers are reduced by the gas products of solid fuel. The slow discharging velocity of oxygen carriers in moving bed reducer ensures a high utilisation efficiency of reactants. The reaction between the char remaining after the release of the volatiles and the oxygen carrier is not direct but involves an intermediate gasification step with the gases. The carbon char in the coal particles is gamified through steam gasification and CO_2 gasification reactions. The reducer can be divided into three zones, as shown in Fig 2.14(b). The 25 kWh CDCL sub-pilot unit at OSU represents the first integrated chemical looping demonstration unit to convert solid fuel with a circulating moving bed system directly. To date, the integrated sub-pilot CDCL process has been designed, constructed and demonstrated with over 680 h of operation experience [102–104]. The combined bench and sub-pilot demonstration units have tested metallurgical coke, lignite, sub-bituminous and bituminous coal, anthracite, and wood pellet-based biomass feeds with successful continuous performance results for all solid fuel types.

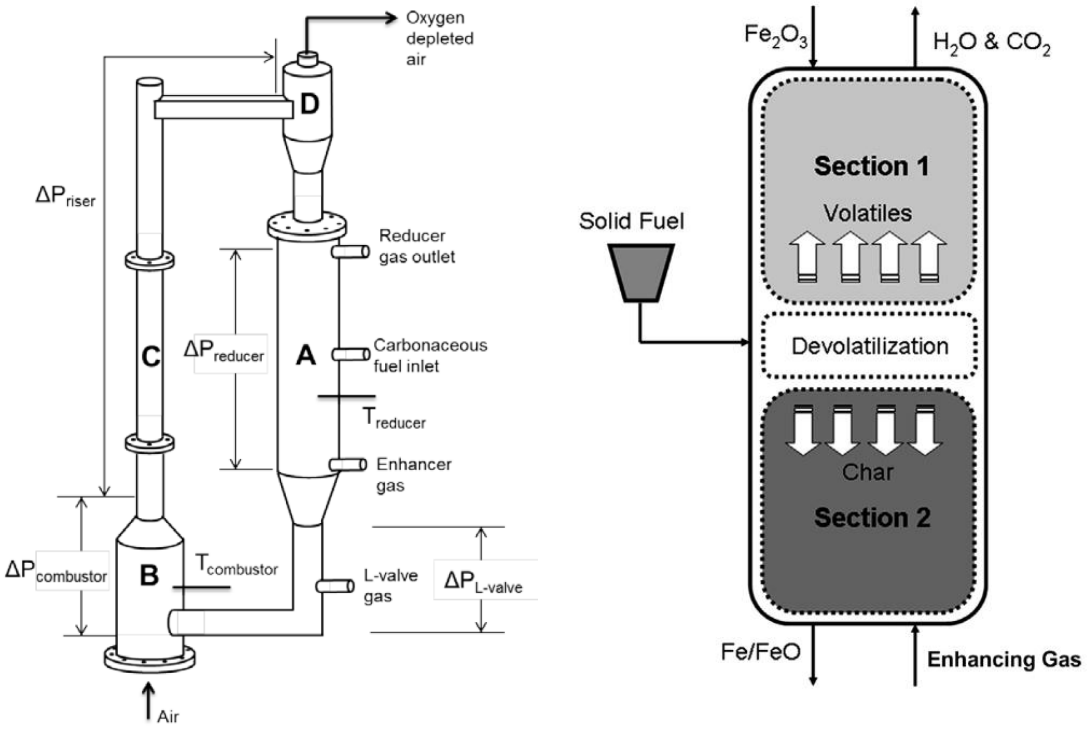

(a) (b)

Fig 2.14. A sketch of 25 kWh CLC system (a) and moving bed reducer (b) at OSU [102–104].

2.6. Simulation and modelling of CLC

Although significant developments have been made in the combustion of fossil fuels using the CLC technology during the last decades, the detailed inner information cannot be obtained by experiments because of complicated flow patterns in the system and poor measuring equipment. By summarising experimental works of literature, it can be found the present knowledge, understanding, and experience of the CLC process, however, mainly come from a limited number of research groups that have been operating small CLC plants. Besides, it is well known that, in general, the hydrodynamics of small-scale fluidized beds can differ significantly from the hydrodynamics of large fluidized beds, and that often this difference leads to negative results. If this hydrodynamic difference is not taken into account in the design, the yields from the large process may be inferior to those experienced on the small scale [105]. Therefore, the lab- or pilot-scale results are difficultly translated to an industrial scale, the performance of the actual industrial CLC

unit is still uncertain. Having a deep understanding of the dynamic characteristic and reaction performance is essential for optimal design and scale-up of the CLC system.

With the development of computer technology and parallel computing, numerical simulation has become the primary method to accelerate the development of the CLC technology, reduce the cost of design and operating time, as well as reduce the technical risks. The existing CFD methods can be divided into two main categories, i.e., Eulerian-Lagrangian method and Eulerian-Eulerian method. In the Eulerian–Eulerian model, the gas and solid phases are treated mathematically as interpenetrating continua. Thus, the computational load is affordable even towards the industry-scale simulations. The two-fluid model (TFM) is a typical Eulerian-Eulerian method and has been widely used to study the CLC processes in the past years. For the solid phase, the so-called kinetic theory of granular flow (KTGF) is used to close the solid pressure and viscosity [106]. It is based on the kinetic theory of non-uniform dense phase describing the particle-particle collisions. This approach uses a one-equation model to describe the turbulent kinetic energy of the particle, introduced with the concept of granular temperature. For this method, some physical characteristic of the solid particles such as the shape and size are simplified and calculated through empirical relations, so that the model accuracy is limited. Another approach is the Eulerian-Lagrangian approach, which treats the particle phase using the discrete element/particle method (DEM/DPM). It can provide detailed particle motion information, such as the trajectories and transient forces acting on individual particles and thus is very accurate to describe the gas-solid flow behaviours. However, an extremely large computational resource (CPU and memory resource requirements) is required based on Lagrangian methods to simulate the gas-solid system in the actual experimental unit, let alone the industrial plants. The priority of the two methods depends on the research object and application background. For the CFD study of CLC processes, both methods have been adopted to investigate the flow and reaction behaviours. Table 2-8 comprehensively reviewed and summarized the application of CFD models to CLC processes.

Table 2-8 A summary of the CLC simulation studies in the last 5 years.

Author	Configuration	Dimension	Method	Investigation	Oxygen carrier	Fuel
Hamilton et al. (2016) [107]	Full-loop	3D	MP-PIC	Flow+ reaction	Cu-based	Solid
Guan et al. （2016）[108]	Ful-loop	3D	TFM	Flow	-	-
Banerjee et al. (2016) [109]	Full-loop	3D	TFM	Flow+ reaction	Fe-based	Gas
Breault et al. (2016) [110]	Full-loop	2D	TFM	Flow+ reaction	Fe-based	Solid
Harichandan et al. (2016) [111]	FR	2D	TFM	Flow+ reaction	Ca-based	Gas
Banerjee et al. (2016) [112]	FR	3D	CFD-DEM	Flow	-	-
Hamilton et al. (2016) [113]	Full-loop	3D	MP-PIC	Flow	-	-
Banerjee et al. (2016) [114]	Full-loop	2D/3D	TFM	Flow+ reaction	Fe-based	Gas
Zhang et al. (2017) [115]	Partial-loop	2D	TFM	Flow+ reaction	Cu-based	Gas
Shao et al. (2017) [97]	Full-loop	3D	TFM	Flow	-	-
Zhang et al. (2017) [116]	Partial-loop	2D	TFM	Flow+ reaction	Ni-based	Gas

Breault et al. (2017) [117]	FR	3D	MP-PIC	Flow+ reaction	Fe-based	Gas
Sharma et al. (2017) [118]	FR	3D	TFM	Flow+ reaction	Fe-based	Solid
Sornumpol et al. (2017) [119]	FR	2D	TFM	Flow+ reaction	Ni-based	Gas
Chen et al. (2017) [120]	FR	3D	TFM	Flow+ reaction	Cu-based	Gas
Menon et al. (2017) [121]	FR	2D	TFM	Flow+ reaction	Fe/Gu-based	Solid
Luo et al. (2018) [122]	Full-loop	3D	CFD-DEM	Flow+ reaction	Ni-based	Gas
Ben-Mansour et al. (2018) [123]	FR	2D	TFM	Flow+ reaction	Ca-based	Gas
Feng et al. (2018) [124]	AR	3D	TFM	Flow	-	-
Sheth et al. (2018) [125]	FR	2D	TFM	Flow+ reaction	Ni/Gu-based	Gas
Wang et al. (2018) [126]	FR	3D	TFM	Flow+ reaction	Fe-based	Solid
Wang et al. (2018) [127]	FR	3D	TFM	Flow+ reaction	Fe-based	Solid
Yang et al. (2018) [128]	FR	3D	CFD-DDPM	Flow	Fe-based	Solid
May et al. (2018) [129]	AR+ FR	3D	TFM	Flow+ reaction	Fe-based	Solid

Reinking et al. (2019) [130]	Full-loop	3D	MP-PIC	Flow+ reaction	Cu-based	Solid
Lin et al. (2019) [131]	FR	2D	TFM	Flow+ reaction	Ni–Cu-based	Gas
Wang et al. (2019) [132]	FR	3D	TFM	Flow+ reaction	Gu-based	Solid
Chen et al. (2019) [133]	Full-loop	3D	MP-PIC	Flow+ reaction	Fe-based	Solid
Chen et al. (2019) [134]	Full-loop	3D	MP-PIC	Flow+ reaction	Fe-based	Solid
Li et al. (2019) [135]	FR	2D	TFM	Flow+ reaction	Fe-based	Solid
Hamidouche et al. (2019) [136]	Full-loop	3D	TFM	Flow+ reaction	Perovskite	Gas
Wang et al. (2020) [4]	Full-loop	3D	TFM	Flow	-	-
Shao et al. (2020) [137]	AR	2D	CFD−DEM	Flow	-	-
Lin et al. (2020) [138]	Full-loop	2D	TFM	Flow+ reaction	Ni-based	Gas
Yin et al. (2020) [139]	FR	3D	TFM	Flow+ reaction	Fe-based	Solid
Wang et al. (2020) [140]	Full-loop	3D	TFM	Flow	-	Solid
Hamidouche et al. (2020) [141]	Full-loop	2D	MP-PIC	Flow	-	Solid

Zhu et al. (2020) [142]	Full-loop	3D	MP-PIC	Flow	-	-
Shao et al. (2020) [143]	Full-loop	3D	TFM	Flow	-	-

From Table 2-8, the research field of the simulations is the flow characteristics and reaction performance of variable gas fuels and solid fuels with different oxygen carriers. Most of the research can be roughly divided into two parts: for individual reactors and for the full-loop system.

2.6.1 Single-Reactor Simulation

The modelling of individual FR and AR helps the design, optimization, and scale-up of the CLC process. An interesting number of works can be found in previous work to model the individual reactors in a CLC system, as is presented in Table 2-8.

Air Reactor Simulation.

The AR is generally composed of a wide bottom bed with a narrow riser or only a riser. In a typical CLC configuration, the function of the AR is to oxidize the reduced oxygen carriers at the bottom domain and then smoothly entrain the regenerated oxygen carrier back to the FR. A higher gas velocity than the terminal velocity of oxygen carriers must be ensured in the riser to obtain a fast fluidization state. The wide bottom bed is generally used to increase the reaction time of reduced oxygen carrier and oxygen. The simulations of AR are limited because the reaction in AR is relatively simple compared with the FR.

Wang et al. [144] developed a 2D TFM model where the cluster structure-dependent (CSD) drag coefficient model was incorporated into the TFM to investigate the effect of clusters on flow behaviour and oxidation reaction of gas and Cu-based oxygen carrier in a riser of air reactor. Simulation results were validated by experimental data published in the literature. The holdup distributions and velocity of gas and particles were predicted in the AR. Feng et al. [124] proposed a novel baffle consisting of a ring-type baffle and a convergent pipe to improve the flow pattern and enhance the gas-solid contact in the AR (Fig 2.15). The effect of the baffle on the system hydrodynamics was investigated based on CFD simulations. The results showed that the baffle significantly affected the system hydrodynamics. The baffle opening ratio and the number of baffles were the key factors

to decrease the standard deviation of radial solid volume fraction. Shao et al. [137] adopted a quasi-2D CFD-DEM cold flow model to study a novel multistage moving bed air reactor. Influences of variable operating conditions, geometry and internals on solid's flow pattern and residence time were investigated by using the tracer particles. Results showed that increasing the loop seal gas velocity, the solid flux increased, and the average residence time decreased. The reactor angle had more influence in solids motion near the wall region, while the wedge angle has more effect in the lower part of the reactor. With the decrease of the reactor angle, an increase of the wedge angle, or increase of the down-comer diameter, the bed gets closer to ideal plug flow in the AR. The internals can accelerate the particles in the near-wall region; internals in triangular arrays are better than those in square arrays to slow down the central particles.

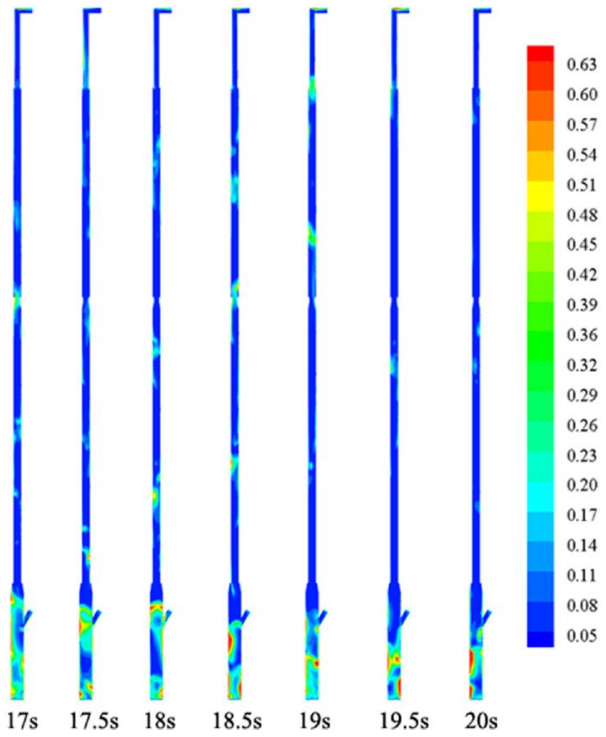

Fig 2.15. Instantaneous solid volume fraction in the air reactor [124].

Fuel reactor simulation.

Reactions in FR are much more complicated than AR where reaction performance in the FR significantly influences the coal combustion efficiency, oxygen carrier conversion, and CO_2 capture efficiency of the whole CLC system. To date, different reactor configurations of FR have been adopted for the CLC process to improve performance. The bubbling fluidized bed (BFB) is widely used due to sufficient mixing and contact time. The spouted fluidized bed (SFB) is also adopted in some CLC units because of favourable gas-solid mixing. The circulating fluidized bed (CFB) is applied in view of the sufficient gas-solid contact caused by intense flow regimes. The moving bed is also adopted in some CLC units due to greater control of the residence time and fuel conversions. Accordingly, simulations are conducted to investigate the flow and reaction characteristics of FRs with different configurations.

Wang et al. [145] proposed a 2D multiphase CFD-based model with gas-solid hydrodynamics and chemical reactions in a BFB FR. The instantaneous solid volume fractions of both reactant and products were predicted and the time-averaged distributions were calculated in the FR by simulation (Fig 2.16). Meantime, simulated flows in FR revealed a high weight fraction of unburned methane in the flue gas mixing with CO_2 and H_2O. This behaviour implied high fuel loss at the exit of the reactor and indicated the necessity to increase the residence time and improve mixing in the fuel reactor using circulating fluidized bed technology.

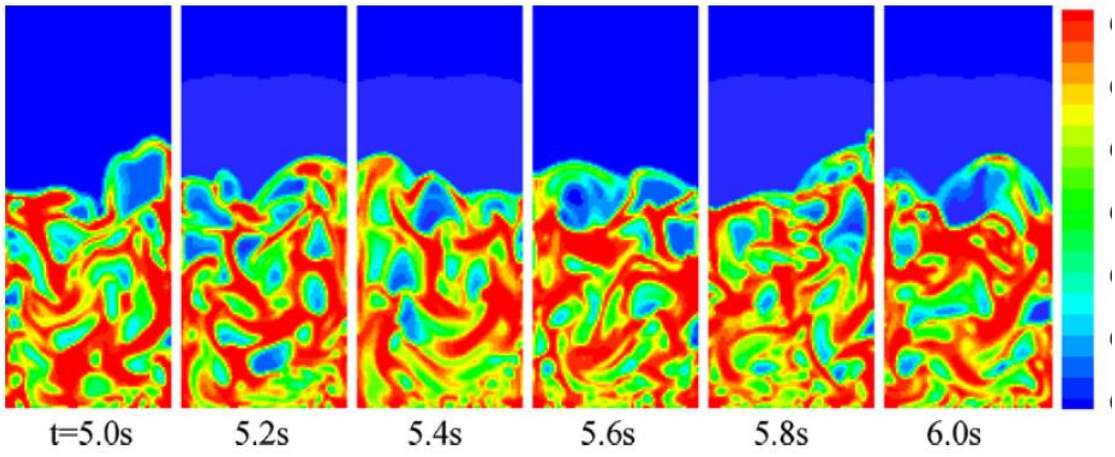

(a)

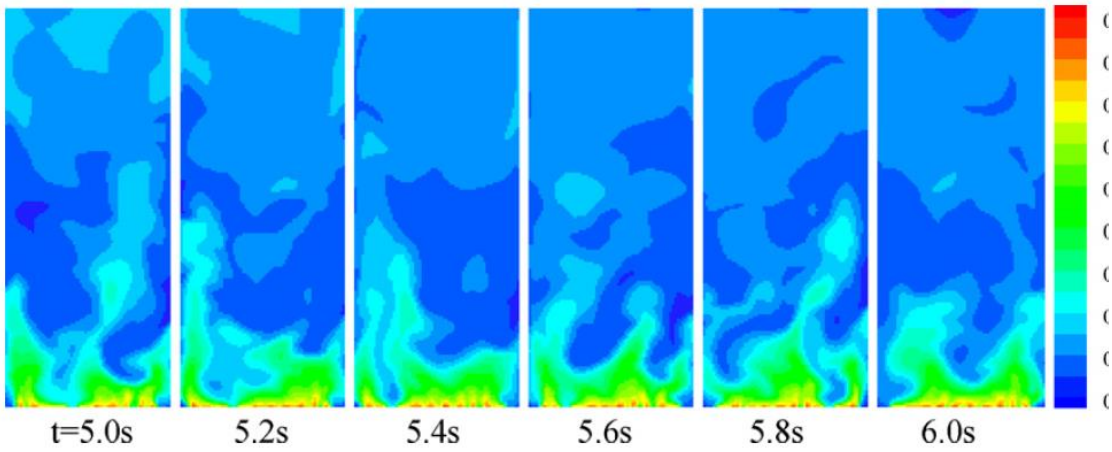

(b)

Fig 2.16. Instantaneous volume fraction of particle (a) mass fraction of CH_4 (b) in the fuel reactor [145].

Wang et al. [132] applied a 3D Eulerian-Eulerian two-fluid model to investigate the char-fuel CLC characteristics in an FR, as shown in Fig 2.17, 2.18. the reactor type of FR in this work is a BFB with a height of 2.0 m and an inner diameter of 0.22 m. The gas-solid flow patterns, composition distributions, and reaction characteristics were obtained by simulation. Moreover, the influences of solids inventory and fluidizing number on the reaction performance were investigated.

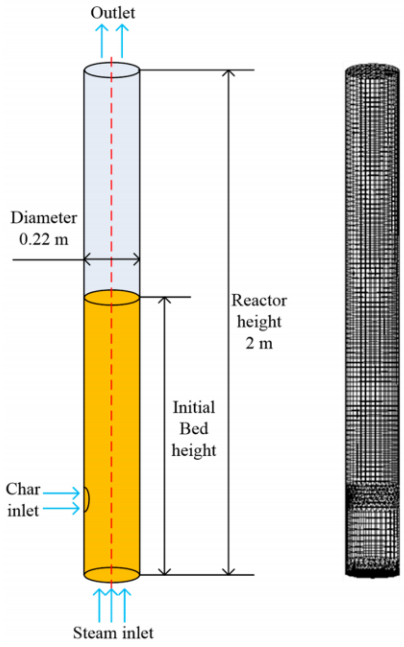

Fig 2.17. Geometry and mesh model of the BFB FR [132].

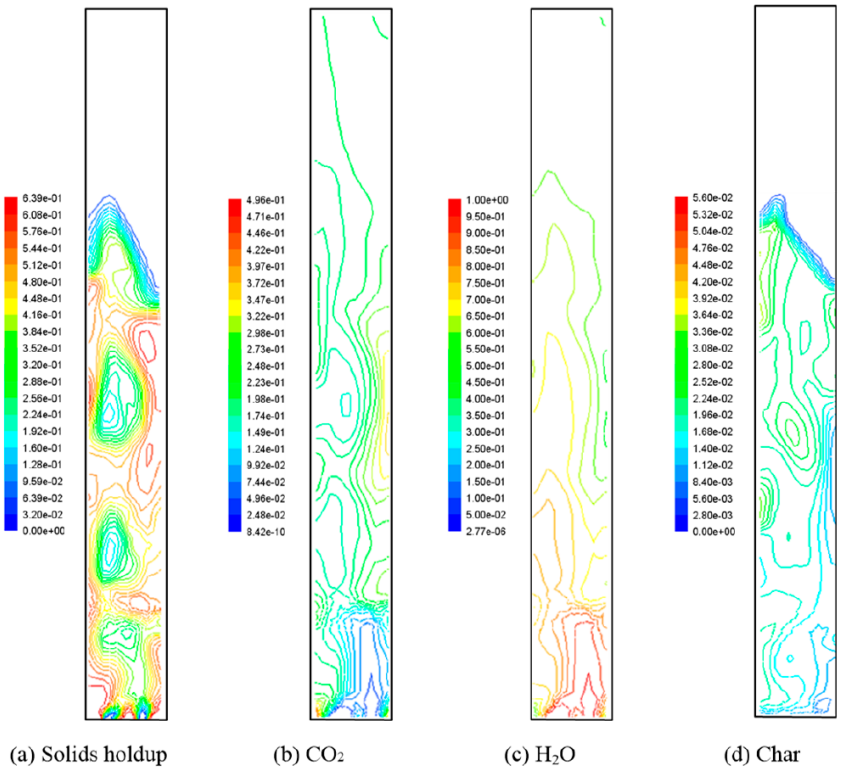

(a) Solids holdup (b) CO_2 (c) H_2O (d) Char

Fig 2.18. Distributions of flow patterns and gas-solid concentrations [132].

Zhang et al. [146] investigated the details of the gas-solid hydrodynamics in the spouted bed FR by employing the CFD-DEM method. The CFD-DEM simulations showed good agreement with the experimental data comparing with a lab-scale FR. The details of solid motion in the FR were obtained, as shown in Fig 2.19. More importantly, simulations proved the spouted bed configuration design of FR significantly enhanced the performance.

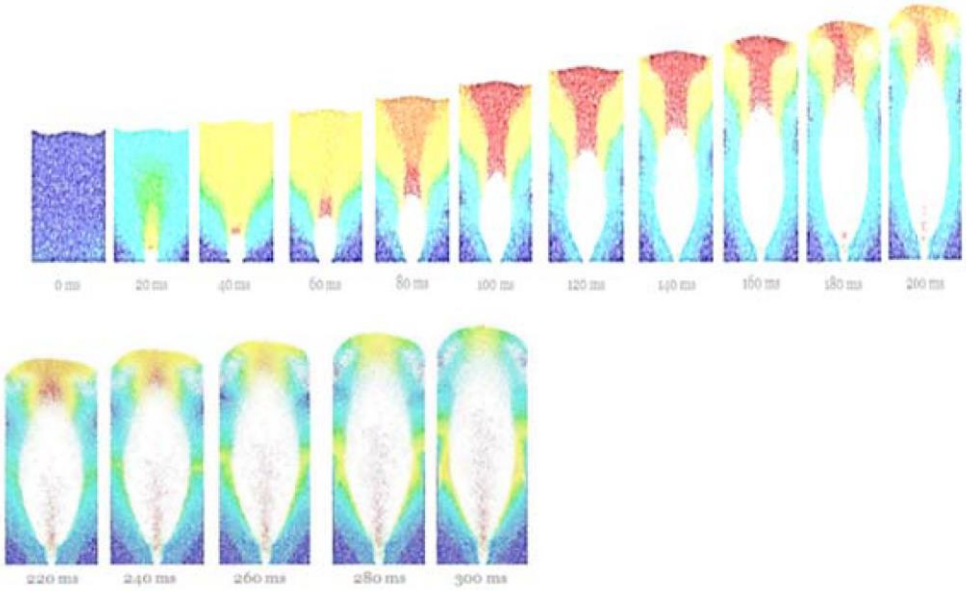

Fig 2.19. Particle distribution and velocity in the spouted bed FR [146].

Banerjee et al. [112] studied a lab-scale spouted bed FR based on CFD-DEM method to characterize the performance of the new scaling law in comparison with existing scaling laws in the previous papers. Simulation results showed (Fig 2.20) the proposed scaling law provides the largest reduction in the number of particles in the system, and hence, the largest reduction in computing cost.

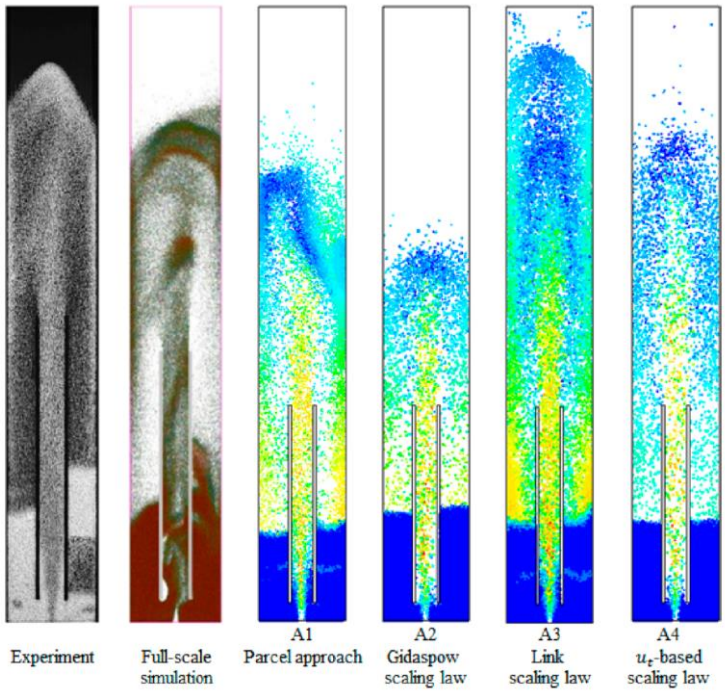

Fig 2.20. Particle tracks after one second for scaled simulation cases A1−A4 compared with the experiment and full-scale simulation results [112] (particles tracks are coloured by nominal velocity magnitude).

Compared to the bubbling bed and spout-fluidized bed-based fuel reactors, a circulating bed riser can provide sufficient gas-solid contact over the whole or majority of the reactor height, which ensures that the gas-solid reactions can happen in a more homogeneous and favourable environment. Wang et al. [147] developed a comprehensive 3D numerical model to simulate the reactive flow using ilmenite as oxygen carrier and coal as the fuel in a pressurized CFB FR (Fig 2.21). Main features of the complex gas-solid flow pattern, such as the velocity and voidage profiles, were predicted. The concentrations of gas-solid species, the conversions of char and oxygen carrier, and the distributions of reaction rates were also obtained.

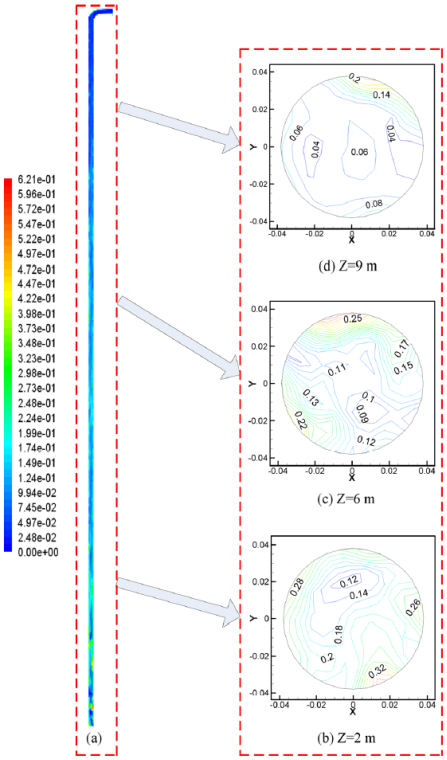

(a)Axial and radial distributions of solids holdup.

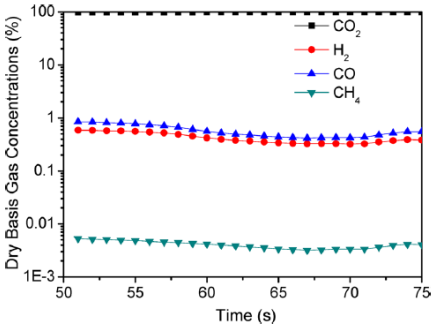

(b) Variation of gas components (dry basis) at the outlet during the quasi-equilibrium state.

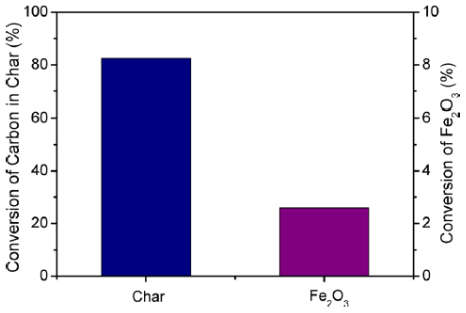

(c)Conversions of carbon in char and oxygen carrier.

Fig 2.21. 3D model of the reactive flow using ilmenite as oxygen carrier and coal as the fuel in a pressurized CFB FR.

2.6.2 Full-loop simulation

At present, the full-loop CLC system is mainly divided into two types: single circulating fluidized bed (CFB) system and double circulating fluidized bed (DCFB) system. In addition, the single circulating fluidized bed CLC system such as moving bed and the spouted bed was established. For the full-loop system, the two reactors are connected by cyclones, loop seal and particle returning apparatuses to realize the circulation of oxygen carrier particles between two reactors.

The simulations of full-loop CLC systems mainly focus on the solid circulation process, gas leakage performance and reaction processes such as reactant distribution, product distribution and temperature distribution. Guan et al. [148][108] established a 3D full-loop model to investigate the hydrodynamics of a single CFB CLC unit, which consists of a riser, a bubbling bed, a cyclone and a loop-seal, based on the Eulerian-Eulerian TFM model. The influence of drag models on the model accuracy was studied. The Gidaspow and the Syamlal & O'Brien drag models both produced accurate predictions in this study (Fig 2.22). The different fluidization states in the full-loop system were captured by simulation. The effects of operating gas velocity, particle size and total solids inventory on the solids circulation rate (SCR) were also investigated based on the system pressure balance. Simulation results showed the SCR increased significantly with the increase of gas velocity in the riser. And the SCR became smaller for larger particles but increased with solids inventory.

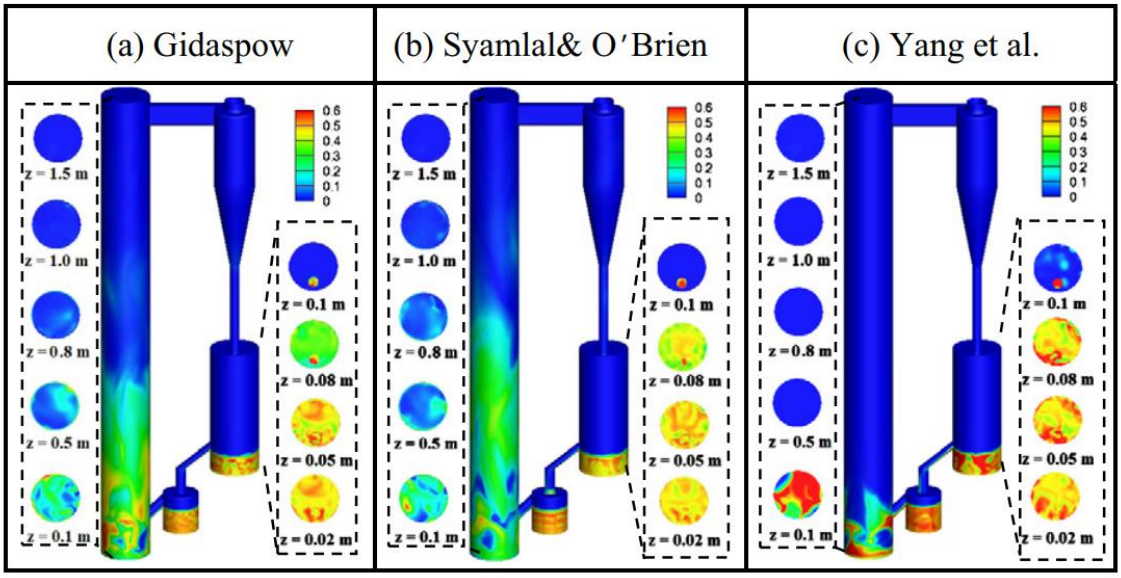

Fig 2.22. Snapshots of the solids volume fraction predicted by different drag models.

Banerjee et al. [149] simulated the transient reacting flow of a CDCL process with the spouted FR based on CFD-DEM method. And the chemical reactions were integrated into

the high-fidelity simulations. This work tracked the motion of individual oxygen carrier particles and captured the gas-solid multiphase hydrodynamics, as shown in Fig 2.23. The materials of oxygen carrier with different properties were compared in this system. The simulations showed a strong dependence of the fluidization regimes on the density of oxygen carrier.

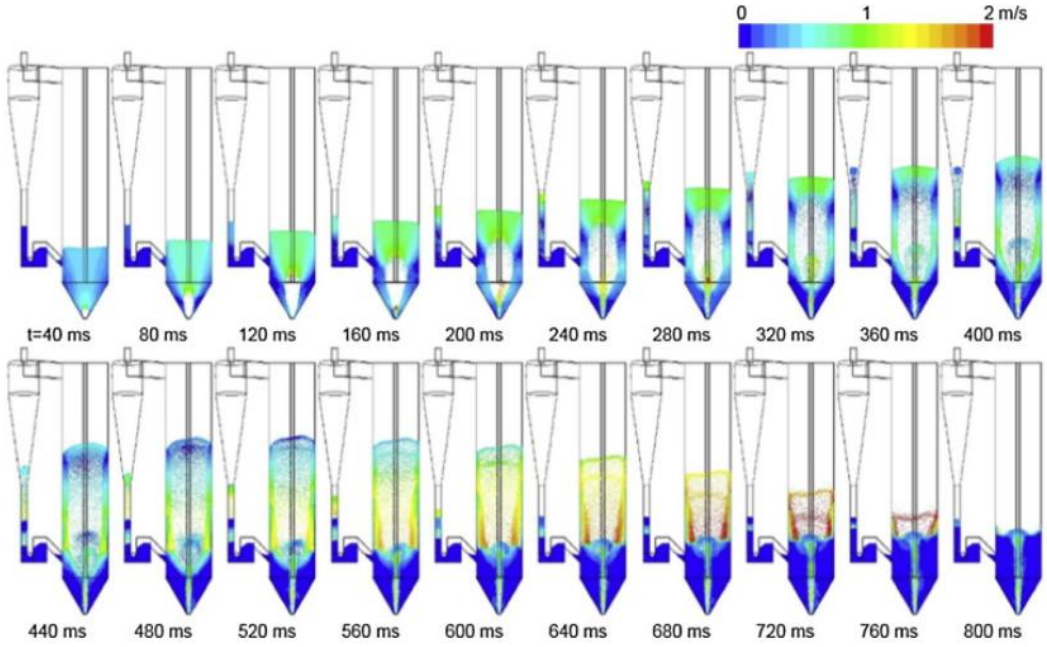

Fig 2.23. Particle tracks coloured by velocity magnitude in reacting flow with Fe_2O_3 particles [149].

Parker [150] investigated a CLC system provided by the National Energy Technology Laboratory (NETL), consisted of an air reactor, cyclone, loop seal, fuel reactor, and L-valve and uses a metal oxide solid carrier to combust a source of fuel based on the CPFD method. Multiple heterogeneous and homogenous reactions are considered in the CLC model, including the oxidation and reduction reactions of the metal oxide carrier and gasification reactions. Within each coal particle, the temperature-dependent devolatilization, moisture release, and particle swelling effects are included. Modelling results showing fluidization regimes, circulation rate, reactor efficiencies, and temperature profiles were presented to demonstrate the utility of the model (Fig 2.24).

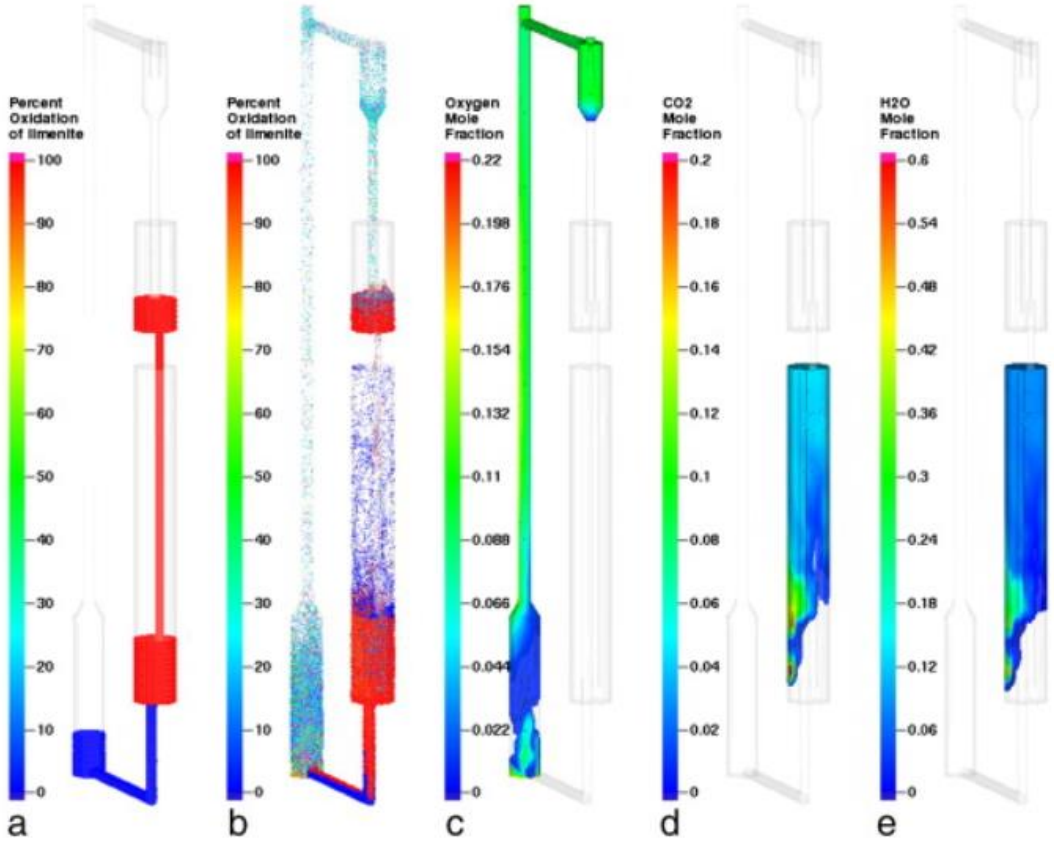

Fig 2.24. Initial particle oxidation levels (a); particle oxidation levels at 50 s (b); mole fraction of oxygen at 50 s (isovolume > 5 mol%) (c); mole fraction of carbon dioxide at 50 s (isovolume > 2 mol%) (d); mole fraction of water at 5 s (isovolume > 5 mol%) (e) [150].

Geng et al. [151] studied the SCR in a full-loop DCFB based on a 3D Eulerian multiphase model with the kinetic theory of granular flow (KTGF). The CLC unit with the DCFB configuration consisted of an AR, height of 1.36 m, diameter of 0.05 m) and an FR (height of 0.97 m, diameter of 0.054 m). The gas-solid flow behaviours, e.g. the fluidization regime, solid distribution and velocity, SCR, were numerically investigated. By simulation results, pneumatic transport regime in AR and turbulent regime in FR was observed (Fig 2.25). Besides, global circulation rate decreased with increasing FR fluidization rate while internal circulation rate increased.

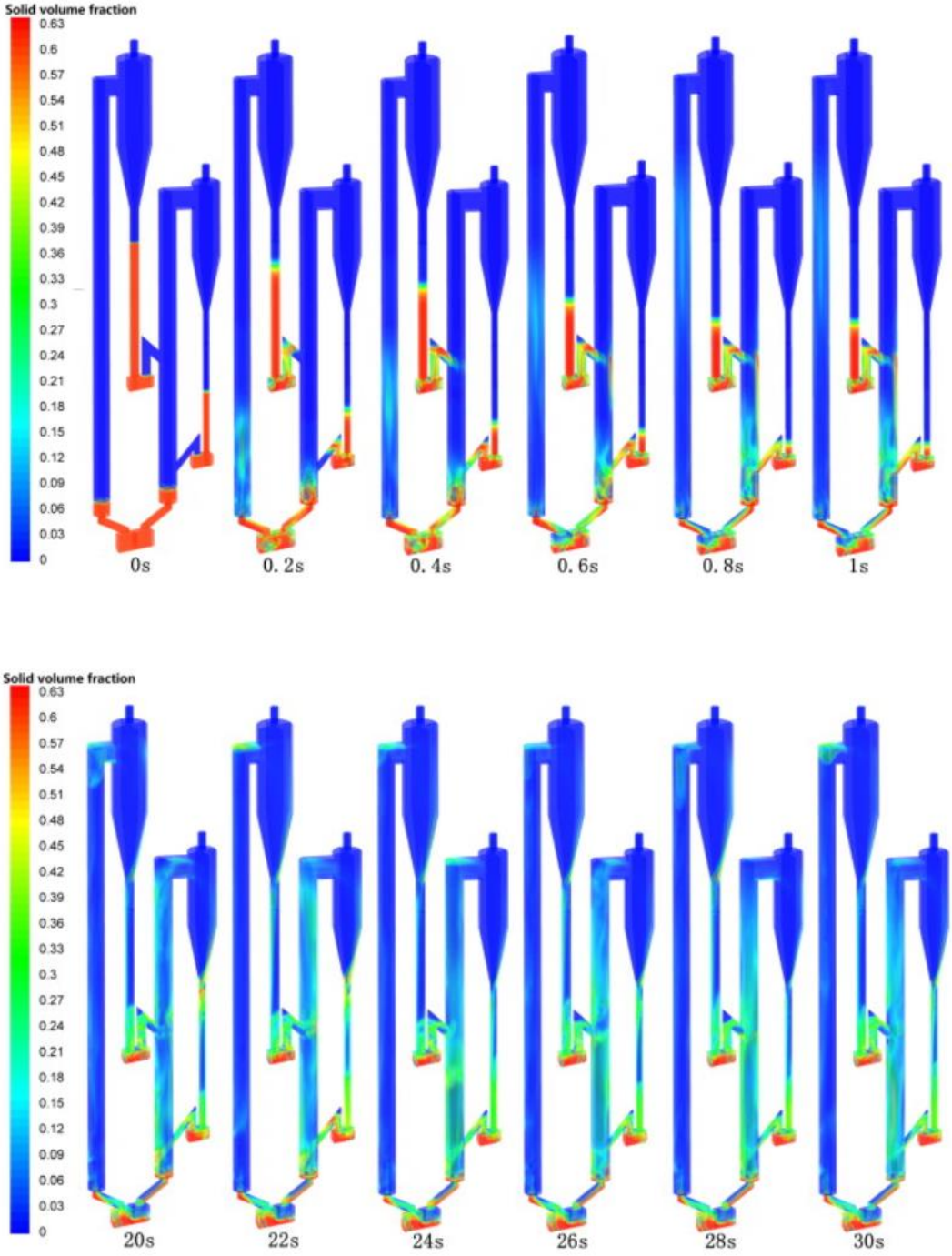

Fig 2.25. The instantaneous concentration of particles in the CLC reactor model [151].

Chen et al. [134] investigated a 50 kWh DCFB reactor for CLC of coal, which was designed, constructed and operated at Huazhong University of Science & Technology (HUST), by using the Computational Particle Fluid Dynamics (CPFD) method. The reliability of CPFD simulation was first validated in this work by comparing outlet gases

concentration and pressure profiles of FR with simulations and experimental measurements. Then, the characteristics of the gas-solid reactive flow in the full-loop system was simulated in detail, and the relationships among the complex factors of hydrodynamics and reactions were better understood (Fig 2.26). The results in this work can help to rationalize reactor design and optimize operation.

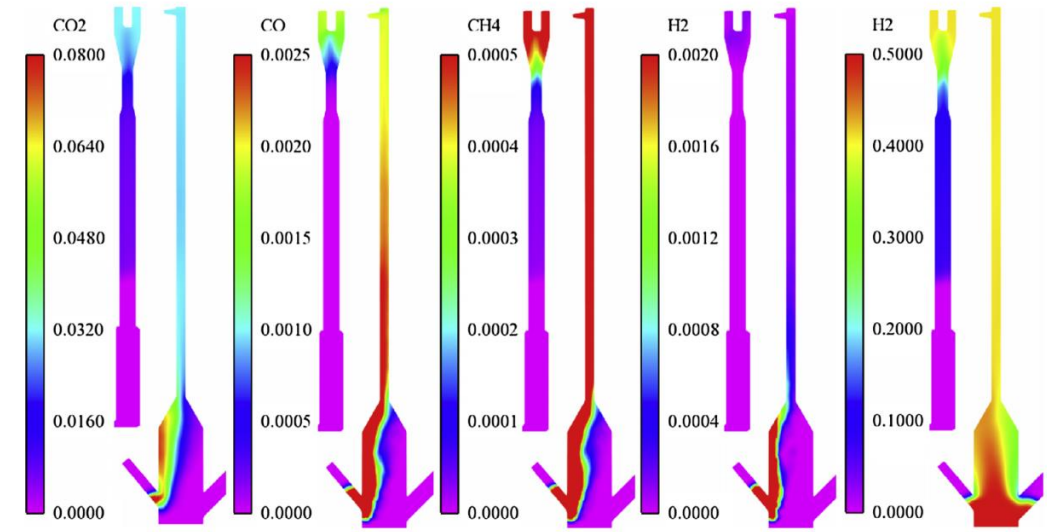

(a)

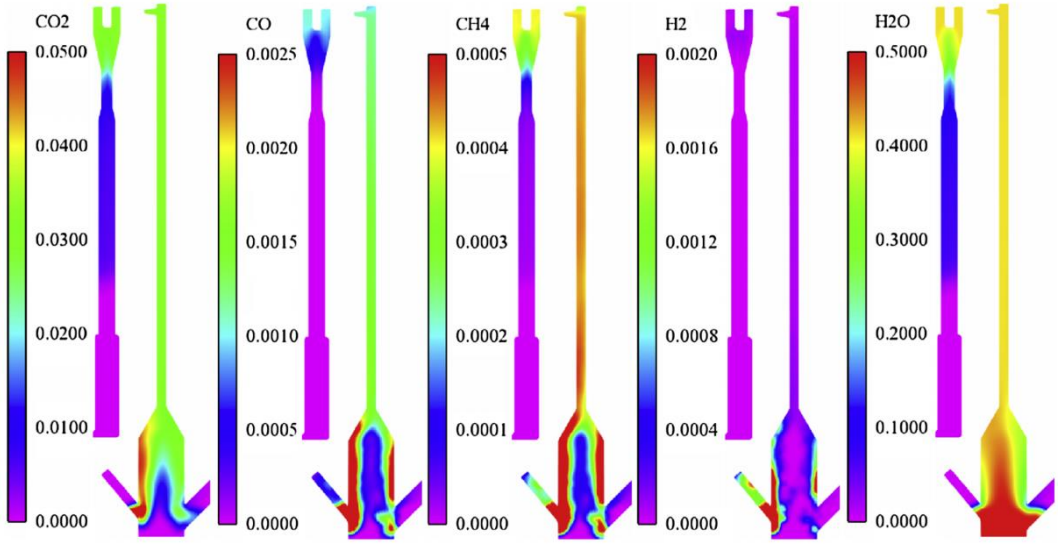

(b)

Fig 2.26. Time-averaged (30–70 s) gas volume fraction profiles in FR under steady-state (a). gas volume fraction profiles in FR under steady-state employing optimal coal feeding mode (b) [134].

2.7. Summary and Research Gaps

CFB reactor units have been widely applied to many chemical engineering processes, due to its good gas-solid mixing, wide fuel flexibility, and excellent heat and mass transfer performance. The complicated configuration and extreme operating environment make the in-furnace behaviours of CFB reactors difficult to understand, which greatly limits its further optimization and scale-up.

Among various CFB chemical systems, the CLC system is regarded as one of the most promising clean combustion technologies because of the inherent CO_2 separation. The CLC technology has attracted more and more attention during the last years as up-and-coming technologies for power plants and industrial applications with CO_2 capture and low energy penalty. For experimental research, most of the previous work discussed in this report involved lab-scale experiments of CLC systems and a limited number of pilot-scale experiments. Setting up and executing an experiment in the lab can be an expensive and laborious process. The study of solid fuels is most competitive when power production is concerned, and meantime the reaction kinetics are more complex than other fuel types. Present limited operation using coal as solid fuel in some small-scale CLC facilities in the worldwide indicates a significant challenge to develop this technology. By tables in section 2.5, although substantial developments have been made in the combustion of fossil fuels using the CLC technology during the last decades, the detailed inner information cannot be obtained by experiments because of complicated flow pattern in the system and backward measuring equipment. The present knowledge, understanding, and experience of the CLC process, however, mainly come from a limited number of research groups that have been operating small CLC plants. Besides, because the lab- or

pilot-scale results cannot safely be translated to an industrial scale, the performance of the actual industrial CLC unit is still uncertain. Having a deep understanding of the dynamic characteristic and reaction performance is important for optimal design and scale-up of the CLC system.

For simulation work, in the last decade, different types of single reactor and full-loop CLC systems have been numerically studied to understand the operation performance and test different types of the fuel and oxygen carrier in an effective and economical way. Multiple numerical methods (TFM, CFD-DDPM, CFD-DEM, MPPIC) are available to investigate the hydrodynamic and thermodynamic behaviours of variable CLC processes according to the detail scale and accuracy demand. However, present simulations are still very limited for the full-loop CLC system, especially some complex configurations. The hydrodynamic and reaction behaviours of the moving-bed CDCL process have not been fully understood yet, where a higher fuel conversion and CO_2 capture efficiency have been reported.

Moreover, for many complicated CFB systems with multiple paths connected in parallel or in series, the non-uniformity phenomena of gas-solid distribution is inevitable, even in symmetrical geometry and operating condition settings. This also makes the prediction of complex CFB system more difficult. So far, the investigation of this non-uniformity phenomenon in complex CFB systems are very limited. It is necessary and important to have a comprehensive and deep study for this phenomenon and explore how to minimize the degree of the non-uniformity, which is beneficial to improve the operation efficiency of CFB processes.

In addition, most of CFD simulations on complex CFB systems only revealed microscale phenomena based on separate reactor components, and the boundary and operating conditions were fixed during the simulation process without the external adjustment and environment change considered. However, in the actual chemical engineering processes, variable operating parameters are adjustable according to the production and safety

requirements. This part of the research work is very limited. In this thesis, one solution to couple CFD modelling and process simulation dynamically is proposed to improve the performance of CFB systems.

CHAPTER.3 Hydrodynamic Behaviours in a Dual Circulating Fluidized Bed

CLC units, as an example of the promising CFB chemical engineering systems, are investigated to obatain more understanding of the CLC processes. In this chapter, a multi-fluid model based on the Eulerian-Eulerian framework is used to study the gas-solid hydrodynamics in a full-looping CLC unit with the DCFB configuration. Simulation results predict unique fluidisation states. The influence of two classical and two recent drag force models on hydrodynamics in DCFB are assessed by comparing with the experimental data.

The paper “Multi-fluid modelling of hydrodynamics in a dual circulating fluidized bed” has been published based on the content of this chapter in the journal of Advanced Powder Technology.

S. Li, Y. Shen, Multi-fluid modelling of hydrodynamics in a dual circulating fluidized bed, Adv. Powder Technol. 31. 7 (2020) 2778-279.

Graphical abstract for this chapter

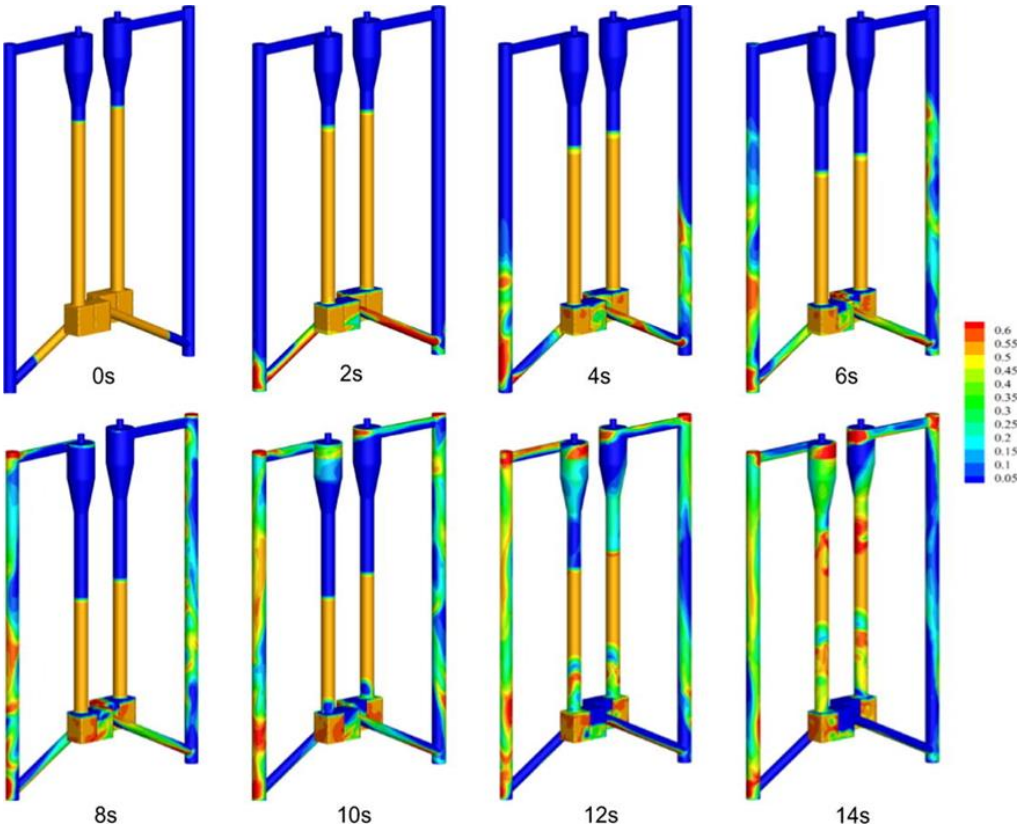

ABSTRACT

In this chapter, a multi-fluid model based on the Eulerian-Eulerian framework is used to study the gas-solid hydrodynamics, such as solid distribution, particle motion and solid velocity, in a three-dimensional (3D) dual circulating fluidized bed (DCFB). The influence of four different drag force models, including two classic models, i.e. Gidaspow, EMMS drag model and two recent drag models, i.e. Rong and Tang drag model, on hydrodynamics in DCFB are assessed. Numerical results show that the characteristics of solid distribution and velocity in different sections are distinct. For qualitative analysis, all the drag models can predict a reasonable radial solid distribution and pressure distribution, but only the EMMS, Rong and Tang drag model can capture the phenomenon of dense solid concentration in the low part. For quantitative analysis, the solid circulating rate predicted by the EMMS drag model is the closest to the experimental value, while the Gidaspow drag model shows the most significant deviation. The overall assessments confirm that the drag model selection significantly influences the simulations of gas-solid flow in DCFBs. This study sheds lights on the design and optimization of fluidized bed apparatuses.

3.1 Introduction

Carbon dioxide (CO_2) emission leads to global climate change. About one-third of the total CO_2 emission has resulted from fossil fuel combustion [152] and fossil fuel is expected to be the primary resource for a long time. In the past decades, many technologies of CO_2 capture have been proposed and utilized for large-scale power production applications [13,153–156]. However, the majority of these technologies require a large amount of energy to separate and collect CO_2 from the exhaust gas, because CO_2 is diluted by N_2 in the air in conventional systems. Chemical looping combustion (CLC) is a recently developed combustion technology and has attracted considerable attention since its inherent CO_2 separation and low energy consumption [51,95,157–160]. A typical CLC system consists of two reactors, a fuel reactor (FR) and an air reactor (AR), as illustrated in Fig 3.1. The solid oxygen carrier, which is often a metal oxide, is circulated between two reactors to transfer oxygen from AR to FR. This way, the fuel is fed into the FR where it is oxidized by lattice oxygen of the metal oxide. CO_2 and water vapour are produced from complete combustion in the FR. Most CLC systems use such configuration of two interconnected fluidized bed reactors [50,152,157,161,162], but they may vary with different designs. For example, in AR designs, some researchers prefer to use a high-velocity riser in view of the fact that the oxygen carriers generally demand a longer particle residence time for reduction action than oxidation action [163,164]. As for the FR, the bubbling fluidized bed is widely utilized in the CLC system [152,165,166]. However, there is a risk of a gas bypass through bubbles in the bubbling fluidized bed. Therefore, the dual circulating fluidized bed (DCFB) is adopted in many CLC units [95,167–170]. In this system, two circulating fluidizing bed (CFB) reactors are linked with a fluidized loop seal at their bottom. The loop seal is able to partly control the solid global circulation. The AR is designed as a fast-fluidized bed that effectively controls the solid global circulation. In contrast, the FR is operated in the turbulent regime to improve the gas-solid contact.

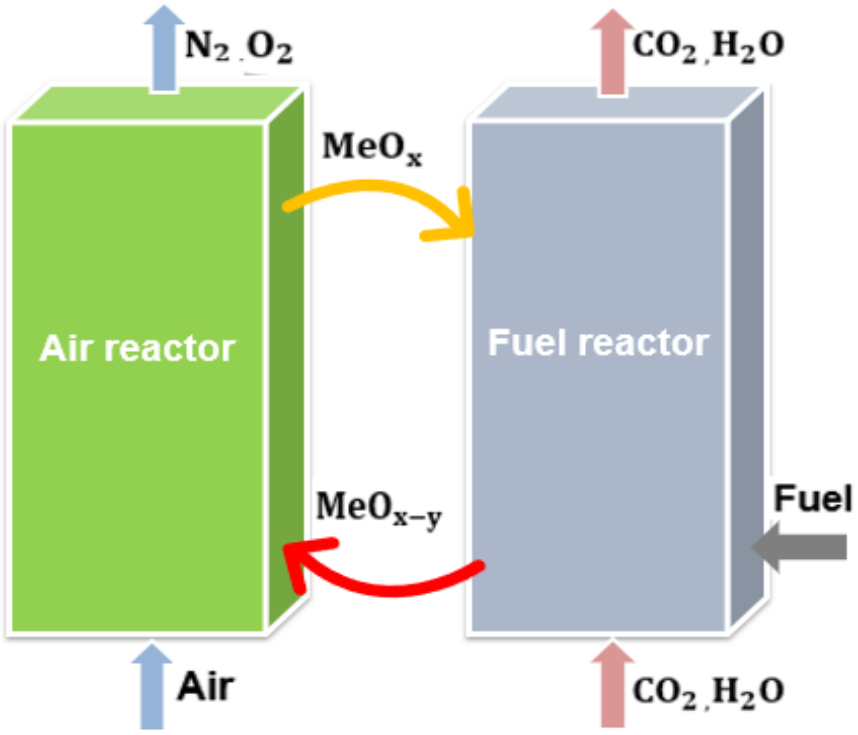

Fig 3.1. Schematic diagram of the CLC process.

Due to the complex structure and multiple operating parameters, it has been a great challenge to study the particles flow behaviours in DCFBs. By experiments, Kolbitsch et al. [167,170] proposed a DCFB reactor system for a 120 kWh CLC pilot rig and made effective control of the solids circulation rate via the primary fast fluidized bed (i.e., AR) without changing the fluidization regime in the secondary reactor (i.e., FR). Ma et al. [95] built a DCFB for in-situ CLC testing of Chinese bituminous coal as fuel and natural hematite as an oxygen carrier. The effect of operational parameters, such as the FR temperature and coal feeding rate on three factors (i.e., combustion efficiency, carbon capture efficiency and CO_2 yield) were investigated. However, only global experimental results can be obtained in these experimental works and more detailed internal flow information was missing. It is necessary to develop a deep understanding of hydrodynamics for the design and operation of CLC systems, especially in the DCFB configuration. As an alternative, mathematical modelling, especially computational fluid

dynamics (CFD), is a cost-effective tool to offer insights of gas-solid hydrodynamics in dense multiphase systems [171–175]. However, due to the complicated geometries and complex operating parameters, only few CFD studies on DCFB reactor for CLC were reported. The existing CFD methods can be divided into two main categories, i.e. Eulerian-Lagrangian method and Eulerian-Eulerian method. The former method tracks each particle/parcel under the Lagrangian framework. It requires a large computational resource under pilot- and industry-scale conditions. For example, Gu et al. [176] used an Eulerian-Lagrangian method based on the Multi-Phase Particle-In-Cell (MP-PIC) scheme to study the solid behaviours in a 3D DCFB. In order to reduce the computational load, the geometry configuration of the test rig was scaled down by three times. Compared with the Eulerian-Lagrangian method, the Eulerian-Eulerian method treats the solid particles as a continuum phase via the governing equations as similar to the gas phase. Thus, the computational load is affordable even towards the industry-scale simulations. The two-fluid model (TFM) is a typical Eulerian-Eulerian method and has been widely used to study the CLC processes in the past years. For example, Wang et al. [177] adopted a 2D TFM to investigate the flow and heterogeneous chemical reactions in a DCFB in CLC processes. The influence of reaction temperature and air/fuel ratio on the performance of the DCFB reactor were also evaluated. Su et al. [178] simulated a 5 kWh coal-fired CLC DCFB system for understanding gas leakage, flow pattern and combustion efficiency. A new operation condition was simulated by increasing the reactor temperature and decreasing the coal feeding rate to improve the combustion efficiency. Li et al. [179] compared the difference between 2D and 3D numerical simulations in circulating fluidized bed risers. From previous simulation works, it can be seen that the TFM method is feasible for simulation of complex multiphase flows in practical applications. Recently, extensive attention has been paid to improving its accuracy. It is noted that the momentum transfer between the gas and solid phase is performed via coupling the interphase forces, including drag, lift, and virtual mass forces. Among these forces, the drag force is the most significant force in dominating gas-solid flows, thus it is essential to select a suitable

drag model for TFM simulations. Several drag models have been proposed over the past several decades, such as Wen-Yu [180], Syamlal-O'Brien [181] and Gidaspow [182] drag models, in which the gas-solid momentum transfer is realized by incorporating a semi-empirical drag model derived from the experimental study. Among these drag models, the Gidaspow (1994) [182] drag model is the most commonly used one which is a combination of the Ergun equation [183] and the Wen and Yu [180] drag model, and describes gas-solid flow hydrodynamic in both dense and dilute phases. The energy-minimisation multi-scale (EMMS) approach is also a classic drag model and derived based on energy minimization of suspension and transportation of gas-solid flow which has the capacity of predicting the heterogeneous structure of dense solid phase [184]. Up to now, many simulations have been done to compare the performance of the aforementioned semi-empirical drag models and EMMS drag model. For example, Guan et al. [148] studied the effect of several classic drag models on computational results. It was found that the Gidaspow and Syamlal-O'Brien drag model produced more accurate predictions than the EMMS model in their simulation. Wu et al. [185] applied two classic drag models, namely the EMMS model and the Gidaspow model, to simulate the coal combustion in a circulating fluidized bed combustor. It was found the EMMS drag model gave rise to a better agreement with the experimental data compared to the Gidaspow drag model. In addition to the classic drag models described above, more recently, several drag models have been numerically developed [186–194] and can be divided into two main types due to their different origins. One type is derived from the Lattice-Boltzmann method (LBM). In these studies, particle resolved simulations of a periodic domain with several randomly positioned particles are conducted to capture the interphase exchange force at the boundary of each particle. The numerically calculated particle-scale forces are then used to calculate an averaged drag force in the flow domain. For example, Rong et al. [195] proposed a drag model by fitting a curve to the data generated from several simulations performed using parallel Lattice-Boltzmann model in which different packing structures and porosities of monodisperse solids were emulated by the Discrete

Element Method (DEM). Another type is derived from Direct Numerical Simulation (DNS). For example, Tang et al. [193] proposed a drag model by considering the effects of granular temperature for a wide range of particle Reynolds numbers and solid volume fractions based on Immersed Boundary Method-Computational Fluid Dynamics (IBM-CFD) computations. However, there is a lack of comprehensive work to assess the performance of the above four kinds of drag models in DCFB simulations for CLC processes.

In this chapter, a multi-fluid model is used to study hydrodynamics in a 3D DCFB. The typical gas-solid flow characteristics, such as solid distribution, particle motion and solid velocity, are comprehensively described. Then, the influences of four different drag models, namely Gidaspow, EMMS, Rong and Tang drag models, on hydrodynamics are assessed in terms of Reynolds numbers and then qualitatively and quantitatively compared in terms of gas-solid flow patterns and DCFB performance using the solid circulation rate etc. Finally, the applicability of the four drag models is discussed from the perspective of theory, observation in this work and recently simulation work.

3.2 Mathematical Model

3.2.1 Governing equations

The TFM under the Eulerian-Eulerian framework with the standard kinetic theory of granular flow (KTGF) is used in the present work [106,182]. The gas phase and solid phase are both regarded as continuum phases, and the former is treated as the primary phase while the latter is treated as the secondary phase. The subscript 'g' and 's' stand for the gas phase and solid phase, respectively. The equations for each phase are:

Continuity equations:

$$\frac{\partial}{\partial t}\left(\alpha_g \rho_g\right) + \nabla \cdot \left(\alpha_g \rho_g \vec{u}_g\right) = 0 \tag{3-1}$$

$$\frac{\partial}{\partial t}(\alpha_s\rho_s)+\nabla\cdot(\alpha_s\rho_s\vec{u}_s)=0 \tag{3-2}$$

Momentum equations:

$$\frac{\partial}{\partial t}(\alpha_g\rho_g\vec{u}_g)+\nabla\cdot(\alpha_g\rho_g\vec{u}_g\vec{u}_g)=-\alpha_g\nabla p+\nabla\cdot\bar{\bar{\tau}}_g+\alpha_g\rho_g\vec{g}+\beta(\vec{u}_s-\vec{u}_g) \tag{3-3}$$

$$\frac{\partial}{\partial t}(\alpha_s\rho_s\vec{u}_s)+\nabla\cdot(\alpha_s\rho_s\vec{u}_s\vec{u}_s)=-\alpha_s\nabla p-\nabla p_s+\nabla\cdot\bar{\bar{\tau}}_s+\alpha_s\rho_s\vec{g}+\beta(\vec{u}_g-\vec{u}_s) \tag{3-4}$$

where, α is the volume fraction ($\alpha_g+\alpha_s=1$); ρ is the density; $\vec{u}$ is the velocity vector; β is the gas-solid interphase momentum transfer coefficient; $\vec{g}$ is the gravity acceleration; p_s is the solid pressure; and $\bar{\bar{\tau}}$ is the stress strain tensor.

The stress strain tensor of the gas and solid phases are defined:

$$\bar{\bar{\tau}}_g=\alpha_g\mu_g\left(\nabla\vec{u}_g+\nabla\vec{u}_g^T\right)-\frac{2}{3}\alpha_g\mu_g\nabla\cdot\vec{u}_g\bar{\bar{I}} \tag{3-5}$$

$$\bar{\bar{\tau}}_s=\alpha_s\mu_s\left(\nabla\vec{u}_s+\nabla\vec{u}_s^T\right)+\alpha_s\left(\lambda_s-\frac{2}{3}\mu_s\right)\nabla\cdot\vec{u}_s\bar{\bar{I}} \tag{3-6}$$

where μ is the shear viscosity and λ_s is the solid bulk viscosity. The standard k-ε turbulent model is used for modelling turbulence of gas phase as follows:

$$\mu_{gt}=\rho_g C_\mu\frac{k^2}{\varepsilon} \tag{3-7}$$

$$\frac{\partial}{\partial t}\left(\alpha_g\rho_g k\right)+\nabla\cdot\left(\alpha_g\rho_g\vec{u}_g k\right)=\nabla\cdot\left(\alpha_g\frac{\mu_{gt}}{\sigma_k}\nabla k\right)+\alpha_g G_k-\alpha_g\rho_g\varepsilon+\alpha_g\rho_g\prod_k \tag{3-8}$$

$$\frac{\partial}{\partial t}\left(\alpha_g\rho_g\varepsilon\right)+\nabla\cdot\left(\alpha_g\rho_g\vec{u}_g\varepsilon\right)=\nabla\cdot\left(\alpha_g\frac{\mu_{gt}}{\sigma_\varepsilon}\nabla\varepsilon\right)+\alpha_g\frac{\varepsilon}{k}\left(C_1G_k-C_2\rho_g\varepsilon\right)+\alpha_g\rho_g\prod_\varepsilon \tag{3-9}$$

where, k and ε represent the turbulent kinetic energy and dissipation rate of turbulent kinetic energy, respectively. The constants in the equations are $C_\mu = 0.09$, $C_1 = 1.44$ and $C_2 = 1.92$. The turbulent Prandtl numbers for k and ε are σ_k=1.0 and σ_ε=1.3.

3.2.2 Kinetic theory of granular flow

The solid phase is treated as a fluid in the TFM, and the KTGF is used to close the solid pressure and viscosities [106]. For the sake of numerical convergence, the algebraic approximation of KTGF is adopted in the computation of granular temperature. This is obtained by neglecting convection and diffusion in the transport equation:

$$0=\left(-p_s\bar{\bar{I}}+\bar{\bar{\tau}}_s\right):\nabla\vec{u}_s-\gamma_{\Theta_s}-3\beta\Theta_s \tag{3-10}$$

where $(-p_s\bar{\bar{I}}+\bar{\bar{\tau}}_g):\nabla\vec{u}_s$ is the generation of energy by the solid stress tensor. The collisional energy dissipation term is given by:

$$\gamma_{\Theta_s}=\frac{12(1-e^2)\alpha_s^2\rho_s g_0\Theta_s^{3/2}}{d_p\sqrt{\pi}} \tag{3-11}$$

The solid pressure, which represents the normal force due to particle interaction, is given by Lun et al. [196] as:

$$p_s=\alpha_s\rho_s\Theta_s\left[1+2\alpha_s g_0(1+e)\right] \tag{3-12}$$

where e is the restitution coefficient for the particle-particle collision and g_0 is the radial distribution function, expressed by:

$$g_0=\left[1-\left(\frac{\alpha_s}{\alpha_{s,max}}\right)^{\frac{1}{3}}\right]^{-1} \tag{3-13}$$

The bulk viscosity of the particle phase accounts for the resistance of granular particles to compression and expansion. Here, the Lun et al. [196] model is used by:

$$\lambda_s = \frac{4}{3}\alpha_s^2 \rho_s d_p g_0 (1+e)\sqrt{\frac{\Theta_s}{\pi}} \tag{3-14}$$

The particle shear viscosity is defined as the sum of collisional viscosity, kinetic viscosity and frictional viscosity:

$$\mu_s = \mu_{s,col} + \mu_{s,kin} + \mu_{s,fr} \tag{3-15}$$

$$\mu_{s,col} = \frac{4}{5}\alpha_s^2 \rho_s d_p g_0 (1+e)\sqrt{\frac{\Theta_s}{\pi}} \tag{3-16}$$

$$\mu_{s,kin} = \frac{\alpha_s \rho_s d_p \sqrt{\pi\Theta_s}}{6(3\text{-}e)}\left[1+\frac{2}{5}(1+e)(3e\text{-}1)g_0\alpha_s\right] \tag{3-17}$$

$$\mu_{s,fr} = \frac{p_s \sin\phi}{2\sqrt{I_{2D}}} \tag{3-18}$$

where ϕ is the angle of internal fraction, and I_{2D} is the second invariant of the deviatoric stress tensor.

3.2.3 Drag model

The expressions of interphase momentum transfer coefficient (β) in Eqns of 3-3 and 3-4 are described below for different drag models used in this study, respectively.

Gidaspow drag model [182]

In this model, the interphase momentum transfer coefficient (β) is obtained by:

$$\beta = \frac{3}{4}\frac{\alpha_s \alpha_g \rho_g |\vec{u_s}\text{-}\vec{u_g}|}{d_p} C_D \alpha_g^{-2.65} \qquad for\ \alpha_g > 0.8 \tag{3-19}$$

$$\beta = 150\frac{\alpha_s{}^2 \mu_g}{\alpha_g d_p^2} + 1.75\frac{\alpha_s \rho_g |\vec{u_s}\text{-}\vec{u_g}|}{d_p} \qquad for\ \alpha_g \leq 0.8 \tag{3-20}$$

where C_D is the standard drag coefficient for a particle, expressed by:

$$C_D = \begin{cases} \frac{24}{Re_s}(1 + 0.15Re_s^{0.687}), & Re_s < 1000 \\ 0.44\ , & Re_s \geq 1000 \end{cases} \quad (3\text{-}21)$$

where the particle-based Reynolds number is

$$Re_s = \frac{\rho_g |\vec{u}_s - \vec{u}_g|}{\mu_g} d_p \quad (3\text{-}22)$$

EMMS drag model [184]

This drag model refers to the EMMS drag model, which is expressed by:

$$\beta = \frac{3}{4} \frac{\alpha_s \alpha_g \rho_g |\vec{u}_s - \vec{u}_g|}{d_p} C_D \alpha_g^{-2.65} H_D \quad (3\text{-}23)$$

where H_D is defined as β/β_0 (β_0: Wen and Yu) to account for the hydrodynamic disparity between homogeneous and heterogeneous fluidization. The C_D has the same expressions as equation (3-21) in Gidaspow drag model. In this work, the EMMS model built by Lu et al. [197] for full-loop circulating fluidized bed is used. Table 1 summarizes the formulas of H_D for CFB structure.

Table 3-1**.** Formulas of H_D for the DCFB CLC unit.

Formulas ($H_D = a(\mathrm{Re}_s + b)^c, 0.001 \leq \mathrm{Re}_s \leq 1000$)	Range ($\alpha_{mf} < \alpha_g \leq 1$)
$\begin{cases} a = 0.12621 + 0.51327\exp(-0.5(\frac{\alpha_g - 0.51738}{0.05325})^2) \\ c = 0 \end{cases}$	$0.4 < \alpha_g \leq 0.51228$
$\begin{cases} a = 0.06022 + \frac{0.64769}{1 + (\alpha_g / 0.54069)^{38.95056}} \\ b = 1.26148 - \frac{1.25109}{(1 + \exp(-(\alpha_g - 0.49842)/0.00835))}(1 - \frac{1}{(1 + \exp(-(\alpha_g - 0.68685)/0.03593))}) \\ c = 0.27298 - \frac{0.298}{1 + (\alpha_g / 0.55363)^{29.78427}} \end{cases}$	$0.51228 < \alpha_g \leq 0.60826$

$$\begin{cases} a = 1/(15.09342 - 13.31486\alpha_g{}^{6.02771} \\ b = -52.05197 + 346.18273\alpha_g - 914.53136\alpha_g^2 + 1202.33087\alpha_g^3 - 786.52213\alpha_g^4 + 204.82611\alpha_g^5 \\ c = 1/(3.51503 + 3.1596\alpha_g^{4.34314} \end{cases} \qquad 0.60826 < \alpha_g \le 0.9904$$

$$\begin{cases} a = 0.52193 + \dfrac{0.8812}{1+\exp(-(\alpha_g - 0.99662)/0.00112)}\left(1 - \dfrac{1}{1+\exp(-(\alpha_g - 0.99752)/0.00006)}\right) \\ b = 0.47595 - \dfrac{0.22085}{1+(\alpha_g/0.99594)^{2170.31695}} \\ c = 0.13788 - 0.07951\exp\left(-0.5\left(\dfrac{\alpha_g - 0.99841}{0.00142}\right)^2\right) \end{cases} \qquad 0.9904 < \alpha_g \le 0.9997$$

$$a = 1, c = 0 \qquad 0.9997 \le \alpha_g < 1$$

Rong drag model [195]

The model is described as follows:

$$\beta = \frac{3}{4}\frac{\alpha_s \rho_g |\vec{u_s} - \vec{u_g}|}{d_p} C_D \alpha_g^{2-F_0} \tag{3-24}$$

where

$$C_D = \left(0.63 + \frac{4.8}{\sqrt{Re_s}}\right)^2 \tag{3-25}$$

$$F_0 = 2.65(\alpha_g + 1) - (5.3 - 3.5\alpha_g)\alpha_g^2 \, exp\left[-\frac{(1.5 - logRe_s)^2}{2}\right] \tag{3-26}$$

Tang drag model [193]

In this model, the interphase momentum transfer coefficient (β) is obtained by:

$$\beta = \frac{18\mu_g \alpha_s \alpha_g^2 F_0}{d_p^2} \tag{3-27}$$

$$F_0=\frac{10\alpha_s}{\alpha_g^2}+\alpha_g^2\left(1+1.5\sqrt{\alpha_s}\right)+\left[0.11\alpha_s(1+\alpha_s)-\frac{0.00456}{\alpha_g^4}+\left(0.169\alpha_g+\frac{0.0644}{\alpha_g^4}\right)Re_s^{-0.343}\right]Re_s+2.98Re_T\frac{\alpha_s}{\alpha_g^2} \tag{3-28}$$

where the Reynolds number based on the granular temperature is given as

$$Re_T=\frac{\rho_g\sqrt{\Theta_s}}{\mu_g}d_p=2.108Re_s^{0.85}\left(\frac{\rho_s}{\rho_g}\right)^{-0.5} \tag{3-29}$$

3.2.4 Numerical conditions and solutions

As shown in Fig 3.2, the geometry of the DCFB cold model is established according to a pilot-scale apparatus designed by Geng et al. [198]. The whole test rig is coupled by two identical CFB unit A and B. Each CFB unit consists of a riser with an inner diameter of 0.1 m and a height of 3 m, a cyclone separator, a downcomer with an inner diameter of 0.1 m and a height of 1.73 m, an overflow chute, and a loop seal. The solid particles are sand with an average diameter of 140 μm and a density of 2600 kg/m^3. The total amount of solid inventory in the experiments is approximately 70 kg. One inlet for aeration is installed at the bottom of the riser to transport solid materials with a large velocity and two inlets are located at the bottom of loop seal to stabilize the gas-solid flow with a relatively small air flow rate. In the experiment, the overflow chute was kept sealed for both CFB Units A and B. Therefore, the overflow chute is simplified for computational convenience. The main geometrical parameters of the DCFB for simulation are listed in Table 3-2.

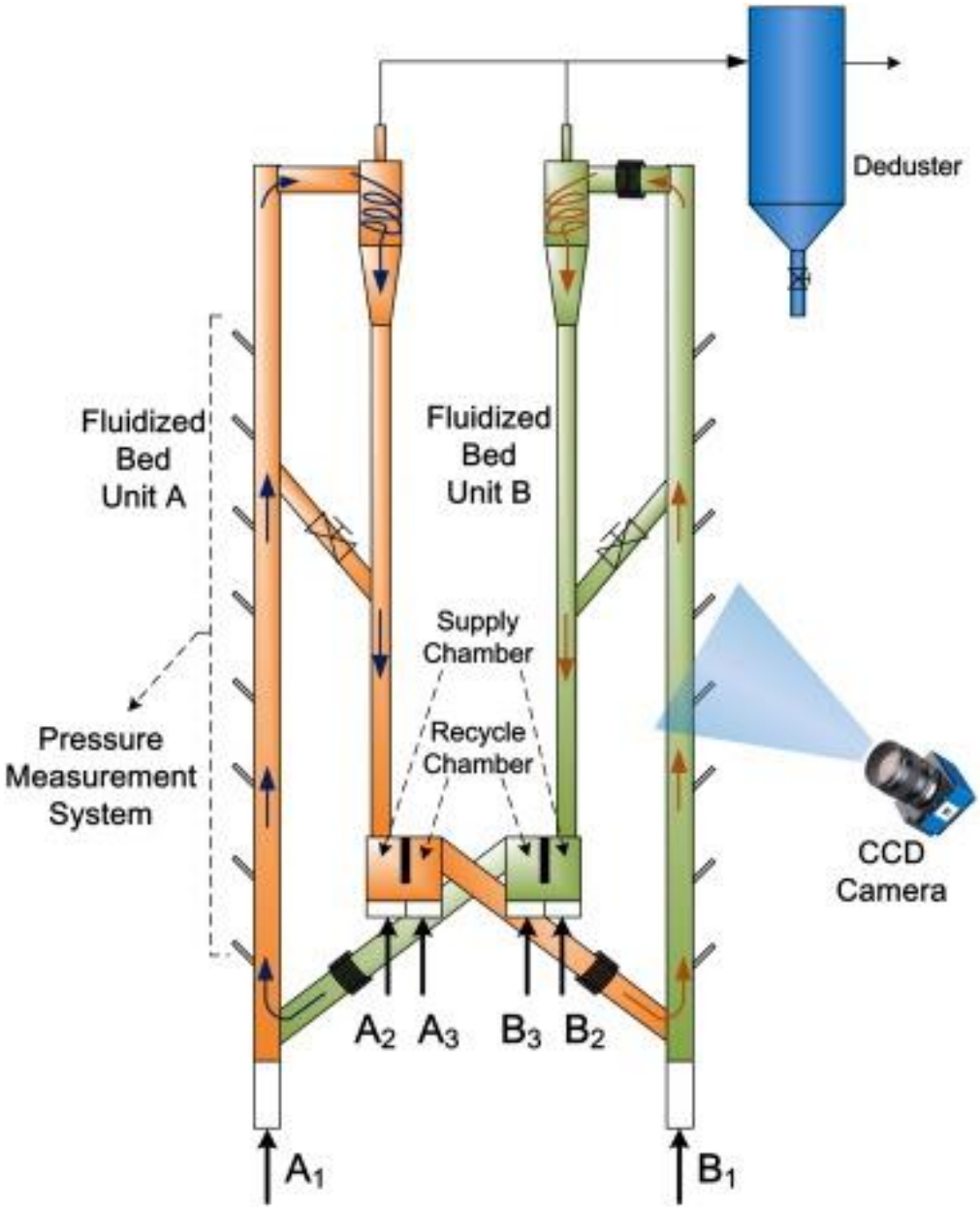

Fig 3.2. Schematic of the cold flow model employed in this work [198].

Table 3-2 Geometrical parameters of the DCFB.

Parameters	**Unit A and B**
Height of riser (mm)	3000
Diameter of riser (mm)	100

Height of downcomer (mm)	1730
Diameter of downcomer (mm)	100
Diameter of cyclone (mm)	145

Fig 3.3 shows the 3D geometry and grids of the DCFB. The majority of computational domains, including risers, downcomers and cyclones, are meshed with hexahedrons. Connecting parts are meshed with the tetrahedrons. A suitable number of computational grids could improve the accuracy of the prediction. A grid-sensitivity analysis is used to ensure the number of the grid is suitable for this simulation. Three different computational domains of 127310, 213600, and 334359 grid elements are tested with the same operation. The analysis (Fig 3.4) shows that the time-averaged pressure profile along the riser height in the case containing 127310 grids is significantly different from those of the others. Meanwhile, the pressures of the 213600 and 334359 grids show similar trends and lower deviations. Therefore, the mesh consisting of 213600 grids is considered as giving sufficiently accurate results and a reasonable computational cost. Besides, according to previous grid-dependence tests for CFB units with similar dimensions [151,176,197,199], such resolution is sufficient to predict the hydrodynamic behaviours in the system with adequate simulation time and numerical accuracy.

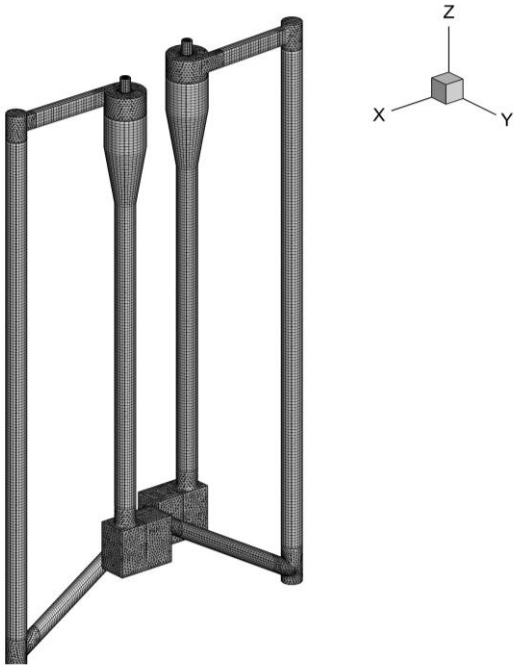

Fig 3.3. Computational domain and mesh used in this work.

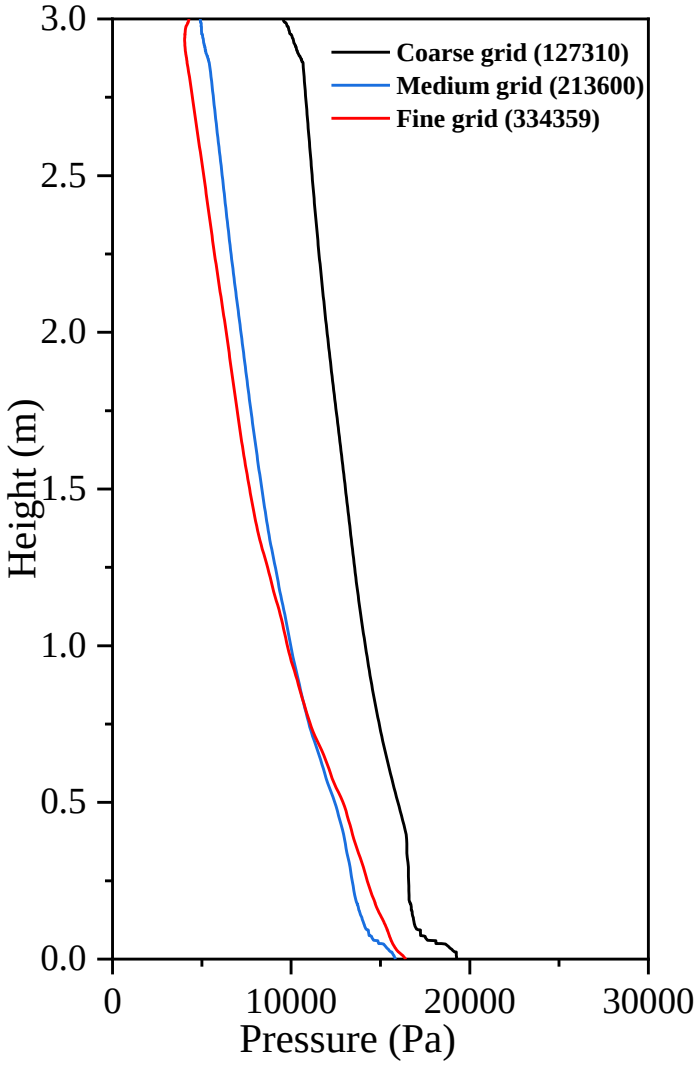

Fig 3.4. Time-averaged pressure profiles along the riser of unit A with different grid numbers.

Initially, the particles are loaded in the DCFB with a solid volume fraction of 0.5. The velocity inlet boundary conditions are set for the inlet of risers and pot-seals of units A and B. The pressure outlet condition is selected for the outlets. The frictional model of Schaeffer [200] for the particle phase and the Johnson and Jackson's model for wall boundary conditions of solid phase [201] is used in this work. The no-slip boundary condition is set for the gas phase. The pressure-based approach is employed to solve the governing equations. Different discretization schemes for convection terms of each governing equation are employed: the second-order upwind scheme is chosen for the momentum equation; the Quadratic Upwind Interpolation of Convective Kinematics

(QUICK) scheme is chosen for the volume fraction; the first-order upwind scheme is chosen for the turbulent kinetic energy and turbulent dissipation rate. The phase coupled Semi-Implicit Method for Pressure Linked Equations (SIMPLE) algorithm is used to deal with pressure-velocity coupling. The time step is assigned as 0.00005 s in this study. The material properties and the simulation parameters are listed in Table 3-3. The mathematical model is solved using commercial software ANSYS Fluent 18.1. The simulations ran for 65 s and the time-averaged computational results are obtained from the period between 45 s and 65 s.

Table 3-3 Gas-solid properties and computational settings.

Solid Properties		**Values**
Density (ρ_s)		2600 kg/m^3
Average particle size (d_p)		140 μm
Restitution coefficient of particles (e_{ss})		0.95
Restitution coefficient of particles (e_{sw})		0.95
Specularity coefficient (ψ)		0.01
Angle of internal friction		30°
Friction packing limit		0.60
Gas Properties		**Values**
Aeration rate	A1	140 m^3/h
	B1	110 m^3/h
	A2	4 m^3/h
	B2	3.45 m^3/h

	A3	30 m^3/h
	B3	30 m^3/h
Gas density (ρ_g)		1.225 kg/m^3
Gas viscosity (μ_g)		1.837×10^{-5} pa·s
Computational Settings		**Values**
Pressure-velocity coupling		Phase coupled SIMPLE
Time step		5×10^{-5} s
Max. number of iterations per time step		50
Convergence criteria		10^{-3}

3.3 Results and discussion

In this session, the typical gas-solid flow patterns in the DCFB are first discussed for a general description in the DCFB. Then, four drag models are compared for different Reynolds numbers to confirm their mathematical difference. And then, the four drag models are applied to the DCFB and quantitatively compared in terms of gas-solid flow patterns including solid volume fraction and pressure balance, and then further compared in terms of solid recirculation rate against experiment measurement. Finally, the applicability of four drag models are discussed from the perspective of theory, observation in this work and recently simulation work.

3.3.1 Description of typical gas-solid flow in the DCFB

In this part, the simulation results using the classic Gidaspow drag model as an example are used to describe the general internal gas-solid flow patterns and evolutions. Fig 3.5 shows the instantaneous solid volume fraction distribution in the DCFB. Initially, the particles are loaded in the downcomers and pot-seals. As the gas is introduced, the bed materials are fluidized. Particles exist from the top of the riser and return to the downcomer and pot-seal through the cyclone; finally, particles in the downcomer of unit B are fluidized by the air flow into the riser of unit A again via the pot-seal. Thus, the flow state of the parallel and interactive particle cycle is formed. The height of the bed material in the downcomers gradually decreases until the stable circulating flow is established. Different fluidization regimes can be observed in the whole system: fast fluidization in the riser, and bubbling fluidization in the pot-seals and downcomers. In order to explore the flow pattern of the solid phase in the different regions of the apparatus, Fig 3.6 illustrates the instantaneous local structure of the solid phase in the DCFB at time instant of 60 s. The particles in the bottom region of the riser move chaotically, mainly resulting from the mutual influence of back-mixing of solid phase along the wall region, the solid phase returned from pot-seal, the fluidizing gas introduced from the inlet, and the intensive particle-particle or particle-wall collisions. Comparatively, more regular motion of the solid phase can be observed in the upper region of the riser. As denoted in Fig 3.6, solid particles change flow direction from the vertical direction to the horizontal direction in the top region of the riser and enter the cyclone. Due to the restriction effect of the cyclone on the solid motion, the drag force on the particles is mainly not in the gravitational direction. Thus, the particles fall along the cyclone surface under the influence of gravity in a spiral status. The velocity of the solid phase decreases in the falling procedure. The most uncomplicated motion of the solid phase can be observed in the downcomer and pot-seal. In the pot-seal, particles move in a nearly packed status. Fig 3.7 and 3.8 show the radial distribution of time-averaged solid volume fraction and axial velocity at different heights in the riser A and B, respectively. Due to the effect of the

solid inlet, particles enter the riser from an inclined inlet tube at the bottom with a certain initial velocity. Therefore, a higher solid volume fraction can be observed on the opposite side of the inlet position in both riser A and B. As a result of high solid volume fraction, the solid velocity is relatively low on this side. Except for the influence of outlet, with the increase of height, the profiles of solid volume fraction and axial velocity over the cross section gradually become flat.

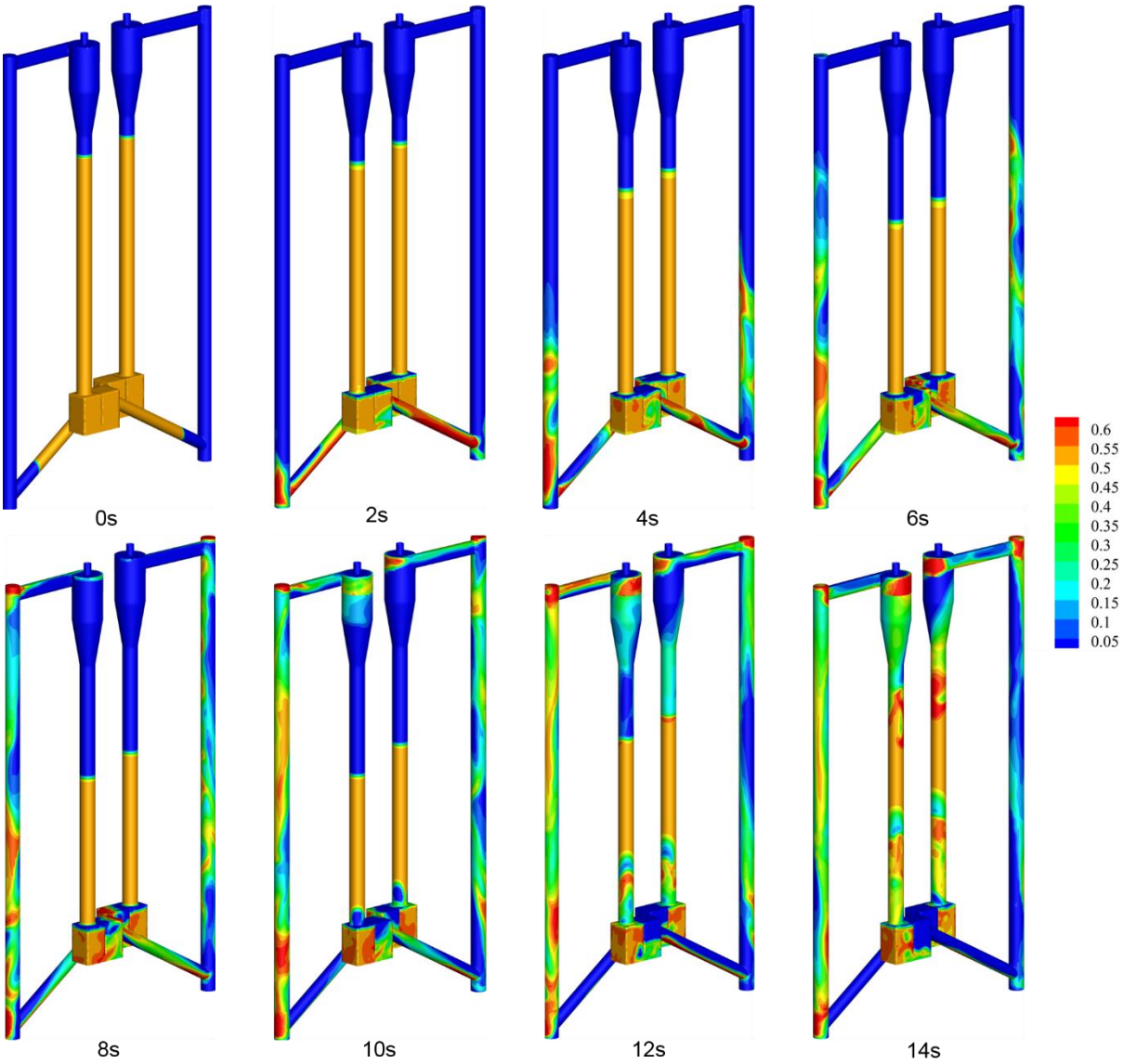

Fig 3.5. Contours of instantaneous solids volume fraction in the dual interconnected fluidized bed.

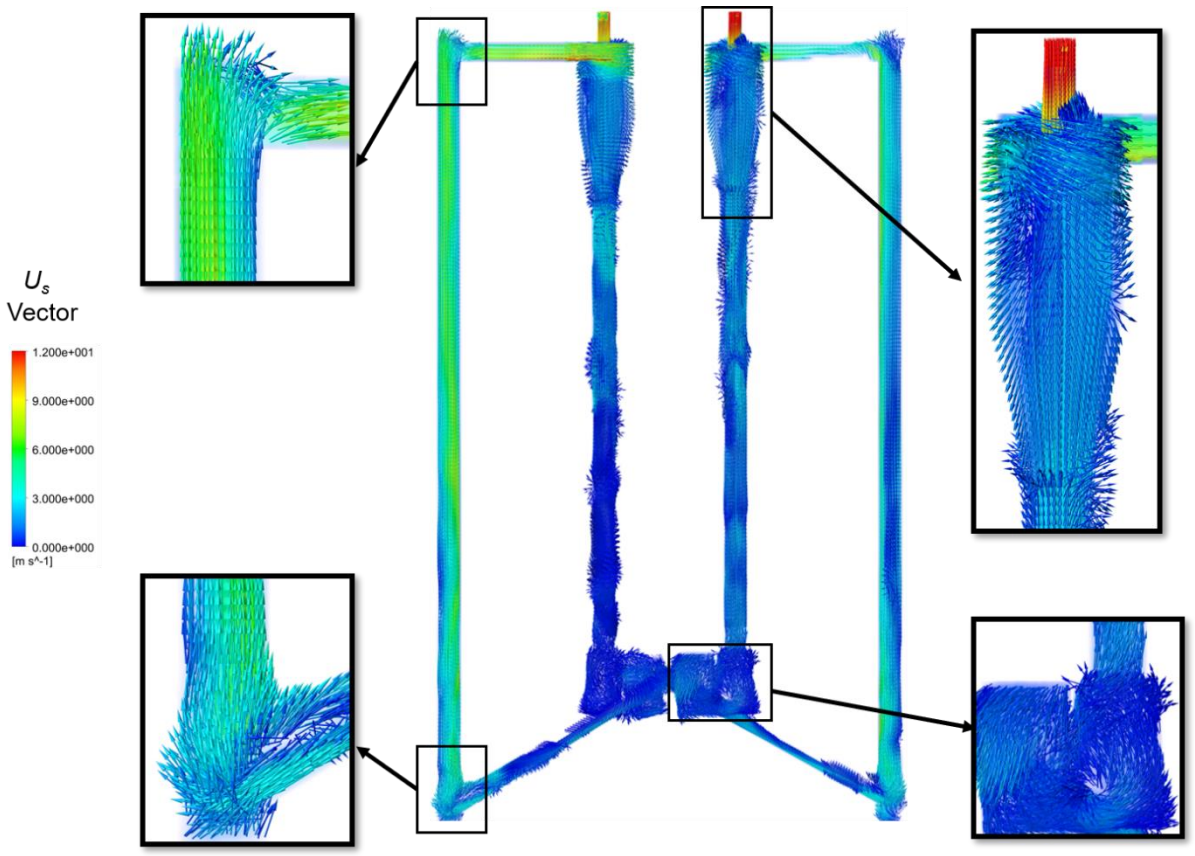

Fig 3.6. Instantaneous structure of solid motion, t= 60 s.

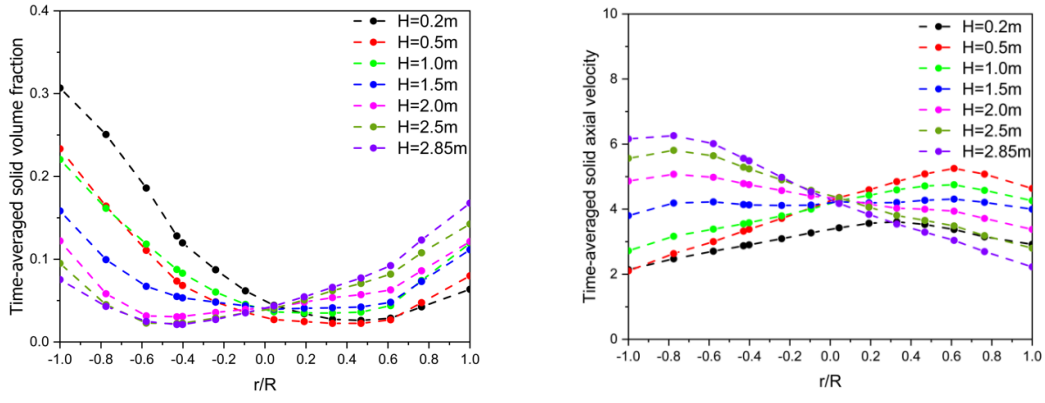

Fig 3.7. Radial distributions of solid volume fraction and axial velocity at different heights in the riser A.

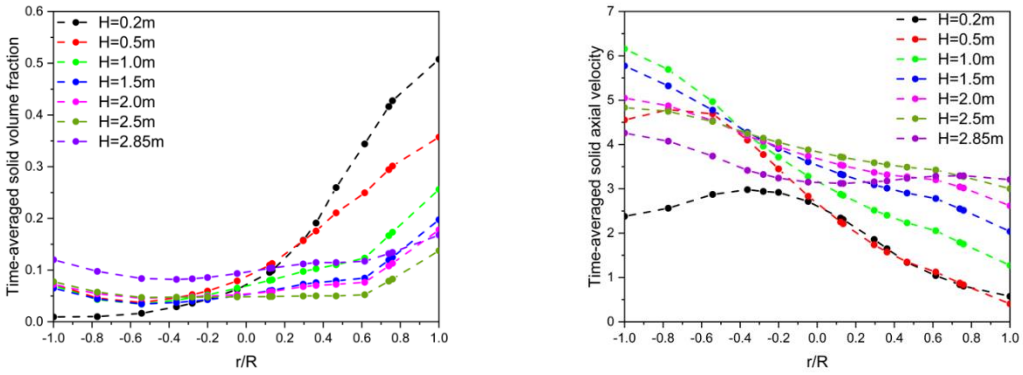

Fig 3.8. Radial distributions of solid volume fraction and axial velocity at different heights in the riser B.

3.3.2 Pre-assessment of four drag models

The interaction between the gas phase and the solid phase is considered by incorporating the drag force term $\beta(\vec{u_g}\text{-}\vec{u_s})$ for which, the interphase momentum exchange coefficient, β, is denoted by different drag models. Its value is drawn as the function of local Reynolds number and voidage under the relevant operating conditions. Therefore, four drag force models derived from different methods in this part are compared for different Reynolds numbers by plotting β against α_s, as shown in Fig 3.9. It is observed that the EMMS drag models [197] and Rong drag model [195] give significantly higher values of β for all the range of Reynolds numbers that are studied here. The EMMS model shows a rather unusual behaviour between 0.48 and 0.6 of α_s because of the strong influence of the heterogeneity index of clusters. At the incipient fluidization voidage, the β of EMMS model is lower than all other drag models. In the voidage range from 0.48 to 0.7, the β first decreases and then increases quickly. The models by Gidaspow [182] and Tang et al. [193] show very similar behaviours for all Reynolds numbers. It is inferred that the four models are very different mathematically.

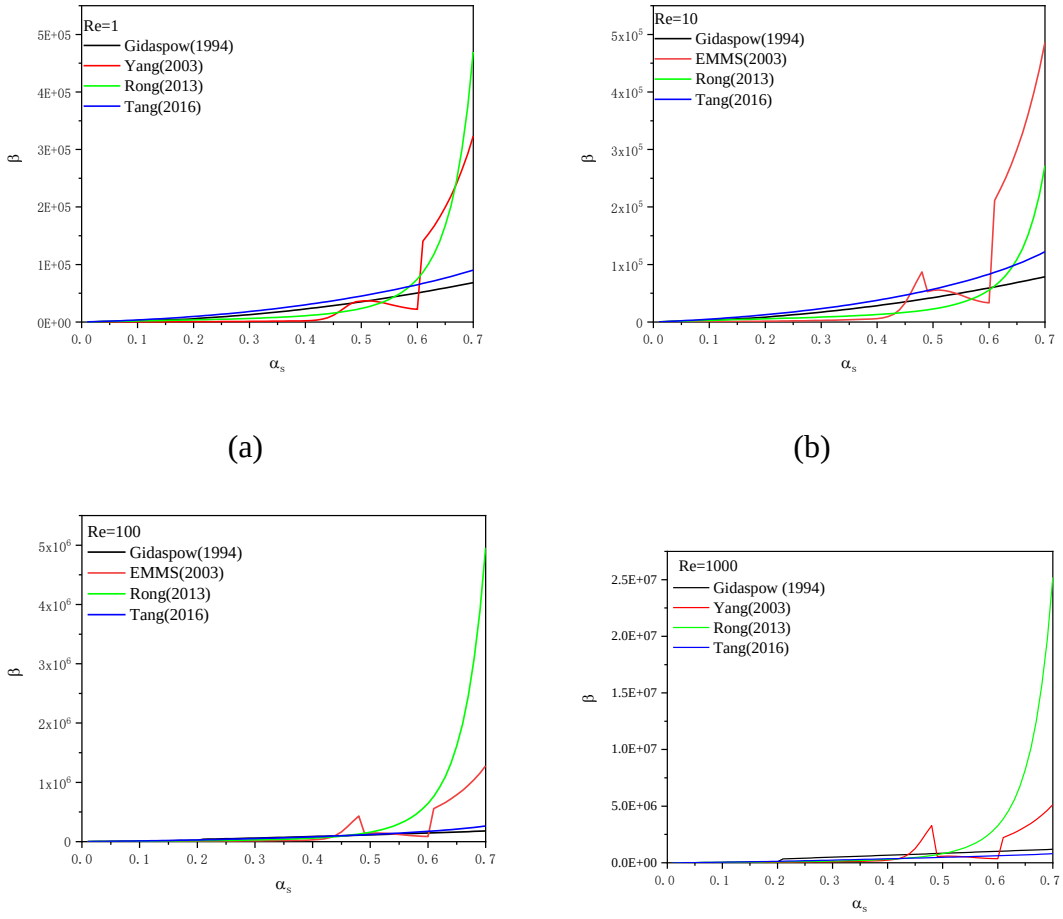

Fig 3.9. Comparison of drag model equations for different values of Re_s. Re_s=1 (a); Re_s=10 (b); Re_s=100 (c); Re_s=1000 (d).

3.3.3 Quantitative comparisons

Time-averaged solid volume fraction distribution

Fig 3.10 compares the time-averaged solid volume fraction distribution throughout the full-loop system with several horizontal cross sections at different heights of the riser in unit A and B for the four drag models. In comparison, the non-uniform distribution of solid concentrations can be recognized for all simulations with different drag models. Most particles are accumulated in the downcomer and pot-seal while much fewer particles can be found in the riser. From contours of solid concentration at different heights, a similar phenomenon can be predicted by four drag models that the solid volume

fraction α_s is dilute in the centre and dense near the wall, showing a significant core-annulus flow structure in both risers. Meanwhile, with the increasing of the height in both risers, the difference of α_s along the radial direction gradually diminishes, and the distribution of particles tends to be uniform. Fig 3.11 shows the time-averaged axial profiles of cross-sectional averaged solid volume fraction for different drag models in the riser of unit B. It can be seen the axial voidage profile predicted by Gidaspow drag model is close to a vertical line. This result also can be found in some simulation literature [202–204]. However, the experimental data show that the solid volume fraction is large at the bottom and small at the top of the riser. The simulation with EMMS, Rong and Tang drag models can capture this phenomenon. However, all these three drag models have an underestimated bed density in the dense phase, while an overestimated one in the dilute phase of the bed. This should be attributed to the lack of consideration of the effects of cohesive forces and agglomeration, which results in a higher drag force.

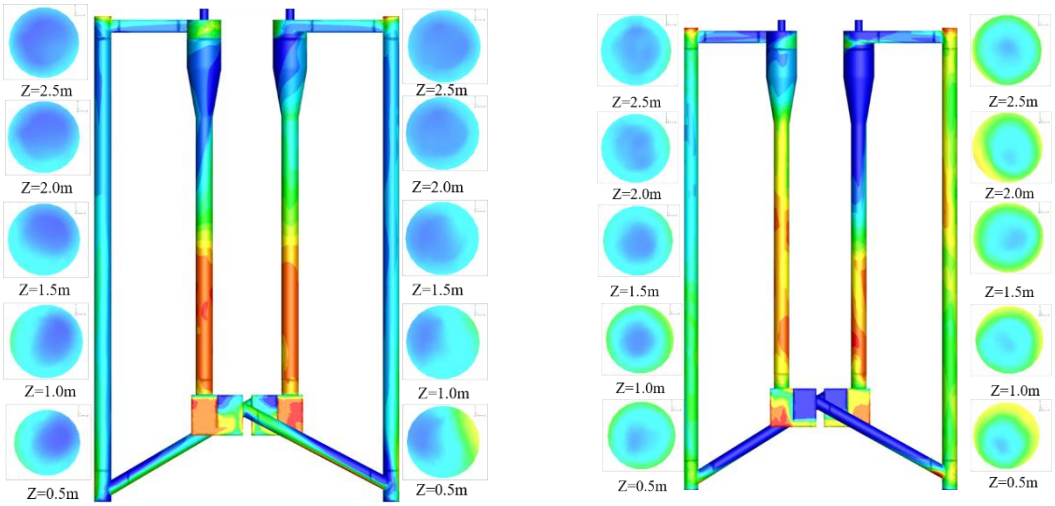

(a) Gidaspow (b) EMMS

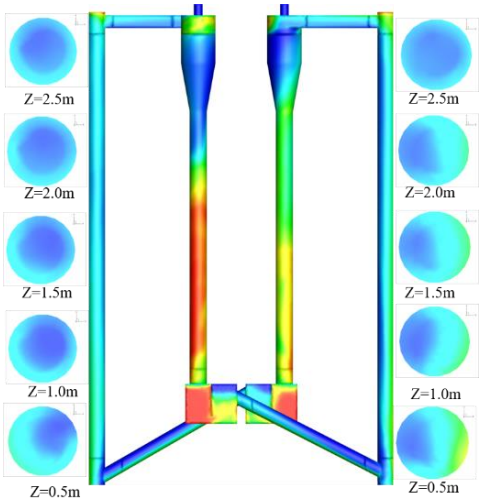

(c) Rong et al.

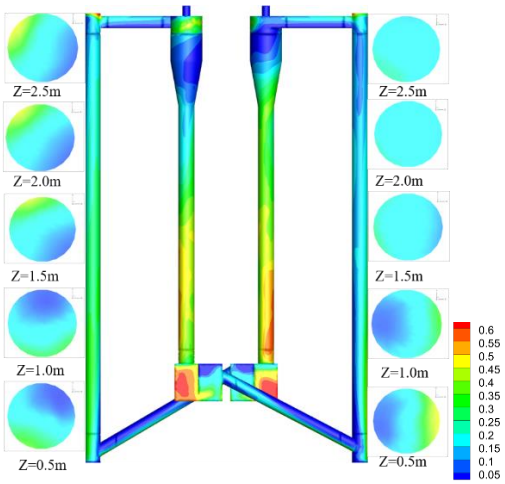

(d) Tang et al.

Fig 3.10. Time-averaged solid volume fraction distribution throughout the full-loop system with several horizontal cross sections at different heights of the riser in unit A and B.

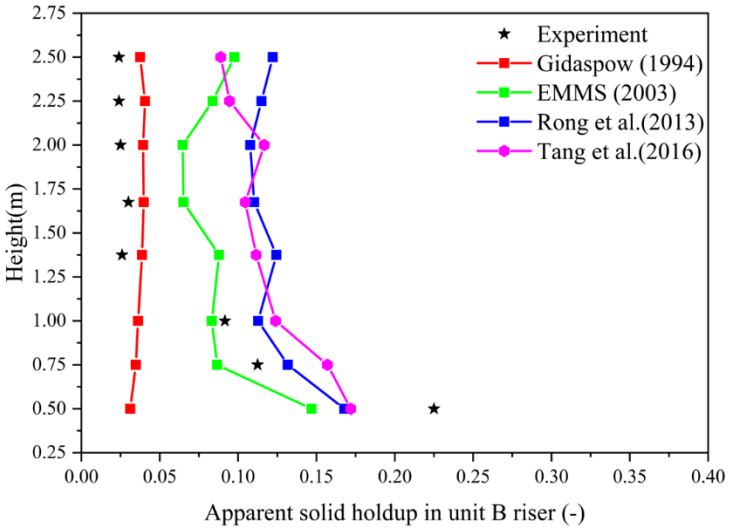

Fig 3.11. Axial solid volume fraction in Unit B for different drag models.

Pressure balance in the CLC system

The pressure balance is a crucial issue for the chemical looping process because it maintains the solid circulation between the AR and FR and can also prevent gas leakage within the full system. Fig 3.12 compares the time-averaged pressure profiles along the centre line throughout the full-loop system for the four drag models. From results of all these four simulation cases, the similar characteristics of pressure distribution can be observed that pressure gradient is large at the bottom and comparatively small at the top, and the largest gradient occurs at the downcomer and pot-seal, which agrees qualitatively with the empirical knowledge [108,205,206]. It is noted that pressure decreases along with the height of the riser and is small, ranging from the riser outlets to the cyclone inlets. The pressure is nearly constant in the cyclone. The pressure drop for the cyclone and downcomer is roughly more than three times of that for riser when using the Gidaspow, Rong and Tang drag models, while it seems quite close if the EMMS model is employed. In further comparison, it can be seen that the pressure in the body region of the cyclone is lower than those in the pot-seal and lower part of the riser. The pressure in the downcomer is lower than that in the riser and pot-seal. The relationships between these parts are responsible for the closure of the system pressure balance. The full-loop pressure distribution feature is consistent with some open literature [171,197,207].

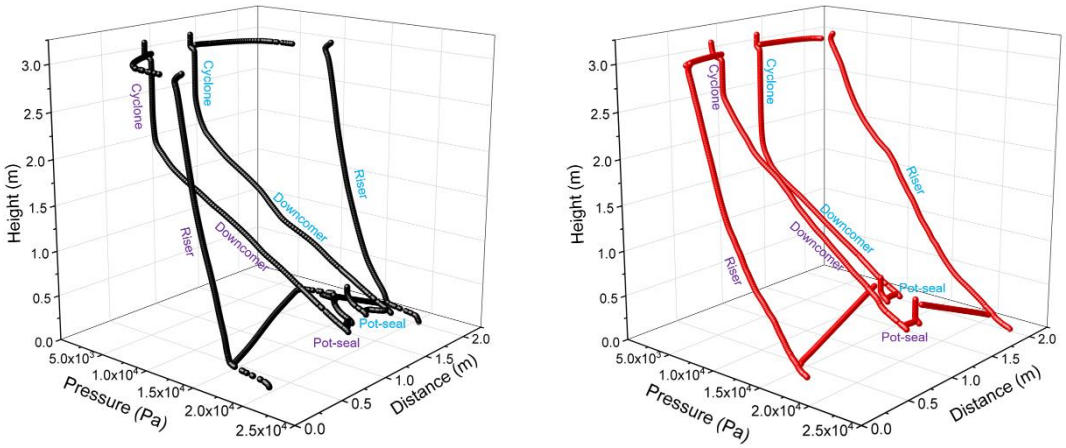

Gidaspow EMMS

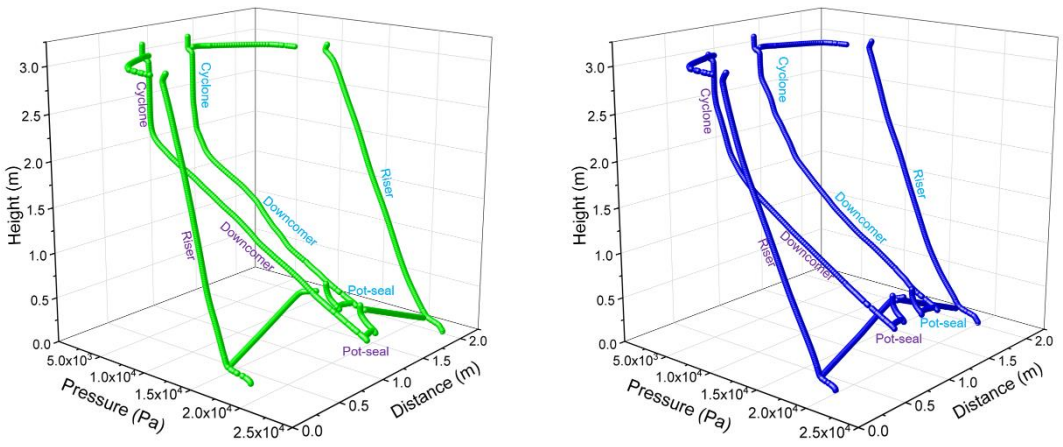

Rong et al Tang et al

Fig 3.12. Time-averaged pressure profile along the center line throughout the full-loop system.

Comparison with experiments in terms of solid circulation rate

In the DCFB for the CLC process, the solid circulating rate between the AR and FR plays a critical role to determine the heat transportation and chemical reactions [208,209]. It is a measurable index in DCFB CLC processes. In order to further investigate which drag model may predict a more accurate simulation, the simulation results using the four drag models are compared with the experiment measurement [198].

Fig 3.13 (a) shows the profiles of the solid mass flow rates with different drag force models, where the solid mass flow rates are sampled from a horizontal cross-section set in the riser of unit A. The intense fluctuations of solid mass flow rates between 0 and 30 s of the computational time are removed, which could be regarded as the start-up process. Afterwards, the solid mass flow rates fluctuate around a constant value, indicating the achievement of quasi-stable solid circulation in the whole system. By comparison, the strongest fluctuations can be observed using the Gidaspow drag model while the EMMS drag model oscillates in a narrow range. The instantaneous values of solid circulating rates are averaged between 45 s and 65 s when all curves oscillate around certain constant

values. The data presented in Fig 3.13 (b) show that the time-averaged values predicted by different models do not match very well with the observed experimental value. It can be seen that the all these four drag models predict a higher solid flow rate than the experimental value, but the EMMS result is much lower than the other models as the heterogeneous flow structure can significantly reduce the gas-solid drag force, which is consistent with the Yang's results [210]. By comparison among the drag models presented in this work, the solid circulation rate predicted by the EMMS drag model is the closest to the experimental value. In contrast, the results predicted by the Gidaspow drag model show the most significant deviation in the system and conditions investigated.

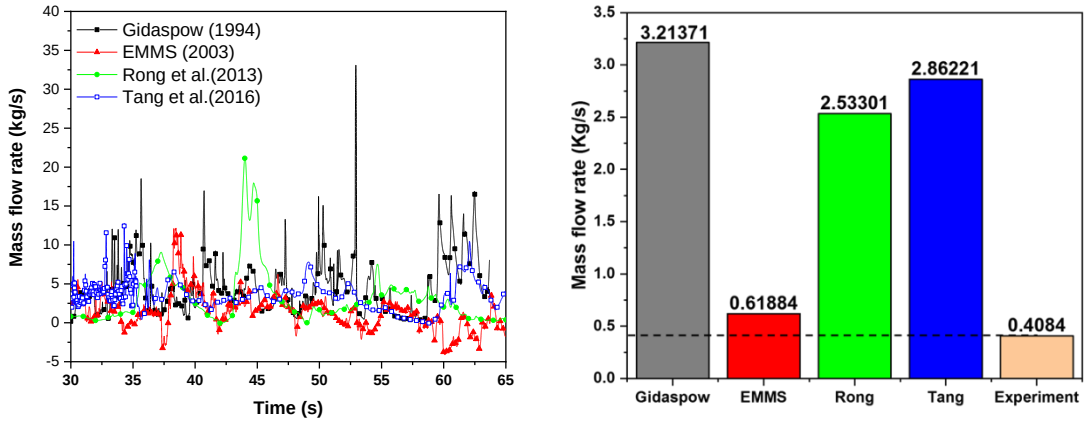

(a) (b)

Fig 3.13. Profile of the solid mass flow rate with different drag model (a) solid mass flow rate fluctuations with the computational time and (b) time-averaged solid mass flow rates at the quasi-stable state.

3.3.4 Discussion of model applicability

In this section, the applicability of four drag force models used in this work is discussed from the perspective of theory, observation in this work and recently simulation work.

The Gidaspow [182] drag model has a sharp alternation at $\alpha_g = 0.8$ due to the discontinuity caused by switching from Ergun correlation [183] to Wen-Yu [180] correlation which can give rise to numerical instability. The Gidaspow model thus cannot accurately capture the phenomenon (e.g., cluster) in the low part of the circulating fluidized bed with high particle concentration and the resulting heterogeneous structures. It is applicable to homogeneous fluidization with the effect of frequently temporal and spatial evolutions of gas-solid flows omitted. In this work, the Gidaspow drag model cannot capture the phenomenon of dense α_s in the low part and shows the largest deviation with the experimental data. This is also observed in many previous simulation studies [185,208,211,212].

The EMMS [184] drag model divides the flow into three pseudo phases: dilute phase, dense phase and suspended clusters. The dilute phase represents the individual particle in the gas phase. The dense phase represents particles and gas residing inside clusters, whereas the suspended clusters phase represents the individual cluster as a whole entity that moves in the gas phase. Particle clusters continuously form and break in heterogeneous flows, especially for small particles such as Geldart A particles. The clustering of particles results in a heterogeneous solid distribution, with high gas-solid slip velocity and remarkable drag reduction [213–215]. Quantifying the clusters and their effects on the drag is critical for the realistic simulations of heterogeneous gas–solid flows. The EMMS drag model calculates drag force in every three pseudo phases by using a conventional Wen-Yu drag model. Drags in the dilute phase and dense phase are calculated by using the particle diameter, while drag in the suspended cluster phase is calculated by using the cluster diameter [216]. The EMMS drag model is regarded as suitable for turbulent or circulating fluidized beds [217,218]. However, there are still some problems to be solved concerning the correlation of cluster diameter. Additional assumptions have to be made to numerically correct the axial and radial EMMS drag models for a specific operating condition which significantly increase the difficulty of using this model [216]. In this work, it can be seen that the EMMS drag model predicts a

higher solid flow rate than the experimental value, but it is much lower than the other models as the heterogeneous flow structure can greatly reduce the gas-solid drag force. This result is consistent with some previous simulation works [219–221].

Rong [195] drag model was proposed by fitting a curve to the data generated from several simulations in the packed bed of uniform spheres by using the Lattice Boltzmann Method (LBM) in the range of solid volume fraction $0.1 \leq \alpha_s \leq 0.6$ and mean slip Reynolds number $0.002 \leq Re_s \leq 3000$. For this model, particles are fixed in space without relative motion and the effect of particle fluctuations is not accounted for. Until now, this model is just applied in packed bed [222–224] or porous media [219,225,226].

Tang [193] drag model is probably the first one to take into account the effect of granular temperature for a wide range of particle Reynolds numbers ($50 \leq Re_s \leq 1000$) and solid volume fractions ($0.1 \leq \alpha_s \leq 0.6$) based on the Immersed Boundary Method (IBM) in which particles were allowed to move freely under the influence of fluid-particle interactions and elastic particle-particle collisions. In this model, however, all the particles were uniformly distributed throughout the domain during the simulations. Thus the system seems to be homogenous. Some previous simulation works show that this model is not able to produce good results in their computation [227,228]. In this work, both Rong and Tang drag model give a higher prediction compared with the experimental data. To date, no relevant simulation work can be found to study hydrodynamics in the CFB system with these two drag models.

Several fluidization regimes can be observed in the DCFB, including bubbling fluidization, turbulent fluidization, fast fluidization, and dilute phase transport regimes. The complex interaction between solid and gas phases makes the flow unstable and produces non-uniform and time-varying multiscale structures [229–231]. Therefore, based on the discussion of the model applicability above, the EMMS drag model is regarded as more suitable in the DCFB simulations.

3.4 Conclusions

A 3D TFM hydrodynamic model is developed for a DCFB of CLC unit based on Eulerian-Eulerian TFM with the kinetic theory of granular flow. The influence of four different drag force models derived from different methods, namely Gidaspow drag model, EMMS drag model, Rong drag model and Tang drag model, on the hydrodynamics of DCFB are studied in terms of internal flow pattern and overall performance. The main conclusions can be drawn as follows:

1) The overall assessment confirms that the drag model selection has a significant influence on simulations of gas-solid flows in DCFBs for chemical looping combustion.

2) For qualitative analysis, all the drag models can predict a reasonable radial solid distribution and pressure distribution, but only the EMMS, Rong and Tang drag models can capture the phenomenon of dense α_s in the low part of the riser.

3) For quantitative analysis, the solid circulating rate predicted by the EMMS drag model is the closest to the experimental measurements. In contrast, the results predicted by the Gidaspow drag model show the most significant deviation.

In summary, in the system and conditions investigated, the EMMS drag model gives the best results for simulating dense gas-solid flows in DCFB, followed by Rong and Tang drag models. The Gidaspow drag model shows the most significant deviation. The results shed lights on the drag force model sections and the optimization of DCFBs.

CHAPTER.4 Hydrodynamic Behaviours in a Coal-direct Chemical Looping Combustion with Moving-bed Fuel reactor

This chapter continues to take the CLC process as an example to study the hydrodynamics in the CFB system. Different from the last chapter, a new type of CLC system, which has a unique moving bed configuration, is used in this chapter. A multi-fluid model based on the Eulerian-Eulerian framework is used to study the gas-solid hydrodynamics in a full-looping moving-bed CDCL unit. In this chapter, the study is divided into two steps: firstly, a 3D CFD model is used to investigate the gas-solid flow in the air reactor of the CDCL unit used in this chapter. The unique fluidisation state of Geldart type D particle is detailed studied. The effects of several variables in terms of the operation condition and model selections on the gas-solid flow in the air reactor are also explored, including gas velocity, specularity coefficient and different drag models. The model is qualitatively and quantitatively validated. Then, the validated model settings are applied to build the 3D full-looping moving-bed CDCL unit. Unique fluidisation states are predicted in different domains by simulation results. And the influence of several boundary conditions on the solid circulation rate and pressure distribution are investigated.

The paper “Numerical study of gas-solid flow behaviors in the air reactor of coal-direct chemical looping combustion with Geldart D particles” has been published based on the content of this chapter in the journal of Powder Technology.

The paper “Numerical simulation of the coal-direct chemical looping combustion process” is under revision based on the content of this chapter.

S. Li, Y. Shen, Numerical study of gas-solid flow behaviors in the air reactor of coal-direct chemical looping combustion with Geldart D particles, Powder Technol. 361 (2020)74–86.

S. Li, Y. Shen, Numerical simulation of the coal-direct chemical looping combustion process. (under revision)

Graphical abstract for this chapter

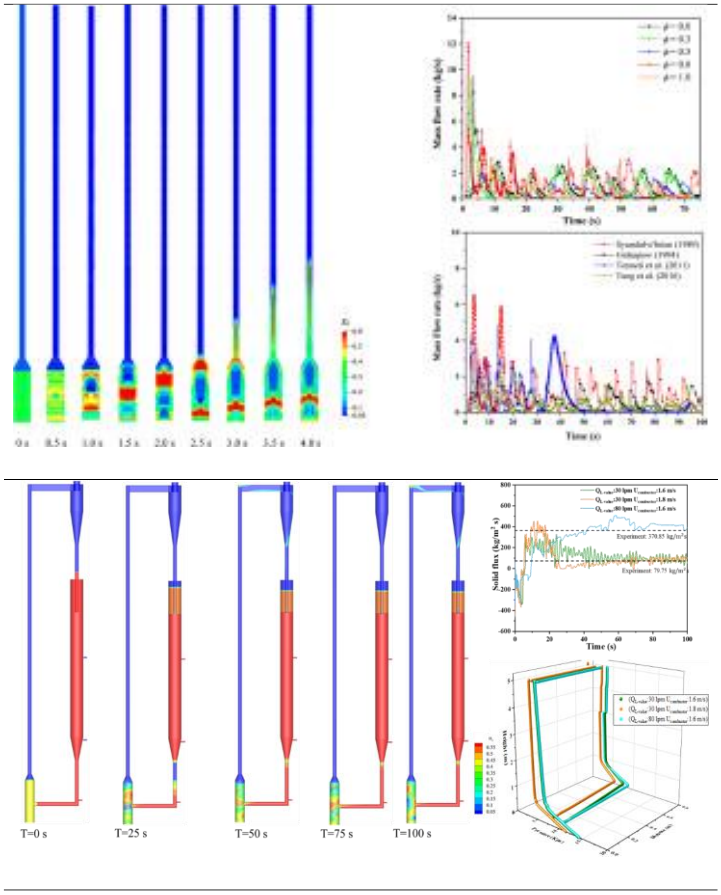

ABSTRACT

Chemical Looping Combustion (CLC) is a promising clean combustion technology alternative to conventional oxy-combustion because of its technical feasibility to achieve intrinsic separation of CO_2. In this chapter, a multi-fluid model based on the Eulerian-Eulerian framework is used to study the gas-solid hydrodynamics in a unique moving-bed Coal-Direct Chemical Looping (CDCL) unit. In this Coal-Direct Chemical Looping (CDCL) process, iron-based oxygen carriers belonging to Geldart D particles are used. Such systems have been seldom studied. In particular, the study is divided into two steps: firstly, a two-fluid model (TFM) is adopted for describing the gas-solid flows in a bottom-enlarged air reactor of the CDCL process. The model is qualitatively and quantitatively validated. The simulation results indicate that the oxygen carrier particles show a slugging flow pattern in the bottom section of the air reactor, an anti-core-annulus structure in the riser and a periodic fluctuation in the whole air reactor. The effects of several variables on the gas-solid flow in the CDCL air reactor are also studied, including gas velocity, specularity coefficient and different drag models. The simulation results indicate that the higher gas inlet velocity can increase the pressure drop over the air reactor and show a significant influence on solid allocation in the bottom section and the riser. Specularity coefficient of zero and Syamlal-O'Brien drag model give the closest mass flow rate by comparing with experimental values, indicating that they are suitable for the three-dimensional air reactor modelling. This model provides a cost-effective tool for a better understanding of gas-solid flows in the air reactor of CDCL systems. Then, the validated

model settings are applied to build the 3D full-looping moving-bed CDCL unit. Unique fluidization states are predicted in different domains of the full-looping system by simulation results. And the influence of several boundary conditions on the solid circulation rate and pressure distribution are investigated. Compared with the dual fluidized bed CLC unit, the pressure drop in this moving bed CDCL unit is low which indicates the system is more stable. Results also show that the solid flux through the L-valve is not affected when the combustor gas velocity increases from 1.6 m/s to 1.8 m/s. The solids circulation rate is controlled by the flow rate of aeration gas on the standpipe of the L-valve.

4.1 Introduction

Over the past decades, carbon dioxide emission has caused the increasing concentration of greenhouse gases in the atmosphere. It contributes to many irreversible severe environmental issues, such as atmospheric warming, sea-level rise and so on [8]. It is well known that carbon dioxide is mainly formed by the combustion of fossil fuels. In recent years, Carbon Capture and Storage (CCS) has drawn more and more attention, which is an economically-attractive method of reducing greenhouse gases emissions from the combustion of fossil fuels. CLC technology is regarded as the latest and most promising technology with the inherent separation of CO_2 [13]. In conventional combustion processes, the fuel will mix directly with air or high concentration oxygen in the combustor to produce heat and energy. Therefore, a massive volume of exhaust gas

mixture will exit from the combustor, which consists of primarily carbon dioxide, steam and nitrogen. Separating CO_2 from the N_2 requires significant energy and extra costs. However, in CLC technology, CO_2 separation can be easily achieved because the fuel is not in touch with air directly during this process. The net chemical reaction and energy release of the CLC process are identical to that of the conventional combustion of fossil fuels. A small amount of energy is spent on solid circulation (0.3% of the total energy released) [14]. The conventional CLC consists of two separate reactors: an air reactor and a fuel reactor. A solid oxygen carrier, which is often a metal oxide, is circulated between the reactors to transfer oxygen from the air to fuel reactor. The fuel is fed into the fuel reactor where it is oxidized by the lattice oxygen of the metal oxide into CO_2 and H_2O. In the air reactor, reduced oxygen carrier particles are regenerated by air.

Over the last decade, the chemical looping technology has shown significant advancement from its concept to lab and bench-scale testing (<5 kWh) [51,64,65,95], sub-pilot scale testing (5-50 kWh) [50,159], and pilot-scale testing (50 kWh - 5MW_{th}) [42,158,167,232]. Most CLC processes are developed based on a typical circulating fluidized bed, conducted in the bubbling, turbulent, fast fluidized-bed, or spouted bed regime. Ohio State University (OSU) Coal-Direct Chemical Looping (CDCL) process utilized a unique counter-current moving bed reactor design for the conversion of solid fuels to sequestration-ready CO_2 [102,233]. Here, a composite iron-based particle which belongs to the Geldart D particle was used as the oxygen carrier, different from any previously CLC works. It has been proven by long-term research and experimentation

that this CDCL sub-pilot unit can achieve a high coal conversion using the counter-current moving bed reducer and the synthesized iron-based oxygen carriers. Many experiments and process analysis by ASPEN PLUS of the bench-scale and sub-pilot scale unit have been carried out to verify the improved performance [102,104,234]. However, most of the data obtained are global thermal characteristics, such as coal and oxygen carrier conversion rates, gas composition at the reducer outlet and temperature at different ports. The detailed inner phenomenon such as local flow pattern, temperature distribution and product concentration distribution cannot be observed because of the limited experimental measurements. Thus, an in-depth understanding of gas-solid hydrodynamics is needed for process design and scale-up.

Computational fluid dynamics (CFD) is a cost-effective tool to offer insights into complex fluid dynamics and has become a fundamental method to study multiphase systems [235–237]. Several hydrodynamic CFD studies on chemical looping applications have been published in the literature. For example, Wang et al. [238] developed a comprehensive three-dimensional (3D) numerical model with reaction kinetics model to simulate the CLC process in the fuel reactor. The flow patterns, distribution of gas components, profile of bubbles and conversions of gas reactants were obtained. In addition, the effects of particle diameter and superficial gas velocity on the fuel conversion were studied. Geng et al. [151] developed a 3D TFM model for simulating the full-looping solid circulation in a dual circulating fluidized bed (DCFB) CLC reactor model. Key gas-solid flow behaviours related to gas-solid behaviours, e.g. the transient

flow regime, solid velocity, solid distribution and circulation characteristics, were numerically investigated. Liu et al. [239] used a 3D computational particle fluid dynamics (CPFD) model of a pilot scale circulating bed to simulate its solid-solid characteristics. The bed pressure drop characteristics of the CFB were obtained for different bed material heights. Wang et al. [240] studied the effect of superficial gas velocity on solid behaviours in a full-loop circulating fluidized bed using computational fluid dynamics-discrete element method (CFD-DEM). These modelling works provide a guide for further understanding of the flow characteristics in CFBs. However, the majority of modelling simulations of CLC units are based on the fuel reactor and full-looping system using fine and light particles classified to Geldart A or B group. Few CLC simulation works are done for understanding the flow behaviour of Geldart D oxygen carrier in the CLC.

In this work, a 3-D CFD model is adopted to investigate the unique gas-solid flow characteristics in the two-stage air reactor of the CDCL system. The model is validated against the measurements in a lab-scale slugging fluidized bed. Experimental results from a pilot-scale CDCL unit in terms of the solid mass flow rate and pressure drop are also used to evaluate the performance of different parameters. The influence of superficial gas velocity, wall boundary condition, and drag models on the pressure fluctuation, solid concentration and solid axial velocity are then studied.

4.2 Mathematical Model

The TFM model under the Eulerian-Eulerian framework with the standard kinetic

theory of granular flow is used in the present work [106,182]. The gas phase and solid phase are both regarded as a continuum phase, and the former is treated as the primary phase while the latter is treated as the secondary phase. The details of TFM formulations are summarized in Sections 3.2.1 and section 3.2.2.

The momentum transfer between the two phases is considered by coupling the inter-phase forces, including drag, lift, and virtual mass forces. Since the drag force is the key accelerating force acting on the solid particles, the drag model must be carefully selected to ensure reliable results. There are several drag models that have been proposed over the past several decades. They can be basically divided into two main categories: some are derived from experimental tests and others are derived from numerical simulations. For example, Syamlal and O'Brien's (1989) drag model [181] is based on the terminal velocity of a single particle in a fluid. This model assumes that, at terminal velocity, the drag force on a particle is equal to its buoyant weight. Gidaspow (1994) drag model [182] is a combination of the Ergun equation [183] and the Wen and Yu (1966) [180] drag model, and describes gas-solid flow hydrodynamic in both dense and dilute phases. These two drag models mentioned above are derived from the experimental results for homogeneous system such as the fixed beds or particulate fluidization and have been used as the standard drag models in many fluidized bed simulations. Recent simulation works dedicated to improving the accuracy of predictions of the drag force acting on assemblies of spheres for a wide range of Reynolds numbers focused in two aspects: (1) developing highly accurate solid–fluid boundary conditions [192,241] and (2) introducing granular

temperature into the drag force correlation for assemblies of spheres [193]. For example, the drag force model by Tenneti et al. (2011) [192] is based on Particle-resolved Uncontaminated fluid Reconcilable Immersed Boundary Method (PUReIBM) simulations of monodisperse particles and worked well in the two-fluid model framework. Based on the results of PR-DNS simulations, Tang et al. (2016) [193] proposed a drag model, which is probably the first one to take into account the effects of granular temperature for a wide range of particle Reynolds numbers and solid volume fractions based on Immersed Boundary Method-Computational Fluid Dynamics (IBM-CFD) computations in which particles were allowed to move freely under the influence of fluid-particle interactions and elastic particle-particle collisions. They will be compared in this work. The expressions for β in different drag models studied in this article are collected and described in Table 4-2.

Table 4-1 Gas-solid drag relations.

Syamlal-O'Brien (1989) [181]
$\beta = \frac{3}{4}\frac{\alpha_s \alpha_g \rho_g}{v_{r,s}^2 d_p} C_D\left(\frac{Re_s}{v_{r,s}}\right)\left\|\vec{u}_s - \vec{u}_g\right\|$ (4-14)
where
$C_D = \left[0.63 + \frac{4.8}{\sqrt{Re_s / v_{r,s}}}\right]^2$ (4-15)
$\upsilon_{r,s} = 0.5(A - 0.06\,\mathrm{Re}_s + \sqrt{(0.06\,\mathrm{Re}_s)^2 + 0.12\,\mathrm{Re}_s(2B - A) + A^2})$ (4-16)

$$A = \alpha_g^{4.14}, B = 0.8\alpha_g^{1.28} \qquad for \quad \alpha_g \leq 0.85 \tag{4-17}$$

$$A = \alpha_g^{4.14}, B = 0.8\alpha_g^{2.65} \qquad for \quad \alpha_g > 0.85 \tag{4-18}$$

Gidaspow (1994) [182]

$$\beta = \frac{3}{4} C_D \frac{\alpha_s \alpha_g \rho_g |\vec{u}_s - \vec{u}_g|}{d_p} \alpha_g{}^{-2.65} \qquad \text{for} \quad \alpha_g > 0.8 \tag{4-19}$$

$$\beta = 150 \frac{\alpha_s{}^2 \mu_g}{\alpha_g d_p{}^2} + 1.75 \frac{\alpha_s \rho_g |\vec{u}_s - \vec{u}_g|}{d_p} \qquad \text{for} \quad \alpha_g \leq 0.8 \tag{4-20}$$

where

$$C_D = \begin{cases} \frac{24}{\alpha_g Re_s} [1 + 0.15(\alpha_g \cdot Re_s)^{0.687}] & for \quad Re_s \leq 1000 \\ 0.44 & for \quad Re_s > 1000 \end{cases} \tag{4-21}$$

$$\mathrm{Re}_s = \frac{\rho_g \left| \overrightarrow{u_s} - \overrightarrow{u_g} \right|}{\mu_g} d_p \tag{4-22}$$

Tenneti et al. (2011) [192]

$$\beta = \frac{18 \mu_g \alpha_s \alpha_g{}^2 F_0}{d_p{}^2} \tag{4-23}$$

$$F_0 = \frac{K_1}{\alpha_g^3} + K_2 + K_3 \tag{4-24}$$

Where

$$K_1 = 1 + 0.15\, Re_s{}^{0.687} \tag{4-25}$$

$$K_2 = \frac{5.81 \alpha_s}{\alpha_g^3} + \frac{0.48 \alpha_s^{\frac{1}{3}}}{\alpha_g^4} \tag{4-26}$$

$$K_3 = \alpha_s^2\, Re_s (\, 0.95 + \frac{0.61 \alpha_s^3}{\alpha_g^2}) \tag{4-27}$$

$$\mathrm{Re}_s = \frac{\rho_g \left|\overrightarrow{u_s} - \overrightarrow{u_g}\right|}{\mu_g} d_p \tag{4-28}$$

Tang et al. (2016) [193]

$$\beta = \frac{18\mu_g \alpha_s {\alpha_g}^2 F_0}{{d_p}^2} \tag{4-29}$$

$$F_0 = \frac{10\varepsilon_s}{\varepsilon_g^2} + \varepsilon_g^2(1+1.5\sqrt{\varepsilon_s}) + [0.11\varepsilon_s(1+\varepsilon_s) - \frac{0.00456}{\varepsilon_g^4} + (0.169\varepsilon_g + \frac{0.0644}{\varepsilon_g^4})\mathrm{Re}_s^{-0.343}]\mathrm{Re}_s + 2.98\mathrm{Re}_T \frac{\varepsilon_s}{\varepsilon_g^2} \tag{4-30}$$

where

$$\mathrm{Re}_s = \frac{\rho_g \left|\overrightarrow{u_s} - \overrightarrow{u_g}\right|}{\mu_g} d_p \tag{4-31}$$

$$\mathrm{Re}_T = \frac{\rho_g \sqrt{\Theta_s}}{\mu_g} d_p = 2.108\,\mathrm{Re}_s^{0.85} (\frac{\rho_s}{\rho_g})^{-0.5} \tag{4-32}$$

The frictional model of Schaeffer [200] for the particle phase and the Johnson and Jackson's model for wall boundary conditions of solid phase [201] is used in this work. The no-slip boundary condition is set for the gas phase. The pressure-based approach is employed to solve the governing equations. Different discretization schemes for convection terms of each governing equation are employed: second-order upwind scheme is chosen for the momentum equation; the Quadratic Upwind Interpolation of Convective Kinematics (QUICK) scheme is chosen for the volume fraction of gas and solid. The phase coupled Semi-Implicit Method for Pressure Linked Equations (SIMPLE) algorithm is used to deal with pressure-velocity coupling. A time step for 0.00005s is selected for this study. The mathematical model is solved using commercial software ANSYS Fluent

18.1. The simulations ran for 100 s and time-averaged computational results are obtained from the period between 60 s and 100 s.

4.3 Simulation conditions

In CLC systems, the air reactor is usually a column riser. However, in the CDCL unit, the air reactor is composed of a combustor and a riser. In the CDCL unit, the combustor is an enlarged-bottom column with 6 in inner diameter and 25 in height. During experiments [242], the gas with a low velocity but slightly larger than the minimum fluidization velocity was introduced into the combustor and the solid particles was in a bubbling state. The aim of this design was to increase the solids residence time and the solids concentration in the riser and enhance the gas-solid contact without influencing the flow behaviour. The inner diameter of upper riser is 2 in and the height is 161 in. Because of the reduced cross-sectional area, the gas from the combustor enters the riser with a velocity over the terminal velocity so that particles can be transported upwards and back to the fuel reactor. A transition section was designed between the two reactors to avoid the sudden change of inner phenomenon and smooth the gas-solid flow. The reduced oxygen carrier particles from the fuel reactor, Fe_3O_4, were fed into the combustor from the bottom inlet as the bed material. Air was introduced into the reactor from the bottom to support the oxidant for the regeneration of oxygen carrier and transport particles back to the fuel reactor. These settings are primarily reproduced in the simulations. Moreover, the top section is set as the outlet at atmospheric pressure. Solid particles escaping from the outlet of air reactor will be recirculated through the side inlet to keep solids constant

in this work. Therefore, the boundary condition of the solid inlet is continuously changing as the total solid inventory in the air reactor changes. It should be noted that the effects of gas distributor above the bottom gas inlet are ignored and it is considered as a uniform inlet boundary condition for the sake of model simplification. Figure 1 shows the 3-D geometry and grids generated by ANSYS ICEM. The grids are meshed with hexahedrons in order to optimize the quality of the mesh. A calculation domain of 85941 cells is used. A comprehensive grid independence test is also done to ensure that the mesh used in this study is reasonable. In addition, a similar grid size was used in other simulations of similar systems [243–246]. These two points can clarify that such resolution is sufficient to predict the hydrodynamic behaviours in the system with acceptable simulation time and numerical accuracy. The material properties and the simulation parameters used of the base case are listed in Table 4-3.

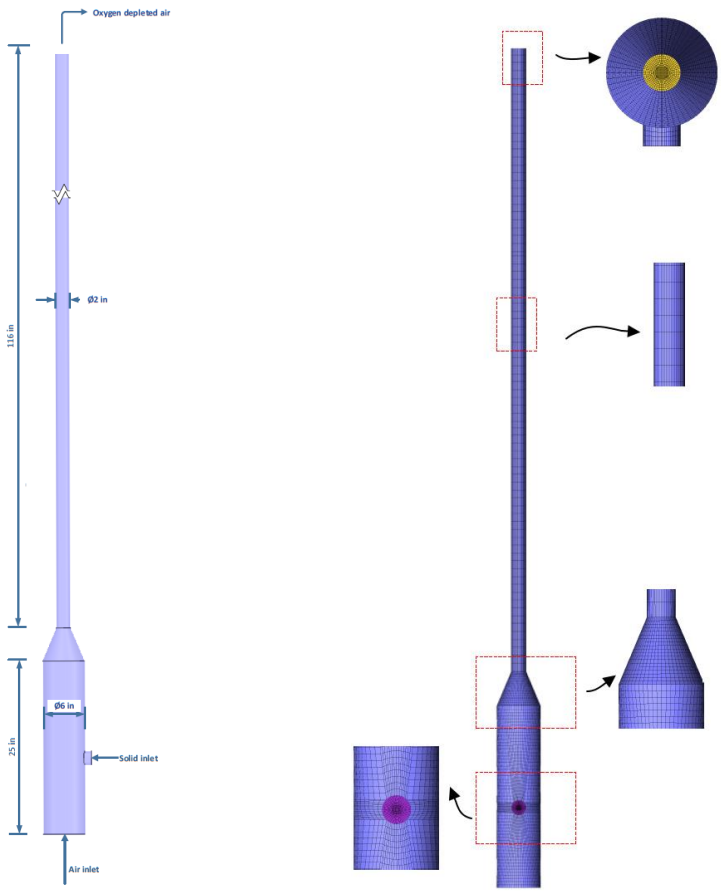

(a) (b)

Fig 4.1. Schematic geometry and mesh of simulated 3-D air reactor.

Table 4-2 Material properties and computational settings of the base case.

Solid Properties	**Values**
Density (ρ_s)	2500 kg/m^3
Average particle size (d_s)	1.5 mm
Minimum fluidization velocity (U_{mf})	1.12 m/s
Restitution coefficient of particles (e_{ss})	0.95

Restitution coefficient of particles (e_{sw})	0.95
Specularity coefficient (ϕ)	0.5
Angle of internal friction	30°
Friction packing limit	0.60
Packing limit of solid	0.63
Gas Properties	**Values**
Inlet gas velocity (U_f)	1.6 m/s
Gas density (ρ_g)	1.225 kg/m^3
Gas viscosity (μ_g)	1.837×10^{-5} pa·s
Computational Settings	**Values**
Pressure-velocity coupling	Phase coupled SIMPLE
Gas-solid drag model	Gidaspow [182]
Time step	5×10^{-5} s
Max. number of iterations per time step	50
Convergence criteria	10^{-3}

4.4 Results and Discussion

4.4.1 Model validation

Due to the insufficient experimental data for the air reactor used in this study, the same model settings are applied to a lab-scale slugging fluidized bed [247] where the same fluidized particles were used in experiments. The slugging fluidized bed consists of a stainless-steel column with an inner diameter of 76.2 mm and 0.76 m height. An enlarged section with a diameter of 154 mm and a height of 0.3 m is installed on top of the 76.2 mm section to reduce the gas velocity and disengage the particle from the gas flow, so that there is no particle loss during the experiment. In the stainless-steel column experiments, the initial bed height under the fixed bed condition is 0.4 m. Besides the geometry and initial conditions, the materials and model settings are consistent with the model of the air reactor. A technology called electrical capacitance volume tomography (ECVT) was used in this experiment for 3-D multiphase flow imaging. In simulation setting, the transient solid volume fraction at the same domain as ECVT is monitored. Then solid volume fractions can be compared with the experimental data.

First, the instantaneous solid volume fraction at a different time is shown at U_g=1.56 m/s (Fig 4.2). It can be seen that the developed slugs under current condition fill the cross-section of the bed completely, giving the so-called square-nosed slugs [248]. This phenomenon also can be observed from the reconstructed slug images through the ECVT sensor in experiments [247].

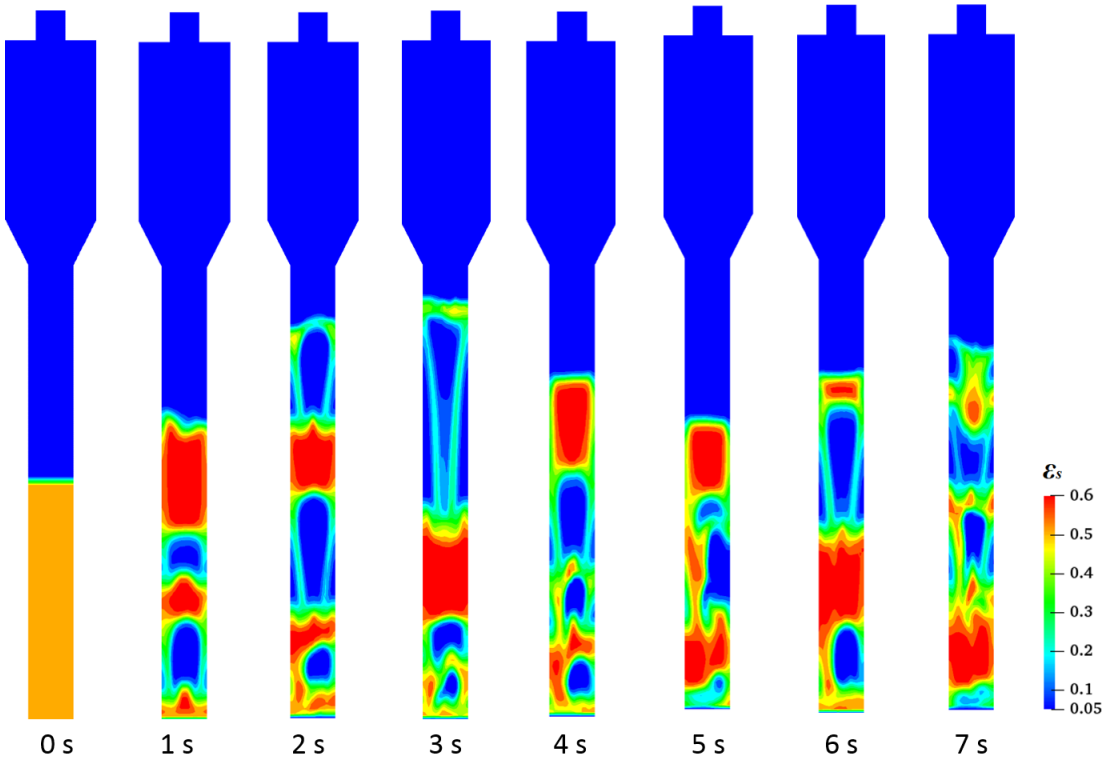

Fig 4.2. Instantaneous snapshots of solid concentration distribution (25 ℃, 1.56 m/s).

Then, the results of simulations and lab experimental measurements are compared at different superficial gas velocities of 1.56 m/s, 1.89m/s and 2.39 m/s. By counting the numbers of the recurring changes in the average solid volume fraction through the ECVT region, the average time intervals between two successive slugs can be obtained. As shown in Fig 4.3(a), when the superficial gas velocity is 1.56 m/s, the average time interval between two slugs is 1.82 s by removing the initial 5 s instability, which is comparable with the measured time interval ranging from 1.75 to 2 s in the experiment (Fig 4.4). When the superficial gas velocity is 1.89 m/s and 2.39 m/s, the average time interval between two slugs is around 1.58 s and 1.05 s, respectively. They are all within

the range of experimental measurements, as shown in Fig 4.4. That is, the average time internals from the simulation results agree quantitatively well with experimental data in a wide range of superficial velocity.

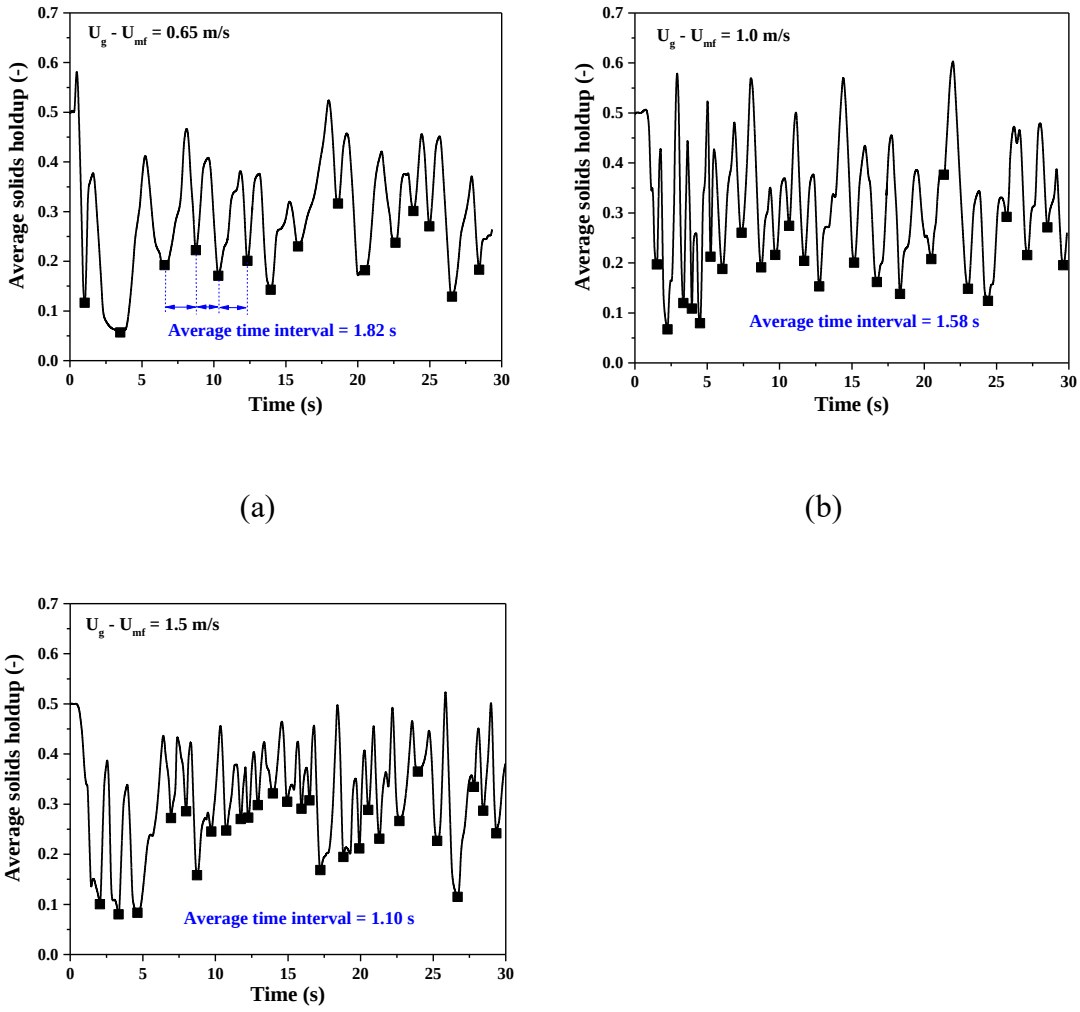

Fig 4.3. Time-evolution profiles of average solids holdup in ECVT region under three typical velocities: U_g=1.56 m/s (a); U_g = 1.89 m/s (b); U_g = 2.39 m/s (c).

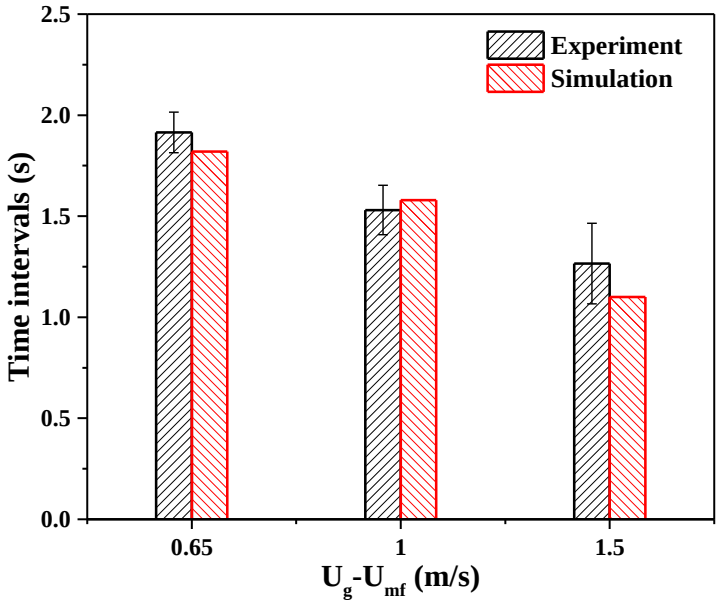

Fig 4.4. Comparison of time intervals between experimental data [247] and simulation results under different velocities.

4.4.2 Typical flow patterns

Fig 4.5 shows the instantaneous snapshots of solid volume fraction distribution of the base case. From the contours of solid volume fraction at different time, segregation of gas and solid phases along the combustor can be seen obviously. By comparison, the flow in the combustor belongs to the round-nosed slug which is consistent with experiment observation [242]. In the riser, the solid phase distribution is dilute because of high gas velocity, larger than the terminal velocity.

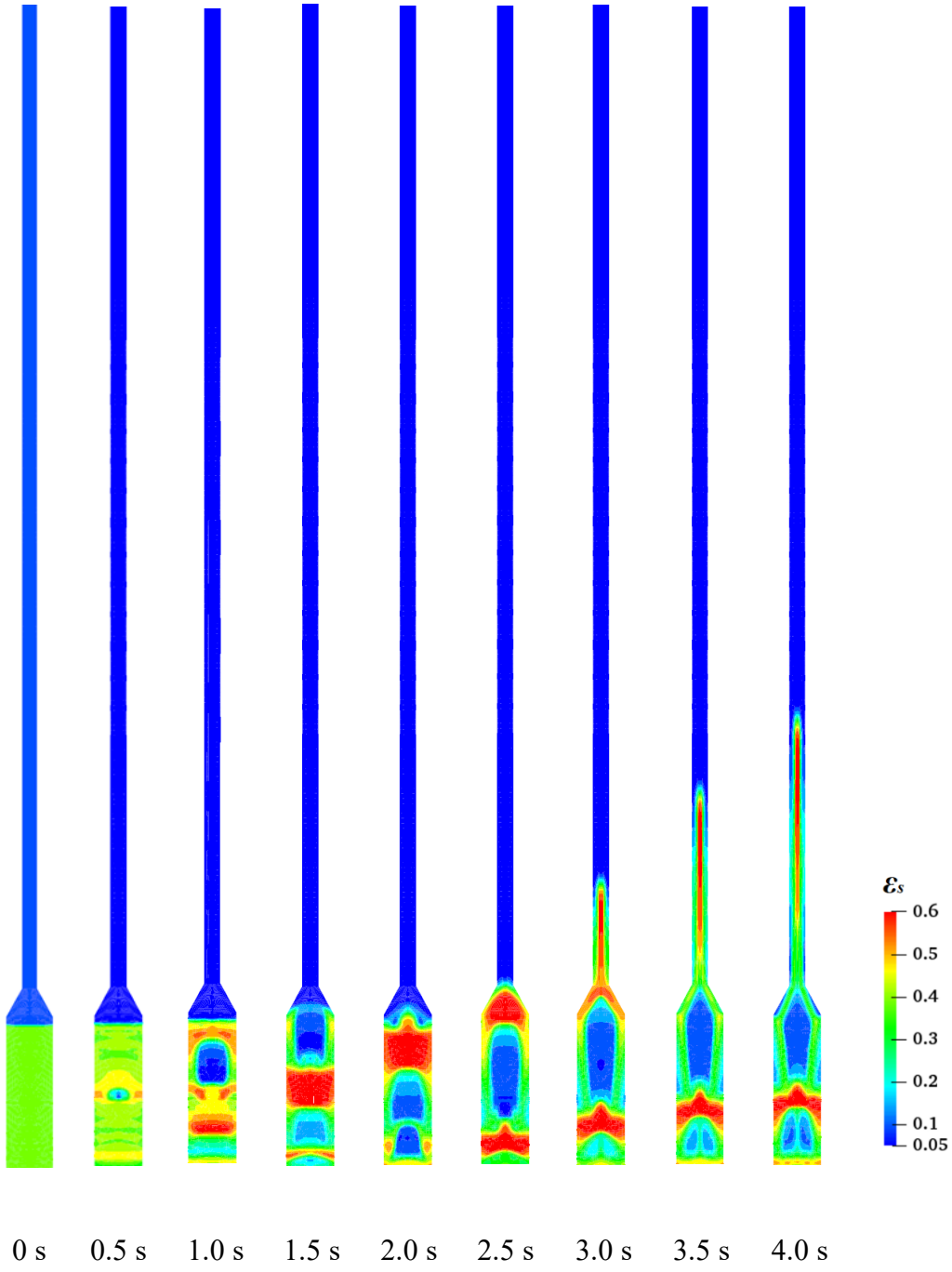

Fig 4.5. Instantaneous snapshots of solid volume fraction for the base case, U_f = 1.6 m/s.

For the base case, the axial distribution of the time-averaged solid volume fraction is illustrated in Fig 4.6 by averaging cross-sectional solid volume fraction at different

heights. It can be seen that a lot of particles accumulate in the combustor which is beneficial to increase the solid inventory of the air reactor. Besides, the solid volume fraction shows a sudden decrease at the height of 0.65 m because of the smaller cross-sectional area of the riser. In the riser, the time-averaged distribution of solid is dilute and uniform ranging from 0.031 to 0.035 due to high superficial gas velocity.

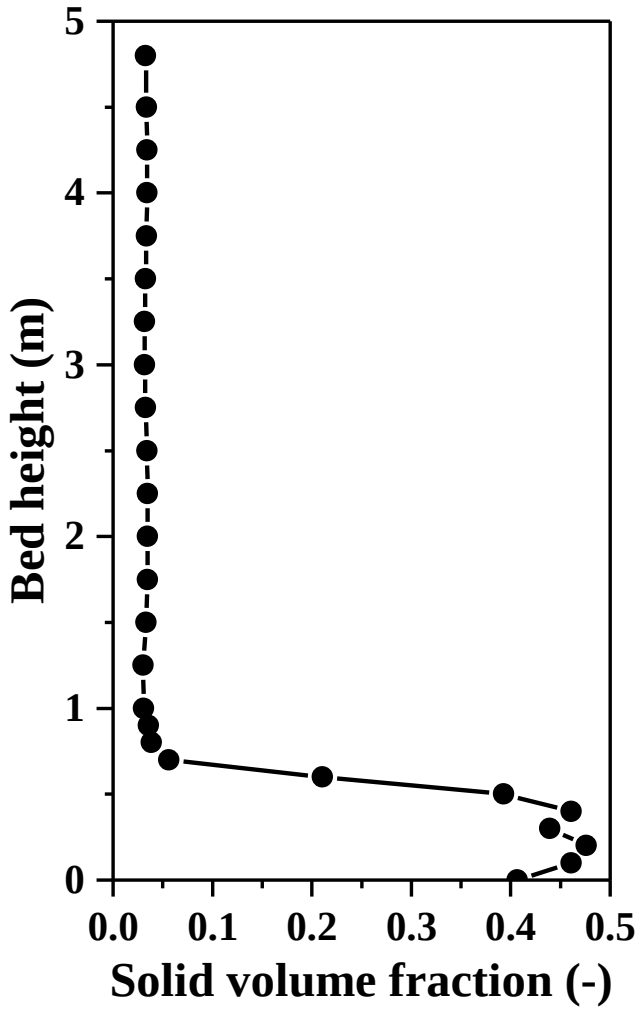

Fig 4.6. Time-averaged solid holdup at different heights (U_f = 1.6 m/s.).

Fig 4.7 shows the radial distributions of solid concentration at different heights in the air reactor. By comparing values at different radial positions, it can be found that in the

combustor, the solid concentration is small at the centre and large near the wall. This is because the slugs move upward in the central region and most particles are pushed to the wall. However, in the riser, the values of solids volume fraction are higher at the centre comparing with the wall which is a special phenomenon of Geldart D type particles at high superficial gas velocity-high solids flux conditions called the anti-core-annulus structure. It eliminates the undesirable core-annular regime which has been reported by many works of literature for the circulation of much smaller and lighter Geldart A and B particles [249–252]. Moreover, Kashyap (2011) [253] also observed a similar phenomenon for Geldart D particles under slugging condition. One explanation is that the flow of large and dense particles under high solid flux condition can break up the core-annular regime due to the larger particle inertia. Another explanation is that the particle-particle interaction for Geldart group D particles is weak, so heterogeneous structures like core-annulus structure will not form [254].

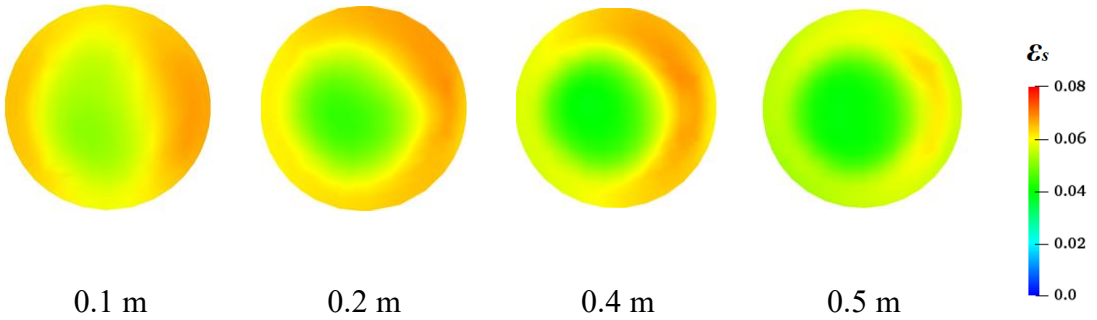

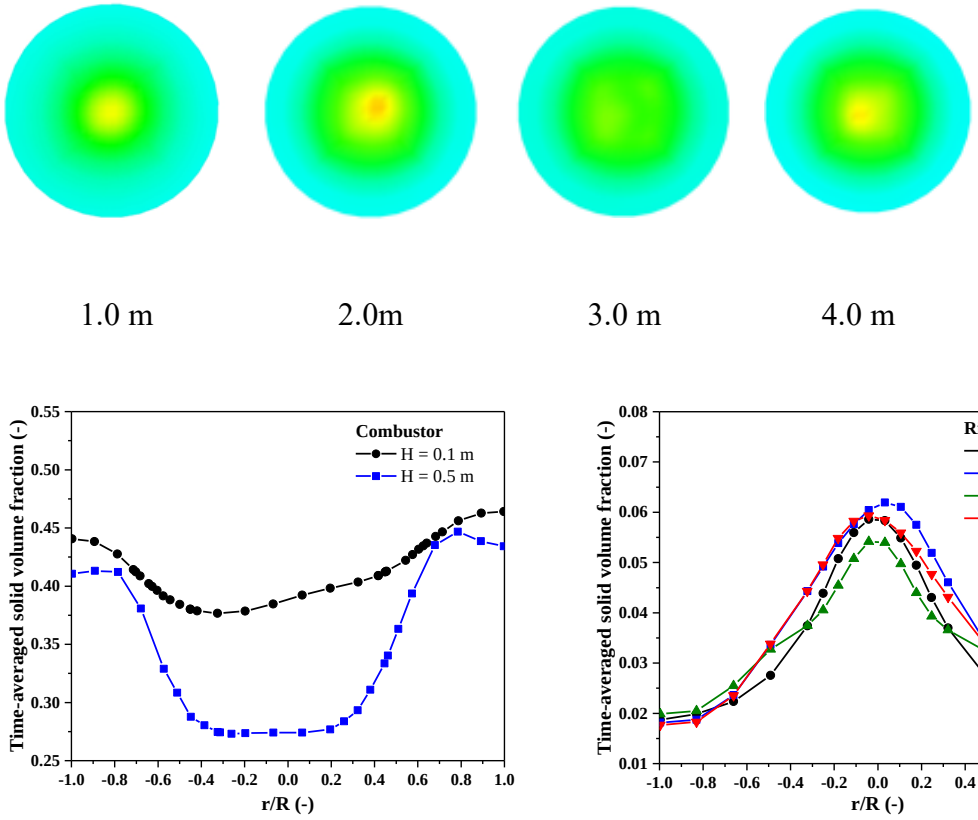

Fig 4.7. The radial distributions of solid concentration at different heights in the air reactor (U_f = 1.6 m/s.).

The radial distribution profiles of solid velocity at different riser heights are shown in Fig 4.8. The simulated results show that particles move upward in the central region and drop down near the wall in the combustor. This flow characteristic causes the internal circulation of particles and extends the residence time of the oxygen carrier for higher oxidation efficiency. In the riser, the simulated results show that particles move upward and no solid back-mixing happens across the whole cross section, which can provide a better circulation efficiency than general risers with undesirable core-annulus structure.

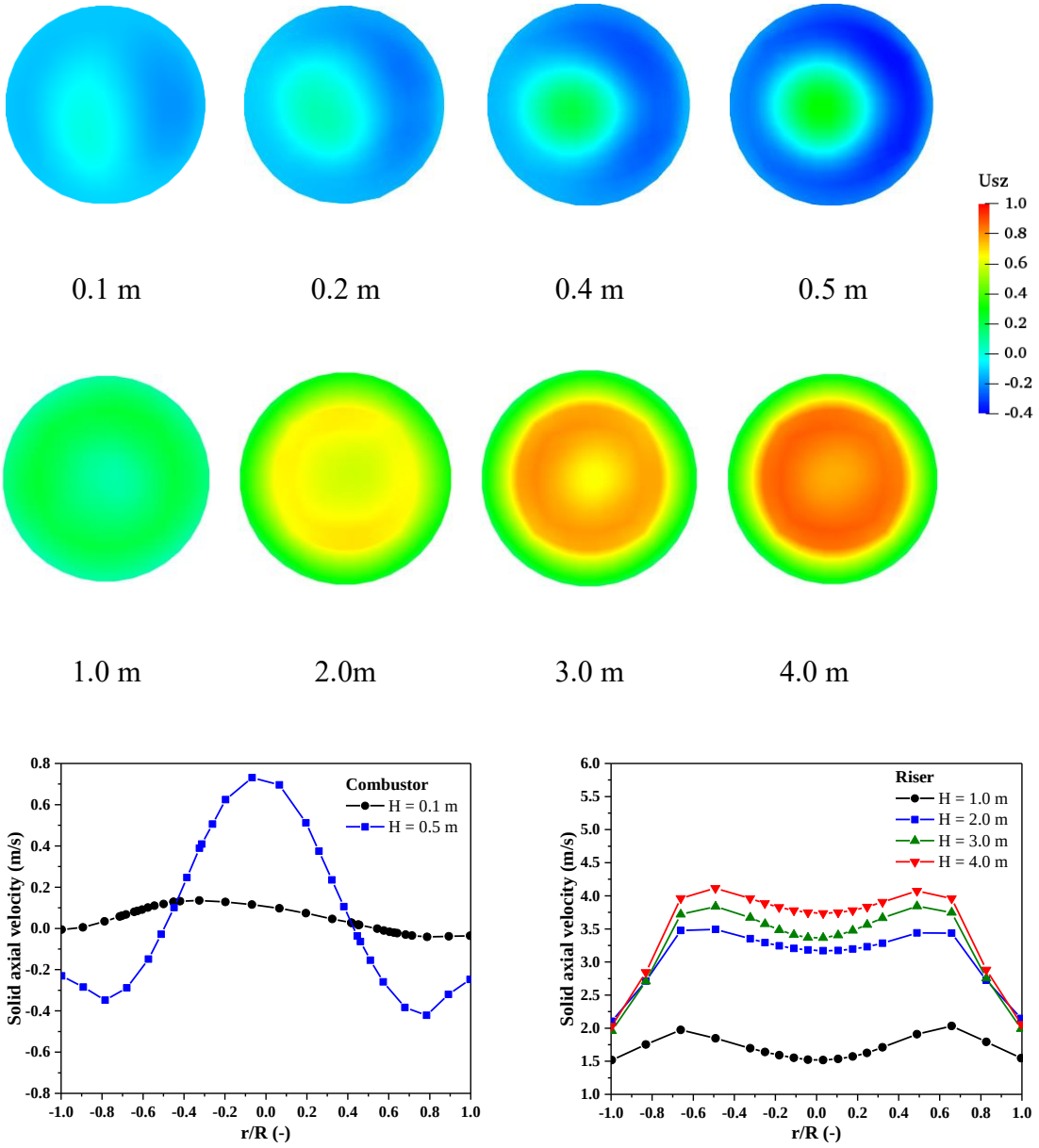

Fig 4.8. The radial distributions of solid axial velocity at different heights in the air reactor (U_f = 1.6 m/s.).

4.4.3 Effect of gas inlet velocity

In this section, a series of gas inlet velocity from 1.6 m/s to 3.0 m/s are chosen to investigate the effect of boundary condition on the flow pattern of Geldart D particles in

this air reactor. As shown in Table 4, the pressure between the bottom and top of the air reactor increases with increasing gas velocity. This is in contrast to the situation for bubbling and homogeneously fluidized system [255–258]. The phenomenon appears to be largely due to the transformation, and eventual dissipation, of the potential energy developed by the rising solid slugs [258].

Table 4-3. Pressure drops between the bottom and top of the air reactor for different gas inlet velocity.

Superficial gas velocity (m/s)	1.6	1.8	2.0	2.5	3.0
Pressure drops (kPa)	11.44	13.36	20.23	54.00	119.14

The axial distribution of the time-averaged solid volume fraction in the air reactor under different gas inlet velocities are plotted in Fig 4.9. Similar flow patterns can be observed under different gas inlet velocity: a dense flow regime in the bottom ($h < 0.65$m) with solid volume fraction ranging approximately from 30% to 50% and a typical dilute pneumatic transport section in the upper part where the holdup is about 3-15%.

By comparing the solid volume fraction distribution under different gas inlet velocity at the same height, it can be seen that the gas inlet velocity shows a significant influence on solid distribution in the case of constant solid inventory. In the combustor, increasing the gas inlet velocity reduces the solid concentration, meaning the amount of solid material and solid residence time decrease in this section. In the riser, the solid

concentration increases with the increase of gas inlet velocity, which means the transport efficiency increases.

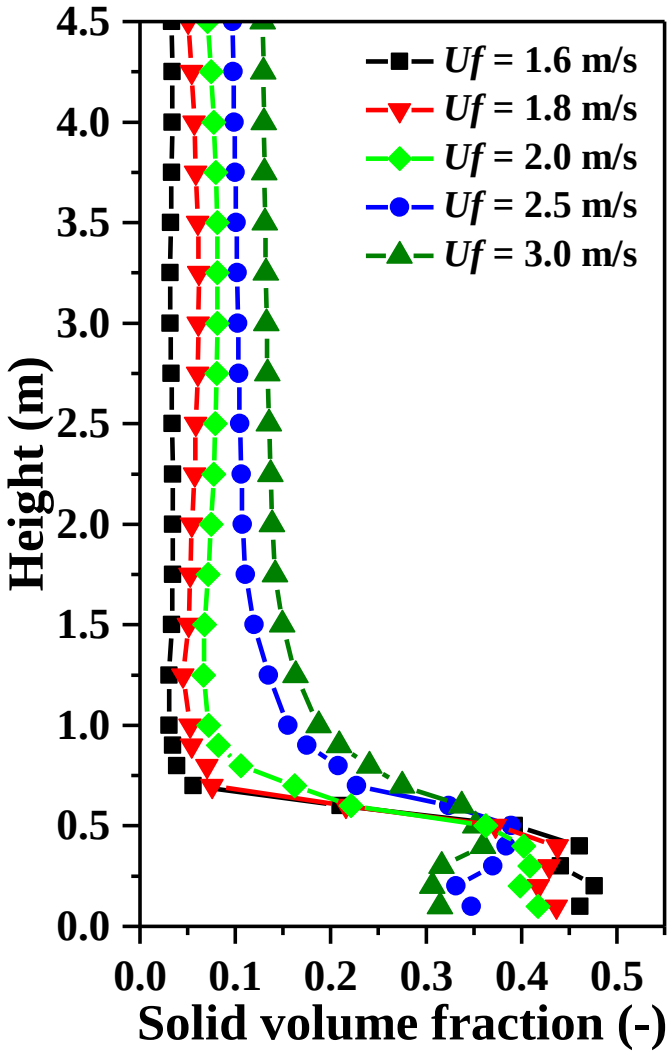

Fig 4.9. Apparent axial solids holdup profiles of the air reactor under different gas inlet velocities.

Fig 4.10 shows the radial distribution of solid volume fraction under different gas inlet velocity. The results show that at the same height of combustor, with the gas inlet velocity increases, the solid volume fraction decreases over the whole cross section which means fewer solid are left in the combustor. Meanwhile, on the contrary, solid volume

fraction increases with the increase of gas inlet velocity in the riser, which means more solids are transported. Therefore, the gas inlet velocity has a significant influence on the efficiency of the CLC process and should be chosen carefully according to the required residence time for complete conversion of oxygen carrier and moderate solid circulation rate.

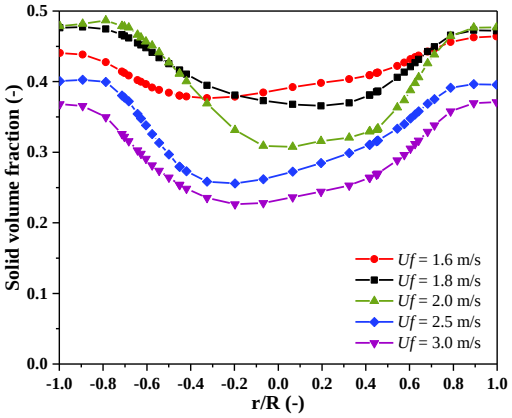

0.1 m

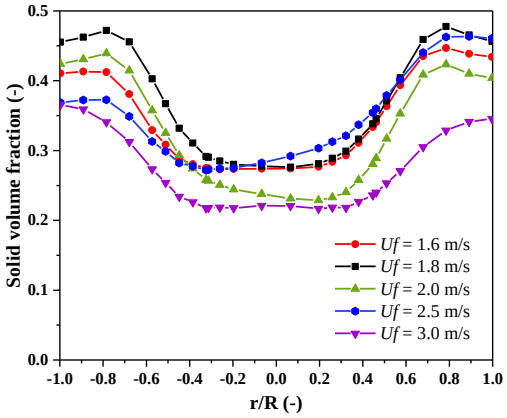

0.5 m

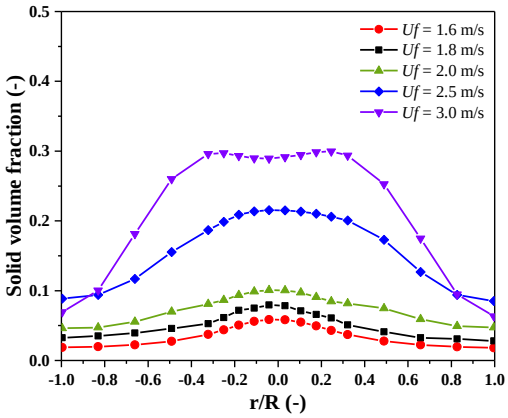

1.0 m

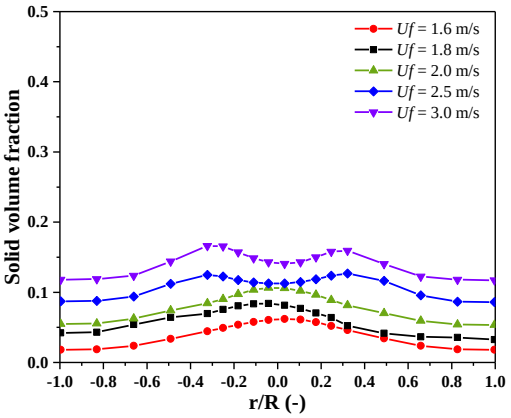

2.0 m

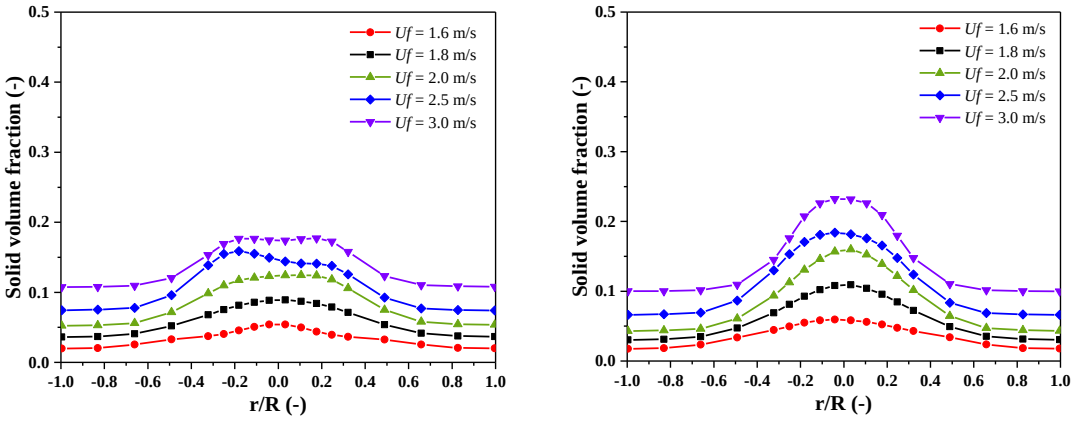

Fig 4.10. Radial distributions of solid axial velocity at different gas inlet velocities in the air reactor.

4.4.4 Effect of wall boundary conditions

In addition to the governing equations, initial and boundary conditions are necessary for a complete description of gas-solid flow systems. In this model, as showed in Table 4-1, the specularity coefficient (ϕ) is a parameter to describe the roughness of the reactor walls, which is difficult to determine and usually treated as an adjustable parameter in simulations. The values of specularity coefficient vary between zero and unity, which represent the roughness of the reactor walls. In this study, five values of 0, 0.3, 0.5, 0.8, and 1.0 are set to account for different slip boundary conditions to obtain an appropriate specularity coefficient for the air reactor model.

Table 4-5 shows the values of the pressure drop over the whole air reactor for different specularity coefficients. It can be seen that a significant increase in pressure drop can be observed with the increase of specularity coefficients. This observation is

consistent with the findings of Loha et al. [49] for bubbling fluidized bed. By comparison with the experiment results, a low value ϕ = 0.0 is the closest to the experimental value and should be chosen for the model setting.

Table 4-4 Pressure drops between the bottom and top of the air reactor for different specularity coefficients (U_f = 1.6 m/s).

Specularity coefficient	0	0.3	0.5	0.8	1.0	Exp
Pressure drops (kPa)	5.877	8.781	11.44	11.666	12.593	5.226

The fluidization behaviour is illustrated in Fig 4.11, which shows instantaneous solid volume fraction contours in a combustor for the five specularity coefficients at t = 1.0 s (U_f = 1.6 m/s.). For ϕ = 0.0, the bubbles formed at the bottom of the bed are large and they merge very close to the inflow to create large slugs with a diameter approximately equal with the bed width. A similar picture of fluidization is shown in Fig 4.11 for ϕ=0.3, 0.5, 0.8, 1.0. It can be seen that all of the fluidization behaviours lie in the slugging regime, but the size of the slugs is smaller than in the previous case. As the specularity coefficient increases, the formation of slugs is suppressed according to Fig 4.11.

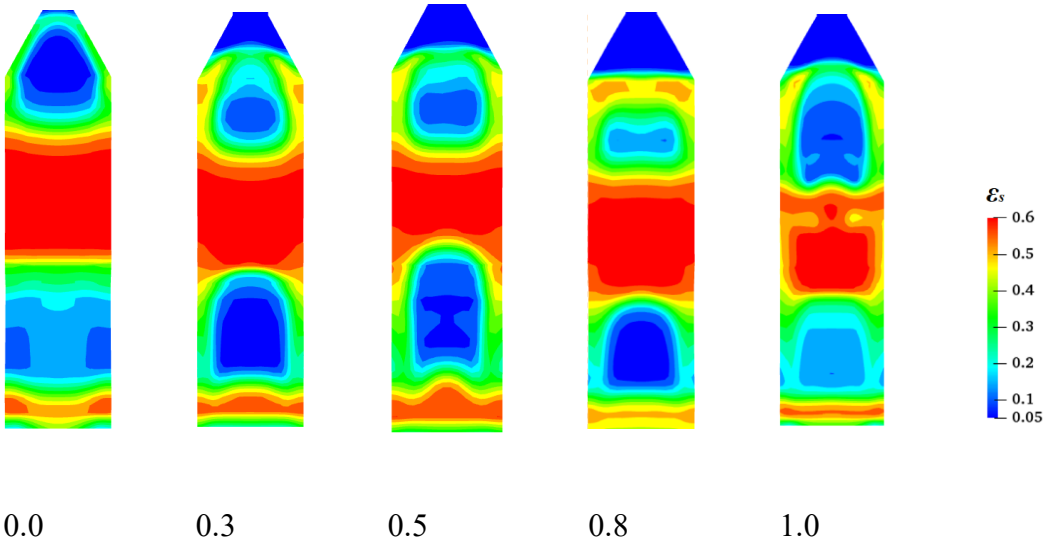

Fig 4.11. Instantaneous snapshots of solid concentration distribution for different specularity coefficients (U_f = 1.6 m/s).

Fig 4.12 shows the profiles of the solid mass flow rates with different specularity coefficients, where the solid mass flow rates are monitored from the outlet of air reactor. In Fig 4.12 (a), the intense fluctuations of solid mass flow rates can be observed for all different specularity coefficients in the first 20 s, which can be regarded as the start-up process. Afterwards, the values of solid mass flow rates fluctuate around a constant value, which means the simulation results reach the quasi-stable state.

For more accurate comparison among different specularity coefficients, the time-averaged solid mass flow rates are calculated between 50 s and 75 s, as shown in Fig 4.12 (b). It can be seen that the specularity coefficient of 0.0 shows reasonable data with the relative error of less than 3.1% by compared with the experiment value. With the increase of the values of specularity coefficients, the statistic solid mass flow rates decrease and all underpredicted it.

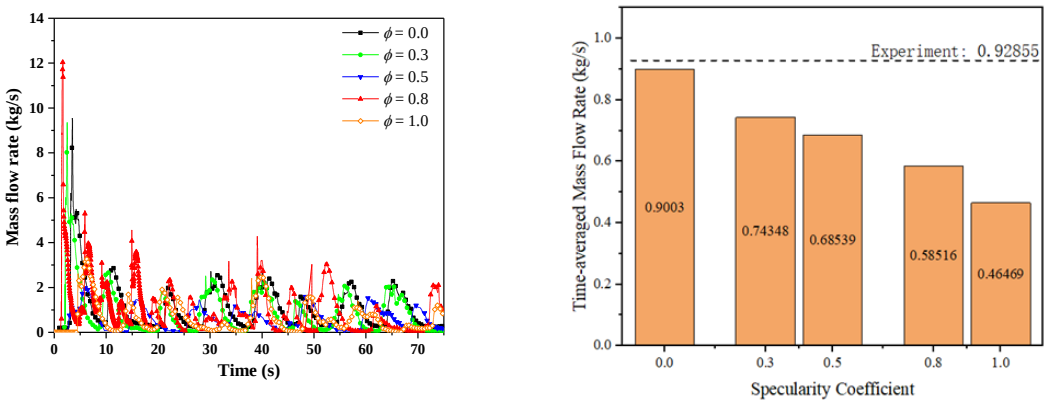

(a) (b)

Fig 4.12. Solid mass flow rates with different specularity coefficients: (a)solid mass flow rates with the computational time and (b) time-averaged solid mass flow rates at the quasi-stable state (U_f = 1.6 m/s).

4.4.5 Effect of drag models

In the TFM, the interaction between the phases is accounted for by incorporating the drag force term $\beta(u_g\text{-}u_s)$, and the interphase momentum exchange coefficient β is provided by different drag models. The various expressions for β in different drag models studied in this article are described in Table 4-2.

Fig 4.13 illustrates the comparison of time-averaged solid volume fraction and axial velocity distribution in the combustor section using different drag models under U_f = 1.6 m/s. The existence of core-annular structure of the flow pattern where the dilute particles are carried up by the gas in the central region and fall down along the wall can be clearly observed by four drag models. By comparison, the Gidaspow and Tenneti drag model

gives very similar results. Meanwhile, the Tang drag model shows a significantly different solid concentration and axial velocity distribution.

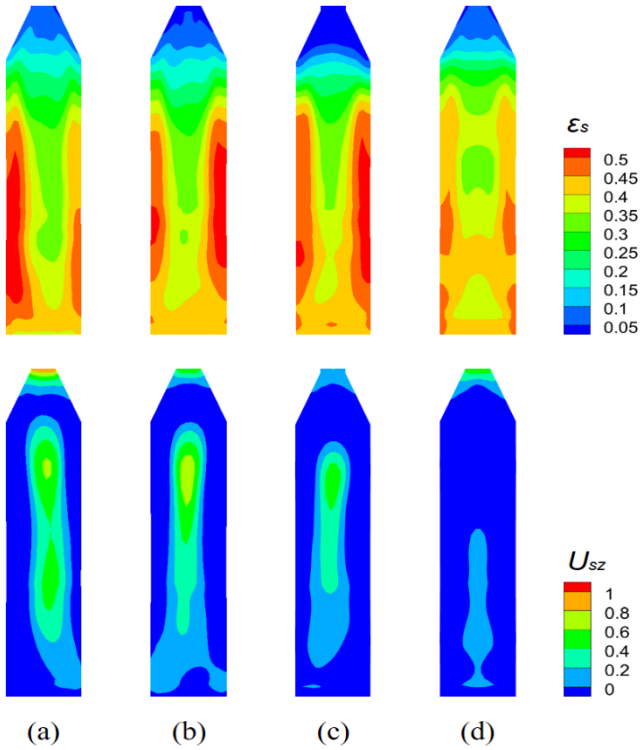

Fig 4.13. Time-averaged solid concentration and axial velocity distribution in the combustor section using different drag models: (a) Syamlal-O'Brien; (b) Gidaspow; (c) Tenneti et al; (d) Tang et al. (U_f= 1.6 m/s).

Fig 4.14 shows the profiles of solid mass flow fluctuations with the computational time with different drag correlations. The data presented in Fig 4.14 (b) shows the time-averaged values predicted by different models do not match very well with the observed experimental value. All the drag models predict a lower solid flow rate than the experimental value. By comparing the drag models presented in this work, the solid flow rate predicted by Syamlal-O'Brien drag model is closest and should be chosen in the relevant simulations.

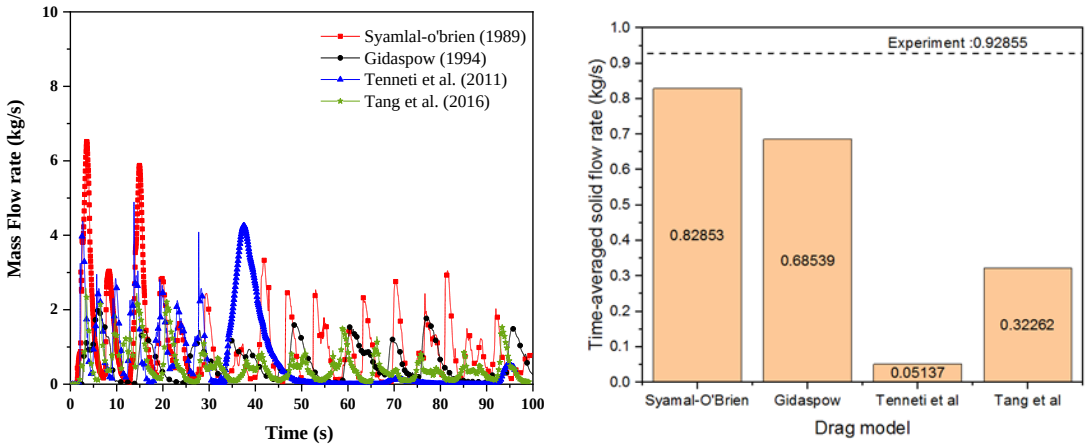

(a) (b)

Fig 4.14. Profile of the solid mass flow rate with different drag model (a) solid mass flow rate fluctuations with the computational time and (b) time-averaged solid mass flow rates at the quasi-stable state. (U_f = 1.6 m/s).

4.5 Full-loop CDCL simulation

Based on the parameters study of the air reactor model in the Ohio CDCL unit, the optimized mathematical model is applied to simulate the full-loop CDCL unit.

4.5.1 Simulation conditions

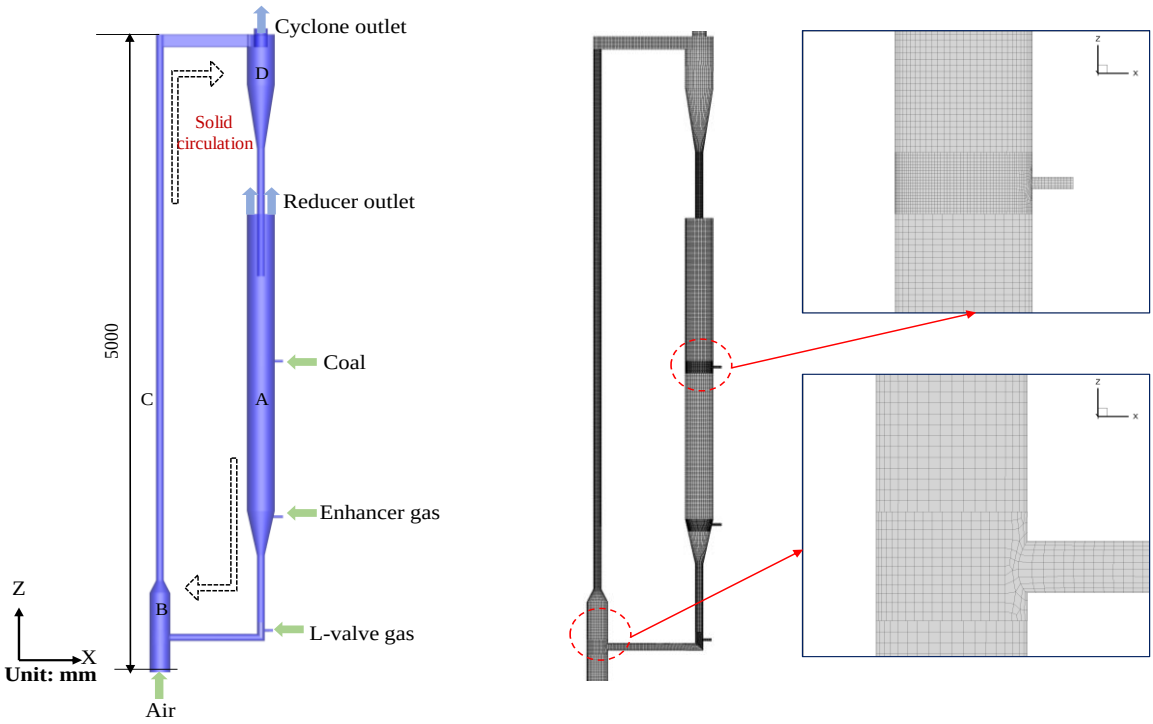

Fig 4.15. Schematic geometry and grids of the 25 kWh coal direct chemical looping subpilot system. A-Reducer, B-Combustor, C-Riser, D-Cyclone.

The schematic geometry of the 25 kWh CDCL sub pilot system constructed at OSU is shown in Fig. 4.15. It can be seen that the CDCL unit consists of two main reactors, a combustor (or AR) and a reducer (or FR), and these two reactors are connected by a cyclone and a non-mechanical L-valve to form a circulation loop. The FR in this CDCL unit adopted a counter-current moving bed design where the solid oxygen carriers move down by virtue of gravity in a dense phase. In contrast, gases, such as the fuel gasification enhancer (CO_2 in this work) as well as the gasification products, move upward, counter-current to the solids flow direction. The gas-solid counter-current moving bed provides many advantages over a fluidized bed such as greater control of the fuel residence time and conversion and the oxygen carrier conversions. In the reducer, the solid fuel particles are injected at the middle of the reducer. Then, the oxygen carriers are reduced by the gas products of solid fuel and the slow discharging velocity of oxygen carrier in moving bed reducer ensures a high utilisation efficiency of reactants. The reduced oxygen carrier

particles exit the reducer through a non-mechanical L-valve and flow into the combustor reactor. The role of the non-mechanical L-valve is to regulate the oxygen carrier circulation rate while providing the gas sealing between the combustor and the reducer. In the fluidized combustor reactor, the reduced iron particles are regenerated with air at high temperatures. The oxygen carrier particles reaching above the freeboard region of the combustor reactor become entrained into the riser section and pass through a cyclone to replenish the oxygen carrier at the top of the reducer reactor. The total height of the system is 5m. The more detailed physical dimensions can be found in the experimental study and Table 4-6. Fig. 4.15 also shows the grids of the CDCL unit used in this work. The computational domain, including AR, FR, cyclone and L-valve, are meshed with hexahedron elements.

Table 4-5 Dimensions used for the three-dimensional simulation of the CDCL unit.

Parameters	**Value in simulation**
AR reactor height	25 in
AR reactor diameter	6 in
FR reactor height	104 in
FR reactor diameter	8 in
Riser height	161 in
Riser diameter	2 in
L-valve length — Vertical	26 in
L-valve length — Horizontal	34 in
L-valve diameter	2 in
Cyclone diameter	8 in

Coal inlet diameter	1 in
Enhancer gas inlet diameter	1 in
L-valve gas inlet	1 in

The velocity inlet boundary conditions are set for all the gas inlets and coal inlet. The pressure outlet boundary condition is selected for the cyclone top outlets and reducer outlet. The Schaeffer frictional model [200] for particle phase and the Johnson and Jackson's model [200] for wall boundary conditions of the solid phase are used. The no-slip boundary condition is adopted for the gas phase. Variable discretisation schemes for convection terms of each governing equation are employed: The Quadratic Upwind Interpolation of Convective Kinematics (QUICK) scheme is chosen for the volume fraction of gas and solid phases; the second-order upwind scheme is chosen for the momentum equation and the first-order upwind scheme is set for the turbulent kinetic energy and turbulent dissipation rate. The phase coupled Semi-Implicit Method for Pressure Linked Equations (PC-SIMPLE) algorithm is used to deal with pressure-velocity coupling. The Green-Gauss cell-based method is applied to estimate the gradients. The simulation is performed on the platform of commercial software ANSYS Fluent 19.2. The time step is assigned as 0.0001 s. The simulation parameters are listed in Table 4-7.

Table 4-6 Gas-solid properties and computational settings.

Properties	**Values**
Restitution coefficient of particles (e_{ss})	0.95
Restitution coefficient of particles (e_{sw})	0.95
Specularity coefficient (ϕ)	0.01
Angle of internal friction	30°
Friction packing limit	0.60
Gas density (ρ_g)	1.225 kg/m^3

Gas viscosity (μ_g)		1.837×10^{-5} pa·s	
Boundary condition			
AR gas	Flow rate	Air	1.6 m/s
L-valve gas	Flow rate	Air	30 lpm
Computational Settings		**Values**	
Pressure-velocity coupling		Phase coupled SIMPLE	
Time step		1×10^{-4} s	
Max. number of iterations per time step		50	
Convergence criteria		10^{-4}	

4.5.2 Results and discussion

In this session, the typical gas-solid flow patterns in the DCFB are discussed first for a general description in the DCFB. Then

Model validation

In this section, the model validation is conducted by setting the model to the cold and hot experimental conditions [259] and comparing the simulation results with the measurements. Fig. 4.16(a) shows the profiles of the solid flux monitored at the L-valve outlet. The intense fluctuations of solid flux between 0 and 30 s can be observed, which is commonly regarded as the start-up process. Afterward, the solid fluxes fluctuate around a constant value, which generally is regarded as the quasi-stable state. The instantaneous values of solid fluxes are averaged during the quasi-steady state. Fig. 4.16(b) shows that the time-averaged values at the L-valve show reasonable agreement with experimental data.

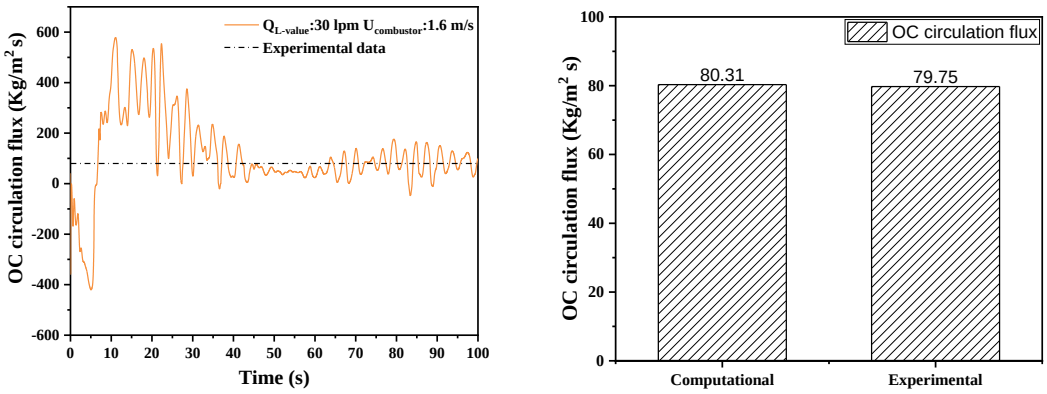

(a) (b)

Fig 4.16. Time-evolution of solid flux (a) and time-averaged solid flux (b) at the L-valve.

Typical gas-solid flow in CDCL

Initially, the solid loadings are packed in the lower part of the CDCL unit with an initial solid volume fraction 0.5 at FR and L-valve, 0.4 at AR for faster convergence. As different gas species are introduced from several inlets, the solid start to circulate in the CDCL unit. Fig 4.17 shows the time-evolution of instantaneous solid volume fraction in the CDCL unit. Different fluidisation regimes can be observed in the system: slugging fluidisation in the bottom combustor, fast fluidisation in the riser, and moving bed fluidisation in the L-valve and reducer, which corresponds to their functions. The cyclone dipleg is always under the bed material in the reducer, forming a seal to avoid high-temperature coal flowing into the cyclone separator, which may cause blockage and damage of cyclone wall. The dense solid state in the L-valve can effectively isolate the atmosphere between two reactors. During the operating process, a small cavity is formed under the outlet of reducer hopper due to particle blockages at the hopper. The particle blockages at the outlet are a common issue for hopper or silo discharge. When the gas velocity in L-valve is too large, most solid material is blown out to AR and the sealing function will be lost. Therefore, the L-valve gas must be within a suitable range.

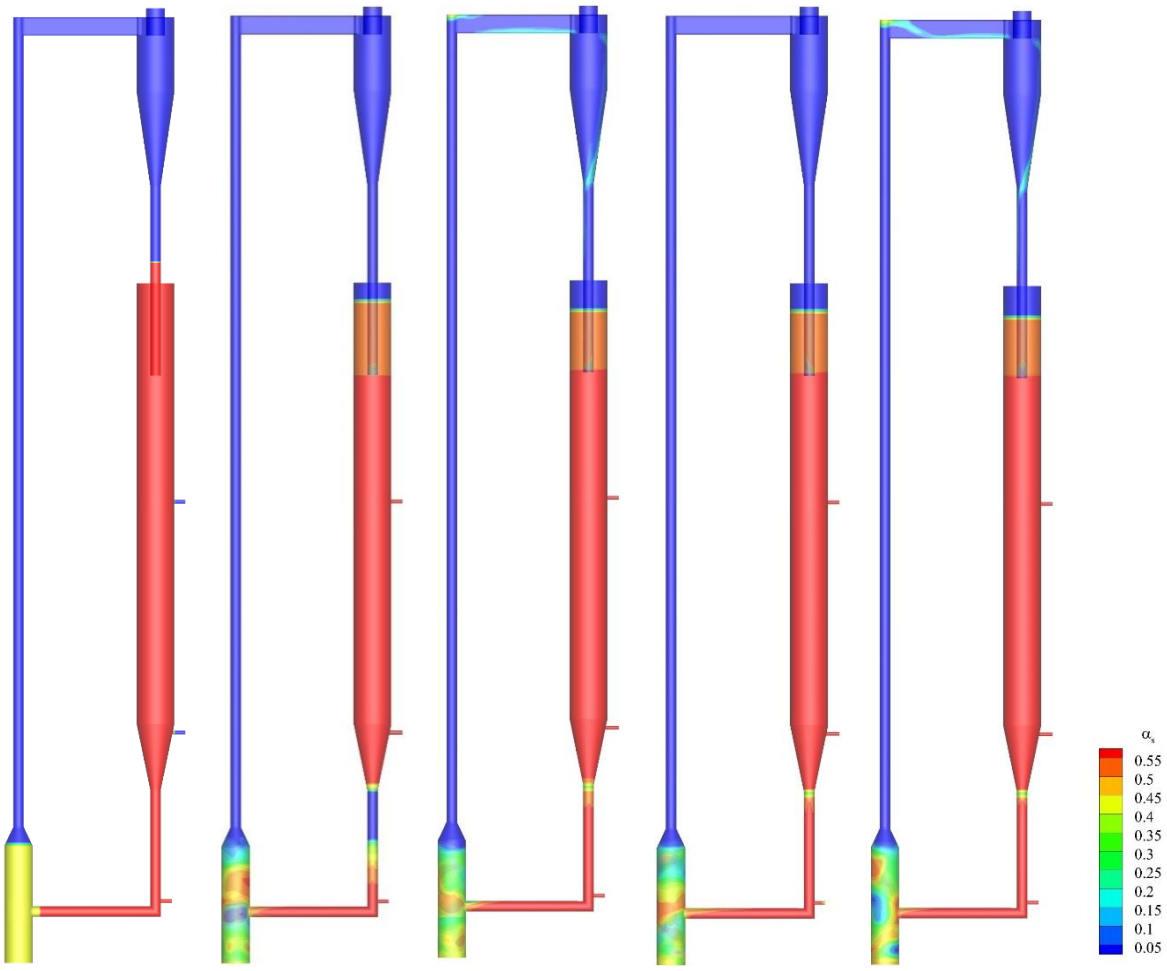

Fig 4.17. Contours of instantaneous solid volume fraction in the CDCL unit.

Fig 4.18 and Fig 4.19 show the time-averaged solid volume fraction and velocity through the full-looping system and two reactors. In the reducer, the bed material is packed in a dense state and flows downward with a slow velocity, which forms a counter-current flow with the enhancer gas and increases the residence time of oxygen carrier for higher conversion. In the combustor, a back-mixing phenomenon occurs, which is beneficial to increase the residence time of the oxygen carrier and ensure the reduced oxygen carrier can be completely oxidised by O_2 in the air. In the riser, the solid phase distribution is

dilute because of the high gas velocity, in which the regenerated oxygen carrier can be transported to the reducer faster.

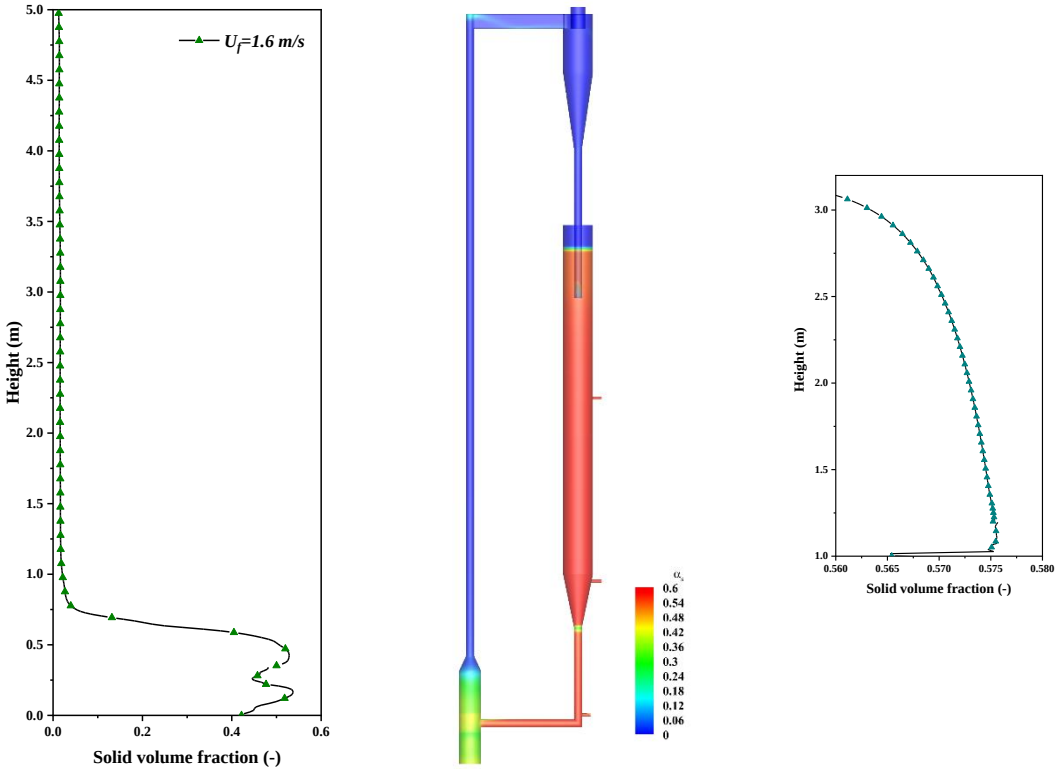

(a) (b) (c)

Fig 4.18. Profile of time-averaged solid volume fraction along the central line of the AR (a); Contours of time-averaged solid volume fraction in the CDCL unit (b); Profile of time-averaged solid volume fraction along the central line of the FR (c).

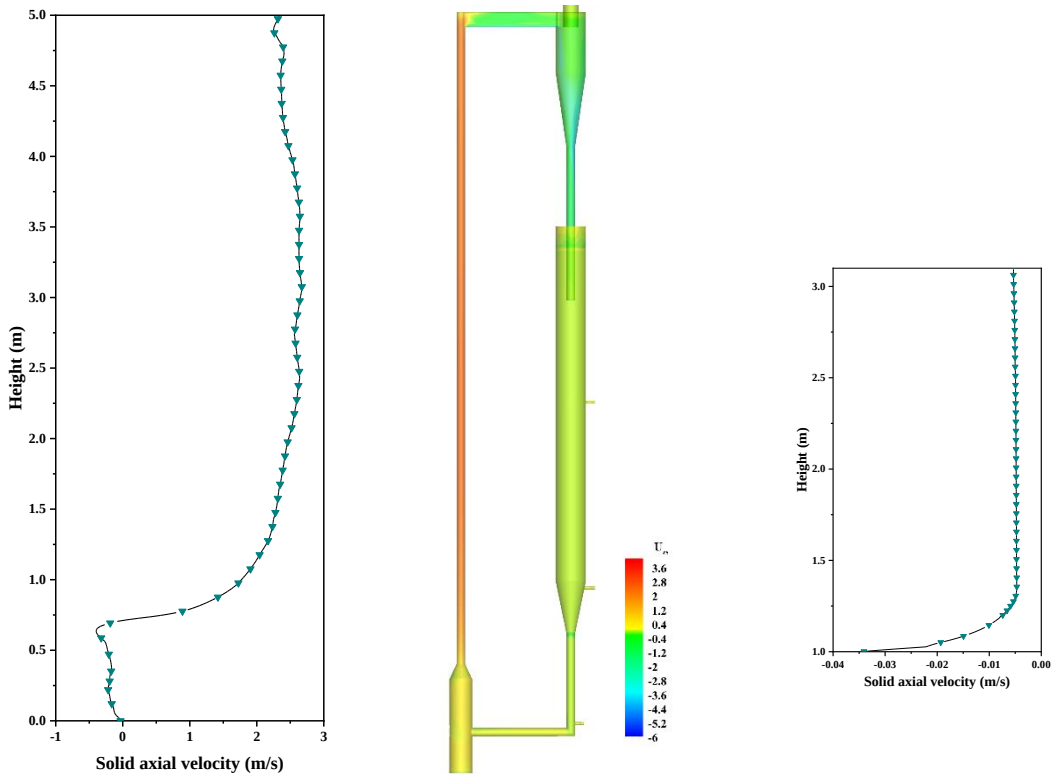

(a) (b) (c)

Fig 4.19. Profile of time-averaged solid velocity along the central line of the AR (a); Contours of time-averaged solid velocity in the CDCL unit (b); Profile of time-averaged solid velocity along the central line of the FR (c).

The pressure balance is an essential property for the complex CFB systems because it maintains the solid circulation between the AR and FR and can also reflect the fluidisation state within the full system. Fig 4.20 (a) shows the time-averaged pressure profiles along the centre line throughout the full-loop system. The characteristics of pressure distribution in the CDCL unit can be observed that the pressure gradient is large at the bottom and comparatively small at the top. It is noted that pressure decreases along with the height of the riser and is small, ranging from the riser outlets to the cyclone inlets. The pressure is nearly constant in the cyclone and reducer. In further comparison, it can be seen that the pressure in the L-valve is slightly lower than that in the combustor, which is the main cause of the gas leakage from the AR to FR. The gas leakage in CLC units is

a very common issue and decreases the efficiency of the CO_2 separation. The result predicted by CFD illustrates that optimisation should be done in terms of operation condition and design to minimise the gas leakage. Compared with dual fluidized bed CLC unit, the pressure drop in this moving bed CDCL unit is low where the system is more stable. For better illustration, the transient pressure drop across the reducer is monitored, as shown in Fig 4.20 (b). After a start-up stage of about 65s, the pressure drop of the reducer reaches a quasi-steady state. The magnitude and fluctuation of pressure drop in the reducer are small, which means the reducer operates in a relatively stable condition.

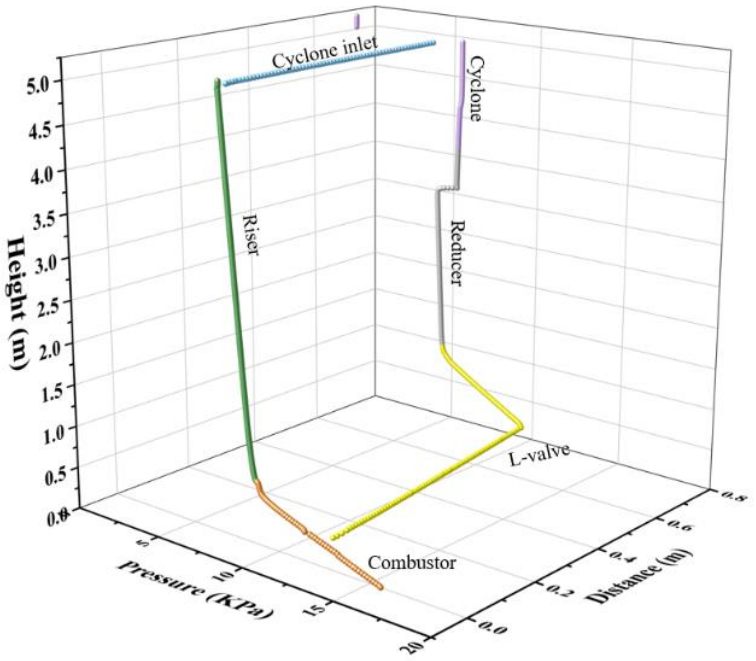

(a)

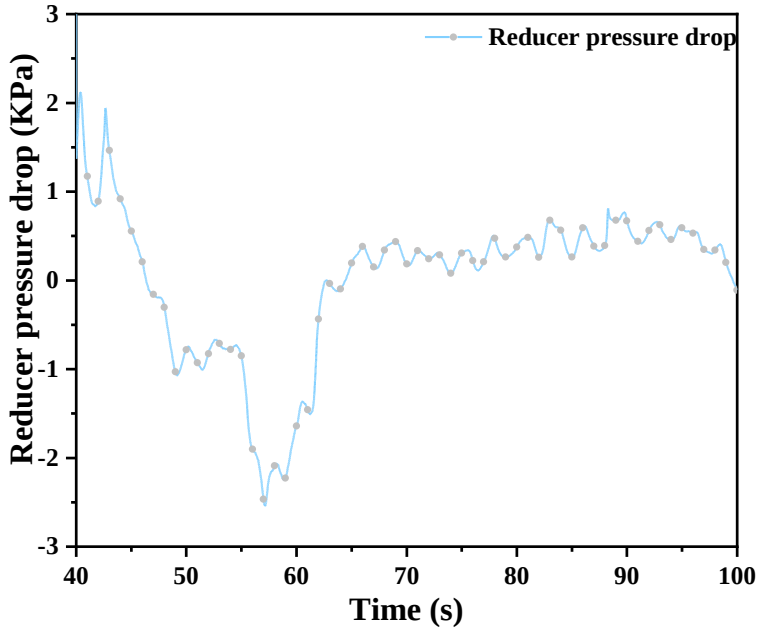

(b)

Fig 4.20. Time-averaged pressure profile along the central line throughout the full-loop system (a); time-evolution of pressure drop across the reducer (b).

The solid circulation rate in the dual circulating fluidized bed reactor is an important factor influencing heat balance and stable operation of CDCL systems. In order to explore the influence of gas velocity in system on the solid circulation rate, different combustor gas velocity and L-valve gas velocity are used in both experiment and simulation. By comparing the results in Fig 4.21. It was also noted that the solid flux through the L-valve is not affected when the combustor gas velocity increases form 1.6 m/s to 1.8 m/s. The solid circulation rate is controlled by the flow rate of aeration gas on the standpipe of L-valve. This conclusion is consistent with the experimental measurements [242].

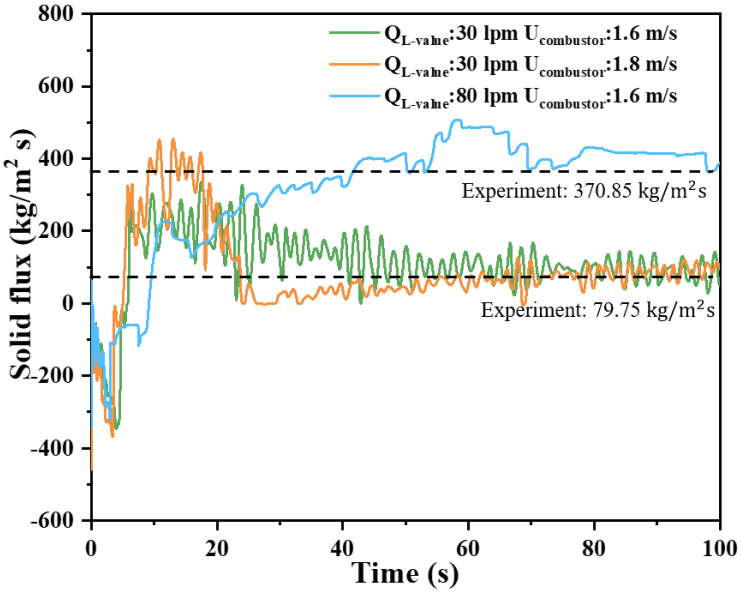

Fig 4.21. Time-evolution of solid fluxes at the L-valve.

The influence of different boundary condition on the pressure distribution is further studied. Fig 4.22 shows the time-averaged pressure profiles throughout the full-loop system for three different boundary conditions. The profiles show, higher combustor gas velocity can reduce the pressure magnitude of the whole system; increase of L-valve gas velocity has slightly influence on the pressure distribution of system but just increase the local pressure at the L-valve. Besides, refer to the previous discussion, increasing the L-valve gas velocity maybe an effective way to minimise the gas leakage, where a high pressure can be built.

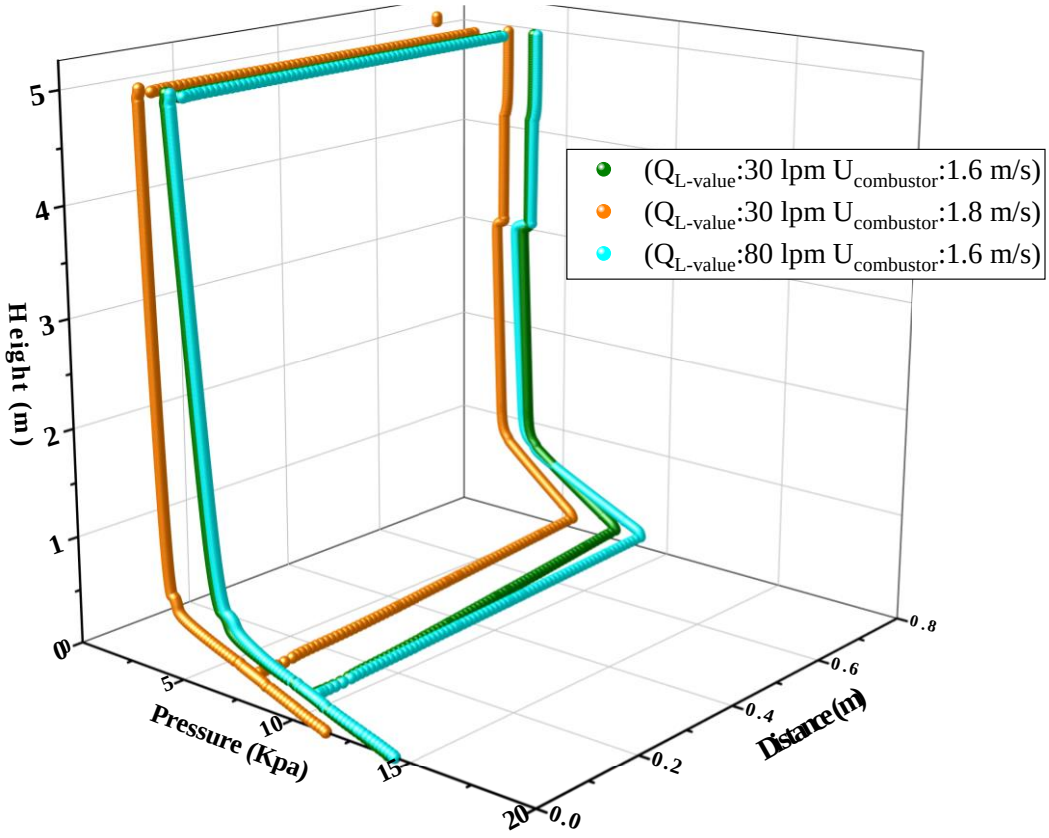

Fig 4.22. Time-averaged pressure profile along the central line throughout the full-loop system.

4.6 Conclusions

In this paper, a comprehensive 3-D numerical simulation has been carried out to simulate the gas-solid flow characteristics in a two-staged air reactor and full-loop CDCL unit using TFM. The gas-solid flow behaviors, especially solid distribution, solid axial velocity and solid circulating characteristics are investigated. Moreover, the effects of gas inlet velocity, specularity coefficient, and drag model is explored in detail. The following conclusions can be drawn:

(1) In the combustor, the solid material shows a dense solids slug movement where the

particles move upward in the central region and drop down near the wall, which is beneficial to increase solid residence time for oxidation. In the riser, the solid phase distribution is dilute because of high gas velocity. The particles move upward in the whole radial positions and shows an anti-core-annulus flow pattern, which is beneficial for solid transportation.

(2) In the combustor, increasing the gas inlet velocity can reduce the solid concentration, meaning the amount of solid material and solid residence time decrease in this section. In the riser, the solid concentration increases with the increase of gas inlet velocity, meaning the transport efficiency increases

(3) The specularity coefficient of zero and Syamlal-O'Brien drag model are found suitable for the 3-D air reactor model to reasonably predict gas-solid flow behaviors.

(4) Different fluidisation regimes can be observed in the system: slugging fluidization in the bottom combustor, fast fluidisation in the riser, and moving bed fluidization in the L-valve and reducer, which corresponds to their functions.

(5) Compared with dual fluidized bed CLC unit, the pressure drops in the whole CDCL unit and moving-bed reducer are low which means the system is more stable.

(6) The SCR is controlled by the flow rate of aeration gas on the standpipe of L-valve.

CHAPTER.5 Reactive Flow Behaviours in an Iron-based Coal Direct Chemical Looping Combustion Process

As a promising combustion technology with the CFB configuration, CLC ia taken as an example to investigate the thermochemical characteristics in the CFB chemical engineering system. In this chapter, a multi-fluid model based on the hybrid of the Eulerian-Eulerian-Lagrangian framework is used to study the reactive flow characteristics in a unique moving-bed CDCL unit. Multiple homogenous and heterogeneous reactions are considered, including the redox reaction of the oxygen carrier, devolatilization, moisture release and char gasification of coal particles. The simulation results show a good agreement with the experimental data. The model predicts transport characteristics of discrete coal powder in the reducer under cold and hot conditions and the results are compared to explain the mechanism of the mixing and separation behaviours between the oxygen carrier and coal in the system. The distribution of gas-solid species and reaction rates are shown to explore the reaction characteristics of this system. This work provides a deep understanding of this unique moving bed CDCL unit and can be used to further design and optimize similar CLC process performance.

The paper “Three-dimensional transient modeling of an iron-based coal direct chemical looping combustion process ” is under revision based on the content of this chapter.

Graphical abstract for this chapter

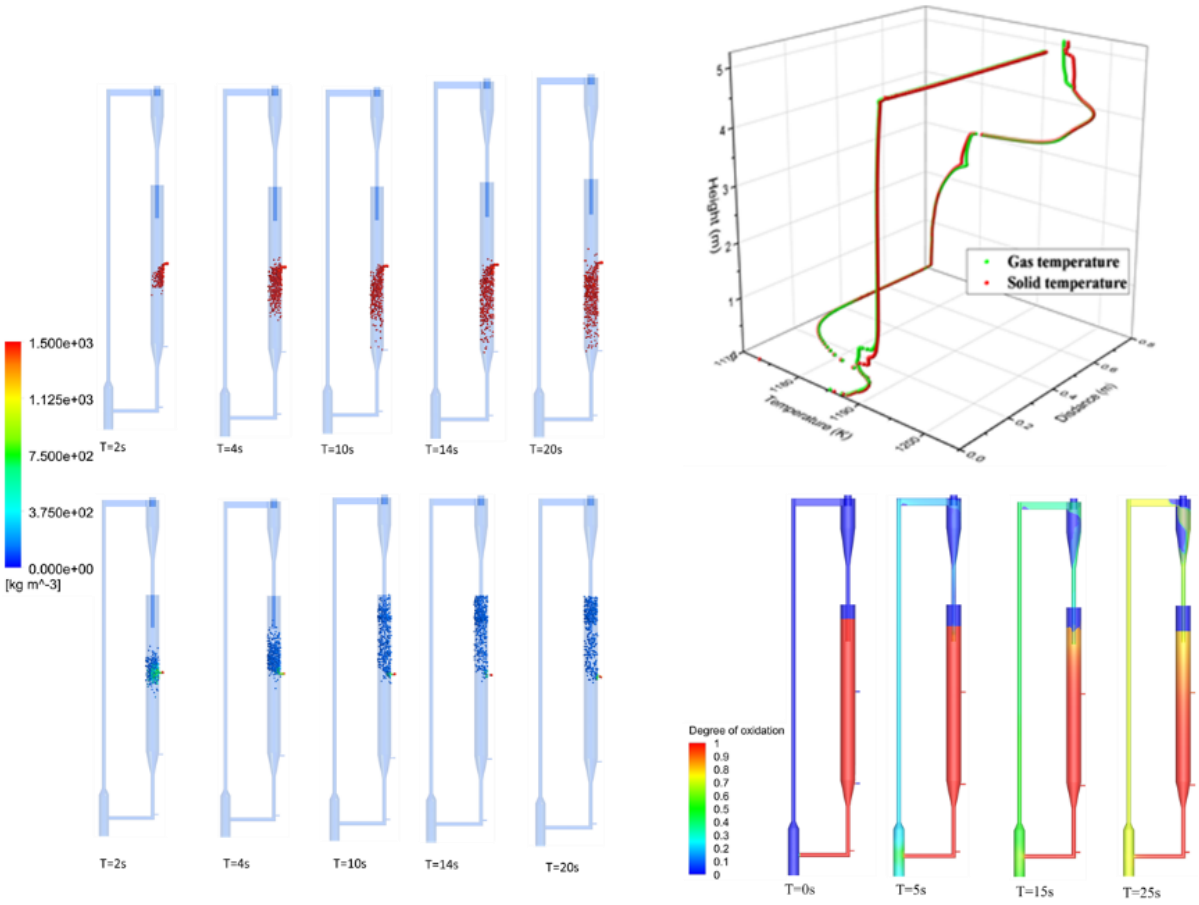

ABSTRACT

In this chapter, a multi-fluid model based on the hybrid of the Eulerian-Eulerian-Lagrangian framework is used to study the reactive flow characteristics in a unique moving-bed CDCL unit. In the CDCL process, iron-based oxygen carriers belong to Geldart D particles are used. The reaction characteristics in such a system have been seldom studied. The gas mixture and dense oxygen carrier phase are treated as the continuum with the two-fluid model (TFM) and the dilute coal powder as the discrete element with the Discrete Particle Model (DPM). Multiple homogenous and heterogeneous reactions are considered, including the redox reaction of the oxygen carrier, devolatilization, moisture release and char gasification of coal particles. The simulation results show good agreement with the experimental data. The model predicts the typical gas-solid flow in the full-looping CDCL unit. Transport characteristics of discrete coal powder in the reducer under cold and hot conditions are compared to explain the mechanism of the mixing and separation behaviours between the oxygen carrier and coal in the system. The gas leakage is captured by simulation and the cause is analysed based on simulation results. Accordingly, some suggestions are given to minimize gas leakage. The distribution of gas-solid species and reaction rates are shown to explore the reaction characteristics of this system. This work provides a deep understanding of this unique moving bed CDCL unit and can be used as a tool for further designing and optimising similar CLC process performance.

5.1 Introduction

In recent decades, chemical looping combustion (CLC) technology has been regarded as the latest and most promising combustion technology due to its unique property [13]. In conventional combustion processes, the fuel usually mixes with air or high concentration oxygen in the combustor to produce heat and energy. A massive volume of exhaust gas will exit from the combustor, consisting of primarily carbon dioxide, steam and nitrogen. Separating CO_2 from the exhaust gas requires considerable energy and extra costs. However, in CLC technology, CO_2 separation can be easily achieved because the fuel is isolated with the air during the operation process. The net chemical reaction and energy release of the CLC process are identical to that of the conventional combustion of fossil fuels without the extra CCS cost. A small amount of energy is spent on solid circulation (0.3% of the total energy released) [14]. A typical CLC system usually consists of two interconnected fluidized bed reactors, a fuel reactor (FR) and an air reactor (AR), as illustrated in Fig 5.1. The solid oxygen carrier, which is often a metal oxide, is usually applied in a chemical looping combustion process to transfer oxygen from the gaseous oxygen source of the air to the fuel, which can effectively avoid the direct contact of gaseous oxygen and fuel and hence decrease the energy penalty of separation.

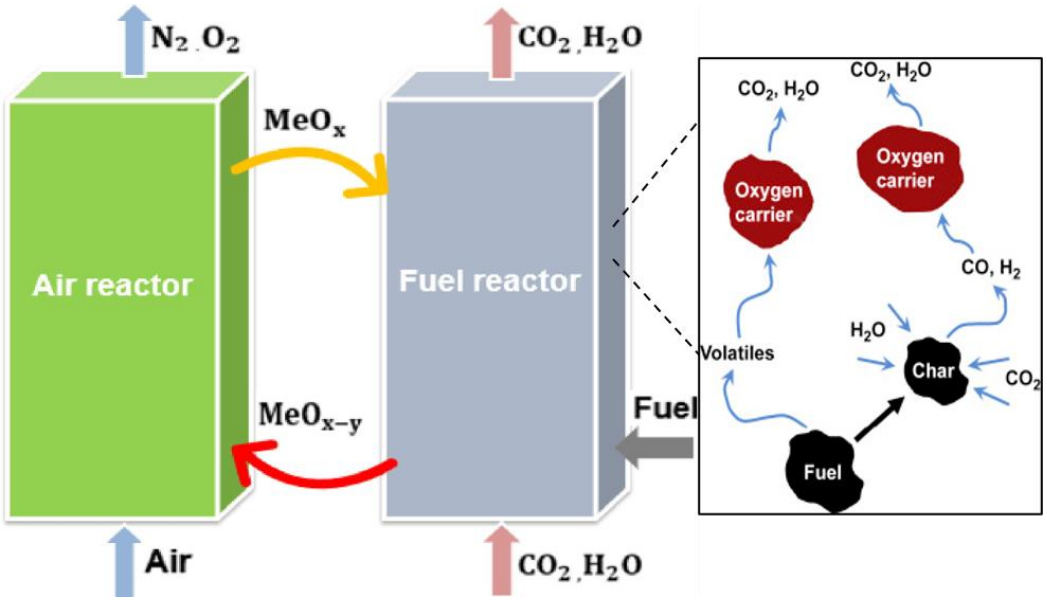

Fig 5.1. Schematic diagram of the CLC process.

In the last decade, there are many CLC plants which have been built and tested worldwide and many researchers carry out amounts of bench-scale or pilot-scale experiments to explore the characteristics of flow, heat and mass transfer inside the chemical looping combustion unit. By 2020, there are 22 testing CLC plants worldwide burning solid fuels, ranging from 0.5 KWh to 4 MWth. The total operational time has exceeded 4000h for over 100 experiments. Many researchers have conducted fundamental experiments to find out optimum operating conditions of industrial units. The first attempt of 10 KWh CLC system with solid fuels was started in 2008 established by Berguerand and Lyngfelt at Chalmers University of Technology [29–31]. They tested the combustion of bituminous coal and petcoke in a 10 KWh experimental rig for solid fuels. Many operational parameter variations, such as particle circulation, fluidising velocities, fuel load and fuel reactor temperature were tested and the influence on the operation performance include CO_2 capture, solid fuel and gas conversions from the fuel reactor were discussed. The research group of Professor. Shen at Southeast University has built

and tested two chemical looping combustion units for 1 KWh [49,51,54] and 10 KWh [50,61]. These two units have similar configurations where the air reactor is a riser and fuel reactor uses a spouted bed. A good performance has been achieved because of the strong solids mixing and long residence time of coal particles in the spout-fluid bed. The exploration of chemical looping technology with the dual circulating fluidized bed configuration experienced rapid improvement at Huazhong University of Science & Technology (HUST) [95,96]. Over 300 h of continuous operation experience of HUST CLC units contributes to the demonstration of this technique. At Ohio State University (OSU), a 25 KWh pilot-scale Coal-Direct Chemical Looping (CDCL) plant has been built for electric power generation with the characteristic of inherent CO2 capture [102–104]. The FR in this CDCL unit adopted a counter-current moving bed design. Over 230 h of operation experience has been conducted.

Although significant developments have been made in fossil fuel combustion using the CLC technology during the last decades, the detailed inner information cannot be obtained by experiments because of complicated flow pattern in the system and backward measuring equipment. The present knowledge, understanding, and experience of the CLC process mainly come from a limited number of research groups operating small CLC plants. Besides, because the lab- or pilot-scale results cannot safely be translated to an industrial scale, the performance of the actual industrial CLC unit is still uncertain. Having a deep understanding of the dynamic characteristic and reaction performance is essential for optimal design and scale-up of the CLC system. With the development of computer technology and parallel computing, numerical simulation has become the primary method to accelerate the growth of the CLC technology, reduce the cost of design and operating time, as well as reduce the technical risks.

The existing CFD methods can be divided into two main categories, i.e. Eulerian-Lagrangian method and Eulerian-Eulerian method. One approach is the Eulerian-Lagrangian approach, which treats the particle phase using the discrete element/particle method (DEM/DPM) or the Computational Particle Fluid Dynamics (CPFD) method. It can provide detailed particle motion information, such as the trajectories and transient forces acting on individual particles and thus is very accurate to describe the gas-solid flow behaviours. However, an extensive computational resource (CPU and memory resource requirements) is required based on Lagrangian methods to simulate the gas-solid system in the actual experimental unit, let alone the industrial plants. In the Eulerian–Eulerian model, the gas and solid phases are treated mathematically as interpenetrating continua. Thus, the computational load is affordable even towards the industry-scale simulations, but the disadvantage is the lower accuracy as the modelling of the granular phase is based on several assumptions and simplifications. The priority of the two methods depends on the research object and application background. For the CFD study of CLC processes, both methods have been adopted to investigate the flow and reaction behaviours [97,107–110,130]. The full-loop CLC systems simulations mainly focus on the solid circulation process, gas leakage performance, and reaction processes such as reactant distribution, product distribution, and temperature distribution. Guan et al. [148][108] established a three-dimensional (3D) full-loop model to investigate the hydrodynamics of a single CFB CLC unit based on the Eulerian-Eulerian TFM model. The different fluidisation states in the full-loop system were captured by simulation. The effects of operating gas velocity, particle size and total solids inventory on the solids circulation rate (SCR) were also investigated based on the system pressure balance. Simulation results showed the SCR increased significantly with the increase of gas

velocity in the riser. And the SCR became smaller for larger particles but increased with solids inventory. Parker [150] investigated a CLC system provided by the National Energy Technology Laboratory (NETL) based on the CPFD method. Multiple heterogeneous and homogenous reactions were considered in the CLC model, including the oxidation and reduction reactions of the metal oxide carrier and gasification reactions. Modelling results showing fluidisation regimes, circulation rate, reactor efficiencies, and temperature profiles were presented to demonstrate the utility of the model. Chen et al. [134] investigated a 50 kWh DCFB reactor for CLC of coal using the CPFD method. The characteristics of the gas-solid reactive flow in the full-loop system were simulated in detail, and the relationships among the complex factors of hydrodynamics and reactions were better understood. However, present simulations are still very limited for the full-loop CLC system, especially the reaction process in some complex configurations. In addition, the simulation work of the hydrodynamic and reaction behaviours of the unique counter-current moving-bed CDCL process has not been investigated yet where details of the flow and reaction have not been revealed and fully understood.

Therefore, the current work is to comprehensively analyse gas-solid flow and reaction characteristics of the 25 kWh sub-pilot unit for the CDCL process developed at OSU (Fig 5.2) based on a 3D hybrid model. The hybrid model of this work is introduced firstly, followed by the validation of numerical results with experimental data. Subsequently, the typical gas-solid flow is discussed. And then the transport characteristics of coal powder in the reducer and gas leakage phenomena in the whole system are all captured and explained through the simulation results. Finally, the reaction behaviours in the system are detailed explored.

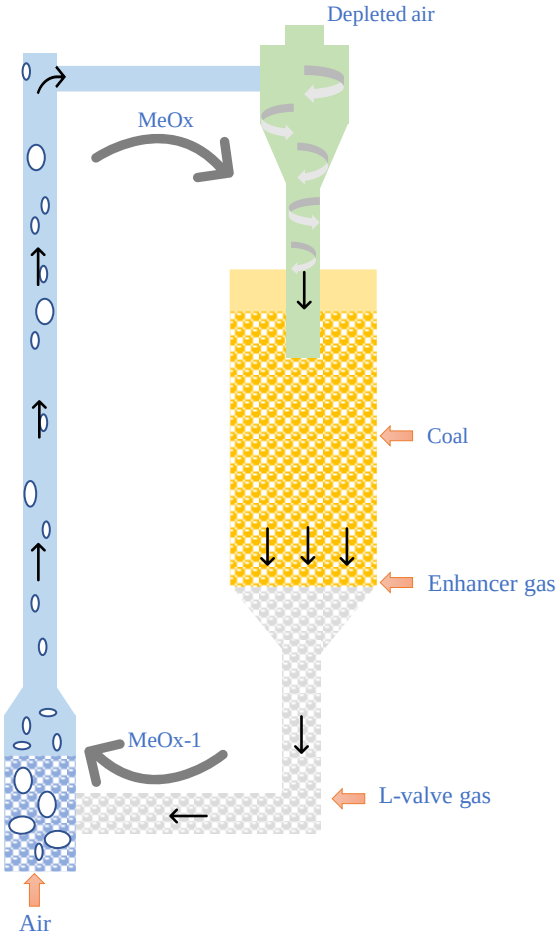

Fig 5.2. Sketch of the CDCL unit.

5.2 CFD model

In the present work, a Eulerian-Eulerian-Lagrangian (E-E-L) hybrid model has been used to study the CDCL unit regarding the exchange of momentum, heat and mass transfer among the gas, oxygen carrier phase and coal powder, as shown in Fig 5.3. This hybrid model treats the dense granular phase of oxygen carrier as the continuum and the dilute particle phase, fine coal powder, as the discrete element. This strategy does not only improve the computation efficiency by describing the macroscopic circulation motion of the oxygen carriers as the continuous granular phase but also takes advantage of the DPM to track the detailed motion of the coal powders in the FR.

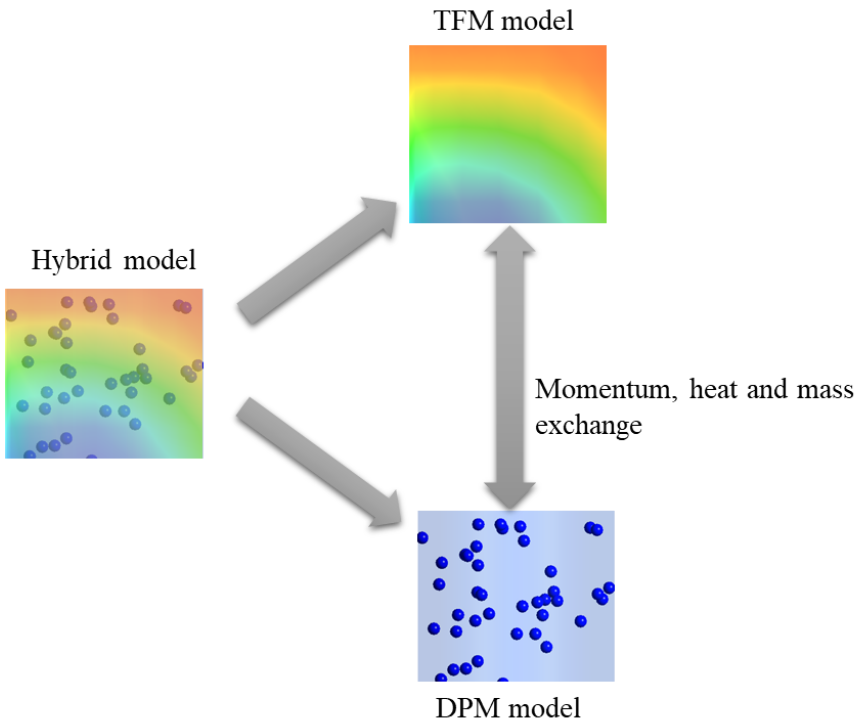

Fig 5.3. Diagram of the TFM-DPM hybrid model.

5.2.1 Governing equations

For the E-E-L hybrid model used in this work, the gas mixture and dense oxygen carrier phase are treated as the continuum with the two-fluid model (TFM) and the dilute coal powder as the discrete element with the Discrete Particle Model (DPM). When describing the solid continuum phase, the kinetic theory of granular flow (KTGF) is used in the transport equation, describing the particle collision and fluctuation. For the dilute coal powder, this work employs a DPM method to track dilute particle motion accurately. Lagrangian particle tracking is combined with a continuum description of the gas phase. The particle movements are calculated based on Newton's second law for DPM, where the gas drag force and the turbulence dispersion are taken into consideration.

The integrated interaction of gas-oxygen carrier reaction and gas-coal reaction should be considered in a two-way fashion. The governing equations of each phase, including the conservations of mass, momentum, and energy, are shown in Table 5-1.

Table 5-1 Governing equations of gas, oxygen carrier and coal phases.

Gas phase

$$\frac{\partial}{\partial t}(\alpha_g \rho_g Y_g)+\nabla\cdot(\alpha_g \rho_g \vec{u}_g Y_g)=-\dot{m}_g + S_{gs} + \dot{m}_p \tag{5-1}$$

$$\frac{\partial}{\partial t}(\alpha_g \rho_g \vec{u}_g)+\nabla\cdot(\alpha_g \rho_g \vec{u}_g \vec{u}_g)=-\alpha_g \nabla p+\nabla\cdot\bar{\bar{\tau}}_g+\alpha_g \rho_g \vec{g}+\beta(\vec{u}_s-\vec{u}_g)+\vec{F}_{td,g} - \dot{m}_{gs}\vec{u}_g \tag{5-2}$$

$$\frac{\partial}{\partial t}(\alpha_g \rho_g h_g)+\nabla\cdot(\alpha_g \rho_g \vec{u}_g h_g)=-\alpha_g \frac{\partial p}{\partial t} + \bar{\bar{\tau}}_g : \nabla\overrightarrow{u_g} - \nabla\overrightarrow{q_g} + S_g + Q_{sg} + \dot{m_{sg}} h_{sg} + Q_{gp} + S_p + Q_{rad} \tag{5-3}$$

Solid phase (oxygen carrier)

$$\frac{\partial}{\partial t}(\alpha_s \rho_s Y_s)+\nabla\cdot(\alpha_s \rho_s \vec{u}_s Y_s)=-\dot{m}_{si} + S_{si} \tag{5-4}$$

$$\frac{\partial}{\partial t}(\alpha_s \rho_s \vec{u}_s)+\nabla\cdot(\alpha_s \rho_s \vec{u}_s \vec{u}_s)=-\alpha_s \nabla p+\nabla\cdot\bar{\bar{\tau}}_s+\alpha_s \rho_s \vec{g}+\beta(\vec{u}_g-\vec{u}_s)+\vec{F}_{td,s} - \dot{m}_{sg}\vec{u}_s \tag{5-5}$$

$$\frac{\partial}{\partial t}(\alpha_s \rho_s h_s)+\nabla\cdot(\alpha_s \rho_s \vec{u}_s h_s)=-\alpha_s \frac{\partial p}{\partial t} + \bar{\bar{\tau}}_s : \nabla\overrightarrow{u_s} - \nabla\overrightarrow{q_s} + S_s + Q_{gs} - \dot{m_{sg}} h_{sg} \tag{5-6}$$

Powder phase (pulverised coal)

$$\frac{dm_p}{dt} = -\dot{m} \tag{5-7}$$

$$\frac{d\vec{u}_p}{dt} = \frac{\vec{u} - \vec{u}_p}{\tau_r} + \frac{\vec{g}(\rho_p - \rho)}{\rho_p} + \vec{F} \tag{5-8}$$

$$m_p C_P \frac{dT_p}{dt} = hA_p(T_\infty - T_p) - f_h \frac{dm_p}{dt} H_{reac} \tag{5-9}$$

The standard k-ε dispersed turbulence model is used for computing the turbulent kinetic energy and the dissipation rate of gas phase is as follows:

$$\mu_{gt}=\rho_g C_\mu \frac{k^2}{\varepsilon} \tag{5-10}$$

$$\frac{\partial}{\partial t}\left(\alpha_g\rho_g k\right)+\nabla\cdot\left(\alpha_g\rho_g\vec{u}_g k\right)=\nabla\cdot\left(\alpha_g\frac{\mu_{gt}}{\sigma_k}\nabla k\right)+\alpha_g G_k-\alpha_g\rho_g\varepsilon+\alpha_g\rho_g \Pi_k \tag{5-11}$$

$$\frac{\partial}{\partial t}\left(\alpha_g\rho_g\varepsilon\right)+\nabla\cdot\left(\alpha_g\rho_g\vec{u}_g\varepsilon\right)=\nabla\cdot\left(\alpha_g\frac{\mu_{gt}}{\sigma_\varepsilon}\nabla\varepsilon\right)+\alpha_g\frac{\varepsilon}{k}\left(C_1 G_k-C_2\rho_g\varepsilon\right)+\alpha_g\rho_g \Pi_\varepsilon \tag{5-12}$$

In eqns (5-10) -(5-12), k represents the turbulent kinetic energy and ε is the dissipation rate of turbulent kinetic energy. Π_k and Π_ε stand for interphase turbulence exchange terms. The constants in the equations are $C_\mu = 0.09$, $C_1 = 1.44$, $C_2 = 1.92$, σ_k=1.0 and σ_ε=1.3.

The Gunn model [260] is adopted to describe the interphase heat transfer. The gas-solid heat transfer coefficient h_{gs} can be formulated as:

$$h_{gs} = \frac{6k_g\alpha_s\alpha_g Nu_s}{d_p^2} \tag{5-13}$$

Nu_s is the Nusselt number:

$$Nu_s = \left(7 - 10\alpha_g + 5\,{\alpha_g}^2\right)\left(1 + 0.7Re_s^{0.2}Pr^{\frac{1}{3}}\right) + (1.33 - 2.4\alpha_g + 1.2{\alpha_g}^2)Re_s^{0.7}Pr^{\frac{1}{3}} \quad (5\text{-}14)$$

k_g is the thermal conductivity of the gas; Re_s is the Reynolds number and Pr is the Prandtl number.

The P-1 radiation model [261] is adopted to simulate the thermal radiation, where the heat source due to radiation is calculated by:

$$Q_{rad} = aG - 4an^2\sigma T^4 \quad (5\text{-}15)$$

Where α is the absorption coefficient, n is the refractive index of the medium, G is the incident radiation, σ is the Stefan-Boltzmann constant.

In the TFM framework, the KTGF is used to express the solid pressure and viscosities in terms of the granular temperature [106] for gas-oxygen carrier submodel.

$$\frac{\partial}{\partial t}(\alpha_s\rho_s\vec{u}_s)+\nabla\cdot(\alpha_s\rho_s\Theta_s\vec{u}_s)=\frac{2}{3}\left(-p_s\bar{\bar{I}}+\alpha_s\bar{\bar{\tau}}_s\right):\nabla\vec{u}_s + \nabla\cdot(k_s\nabla\Theta_s)-\gamma_{\Theta_s}-3\beta\Theta_s \quad (5\text{-}16)$$

The collisional energy dissipation term γ_{Θ_s} is given by:

$$\gamma_{\Theta_s} = \frac{12(1-e^2)\alpha_s^2\rho_s g_0\Theta_s^{3/2}}{d_p\sqrt{\pi}} \quad (5\text{-}17)$$

The bulk viscosity of the particle phase accounts for the resistance of granular particles to compression and expansion, given by Lun et al. (1984) [196]:

$$\lambda_s = \frac{4}{3}\alpha_s^2\rho_s d_p g_0(1+e)\sqrt{\frac{\Theta_s}{\pi}} \quad (5\text{-}18)$$

The particle shear viscosity is calculated by the sum of collisional viscosity, kinetic and frictional viscosity:

$$\mu_s = \mu_{s,col} + \mu_{s,kin} + \mu_{s,fr} \tag{5-19}$$

$$\mu_{s,col} = \frac{4}{5}\alpha_s^2 \rho_s d_p g_0 (1+e)\sqrt{\frac{\Theta_s}{\pi}} \tag{5-20}$$

$$\mu_{s,kin} = \frac{\alpha_s \rho_s d_p \sqrt{\pi \Theta_s}}{6(3-e)}\left[1 + \frac{2}{5}(1+e)(3e-1) g_0 \alpha_s\right] \tag{5-21}$$

$$\mu_{s,fr} = \frac{p_s \sin\phi}{2\sqrt{I_{2D}}} \tag{5-22}$$

where ϕ is the angle of internal fraction; I_{2D} is the second invariant of the deviatoric stress tensor.

The Syamlal-O'Brien drag model [181] is used in this work which was derived based on the terminal velocity of particles. The drag model is written as follows:

$$\beta = \frac{3}{4}\frac{\alpha_s \alpha_g \rho_g}{v_{r,s}^2 d_p} C_D \left(\frac{Re_s}{v_{r,s}}\right)\left|\vec{u}_s - \vec{u}_g\right| \tag{5-23}$$

where

$$C_D = \left[0.63 + \frac{4.8}{\sqrt{Re_s / v_{r,s}}}\right]^2 \tag{5-24}$$

and

$$v_{r,s} = 0.5(A - 0.06Re_s + \sqrt{(0.06Re_s)^2 + 0.12Re_s(2B - A) + A^2}) \tag{5-25}$$

with

$$\mathrm{A} = \alpha_g^{4.14}, B = 0.8\alpha_g^{1.28} \qquad \text{for } \alpha_g \leq 0.85 \tag{5-26}$$

or

$$A = \alpha_g^{4.14}, B = \alpha_g^{2.65} \qquad \text{for } \alpha_g > 0.85 \tag{5-27}$$

Further, the turbulent dispersion force is described by the equation proposed by Lopez De Bertodano [262], which is given by:

$$\vec{F}_{td,g} = -\vec{F}_{td,s} = C_{td}\rho_g k_g \nabla \alpha_s \tag{5-28}$$

Dispersion of Lagrangian coal particles due to the fluctuation of the continuous-phase velocity is modelled by employing the Random Walk model [263] in order to consider the contribution of turbulent dispersion on the trajectory of a Lagrangian particle.

In this hybrid model, the gas-oxygen carrier Eulerian-Eulerian and gas-coal Eulerian-Lagrangian are two-way coupled by exchanging gas phase quantities in terms of flow, temperature and gas species concentrations. Under this framework, the DPM are fully coupled with the gas phase at each time step, in which the data is transferred between the gas and coal phases through the related source term. Meanwhile, the exchange of mass, momentum and energy between the continuous gas and oxygen carrier phases is conducted through the related source terms.

5.2.2 Chemical kinetics

In this model, the complex pulverised coal combustion is regarded as a multistage process involving: (1) preheating; (2) devolatilization of raw coal, producing VM (volatile matter) and char; (3) reduction reaction between VM and oxygen carrier; and (4) gasification of residual char. The pulverised coal is injected at the middle of the moving bed, whereby

the coal inlet splits the reactor roughly into two different reaction sections. In the upper chamber, the volatile matter from the coal devolatilization moves upward and is oxidised by the oxygen carrier to carbon dioxide and steam. Meanwhile, the carbon char which is left after coal devolatilization flows down into the lower chamber and is gasified by the enhancer gas (CO_2 in this work). The detailed reaction steps are shown in Fig 5.4.

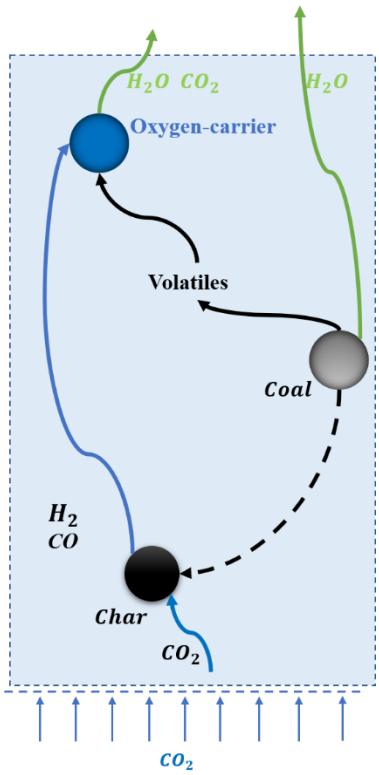

Fig 5.4. Scheme of the iG-CLC process for solid fuel combustion.

The devolatilization model of raw coal

The devolatilization process of raw coal is modelled by the two-competing-reactions model [35] considering the proximate and ultimate analyses of the Powder River Basin (PBR) coal. The PRB coal used in this simulation is a sub-bituminous from the Black

Thunder mine of Wyoming, USA. The material properties of PBR coal used in the simulation are summarised in Table 5-2. Coal particles are assumed to have a constant size distribution 90 μm and to be initially composed of 50.8 wt.% carbon char, 41.29 wt.% volatile organics, 7.91 wt.% ash with an initial particle density of 1470 kg/m^3 [104].

Table 5-2. Properties of PRB coal in CDCL process at OSU.

Proximate analysis		
Component	Value	Units
Ash	7.91	wt.% db
Volatile matter	41.29	wt.% db
Fixed matter	50.8	wt.% db
Moisture	13.505	wt.% ar
Ultimate analysis		
Carbon	71.25	wt.% db
Hydrogen	4.54	wt.% db
Nitrogen	1.13	wt.% db
Sulfur	0.46	wt.% db
Oxygen (by difference)	14.68	wt.% db
Average particle size, d_c	90	μm
Density, ρ_c	1473	kg/m^3

The volatile organics in the coal particles will volatilised into 66.8% methane, 24.4% carbon monoxide, 5.9% water, and 2.83% carbon dioxide on a weight basis [150]. The kinetic reaction model can be expressed as:

$$R_{devo} = (Y_a k_a + Y_b k_b) C_{coal} \quad (5\text{-}29)$$

With C_{coal} is the concentration of non-reacted coal in the solid particles, and the reaction rate constant k_i can be expressed using the Arrhenius form:

$$k_i = A_i exp(-\frac{E_i}{RT_p}) \quad (5\text{-}30)$$

$$Y_a = VM(daf) \quad (5\text{-}31)$$

$$Y_b = 1.25{Y_a}^2 + 0.92Y_a \quad (5\text{-}32)$$

The relevant parameters in the two-competing reaction rate are as follows:

$$A_a = 3.7 \times 10^5 s^{-1}, E_a = 18000K \quad (5\text{-}33)$$

$$A_b = 1.46 \times 10^{13} s^{-1}, E_a = 30189K \quad (5\text{-}34)$$

Char gasification model

The reaction between the char remaining after the release of the volatiles and the oxygen carrier is not direct but involves an intermediate gasification step with the gases. The carbon char in the coal particles is gasified through steam gasification and CO_2 gasification reactions. The detailed reaction relationships are listed in Table 5-3.

Table 5-3. Char gasification reaction models

Steam gasification	$C(s) + H_2O \rightarrow CO + H_2$
	$R_{H_2o,gasi} = 6.36T_{coal} \exp\left(-\frac{22645K}{T}\right)[H_2O]$
CO_2 gasification	$C(s) + CO_2 \rightarrow 2CO$
	$R_{co_2,gasi} = 6.36T_{coal} \exp\left(-\frac{22645K}{T}\right)[CO_2]$

Heterogeneous reaction model

The selected oxygen carrier particles for the CDCL process consist of reactive metal oxides (Fe_2O_3) and inert supports. The iron-based oxygen carrier particles in this study are specially developed for the counter-current moving bed chemical looping processes for the conversion of both gaseous or solids fuel feedstock [104,233]. The material properties of PBR coal used in the simulation are summarised in Table 5-4.

Table 5-4 Properties of oxygen carrier in the CDCL process at OSU

Parameter	**Value**	**Units**
Reactive metal	Fe_2O_3	-
Reduce product	FeO	-
The weight content of inert supports	40% Al_2O_3	wt.%
Density, ρ_{oc}	2500	kg/m^3
Average particle size, d_{oc}	1.5	mm

The reactions for oxidation of ilmenite by oxygen in the AR and the reduction of ilmenite in the FR by methane, hydrogen, and carbon monoxide are represented by the conversion

between FeO and Fe_2O_3. As described in the previous section, the metallurgical coke gasification is the rate-determining step, so the increase in CO_2 flowrate results in higher carbon conversion by enhancing the kinetics of metallurgical coke gasification, as shown in Table 5-5.

Table 5-5. Oxidation and reduction reactions of the oxygen carrier.

CH_4 reduction	$4Fe_2O_3 + CH_4 \rightarrow 8FeO + CO_2 + 2H_2O$
	$R_{CH_4,reduc} = 8.957 \times 10^4 \exp\left(-\frac{1.62617 \times 10^4}{T}\right)(m_{Fe_2O_3})^{2/3}(m_p)^{1/3}[CH_4]$
H_2 reduction	$Fe_2O_3 + H_2 \rightarrow 2FeO + H_2O$
	$R_{H_2,reduc} = 142.153 \exp\left(-\frac{7.81814 \times 10^3}{T}\right)(m_{Fe_2O_3})^{2/3}(m_p)^{1/3}[H_2]$
CO reduction	$Fe_2O_3 + CO \rightarrow 2FeO + CO_2$
	$R_{CO,reduc} = 229.279 \exp\left(-\frac{9.70652 \times 10^3}{T}\right)(m_{Fe_2O_3})^{2/3}(m_p)^{1/3}[CO]^{0.8}$
Oxidation	$4FeO + O_2 \rightarrow 2Fe_2O_3$
	$R_{oxi} = 2.776 \exp\left(-\frac{3.06712 \times 10^3}{T}\right)(m_{FeO})^{2/3}(m_p)^{1/3}[O_2]$

Water-gas shift reaction model

The water-gas shift reaction model is also taken into consideration:

$$CO + H_2O \rightarrow CO_2 + H_2$$

$$R_{wgs} = 1.31706 \times 10^{-5} P^{1.504} {T_{ash}}^2 \exp\left(-\frac{8417.81K}{T} - 8.91\right)[CO][H_2O]$$

5.3 Computational details

The schematic geometry of the 25 kWh CDCL sub-pilot system constructed at OSU is shown in Fig. 5.5. It can be seen that the CDCL unit consists of two main reactors, a combustor (or AR) and a reducer (or FR), and these two reactors are connected by a cyclone and a non-mechanical L-valve to form a circulation loop. The FR in this CDCL unit adopted a counter-current moving bed design where the solid oxygen carriers move down by virtue of gravity in a dense phase. In contrast, gases, such as the fuel gasification enhancer (CO_2 in this work) as well as the gasification products, move upward, counter-current to the solids flow direction. The gas-solid counter-current moving bed provides many advantages over a fluidized bed such as greater control of the fuel residence time and conversion as well as of the oxygen carrier conversions. In the reducer, the solid fuel particles are injected at the middle of the reducer. Then, the oxygen carriers are reduced by the gas products of solid fuel. The slow discharging velocity of oxygen carrier in moving bed reducer ensures a high utilisation efficiency of reactants. The reduced oxygen carrier particles exit the reducer through a non-mechanical L-valve and flow into the combustor reactor. The role of the non-mechanical L-valve is to regulate the oxygen carrier circulation rate while providing the gas sealing between the combustor and the reducer. In the fluidized combustor reactor, the reduced iron particles are regenerated with air at high temperatures. The oxygen carrier particles reaching above the freeboard region of the combustor reactor become entrained into the riser section and pass through a cyclone to replenish the oxygen carrier at the top of the reducer reactor. The total height of the system is 5m. More detailed physical dimensions can be found in the experimental study [103,104,242] and Table 5-6. Fig. 5.5 also shows the grids of the CDCL unit used

in this work. The computational domain, including AR, FR, cyclone and L-valve, are meshed with hexahedron elements.

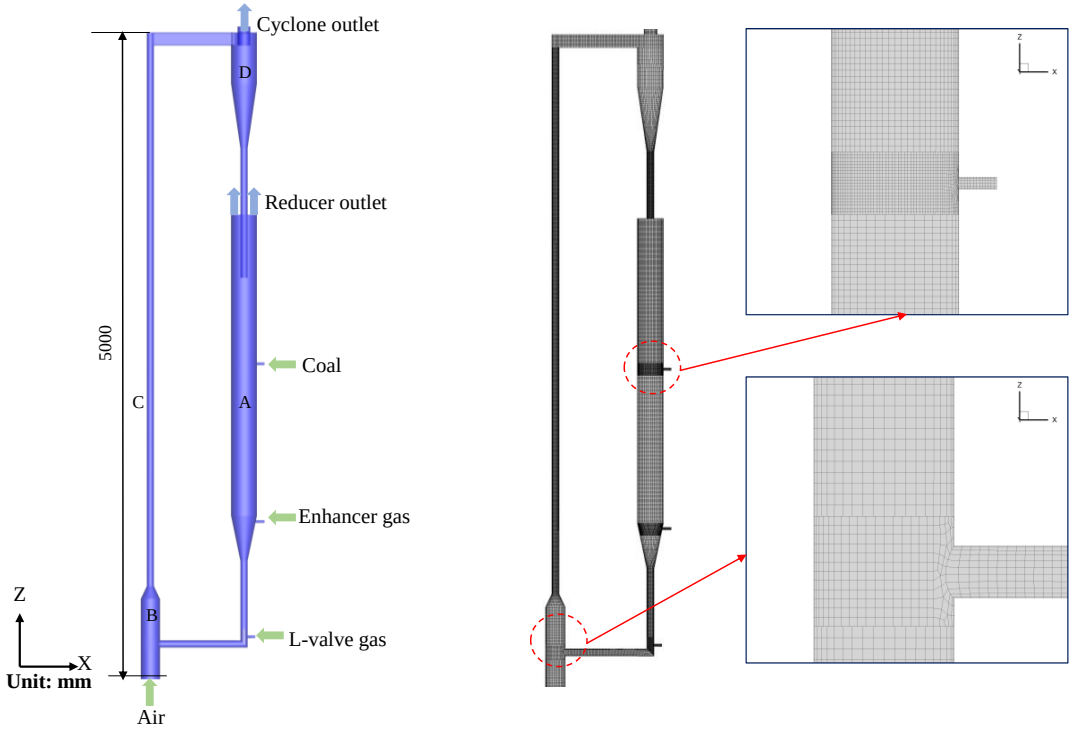

Fig 5.5. Schematic geometry and grids of the 25 kWh coal direct chemical looping sub-pilot system. A-Reducer, B-Combustor, C-Riser, D-Cyclone.

Table 5-6. Dimensions used for the three-dimensional simulation of the CDCL unit.

Parameters	**Value in simulation**
AR reactor height	25 in
AR reactor diameter	6 in
FR reactor height	104 in
FR reactor diameter	8 in

Riser height		161 in
Riser diameter		2 in
L-valve length	Vertical	26 in
	Horizontal	34 in
L-valve diameter		2 in
Cyclone diameter		8 in
Coal inlet diameter		1 in
Enhancer gas inlet diameter		1 in
L-valve gas inlet		1 in

The velocity inlet boundary conditions are set for all the gas inlets and coal inlet. The pressure outlet boundary condition is selected for the cyclone top outlets and reducer outlet. The Schaeffer frictional model [200] for particle phase and the Johnson and Jackson's model [200] for wall boundary conditions of the solid phase are used. The no-slip boundary condition is adopted for the gas phase. Variable discretisation schemes for convection terms of each governing equation are employed: The Quadratic Upwind Interpolation of Convective Kinematics (QUICK) scheme is chosen for the volume fraction of gas and solid phases; the second-order upwind scheme is chosen for the momentum equation and the first-order upwind scheme is set for the turbulent kinetic energy and turbulent dissipation rate. The phase coupled Semi-Implicit Method for Pressure Linked Equations (PC-SIMPLE) algorithm is used to deal with pressure-velocity coupling. The Green-Gauss cell-based method is applied to estimate the gradients. The simulation is performed on the platform of commercial software ANSYS Fluent 19.2. The time step is assigned as 0.0001 s. The simulation parameters are listed in Table 5-7.

Table 5-7. Gas-solid properties and computational settings.

Properties		**Values**	
Restitution coefficient of particles (e_{ss})		0.95	
Restitution coefficient of particles (e_{sw})		0.95	
Specularity coefficient (ϕ)		0.01	
Angle of internal friction		30°	
Friction packing limit		0.60	
Gas density (ρ_g)		Volume-weighted-mixing-law	
Gas viscosity (μ_g)		Mass-weighted-mixing-law	
Boundary condition			
AR gas	Flow rate	Air	1.6 m/s
	Temperature	900 ℃	
Enhancer gas	Flow rate	CO_2	3 lpm
	Temperature	785 ℃	
L-valve gas	Flow rate	N_2	30 lpm
	Temperature	900 ℃	
Coal flow	Flow rate	20.8 g/min	
	Temperature	984 ℃	
Computational Settings		**Values**	
Pressure-velocity coupling		Phase coupled SIMPLE	
Time step		1×10^{-4} s	

Max. number of iterations per time step	50
Convergence criteria	10^{-4}

5.4 Results and discussion

In this session, the numerical results are validated with experimental data. Subsequently, the typical gas-solid flow is discussed. And then the transport characteristics of coal powder in the reducer and gas leakage phenomena in the whole system are all captured and explained through the simulation results. Finally, the reaction behaviours in the system are detailed explored.

5.4.1 Grid independence test

A grid-sensitivity analysis is conducted to ensure a suitable number of the grid for accurate simulation results. Three different computational domains of 232188, 332081 and 522962 grid elements are tested for the same operation. The comparison in Fig 5.6 shows that the time-averaged pressure profile along the air reactor in the coarse-grid case of 232188 grids is significantly different from those of the others. Meanwhile, the pressure using the 332081 (medium) and 522962 (fine) grids show similar trends with small deviations. Therefore, 522962 grids are adopted in this work, as it achieves sufficient accuracy.

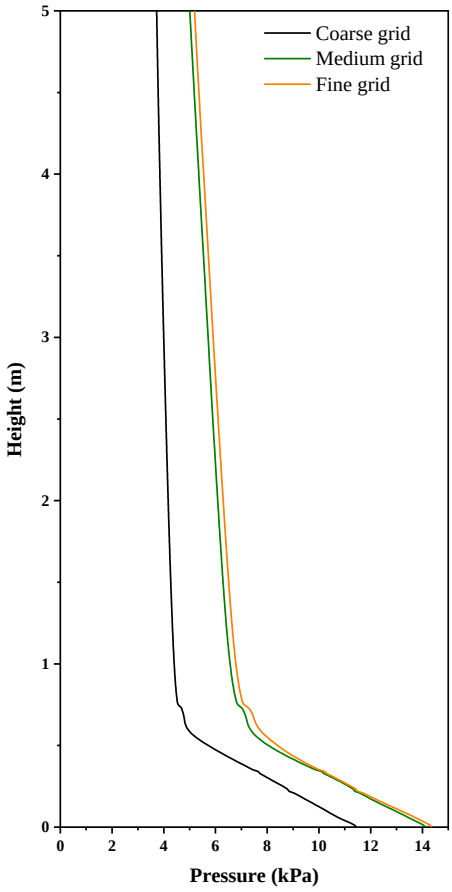

Fig 5.6. Time-averaged pressure profiles along the AR with different grid numbers.

5.4.2 Model validation

In this section, the model validation is conducted by setting the model to the cold and hot experimental conditions [259] and then comparing the simulation results with the measurements. Fig. 5.7(a) shows the profiles of the solid flux monitored at the L-valve outlet. The intense fluctuations of solid flux between 0 and 30 s can be observed, which is commonly regarded as the start-up process. Afterwards, the solid fluxes fluctuate around a constant value, which generally is regarded as the quasi-stable state. The instantaneous values of fluxes are averaged during the quasi-steady state. Fig. 5.7(b)

shows that the time-averaged values at the L-valve show reasonable agreement with experimental data.

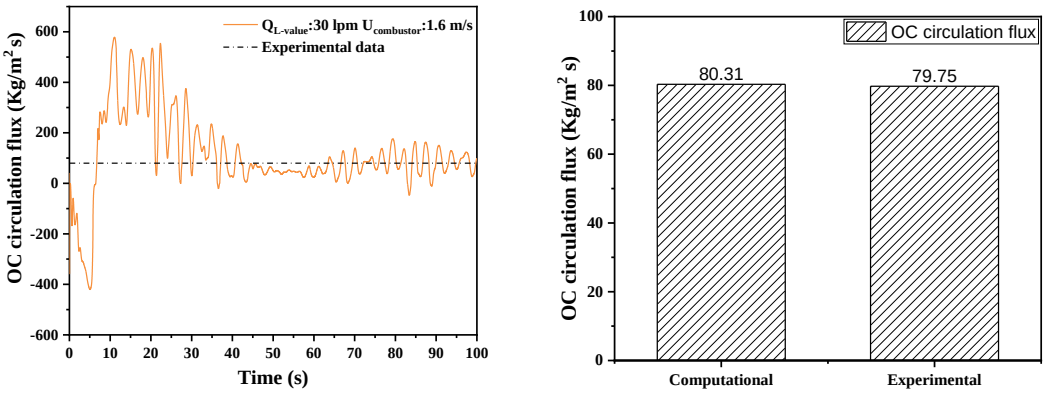

(a) (b)

Fig 5.7. Time-evolution of solid flux (a) and time-averaged solid flux (b) at the L-valve.

Fig. 5.8 (a) gives the time-evolution profiles of the CO_2 volume fraction at the reducer outlet and O_2 volume fraction at the combustor outlet. According to the experiment [103], the steam (H_2O) and Nitrogen (N_2) are removed when calculating the gas volume fraction. At the initial condition, the system is filled by N_2, while the content of other gas species is zero. As the simulation starts, different gas components are introduced into the system with a constant flow rate, as shown in Table 5-7. The O_2 concentration of the combustor is analyzed to monitor the regeneration degree of the oxygen carriers. The concentration profile of O_2 in Fig 5.8(a) is shown to be approximately 18 vol % after the system becomes a quasi-steady state, which is less than atmospheric (21%), indicating consumption of O_2 by the reduced oxygen carrier. The CO_2 monitored at the reducer outlet is mainly generated through various reactions, including the devolatilisation process of raw coal, reduction reactions of the oxygen carrier with the CH_4, H_2 and CO and the water-gas shift reaction. Part of the CO_2 monitored at the reducer outlet is from

the residual enhancer gas. After the system reaches the quasi-steady state, the concentrations of CO_2 in the reducer outlet and O_2 in the combustor outlet are averaged by time and compared with the experimental measurements. It can be seen the simulation results of gas concentrations agree well with the experimental data within an acceptable range. Meanwhile, it also can be observed that the concentration of O_2 in combustor by simulation is slightly higher than experimental data, which represents a lower oxidation degree of the oxygen carrier, and the concentration of CO_2 in reducer by simulation is slightly lower than experimental data, which represents a lower reduction degree of the oxygen carrier. This is because, in this model, the one-step reduction and oxidation reaction are considered, like the most of previous simulation work of CLC processes [150,177,178]. Actually, three-step reduction and oxidation of oxygen carriers occur in this CDCL system due to the unique moving bed reducer design, indicating the oxygen carrier has a higher degree of oxidation and reduction, so more O_2 is consumed in the combustor and more CO_2 is produced in the reducer. However, the complex kinetic model is too computer-consuming to be implemented in the full-loop CDCL model in this work. More exploration of the kinetic model will be done in our future work.

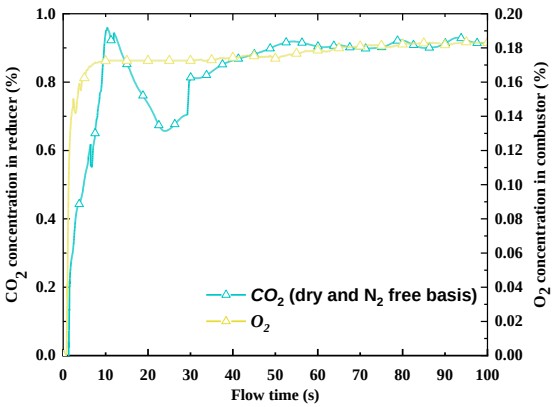

(a)

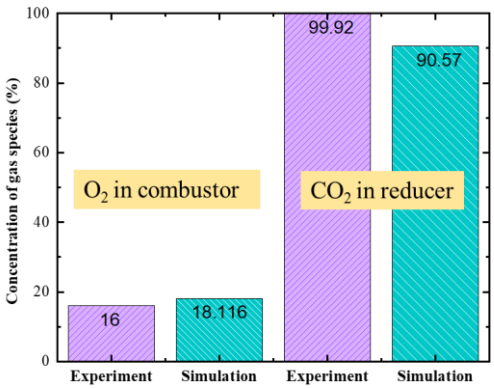

(b)

Fig 5.8. Time-evolution of CO_2 concentration at the reducer outlet and O_2 concentration at the combustor outlet (a); Time-averaged concentration of CO_2 in reducer and O_2 in combustor (b).

5.4.3 Transport characteristics of coal powder in the reducer

In CDCL processes, the fine coal powder is not allowed to flow into the AR and non-combustible waste (e.g., coal ash) must be removed in the reducer. Meanwhile, the migration pattern of the solid fuel powder and its contact time with coarse particles (oxygen carrier) can significantly affect the reaction rate and the product yield. A suitable residence time of coal powder in the FR is an important factor for CDCL performance. In the Ohio CDCL process, the oxygen carrier particle size (Geldart group D) can be an order of magnitude larger than the pulverised coal (Geldart group A), where the coal powder can flow through the interstitial space among coarse particles, as shown in Fig 5.9. Due to differences of the particle size and density, the minimum fluidisation velocity of coarse oxygen carrier particles is orders of magnitude higher than that of the fine coal powder particles. It provides a direct way to control the transport behaviour of coal powders through the reasonable selection of the enhancer gas velocity.

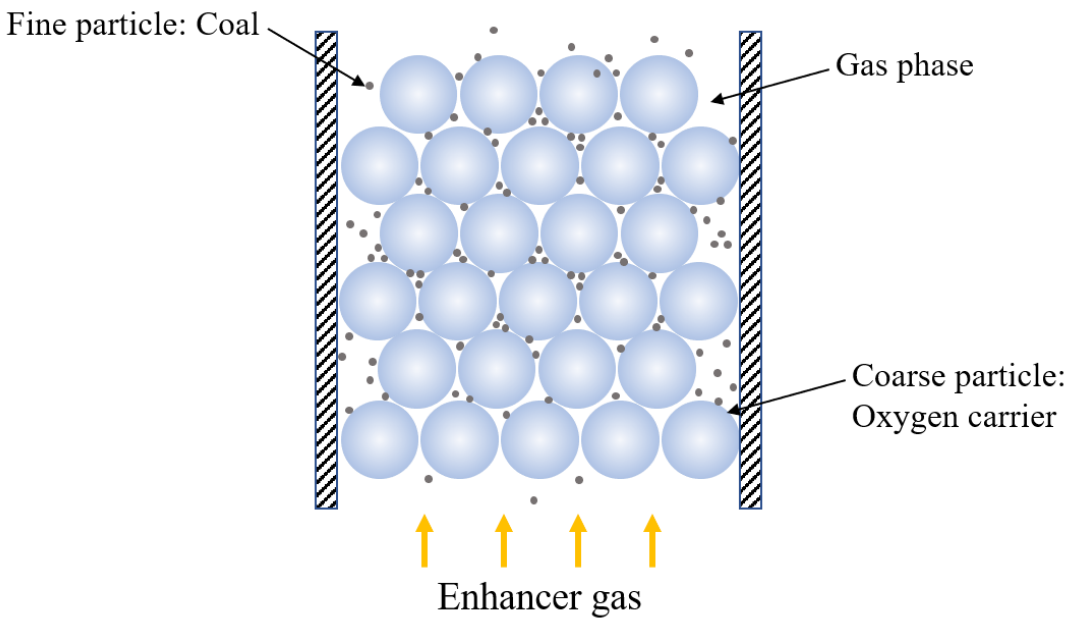

Fig 5.9. Typical fine particles migration pattern with upward aeration.

Fig 5.10 shows time evolutions of the distribution of DPM coal particles in the Ohio CDCL system under the cold condition and hot condition, respectively. Due to numerous particles in the system, for the better display of the particle distribution, only 500 particles were tracked for post-processing. After being injected from the middle coal inlet, the coal particles permeate and transport in the oxygen carrier bed driven by the combination of gravity, drag force (from enhancer gas flow), and collision (interaction with packed oxygen carrier particles) forces. At room temperature, there is no chemical reactions for raw coal particles in the system. Meantime, the gas velocity inside the reducer is lower than the minimum fluidisation velocity of raw coal particles. Therefore, it can be observed clearly by Fig 5.10(a) that the raw coal keeps falling after entering the reducer and finally, it will flow to the AR. Upon heating, the coal powders will rapidly volatilised and release volatile matter into the moving bed, as described in Chapter 4. It

can be founded in Fig 5.10 (b) that near the coal inlet zone the density of coal particles decreases after the fast devolatilization process. Then, the char left in the coal particles continues to permeate into the moving bed and react with the CO_2 and H_2O from the enhancer gas and volatile matter. The density of coal further decreases until all char can be consumed completely. At this time, due to the decrease of density and the production of a large amount of reaction gas, the gas velocity in the reducer is greater than the terminal velocity of coal particles. The ash residue of the coal particles can be carried out of the reducer by the reducer flue gas. By adjusting the enhancer gas velocity under the reducer, the residence time of coal particles can be controlled precisely to ensure the complete coal conversion and the residue in coal particles can be separated directly without needing a separate unit operation.

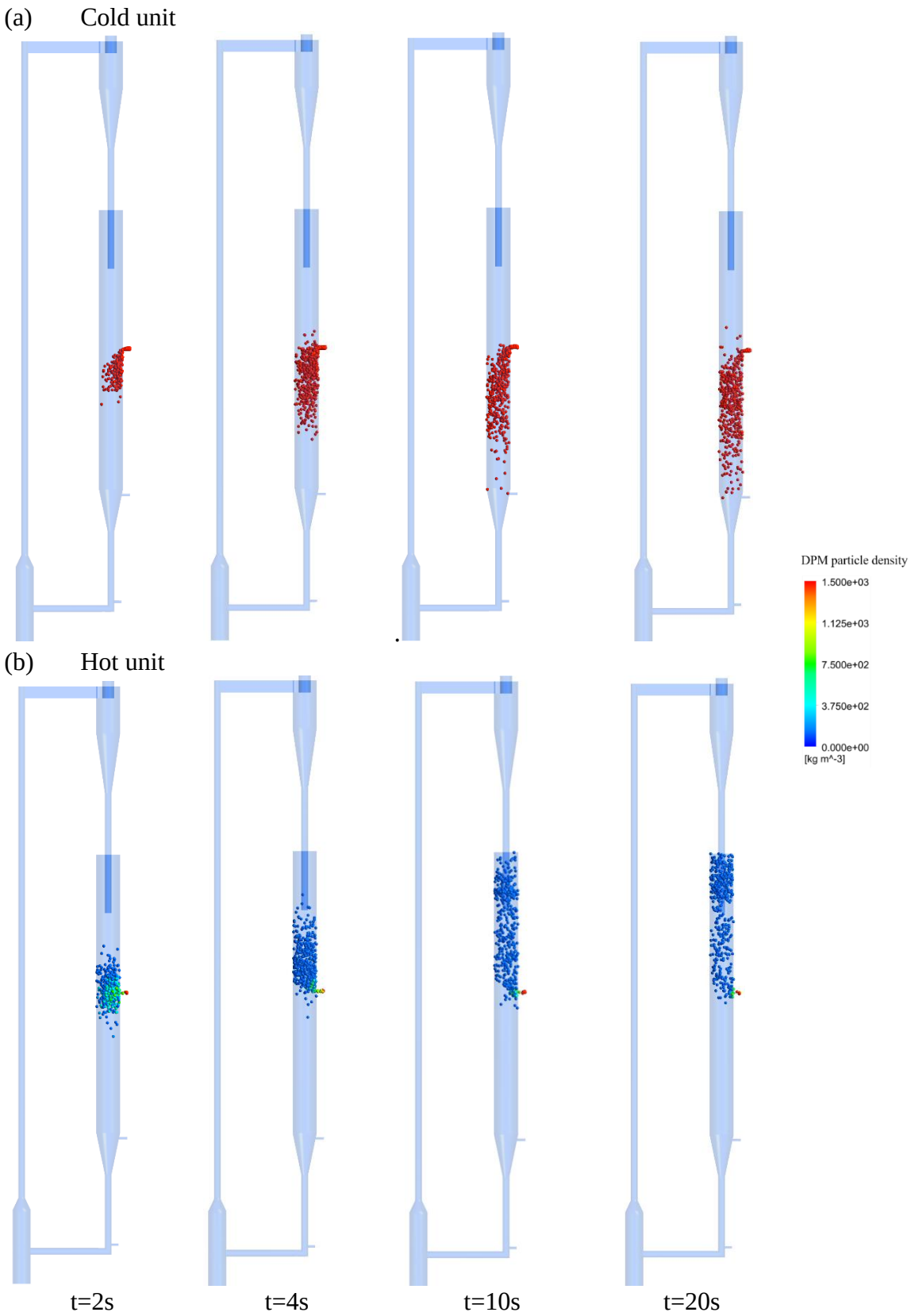

Fig 5.10. Snapshots of the time evolution of DPM particle distribution coloured by the particle density. Cold unit (a); Hot unit (b).

The residence time distribution (RTD) of coal particles in the reducer under the hot unit is quantified by making statistics on all the data during 70~100s. It can be seen from Fig 5.11 that the particle residence time of coal has a wide range of RTD in the reducer, presenting the characteristics of an “early peak with a long tail” pattern from 9s to 62s. Most of the coal particles are concentrated in the range of 10s~20s, which indicates the mean residence time of coal particles in the reducer. The extended range of the RTD indicates the existence of solids back-mixing behaviour, which means that the solids reflux within the bed and cannot exit in time.

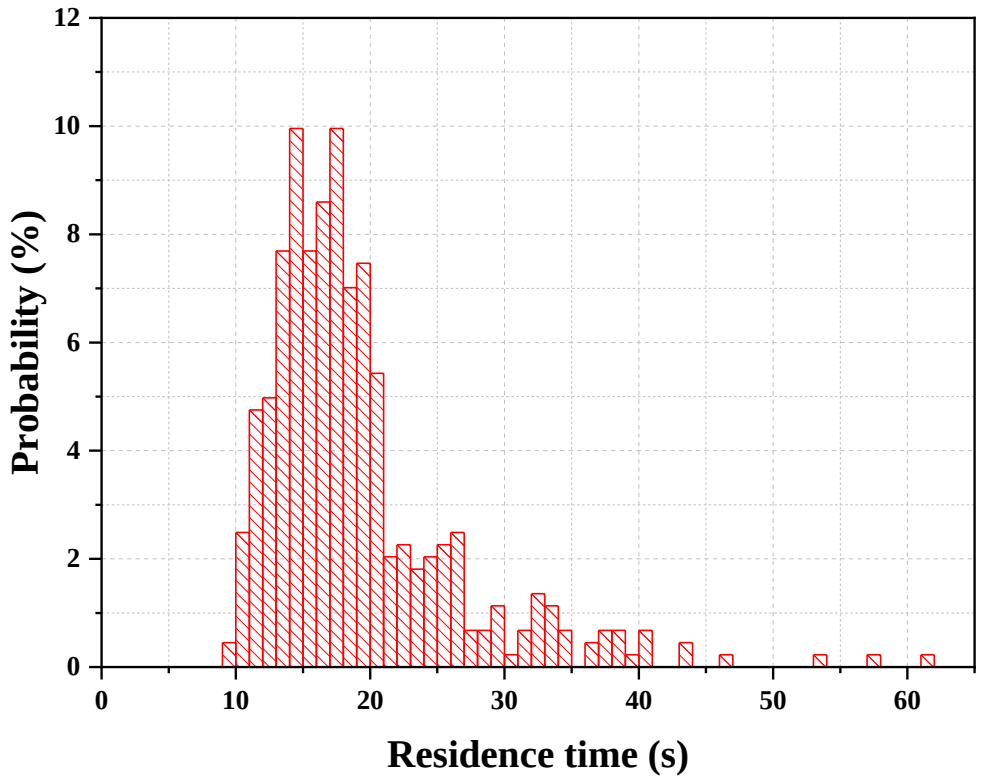

Fig 5.11. The probability density distributions of the coal particle residence time in the reducer during 70~100s.

5.4.4 Analysis of the gas leakage during continuous operation of a CLC reactor

Gas leakage is an issue commonly encountered in the operation of a CLC system. Minimisation of the gas leakage between the AR and FR is essential for high-efficiency CO_2 capture and high coal purity. Although variable loop seals are designed to isolate the atmosphere between AR and FR, some gas leakage is expected in a real CLC system [164,177,264]. Most of the relevant studies focus on the gas leakage of a high concentration CO_2 leaking from the FR to the AR, along with the oxygen carrier circulation [178,265,266]. However, the issues of gas leakage in this work come from different sources.

Fig 5.12 (a) shows the contour of the instantaneous CO_2 distribution in the full reactor over time. According to this figure, a high concentration of CO_2 only exists in the FR and no CO_2 flows into the AR. This is because the circulation rate of the oxygen carrier is relatively slow in this CDCL unit compared with other CLC configurations [178,265,266]. However, in Fig 5.12(b), a small amount of O_2 from the AR leaks into the FR and dilutes the CO_2 at the outlet of the FR, which causes a slight gas leakage phenomenon. The main reason for this phenomenon is the pressure distribution, as shown in Fig 14: The gas always flows from the high-pressure domain to the low-pressure domain. However, the pressure in the L-valve is slightly lower than that in the combustor and higher than the reducer, which is the main cause of the gas leakage from the AR to FR. In this CDCL Unit, the amount of the leaking O_2 in the reducer is limited, which is less than 5%. An effective method to overcome this problem is to add one gas seal between the reducer and L-valve gas inlet to form a high-pressure point, where the pressure should be higher than for the L-valve and combustor.

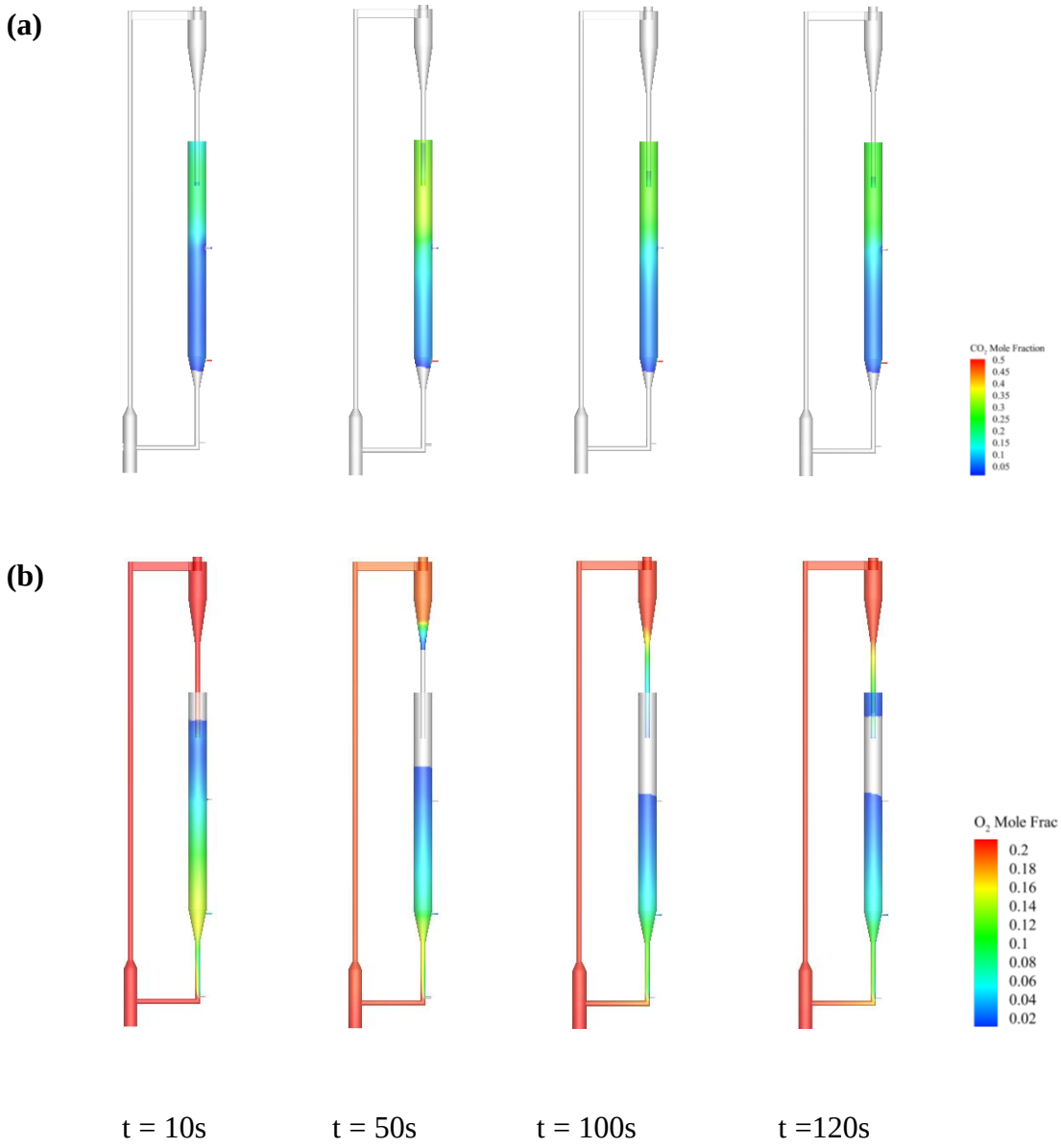

Fig 5.12. Instantaneous distributions of the gas specie molar fraction: Mole fraction of CO_2 (isovolume>1 mol%) (a); mole fraction of O_2 (isovolume>1 mol%) (b).

5.4.5 Temperatures inside CLC system

For coal particles, the temperature decreases near the coal injection zone because the coal devolatilization and char gasification are endothermic reactions. Following the complete conversion, the temperature of coal particles changes little, as shown in Fig 5.13(a). The heat generated in the CLC system is the net result of the exothermic oxidation reaction occurring in the AR and the endothermic reduction and gasification reactions occurring

in the FR. As a result, the high temperatures in the CLC system are seen in the AR riser and in the cyclone whereas the low temperatures are present in the bottom of the fuel reactor and the L-valve, as shown in Fig 5.13(b). A more detailed temperature distribution can be seen in Fig 5.14. With the height increased, both gas and solid temperatures are increased in the AR. Owing to the endothermic reaction in the FR, there is a decrease in both gas and solid temperatures at the middle of the FR where the coal is injected. It can be found that the highest temperature occurs in the cyclone, while the lowest one occurs in the L-valve. Besides, as a result of inter-phase heat transfer between phases, the difference is not obvious.

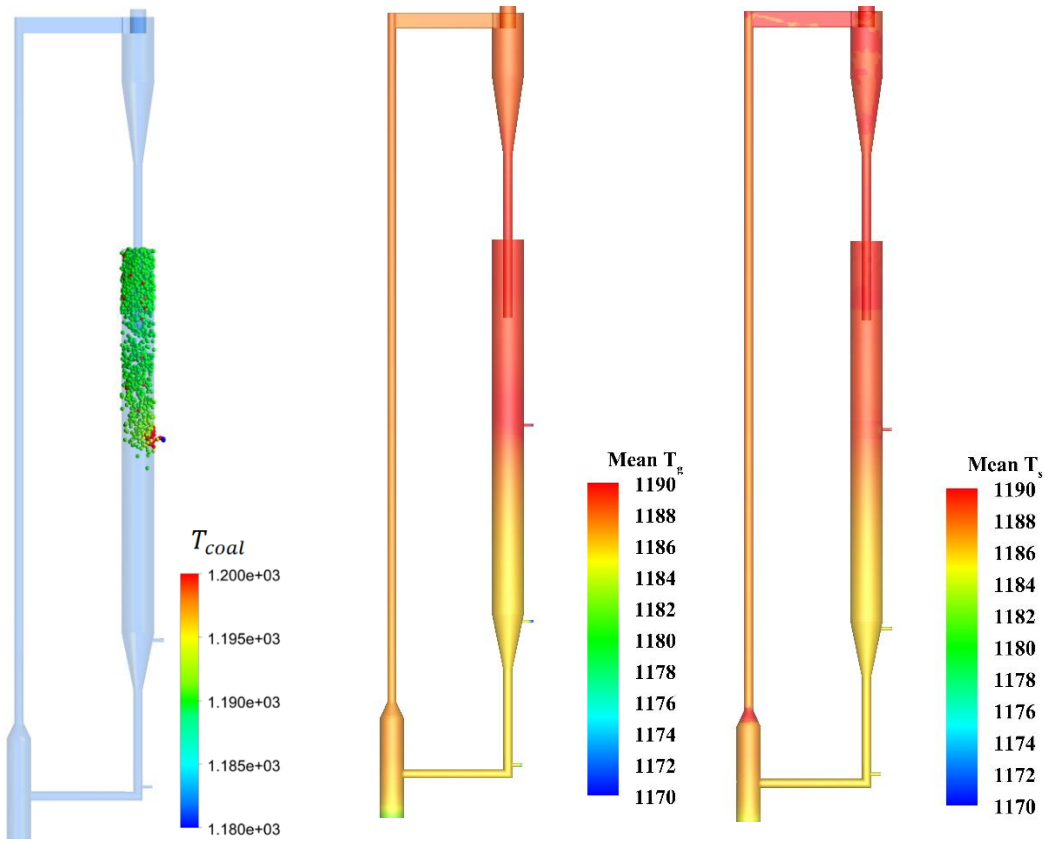

(a) (b) (c)

Fig 5.13. DPM coal particle temperatures at 100 s (a); time-averaged gas temperatures in CDCL system (b); time-averaged solid temperatures in CDCL system (c).

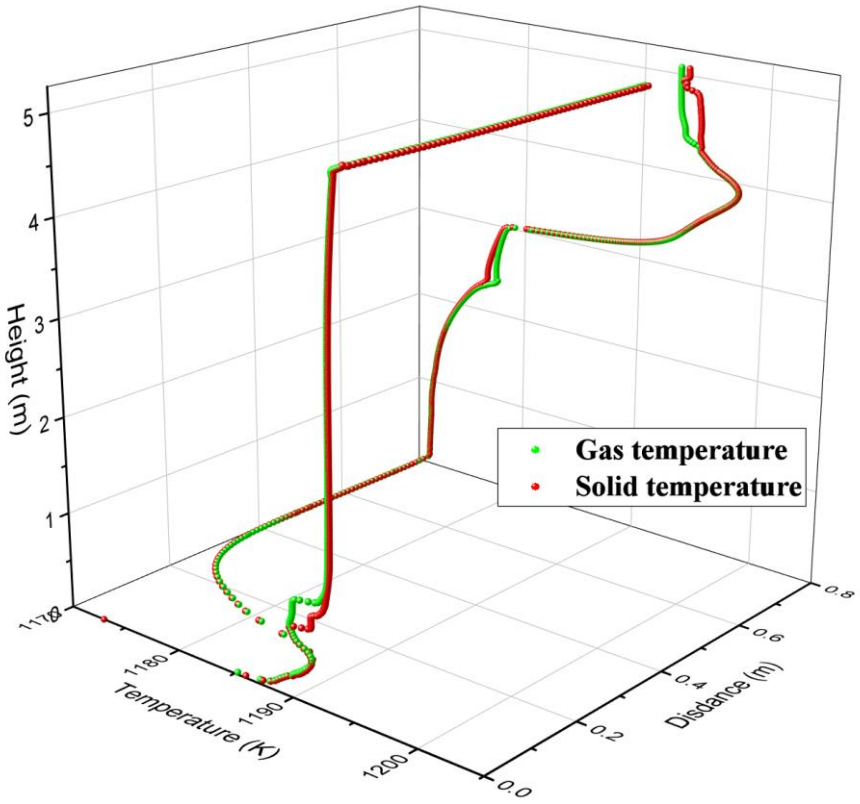

Fig 5.14. Instantaneous temperature profile of the gas and oxygen carrier along the central line throughout the full-loop system.

5.4.6 Analysis of the reactions in the system

Fig 5.15 represents the normalized concentration profile of the reducer gas species during the operation under hot condition. As illustrated by the curves, the CO_2 concentration is maintained greater than 90 vol.% (left y-axis) with negligible concentrations of CO and CH_4 (right y-axis) throughout the demonstration.

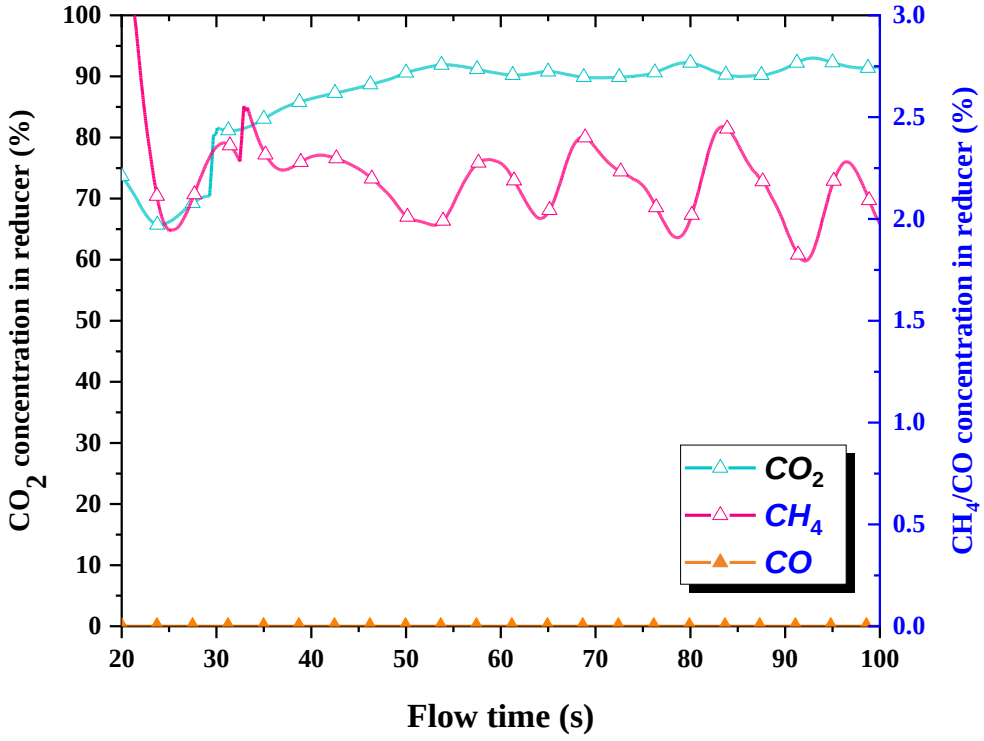

Fig 5.15. Reducer outlet concentration profiles of the CO_2, CH_4 and CO (dry and N_2 free basis).

Fig 5.16 shows the mass fraction of the char in coal particles and the molar fraction distributions of gas species. It can be seen that the change of the char mass fraction goes through two stages: Firstly, the value of char mass fraction increases near the coal injection region. This is because the fast coal devolatilization takes place and the volatile matter releases to variable gas species; and then the char mass fraction decreases because the char reacts with the H_2O and CO_2 and produces H_2 and CO. Accordingly, there is a high concentration of H_2, CO and CH_4 near the coal feeding domain because of the fast coal devolatilization and char gasification. Secondly, the middle products H_2 CO and CH_4 concentrations are decreased along the height of the reducer because they are consumed by the reduction reactions of oxygen carriers and transferred to the final products, H_2O and CO_2. The H_2O volume fraction is relatively low at the bottom of the reducer because only a small amount of coal is consumed in this region. Part of the CO_2 from the enhancer

gas is consumed by the char gasification near the coal injection inlet. Therefore, high concentrations of H_2O and CO_2 are obtained at the top of the reducer.

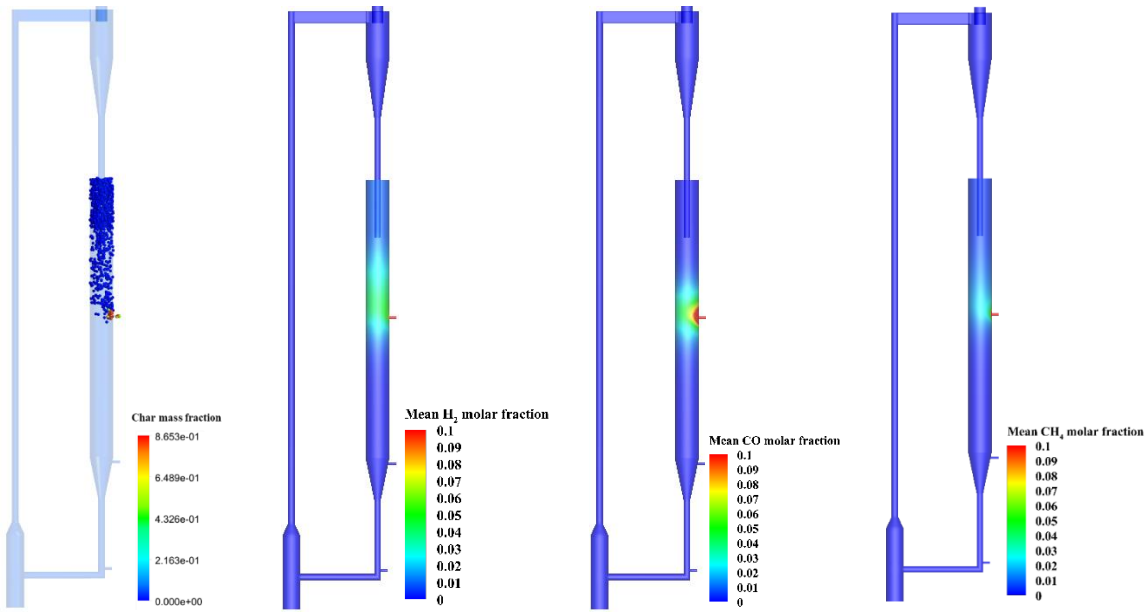

(a) (b) (c) (d)

Fig 5.16 Char mass fraction in coal particles at 100 s (a); Time-averaged molar fractions of gas species. Mole fraction of H_2 (b); Mole fraction of CO (c); Mole fraction of CH_4 (d).

Fig 5.17 shows the heterogeneous reaction rates of the oxygen carrier. It can be seen the oxidation reaction mainly takes place in the combustor because of the high O_2 concentration and FeO content. Besides, a very low reaction rate can be found in the reducer because of the O_2 leakage from the AR, as discussed before. The reductions of oxygen carrier with CH_4, H_2 and CO have a high reaction rate near the coal injection domain because of the high concentration of gas species and mainly occur above the coal injection inlet due to the upward diffusion of devolatilization gas.

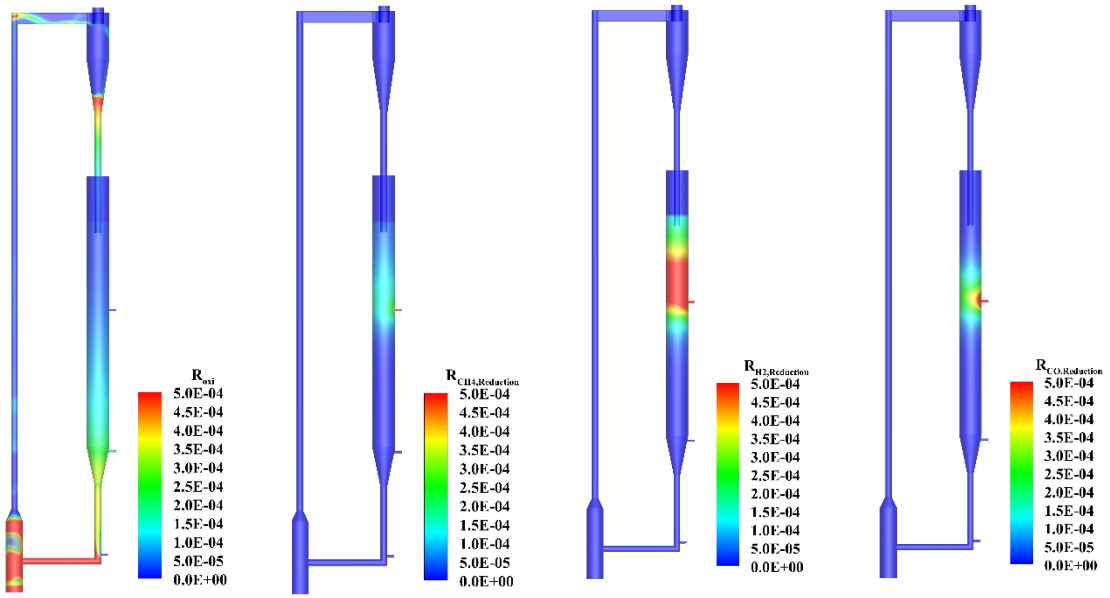

(a) (b) (c) (d)

Fig 5.17 Instantaneous heterogeneous reaction rate of oxygen carrier at 100 s. oxidation rate of oxygen carrier (a); CH_4 reduction rate (b); H_2 reduction rate (c); CO reduction rate.

The optimal reaction state of the AR and FR is to realise the full oxidation and full reduction, respectively. However, the actual reaction degree is always below the optimal reaction state. To better quantify the reaction degree in the CDCL system, the degree of oxidation is defined to estimate the degree of reaction:

$$X = \frac{m - m_{red}}{m_{ox} - m_{red}} \tag{5-29}$$

Where m is the actual mass of the sample, m_{red} is the mass of the sample when fully reduced, and m_{ox} is the mass of the sample when fully oxidised. To better explore the reaction process in the system, at the initial condition, the fully oxidised oxygen carrier (Fe_2O_3) is packed in the reducer and L-valve, while the fully reduced oxygen carrier (FeO) is packed in the combustor. In Fig 5.18, the oxidation levels of the oxygen carrier particles in the system are shown at different times. The oxidation and reduction reactions continue in the combustor and reducer over time, as shown in Fig 5.18 and Fig 5.19, respectively. It can be seen that at the initial condition, a fully reduced oxygen carrier is packed in the

bottom combustor and a fully-oxidised oxygen carrier is packed in the reducer and L-value, and then the degree of oxidation increases in the combustor, riser and cyclone due to the oxidation reaction. while the degree of oxidation decreases at the top of the reducer due to a series of reduction reactions. After the system forms a stable oxygen carrier circulation, the local oxidation degree of the oxygen carrier is the result of two aspects: one is the process of reactions, and the other is the oxygen carrier circulation and mixing between AR and FR. The time-averaged distribution of the oxygen carrier oxidation degree shows there is a lower oxidation degree of oxygen carrier in the reducer because of the various reduction reactions and a higher oxidation degree in the AR because of the oxidation reaction happening. In the AR, as shown in Fig 5.19 (b), the oxidation degree of the oxygen carrier gradually increases along the riser, but the complete oxidation is not being achieved by looking at the particles leaving the riser. In the FR, as shown in Fig 5.19 (c), it has been known that reduction of oxygen carrier mainly occurs above the coal injection, so the oxidation degree of oxygen carrier is lowest above the coal injection region. Near the cyclone outlet, due to the regenerated oxygen carrier from AR, there is an increase in the oxidation degree of the oxygen carrier.

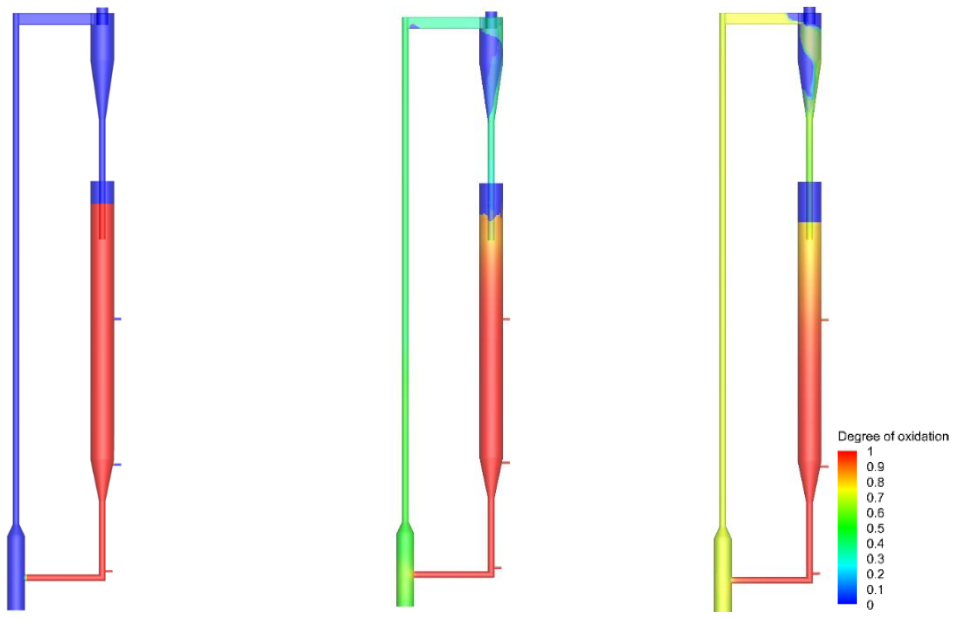

t=0s t=10s t=20s

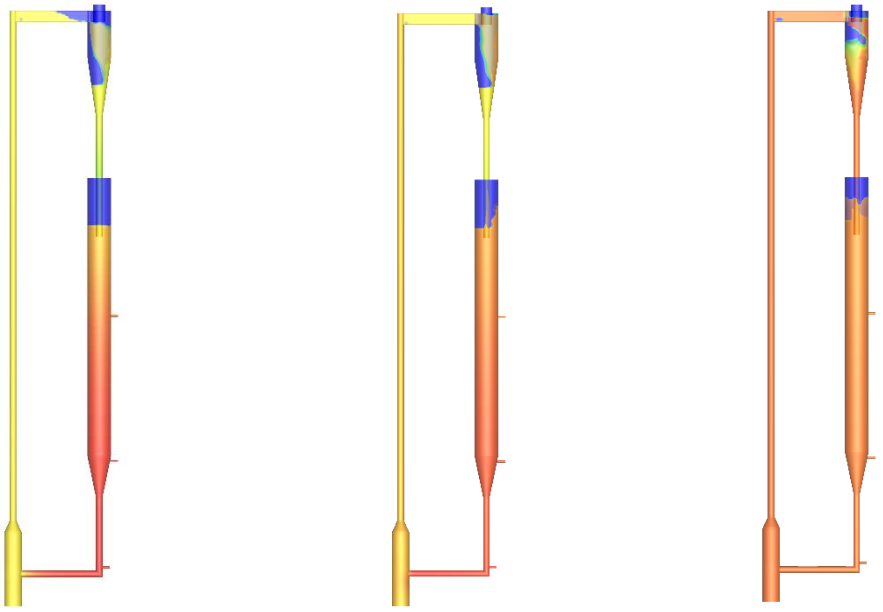

Fig 5.18 Contours of instantaneous oxidation degree of oxygen carrier in the CDCL unit at different times.

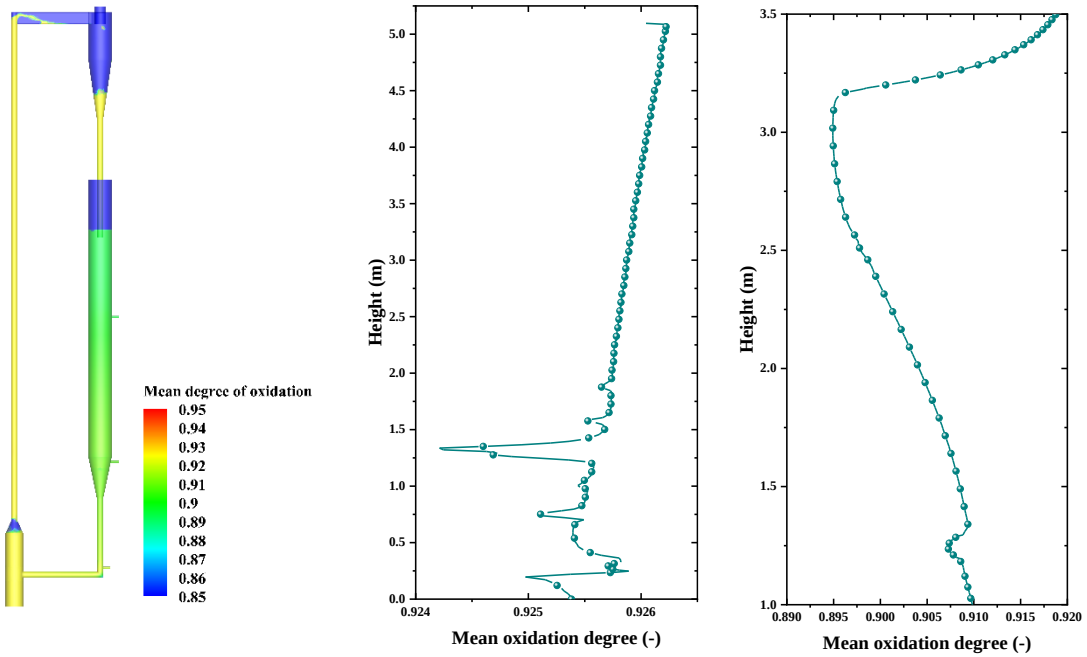

(a) (b) (c)

Fig 5.19. Contours of time-averaged oxidation degree of oxygen carrier in the CDCL unit (a); Profile of time-averaged oxidation degree of oxygen carrier along the centre line of the AR (b); Profile of time-averaged oxidation degree of oxygen carrier along the centre line of the FR (c).

5.5 Conclusions

In the present work, a 3D Eulerian-Eulerian-Lagrangian (E-E-L) hybrid model is used to study the gas-solid flow and reaction characteristics of the 25 kWh sub-pilot CDCL process with the unique moving bed FR developed at OSU. The flow behaviours of both oxygen carrier and powder coal are investigated under cold and hot conditions. And the reaction characteristics are also detailed discussed. Based on the numerical results, conclusions can be drawn as follows:

(1) The mixing and separation process of the coarse oxygen carrier and fine coal powder is captured by simulation, and the mechanism is further explained by numerical results. The residence time of most coal particles in the reducer is concentrated in the range of 10s~20s.

(2) Gas leakage phenomena are analysed by simulation in the system. Results show that there is no CO2 leakage from FR to the AR because of the low circulation rate of the oxygen carrier in the reducer, while a small amount of O2 from the AR leaks into the FR because the pressure in the L-valve is slightly lower than that in the combustor and higher than the reducer.

(3) The high temperatures in the CLC system are seen in the AR riser and in the cyclone, whereas the low temperatures are present in the bottom of the fuel reactor and the L-valve.

(4) The reaction rates and reactants distribution of all reactions considered in this work are reasonably predicted by simulation, showing the applicability of the hybrid model to investigate the CDCL unit.

CHAPTER.6 Investigation of the Non-uniformity in a Full-loop Circulating Fluidized Bed with Symmetrical Parallel Loops

The non-uniformity of the solid distribution is a common issue in most of the CFB system, not only for symmetrical configurations but also existing in all CFB systems with multiple branches. In this chapter, two types of CFB systems with symmetrical configurations is adopted, as two extreme and ideal examples, to investigate the non-uniformities in CFB systems. In this section 1, the maldistribution characteristics of complex symmetrical CFB units with the parallel cyclones are deeply investigated by using the Eulerian multi-fluid model. Simulation results verify the maldistribution phenomenon with parallel symmetrical CFB units, and the model settings are validated by experimental data. The maldistribution phenomena are discussed and evaluated in terms of bed inventory evolution and gas-solid distribution in symmetrical parts. The effects of key operating parameters, including total bed inventory, gas aeration rate, and wall roughness on non-uniformity degree are then studied. Simulation results show that the maldistribution degree between the two symmetrical parts will increase with the increase of total bed inventory and gas aeration rate. And through the analysis of pressure fluctuation, the instability of the system is aggravated. However, wall roughness does not show a clear influence and tendency. Conclusions in this chapter provide an insightful understanding of non-uniformity and will help further optimize symmetrical complex CFB systems.

In section 2, the non-uniformity characteristics of complex symmetrical CFB units with the symmetrical series loops are deeply investigated by using the Eulerian multi-fluid model. The non-uniformity phenomenon in identical symmetrical CFB units is verified by simulation results, and the model settings are validated by experimental data. The non-uniformity phenomena are discussed and evaluated in terms of bed inventory evolution

and gas-solid distribution in symmetrical parts. The effects of key operating parameters, including total bed inventory, gas aeration rate, and wall roughness on non-uniformity degree are then studied. The simulation results show that the non-uniformity degree between the two symmetrical parts will increase with the increase of total bed inventory and gas aeration rate. And through the analysis of pressure fluctuation, the instability of the system is aggravated. However, wall roughness shows an indefinite influence and tendency. This work provides an insightful understanding of non-uniformity and will help further optimise symmetrical CLC systems.

The paper “CFD investigation of maldistribution in a full-loop circulating fluidized bed with double parallel cyclones” has been published based on the content of this chapter in the journal of Powder Technology.

The paper “CFD study of nonuniformity of gas-solid flow through a chemical looping combustion system with symmetrical series loops” has been accepted based on the content of this chapter to the journal of Powder Technology.

S. Li, Y. Shen, CFD investigation of maldistribution in a full-loop circulating fluidized bed with double parallel cyclones, Powder Technol. 381 (2020) 665-684.

S. Li, Y. Shen, CFD study of nonuniformity of gas-solid flow through a chemical looping combustion system with symmetrical series loops. Powder Technol. (2021)

Graphical abstract for this chapter

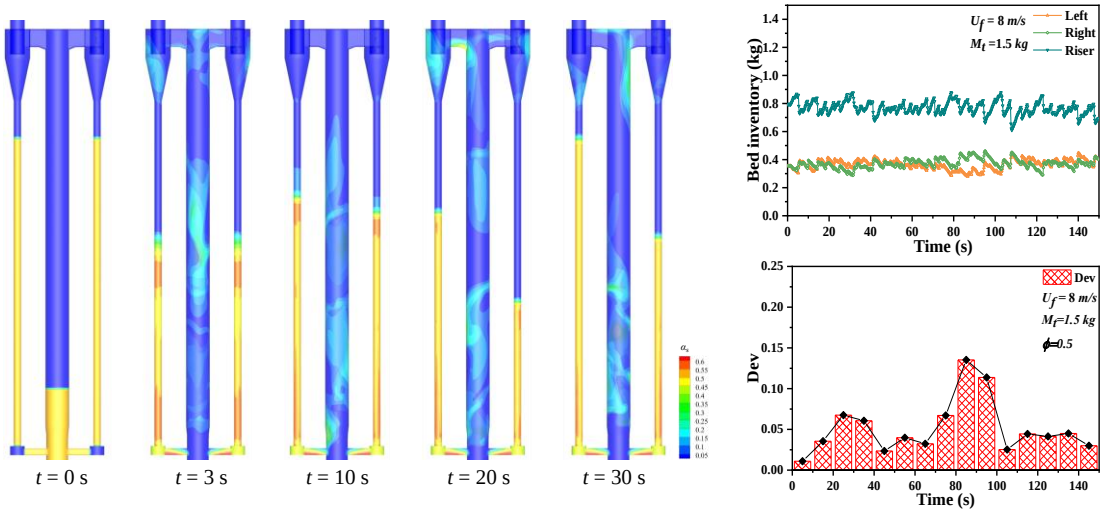

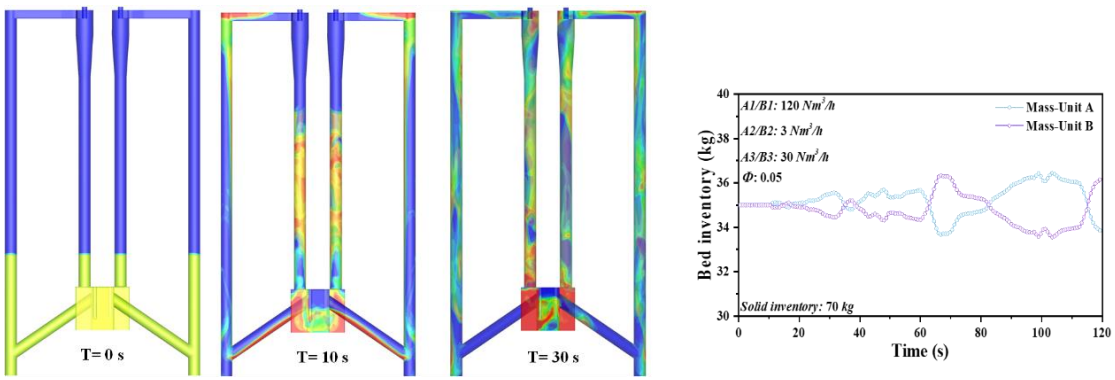

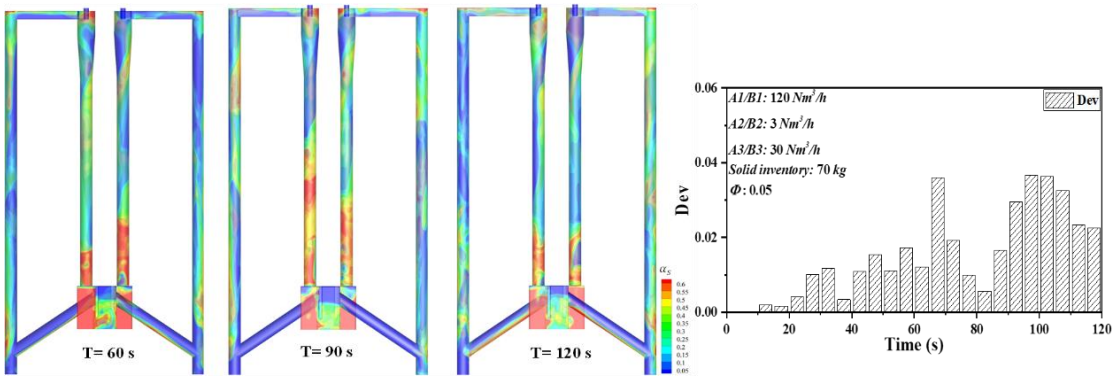

ABSTRACT

In this chapter, the characteristics of the maldistribution phenomenon in a symmetrical dual-side refeed circulating fluidized bed and symmetrical CLC unit are numerically studied. This chapter is divided into two sections. In section 1, the influence of maldistribution on the performance of different sections is discussed. The results show that the maldistribution lowers the total performance of parallel cyclones and the L-valve has a self-balancing to lower the degree of maldistribution. Moreover, the effects of gas inlet velocity, total solid inventory and wall function on the degree of maldistribution are explored. The simulation results confirm that the maldistribution can be captured in the system. The degree of the maldistribution in parallel external loops decreases with the increase of gas inlet velocity and total solid inventory; however, it is not sensitive to the wall roughness. This work provides insight of the cause of gas-solid maldistribution and the influence of different operation conditions on the degree of maldistribution.

In section 2, the non-uniformity in a CLC apparatus is studied. First, the typical non-uniformity phenomenon is evaluated in terms of bed inventory evolution and gas-solid distribution in symmetrical parts. The effects of key operating parameters including total bed inventory, gas aeration rate, and wall roughness on non-uniformity degree are then studied. The simulation results show that the non-uniformity degree between the two symmetrical parts will increase with the increase of total bed inventory and gas aeration rate. And through the analysis of pressure fluctuation, the degree of system instability becomes more serious. However, wall roughness shows an indefinite influence and tendency. This work provides an insight understanding of non-uniformity and will help further optimise symmetrical CLC systems.

6.1. Investigation of the Non-uniformity in a Full-loop Circulating Fluidized Bed with Symmetrical Parallel Loops

6.1.1 Introduction

Multiphase systems where gas-liquid or gas-solid passes going through multiple identical paths in parallel have been commonly practised in many practical chemical engineering processes, such as gas-liquid heat exchangers to exchange heat in parallel channels [267], fuel cells using parallel flow channels [268–270], multi-orifices distributor to assist good fluidization via parallel flow channels [271,272], and gaps between particles in packed beds [273–275] also can be regarded as parallel paths. In these cases, the parallel channels have the function to maximize the interaction area. Specifically, in the chemical industry, a circulating fluidized bed (CFB) is commercially used for fluid catalytic cracking (FCC) [16,276], coal combustion [274,277,278], and biomass gasification [279,280] processes because of its good mixing efficiency, excellent heat and mass transfer, and feedstock flexibility. In a typical CFB configuration, the cyclone is widely used as the primary gas-solid separator to circulate particles between each reactor owing to its simple configuration and ease of operation [281,282]. In order to facilitate the high separation efficiency within the system, multiple cyclones arranged in parallel are commonly adopted in the CFB. However, it has been widely reported in the literature that the flow distribution is largely non-uniform in the parallel-paths of multiphase systems [283–289] including the non-uniform gas-solid flows in parallel cyclones [285–287,290]. It is reported that these non-uniformities will decrease cyclone efficiency, suppress reactor performance, trigger surface erosion, and unbalance heat transfer. Although the maldistribution phenomenon has been frequently reported for years [16,291], the fundamental mechanism is not yet understood well. Thus, it is important to study the maldistribution of gas-solid flow in the circulating fluidized bed system with a parallel cyclone layout.

Many experiments have been conducted to explore the maldistribution of parallel cyclones in CFBs. For example, Masnadi et al. [286] showed that differential fouling exits in the six identical parallel cyclones of an industrial-scale fluidized bed reactor. Zhou et al. [284] measured the gas-solids flow distribution in a CFB with a pant-leg bottom furnace and six parallel cyclones. They found that the non-uniform distribution occurs mainly in the three cyclones on the same side, that is, the middle cyclones have higher particle velocities, lower solids volume fractions, lower solids fluxes, and lower solids circulating rates. Yue et al. [292] carried out several experiments to investigate the fluid dynamics in a 300 MWe CFB boiler with a single-bottom furnace and three parallel cyclones. The results showed that the solid flow rate and the material distribution in the loops differ remarkably. Shuai et al. [293] carried out an experimental study in a cold test-rig of a CFB with two water-cooled pillars and six cyclones. The results showed that non-uniformity exists among the six circulating loops, and the solid circulating rate of the middle cyclones is lower than those of the side cyclones. Although some conclusions have been obtained from the abovementioned experiments towards the maldistribution phenomenon in the CFB system with parallel cyclones, many factors for studying the maldistribution phenomenon in experiments inevitably affect the reliability of experimental data. One possibility is that the observed differences in flow arise from the amplification of minimal geometric differences among the parallel paths. Moreover, the maldistribution may arise from the external parameters, such as the minor differences of blower equipment. Therefore, it is impossible to maintain the experimental conditions exactly the same for each individual path in experiments. Meantime, the data acquired from these experiments may lack the quality due to the limited accuracy of measurement instruments, and thus it cannot provide detailed information inside experimental plants. The above multiple factors inevitably result in some discrepancies of the experimental measurements, and thus a more high-fidelity method to investigate the maldistribution phenomenon is in urgent need.

As an alternative, computational fluid dynamics (CFD) as a powerful tool in modelling multiphase flows can be used to study gas-solid flow dynamics and the maldistribution phenomenon in CFB apparatuses with parallel cyclones [171,294,295]. Specifically, the CFD method can eliminate the influence of structure and external conditions on flow fields by ensuring the symmetry of geometry, boundary and operating conditions in each external loop. For example, Zhang et al. [294] calculated a three-dimensional full-loop CFB boiler with two parallel cyclones using an Eulerian granular multiphase model. They found that minor difference of the average solid mass flux exists in the two cyclones (i.e., 5.74 and 6.05 $kg \cdot m^{-2} \cdot s^{-1}$) and pointed out that the maximum solids mass flux alternates between these two cyclones. Luo et al. [295] and Wang et al. [296] studied gas-solid motions in a three-dimensional full-loop dual-side refeed circulating fluidized bed by using a large-eddy simulation coupled with the discrete element method (LES-DEM) approach. The maldistribution in identical cyclone paths can be observed in both of their works by comparing the solid distribution and pressure fluctuation. Wang et al. [171] further investigated gas-solid hydrodynamics in six parallel cyclones with central symmetry and axial symmetry arrangements in a full-loop CFB. They pointed out that for a uniform distribution of solid mass flux in parallel cyclones, axial symmetry is better than central symmetry. The middle cyclones on both sides have higher solid velocity and solid holdup than other corner cyclones. Although the maldistribution phenomenon has been reported in the past, the geometries, grids and operating conditions in these studies lack an advance verification of symmetry, which means it cannot be ruled out that some minor differences may cause the maldistribution in terms of geometries, grids, and operating conditions during simulations. In addition, there is still a lack of comprehensive work to assess the influence of some parameters on the non-uniform performance of the parallel cyclone arrangement in CFBs.

In this chapter, numerical simulation is used to study the maldistribution phenomenon of gas-solid pneumatic flows through identical external loops in a dual-side re-feed circulating fluidized bed (DRCFB) with symmetry in geometries, grids, and operating

conditions. Moreover, an index for assessing the degree of maldistribution is proposed and the influence of different parameters on the degree of maldistribution are explored. The paper is organized as follows: In section 2, the governing equations of the multifluid model are formulated and the drag model used in this work is presented. In section 3, the geometry configuration and computational grids for studying the maldistribution phenomenon are highlighted. The computational settings, including gas-solid properties and operating parameters, are tabulated. In section 4, the proposed model is validated with the experimental data, and the symmetry of geometry, grid and operation conditions is verified before analysing the maldistribution phenomenon. Then, the maldistribution phenomenon is discussed from various perspectives. Finally, the effects of several key operating parameters (*i.e.*, gas inlet velocity, initial solid inventory, and wall roughness) on the degree of maldistribution are thoroughly investigated.

6.1.2 Mathematical Model

Governing equations

Two-fluid model (TFM) under the Eulerian-Eulerian framework with the standard kinetic theory of granular flow (KTGF) is used in the present work [106,182]. The gas phase and solid phase are regarded as penetrating continua. Subscripts 'g' and 's' represent the gas phase and solid phase, respectively. The governing equations for each phase and KTGF are listed in sections 3.2.1 and 3.2.2.

The Syamlal-O'Brien drag model [181] is used in this work which was derived based on the terminal velocity of particles. The drag model is written as follows:

$$\beta = \frac{3}{4}\frac{\alpha_s \alpha_g \rho_g}{v_{r,s}^2 d_p} C_D\left(\frac{Re_s}{v_{r,s}}\right)\left|\vec{u}_s - \vec{u}_g\right| \tag{6-1}$$

where

$$C_D = \left[0.63 + \frac{4.8}{\sqrt{Re_s/v_{r,s}}}\right]^2 \quad (6\text{-}2)$$

and

$$v_{r,s} = 0.5(A - 0.06Re_s + \sqrt{(0.06Re_s)^2 + 0.12Re_s(2B - A) + A^2} \quad (6\text{-}3)$$

with

$$\mathrm{A} = \alpha_g^{4.14}, B = 0.8\alpha_g^{1.28} \qquad \text{for } \alpha_g \leq 0.85 \quad (6\text{-}4)$$

or

$$\mathrm{A} = \alpha_g^{4.14}, B = \alpha_g^{2.65} \qquad \text{for } \alpha_g > 0.85 \quad (6\text{-}5)$$

Computational details

As shown in Fig. 6.1(a), a lab-scale DRCFB designed in Ref. [295] and [296] is used to study the maldistribution phenomenon of the parallel system. The full-loop DRCFB consists of a riser, two cyclones, two standpipes, and two L-valves. Chemical reactions mainly occur in the riser. The cyclone has a function of gas-solid separation. The standpipe located below the cyclone is usually used as the heat exchanger or the catalytic cracking regenerator. Besides, it is also used for material storage. The non-mechanical L-valve can control solid flow circulation. The height and inner diameter of the riser are 1.2 m and 0.065 m, respectively. Besides, the inner diameter of the cyclone and the standpipe

are 0.07 m and 0.04 m, respectively. Particles enter the riser from two symmetrically rectangular side ports 0.017 m in edge length and 0.029 m above the gas distributor (from the centre line of the L-valve). Particles exit the riser through two symmetrical rectangular side ports 0.06 m in height, 0.022 m in width about 1.17 m above the gas distributor. The solid particles are sand with a mean diameter of 1.5 mm and a density of 2500 kg/m^3, which are categorized as Geldart group D particles. The total amount of solid inventory in the computational domain is adjusted according to different operating conditions. Aeration inlet is assigned at the bottom of the riser to transport solid materials and two inlets are located at the side of L-valves to recirculate particles to the bottom of the riser with a relatively small air flow rate.

Fig. 6.1(b, c) shows the grids of the DRCFB used in this simulation. All the computational domains, including riser, cyclones, standpipes, and L-valves, are meshed with structured hexahedron elements. The distribution of grids in two external loops are identical through the fine control of grid distribution. The total number of grids used in this work is 150028. The independence study of grid resolution is done in section 6.1.4 which shows such grid resolution is sufficient to predict the gas-solid hydrodynamics in such system with a compromise of numerical accuracy and computational costs.

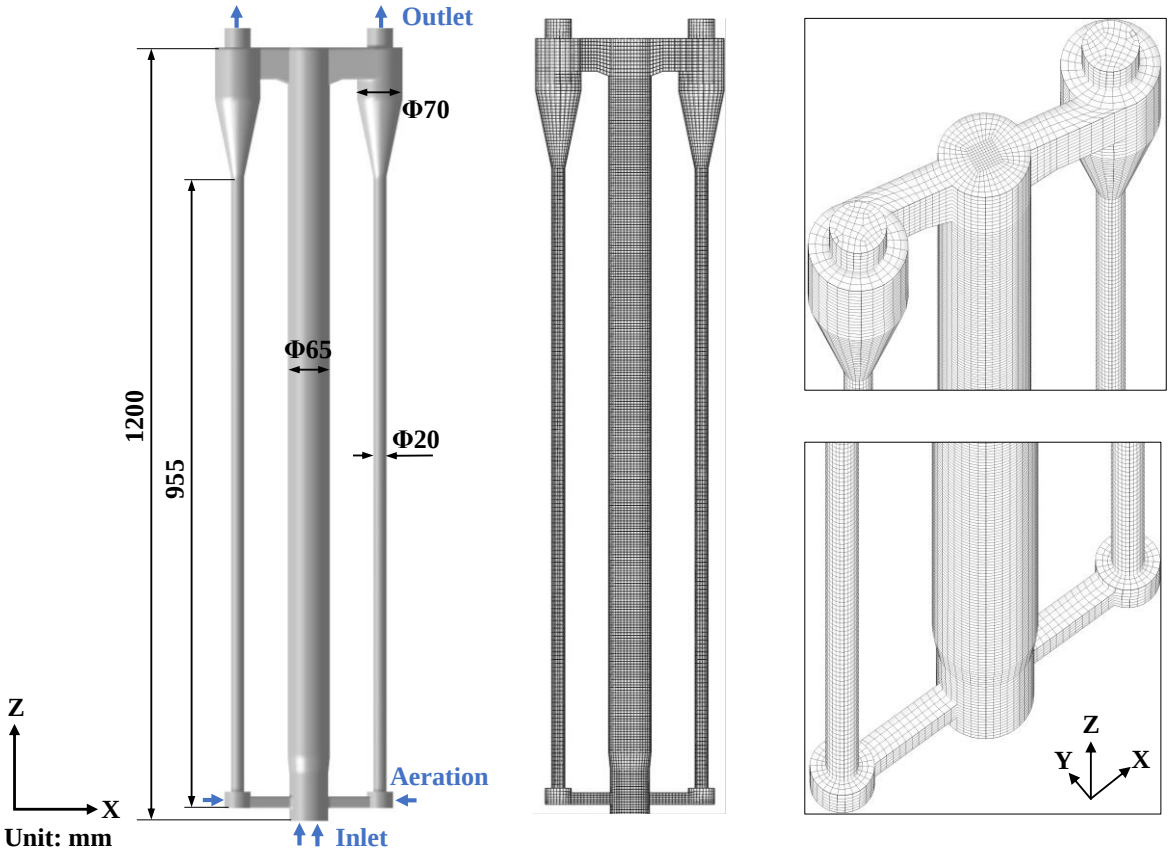

Fig 6.1. Schematic geometry [295] and grids of the investigated three-dimensional DRCFB: geometry (a); grids of the whole bed (b); grids of local regions (c).

Initially, the particles are symmetrically packed in the lower part of the DRCFB with a solid volume fraction of 0.5. The velocity inlet boundary conditions are set for the inlet of the riser and L-valve in both sides. The pressure outlet condition is selected for the cyclone top outlets. The frictional model of Schaeffer [200] for particle phase and the Johnson and Jackson's model [200] for wall boundary conditions of the solid phase are used. The no-slip boundary condition is specified for the gas phase. Different discretization schemes for convection terms of each governing equation are employed: the second-order upwind scheme is chosen for the momentum equation; the Quadratic Upwind Interpolation of Convective Kinematics (QUICK) scheme is chosen for the volume fraction of gas and solid phases, and the first-order upwind scheme is chosen for

the turbulent kinetic energy and turbulent dissipation rate. The Semi-Implicit Method for Pressure Linked Equations (SIMPLE) algorithm is used to deal with pressure-velocity coupling. The simulation is performed on the platform of commercial software ANSYS Fluent 19.2. The time step is assigned as 0.0001 s and the total simulation time for each case is 150 s. The material properties and simulation parameters are listed in Table 6-1.

Table 6-1. Material properties and computational settings for the base case.

Solid Properties	**Values**
Particle density	2500 kg/m^3
Particle size	1.5 mm
Minimum fluidization velocity	1.12 m/s
Restitution coefficient of particles	0.95
Restitution coefficient of particle and wall	0.95
Specularity coefficient	0.5
Angle of internal friction	30°
Friction packing limit	0.60
Packing limit of particles	0.63
Gas Properties	
Gas inlet velocity	8 m/s
Aeration gas velocity	0.2 m/s
Gas density	1.225 kg/m^3
Gas viscosity	1.837×10^{-5} Pa·s
Computational Settings	

Pressure-velocity coupling	SIMPLE
Drag model	Syamlal and O'Brien
Time step	1×10^{-4} s
Max. number of iterations per time step	50
Convergence criteria	10^{-4}

6.1.3 Results and discussions

Grid independence test

A grid-sensitivity analysis is conducted to ensure the number of the grid is suitable for this simulation. Three different computational domains of 86640, 150028 and 255440 grid elements are assigned for the same operation. The comparison in Fig 6.2 shows that the time-averaged pressure profile along the riser height in the coarse-grid case of 86640 grids is significantly different from those of the others. Meanwhile, the pressure using the 150028 (medium) and 255440 (fine) grids show similar trends with small deviations. Therefore, 150028 grids are adopted in this work, as it achieves a trade-off between sufficient accuracy and computational cost.

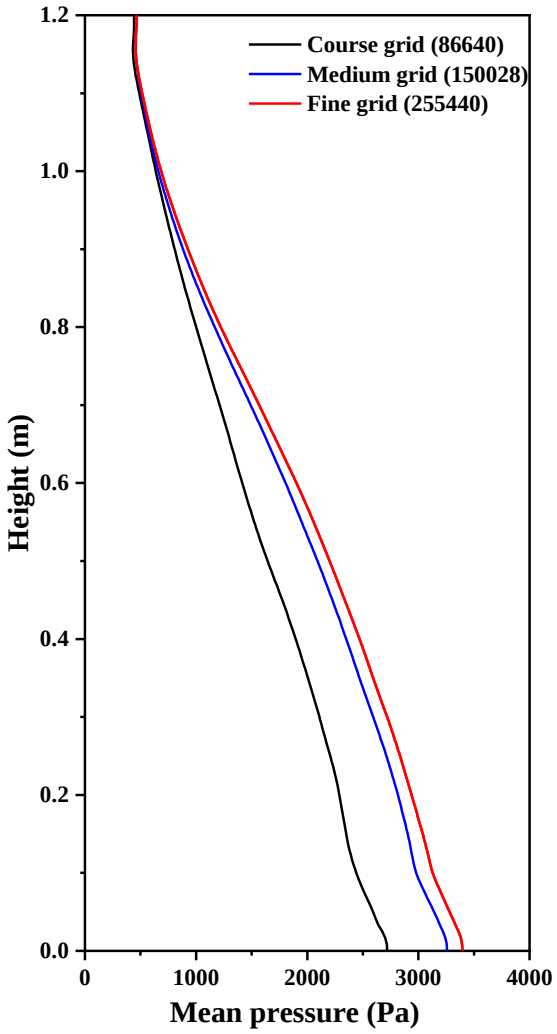

Fig 6.2. Time-averaged pressure profiles along the riser with different grid numbers.

Model validation

The TFM with the KTGF framework has been well validated in previous work towards a slugging bed and a chemical looping combustion system [297]. Hence, the validation work is briefly described below for completeness.

The first validation is based on a lab-scale slugging bed with a height of 0.76 m and an inner diameter of 76.2 mm. The upper part of the bed is an enlarged region with 0.3 m in height and 154 mm in diameter. Particles are initially packed in the bottom region of bed with a height of 0.4 m. The parameters for gas phase and particles in the validation case are the same with that in the experiment [247] The instantaneous solid volume fraction

and associated square-nosed slugs are qualitatively comparable to the experimental observations. Besides, the averaged intervals between two successive slugs are in line with the experimental data in a wide range of superficial gas velocities.

The second validation is based on a pilot-scale air reactor of a chemical looping combustion system [297]. The air reactor is composed of a combustor and a riser. The combustor is an enlarged-bottom column with 6-inch inner diameter and 25-inch height. The inner diameter of the upper riser is 2 inches, and the height is 161 inches. During the experiments, the gas flow with a low velocity but slightly larger than the minimum fluidization velocity is introduced into the combustor and the solid particles are fluidized with a bubbling fluidization regime presented. Because of the reduced cross-sectional area, the gas from the combustor enters the riser with a velocity over the terminal velocity where the solid particles show a fast fluidization regime. The effect of drag models on the simulation results was explored by comparing prediction results with experimental data qualitatively and quantitatively. It was found that the Syamlal-O'Brien drag model showed the best agreement with the experimental results for the time-averaged solid mass flow rate. Therefore, the Syamlal-O'Brien drag model is used in the present study.

Based on the above qualitative and quantitative validations, the current TFM-KTGF with Syamlal-O'Brien drag model is reasonable to study gas-solid hydrodynamics the CFB apparatuses.

Verification of Symmetry

In this work, the target is to ensure identical geometry and grids of the left and right side of this DRCFB system. For further verification of system symmetry, a gas stream is introduced into the empty DRCFB without solid particles and the gas flow behaviour is monitored inside the system. Similar verification method can be found in some literatures [286,288,293]. It is well received that when a fluid phase passes continuously at a steady state through identical parallel paths, the flow may distribute itself uniformly among the

multiple pathways [285,287]. For the DRCFB configuration in this work, the gas flow bifurcates at the top of the riser and then separates into two streams to enter the adjacent cyclones. For gases located at the centre of the riser, the flow direction is a stochastic process and the probability of gas entering different branches should be the same.

Fig. 6.3(a) shows the time-averaged gas velocity distribution throughout the full-loop DRCFB with the single gas phase introduced. In comparison, a symmetrical distribution of gas velocity can be recognized in both riser and external loops. The instantaneous values of the gas mass flow rate are monitored during the simulation and averaged between 30 s and 50 s, and the time-averaged values are 21.6 kg/s at both cyclone inlets. Besides, the flow behaviours in the DRCFB can be characterized and quantified by fast Fourier transform. From Fig. 6.3(b), it can be found by comparing the fluctuation signal that the dominant frequency and amplitude of gas mass flux are identical in both external loops. Therefore, based on the above results, the geometry and grids can be regarded as identical in the left and right external loops.

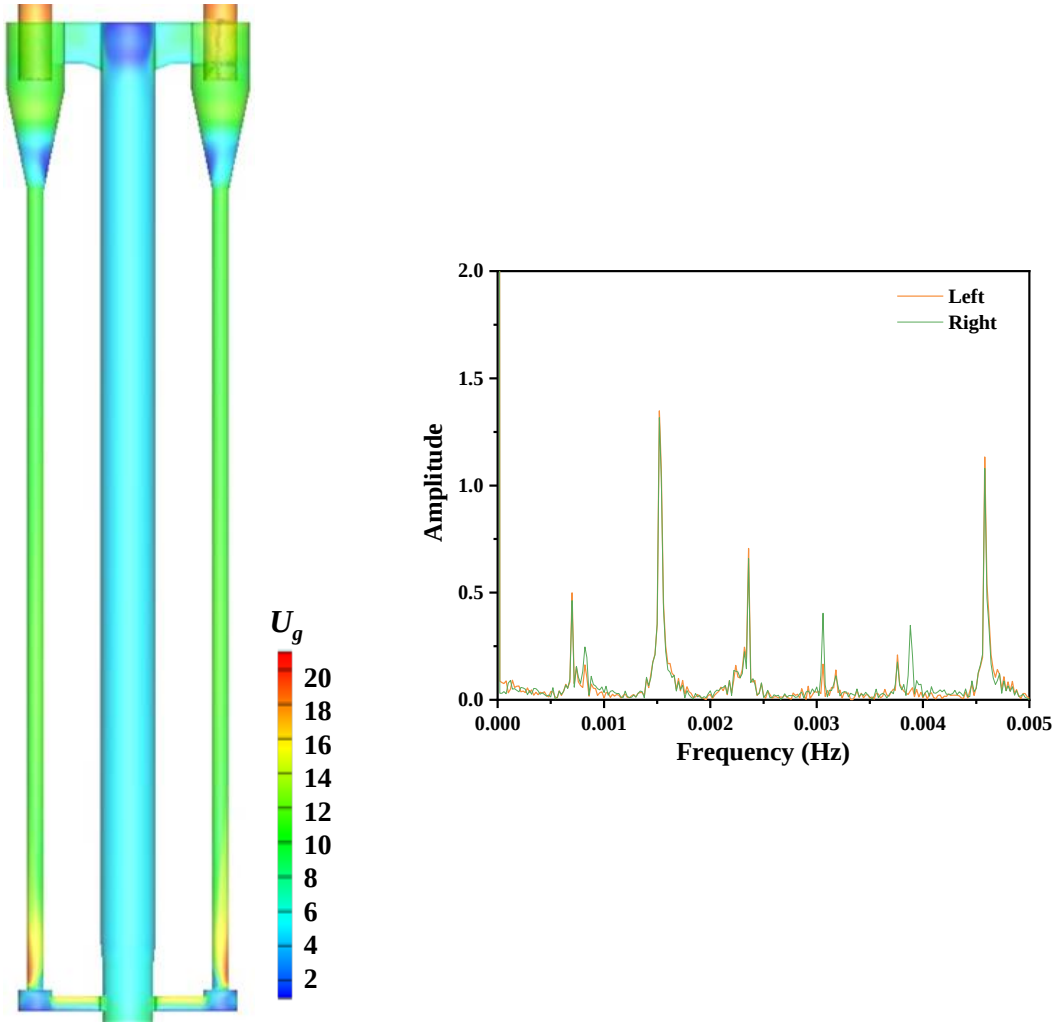

(a) (b)

Fig 6.3. Contours of the time-averaged gas velocity distribution throughout the full-loop system (a); frequency spectra of gas mass flow rate at the left and right cyclone inlet (b).

Maldistribution phenomenon

Fig. 6.4 shows the evolution of instantaneous solid volume fraction in the DRCFB. Initially, all particles are symmetrically packed on the bottom of the riser and two external loops (including a standpipe and an L-valve). Meanwhile, the gas flow is introduced from both sides of L-valve to circulate particles. From initial time to 10 s, the bed heights in the two external loops are symmetric. At around 10 s, the system reaches a breakpoint of balance where the solid mass distribution becomes slightly asymmetric. After this time, an asymmetric mass distribution continuously exists and the bed heights in both sides

keep going up and down. The results demonstrate that even in a symmetric DRCFB system, the unbalanced solid distribution inevitably appears. This non-uniformity phenomenon is commonly termed as maldistribution [298,299]. Moreover, the mass imbalance causes a deflection of the centre of gravity position of the device, which is unfavourable and unsafe for the long-time running of CFB systems.

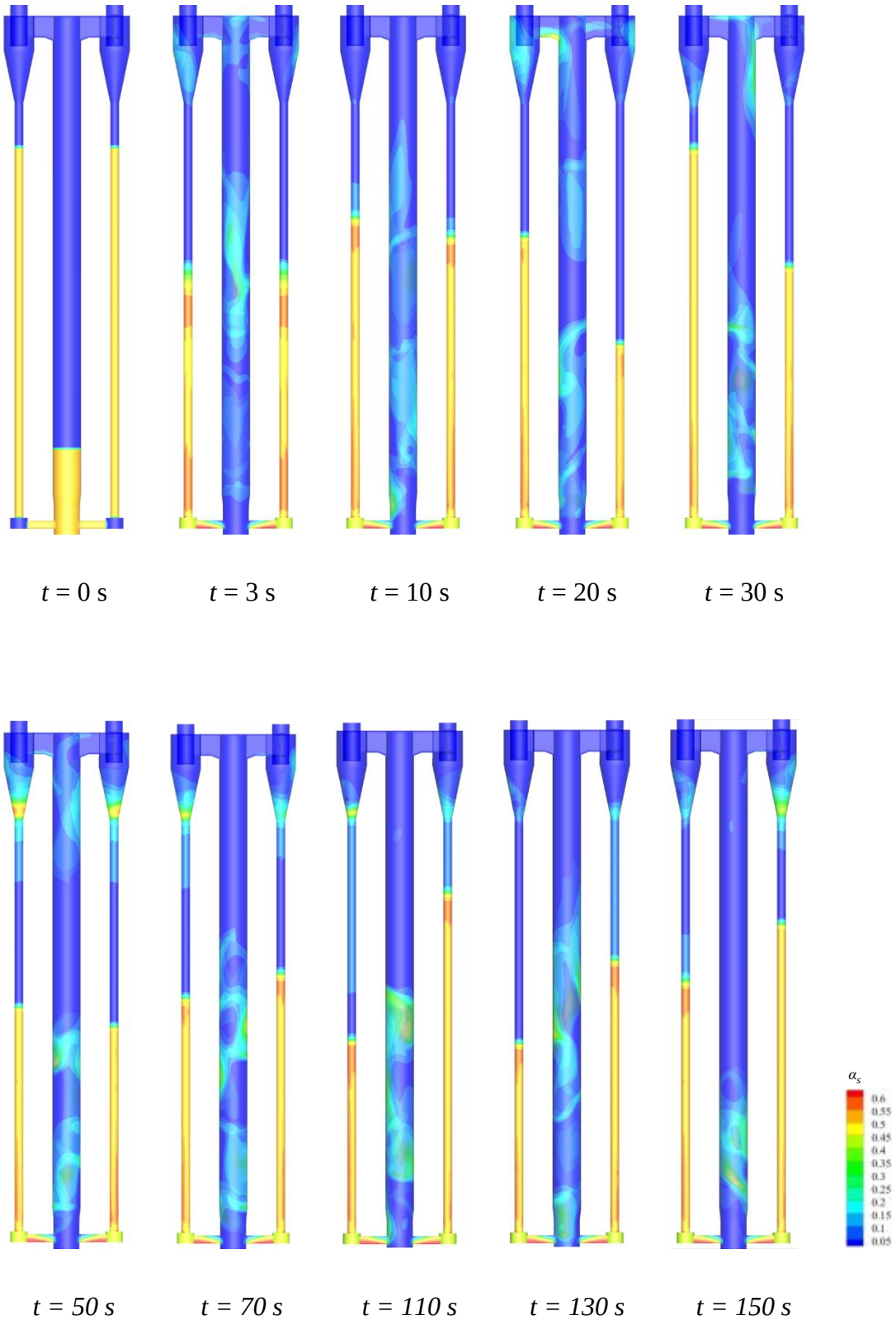

Fig 6.4. Contours of instantaneous solid volume fraction in the DRCFB.

Fig. 6.5(a) shows the time evolution of bed inventory in the external loops and riser. It is noted that the maldistribution phenomenon of bed inventory in the left and right external loops exists in most of the simulation time. Meanwhile, the bed inventory in the riser is relatively stable and slightly fluctuates around an average value, which means the total mass in two external loops is stable and just the proportion of mass continuously changes. In order to quantitatively quantify the maldistribution between two external loops, the relative deviation (*Dev*) of bed inventory is proposed to define the degree of maldistribution:

$$\mathrm{Dev} = \frac{|m_l - m_r|}{m_l + m_r} \tag{6-6}$$

where m_l and m_r are the mass in the left and right external loops, respectively. Dev is a number between 0 and 1. The value of 0 represents the solid mass is same in both external loops, which is an ideal distribution. The value of 1 represents all particles transported into one external loop and the other one is empty, which is the worst situation. Fig. 6.5(b) describes the relative deviation of bed inventory between the left and right external loops. Firstly, the relative deviation gradually increases over time and reaches a peak during 20 s to 30 s. Then, the relative deviation decreases and reaches a new balance during 40 ~ 50 s. Subsequently, the relative deviation rises and falls alternately. The process described as above indicates that the DRCFB system shows a significant maldistribution phenomenon and has a self-balancing ability to some extent at the same time.

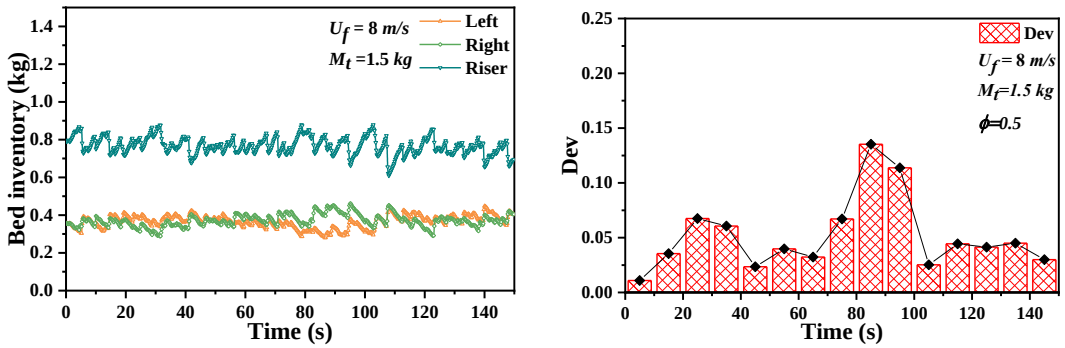

(a) (b)

Fig 6.5. Time-evolution profiles of bed inventory in the external loops and riser (a); and relative deviation (Dev) of bed inventory between the left and right external loops (b).

As seen in Fig.6.6(a), particle flow changes from the vertical direction to the horizontal direction at the top region of the riser and enters the cyclone. Due to the restriction effect of the cyclone, the drag force on the particles is not in the gravitational direction. Thus, the particles spin down along the inner cyclone surface under the influence of gravity. The solid velocity decreases during the falling procedure, as shown in Fig.6. 6(b). By comparison from Fig. 6.6(a, b, c), it can be found the higher solid and gas velocity occurs in the right side which is opposite to the direction of higher solid volume fraction. This phenomenon can be explained that as more particles enter one side, more gas will enter the other side. As a result, the velocity of gas increases at the cyclone inlet with the constant area and the velocity of the particle increase due to drag force. A similar phenomenon can be found in some experimental works [171,284]. The distributions of solid volume fraction, and gas and solid velocity are apparently different in two identical external loops and the asymmetric hydrodynamic behaviours are observed.

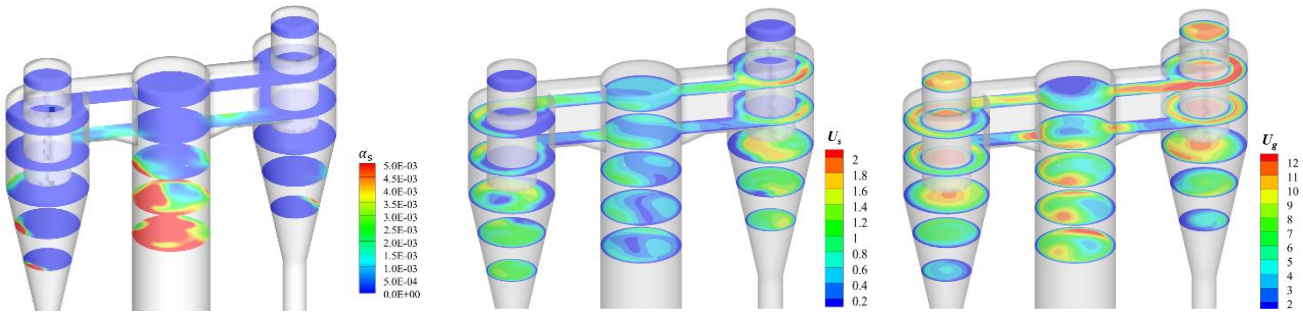

(a) (b) (c)

Fig 6.6. Instantaneous distribution of gas-solid flows at the top section of the DRCFB at t = 30 s: solid volume fraction (α_s) (a); solid velocity (U_s); (c) gas velocity (U_g) (b).

Fig. 6.7(a) shows the profiles of solid flux sampled at the cyclone inlet of the left and right external loops. The solid flux has drastic fluctuations over the entire simulation time and the maximum value alternates in these two cyclone inlets. The solid flux on both sides shows a significant difference and the accumulation of these differences over time leads to the mass maldistribution of the system. The pressure drop over a cyclone is a major performance parameter reflecting the rate of energy dissipation [282,290,300,301]. Fig. 6.7(b)(c) illustrates the pressure drop in the cyclone as a function of solid flux. The results show that the pressure drop of the cyclone experiences a non-linear change by analysing the trend of scatters under the different values of solid fluxes. When the solid flow is dilute, the pressure drop of cyclone decreases with the increase of solid flux due to the drag reduction effect [300] until a turning point is reached. After this point, the pressure drop of cyclones increases with the augment of solid flux. This phenomenon is consistent with experimental observations [284,300,301]. Therefore, the different solid fluxes at the left and right cyclone inlets lead to different pressure drops over two cyclones which reduce the overall performance of the cyclone and severely limit the power output of the whole system.

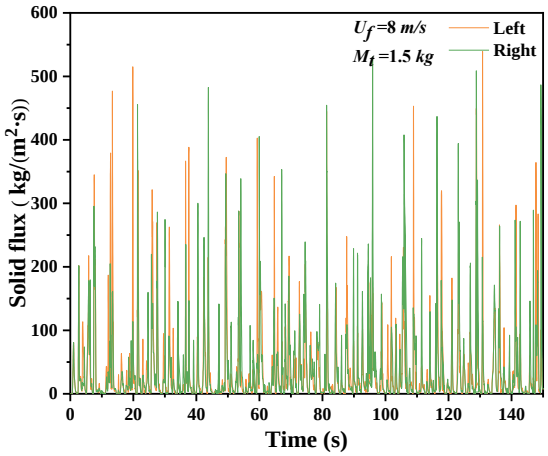

(a)

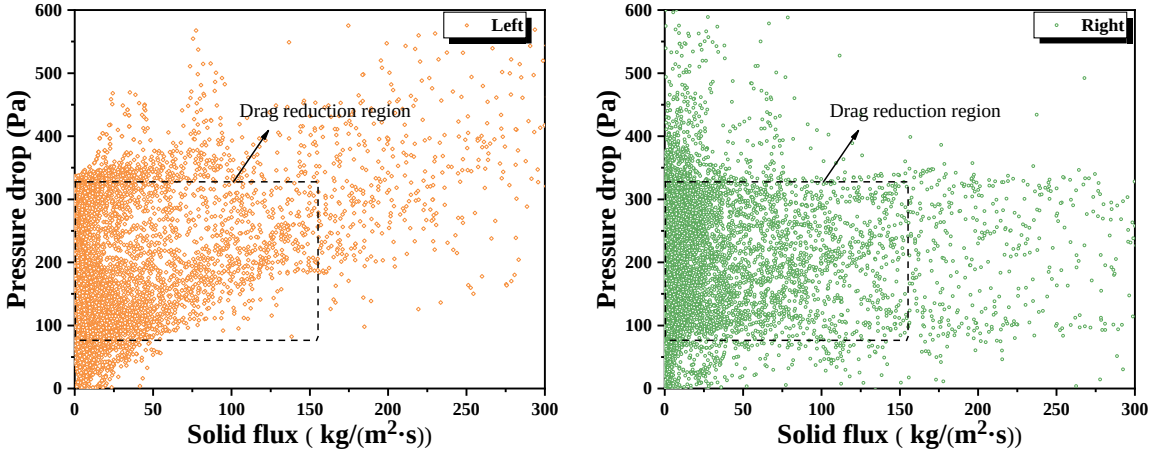

(b) (c)

Fig 6.7. Comparison of solid flux at the cyclone inlet (a); scatter plot of the pressure drops over the left (b) and right (c) cyclones as a function of solid flux.

Fig. 6.8 shows the instantaneous distribution of solid volume fraction, solid velocity, and gas velocity in various cross-sections of the bottom section of the DRCFB. Particles separate from the cyclone deposit with a slowly downward velocity and then form a packed bed in the standpipe with the aim to circumvent gas bypassing. Part of the aeration gas drives particles to transport into the riser via the horizontal component of the L-valve and the rest of aeration gas lose particles packed in the vertical component of the L-valve. By comparing the solid volume fraction and gas-solid velocities at the bottom region of the DRCFB, it is noted that there is no significant difference in the flow pattern at the bottom of the external loops. However, a significantly uneven distribution can be found in the lower part of the riser section.

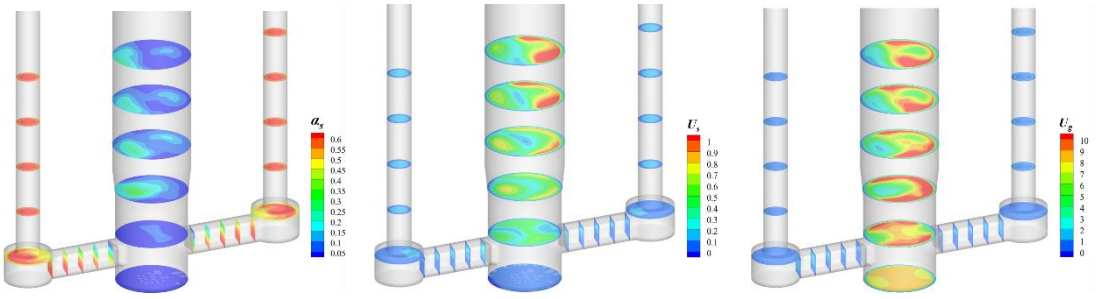

(a) (b) (c)

Fig 6.8. Instantaneous distribution of gas-solid flows at the bottom section of the DRCFB at t = 30 s: solid volume fraction (α_s) (a); solid velocity (U_s); (c) gas velocity (U_g) (b).

Fig. 6.9(a) shows the time-evolution profiles of the solid flux at the L-valve outlet. The solid flux is generally stable over time while it is slightly larger in the side with a larger bed inventory. Increasing the height of particles in the standpipe causes the increase of pressure at the bottom of the standpipe. Larger pressure causes more solid particles to be delivered back to the bottom of the riser. Fig.6.9(b) illustrates the pressure drop over the horizontal section of L-valve as a function of solid flux. It is noted that the solid flux is proportional to the pressure drop, which indicates that the standpipe and L-valve have an automatic control ability [302]. Moreover, the fluctuation amplitude of solid mass flux at the cyclone inlet is more intense than that at the outlet of the L-valve. Therefore, the change of bed inventory in the two external loops mainly depends on the solid flux at the cyclone inlet.

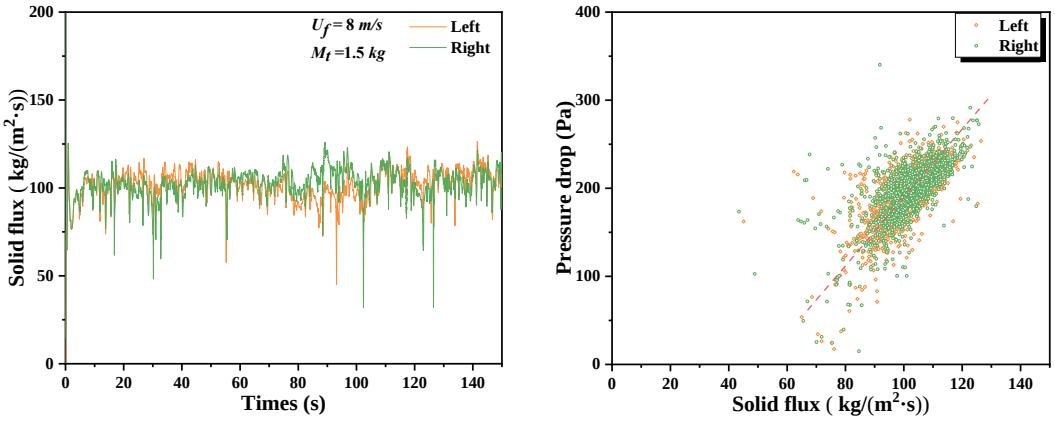

(a) (b)

Fig 6.9. Comparison of solid flux at the L-valve outlet (a); scatter plot of the pressure drops over the L-valve as a function of solid flux (b).

Since the gas flow is uniformly distributed at the bottom of the riser, the flow pattern in the riser is mainly influenced by the flow resistance caused by the uneven distribution of solid volume fraction and solid velocity. Taking the results at 30 s as an example, the distributions of pressure and solid volume fraction along the central line of the left half and right half of the riser are illustrated in Fig. 6.10 (a, c). At t = 30 s, more particles are accumulated on the left side than the right side of the DRCFB, which leads to a lateral pressure drop (Fig. 6.10 (a, c)). The lateral pressure gradient between two sides generates a lateral gas flow from the left to the right side and then leads to a lateral solid flow due to the drag force. Therefore, particles are transported to the right side until the lateral pressure gradient is eliminated. However, due to the inertia of solid particles, particles will continue to be transported to the right side, which causes a new lateral pressure gradient and drives the solid particles back to the left side, as shown in Fig. 6.10 (b). From Fig 6.10 (a, c), it is noted that the lateral pressure gradient and solid clusters alternate between left and right sides below 0.5 m and particles continue to move laterally due to the inertia in the upper region of the riser. Besides, the difference of pressure near the height of the cyclone inlets indicates that the cyclone re-distributes gas-solid flows. The lateral pressure gradient between the left and right side of the riser indicates that there are

two pressure balance loops in the DRCFB. This lateral pressure gradient in the riser and near the cyclone inlets are generally thought to account for the maldistribution of the DRCFB system [284,303].

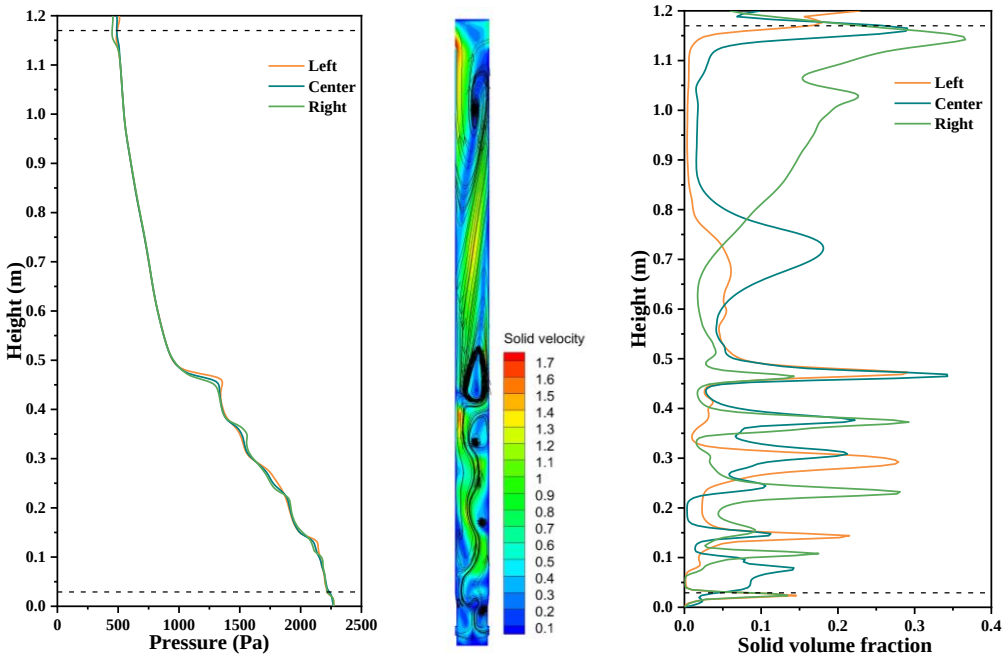

(a) (b) (c)

Fig 6.10. Pressure profiles along the central lines of the left half and right half of the riser at t = 30 s (a); distribution of solid velocity in the riser at t = 30 s (b); solid volume fraction profiles along the central lines of the left half and right half of the riser at t = 30 s (c).

Effect of gas inlet velocity

Fig. 6.11 shows the time-evolution profiles of bed inventory in the external loops and riser with the wall roughness and total bed inventory fixed. It can be found that increasing gas inlet velocity gives rise to the increase of solid carrying capacity in the riser. Specifically, more particles are carried from the riser to the cyclone and then to the standpipe, causing the increase of packed bed inventory in both standpipes. Fig. 6.12 shows the time-evolution of solid flux at the cyclone inlet and L-valve outlet. It is noted

that the fluctuation amplitude of solid flux decreases at the cyclone inlet but increases at the L-valve with the increase of gas inlet velocity in the riser, because higher pressure at the top of L-valve causes more solid particles to return to the riser. The combination of multiple sections in the DRCFB results in the different mass distribution for different operating conditions.

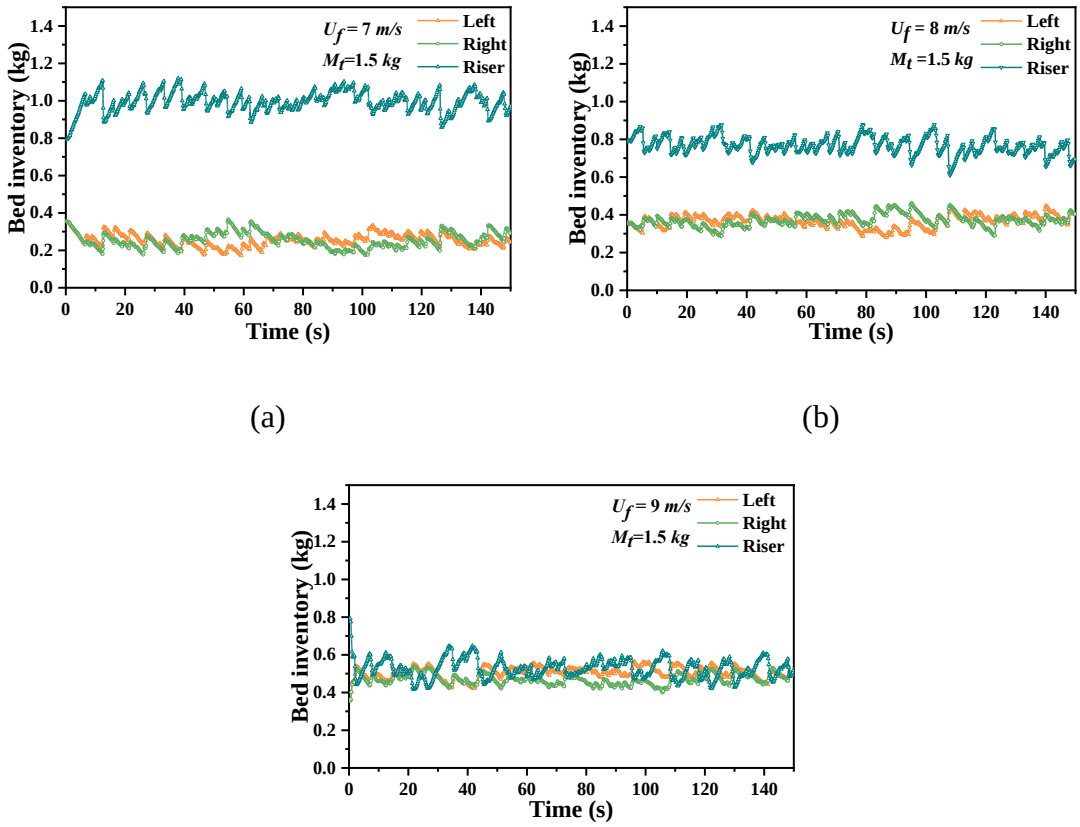

Fig 6.11. Time-evolution profiles of bed inventory in the external loops and riser at different gas inlet velocities: U_f= 7 m/s (a); U_f= 8 m/s (b); U_f= 9 m/s (c).

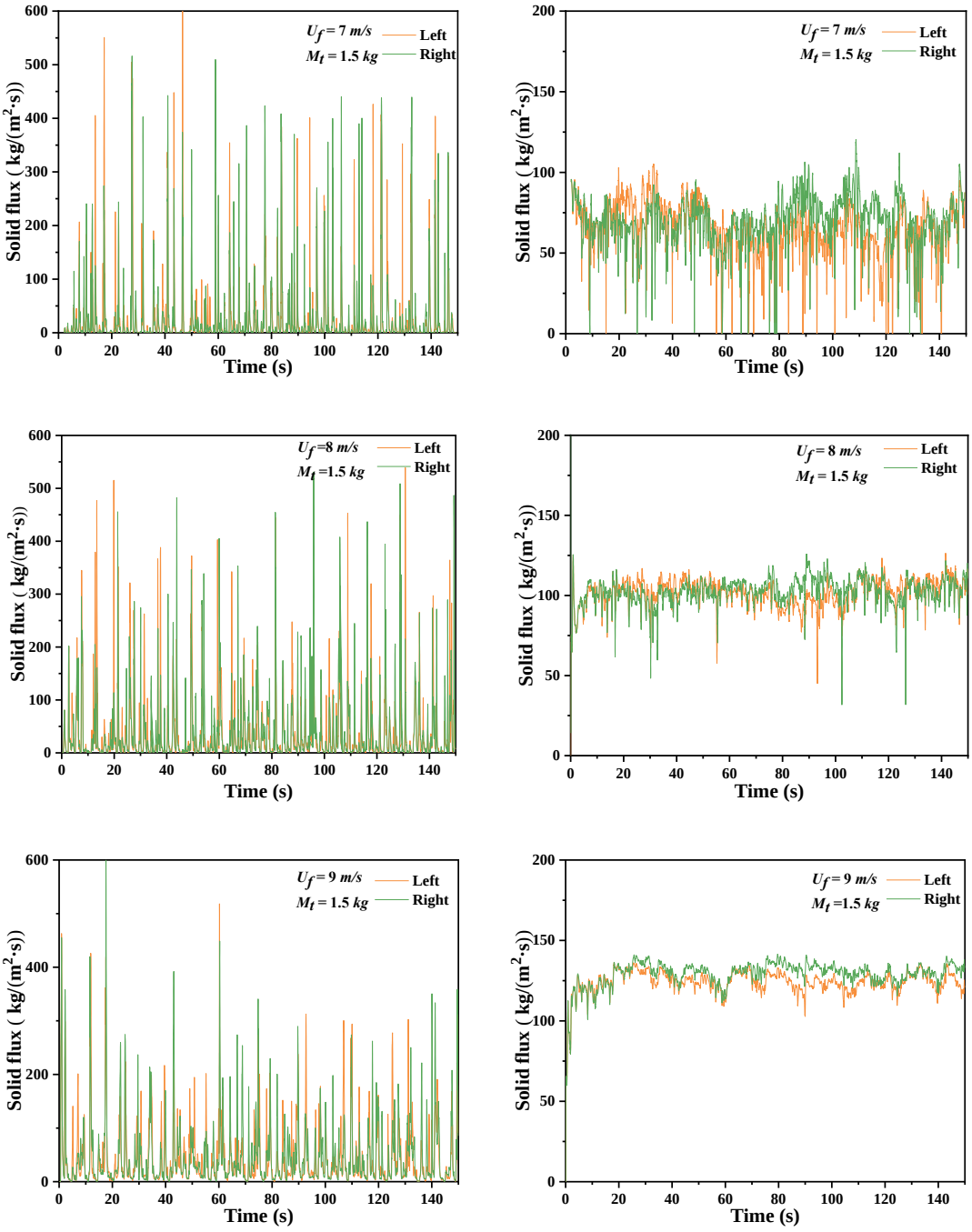

(a) (b)

Fig 6.12. Time-evolution profiles of solid flux at different gas inlet velocities: cyclone inlet (a); L-valve outlet (b).

The particle clusters lead to the heterogeneous solid distribution in the riser, which strongly affects the fluctuation of pressure. Therefore, the pressure fluctuation in a fluidized bed provides potential information about what happens in a specific fluidization

regime. To investigate the influence of gas inlet velocity on solid maldistribution in the DRCFB, the Fourier spectral analysis of pressure drop in the external loops at different gas inlet velocities is compared, as shown in Fig. 6.13(a). The dominant frequency of pressure drops over the loop seal with low gas inlet velocity (U_f = 7.0 m/s) is 0.00795 Hz. As the gas inlet velocity increases, both the dominant frequency and the amplitude of the fluctuation step down gradually. Nevertheless, due to the status of packed bed in the standpipe, the frequency of pressure drop is relatively low (all < 0.01 Hz) when compared with other fluidization regimes. By comparing Fig. 6.14, the relative deviation of the bed inventory in both sides decreases with the increase of gas inlet velocity. In other words, the mass distribution becomes more uniform with the increase of gas inlet velocity to some extent.

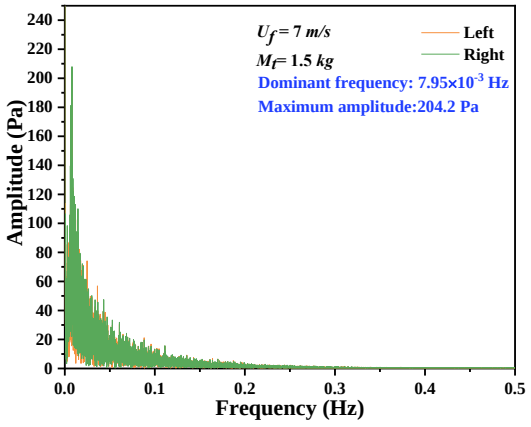

(a)

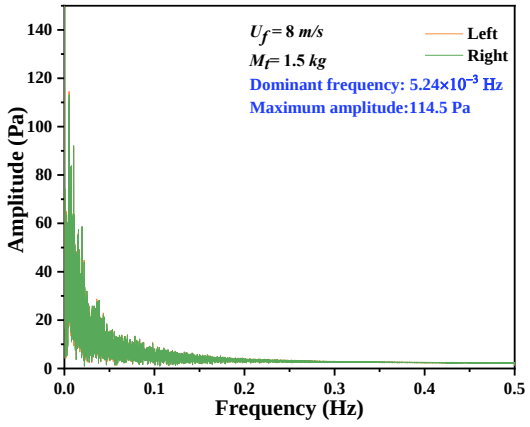

(b)

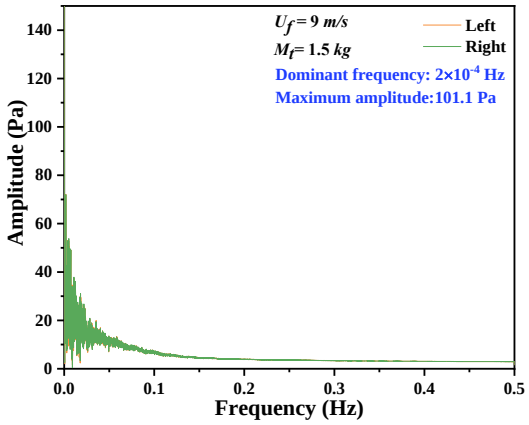

(c)

Fig 6.13. Fourier spectral analysis of pressure drop in the external loops region at different gas inlet velocities: U_f = 7 m/s (a); U_f = 8 m/s (b); U_f = 9 m/s (c).

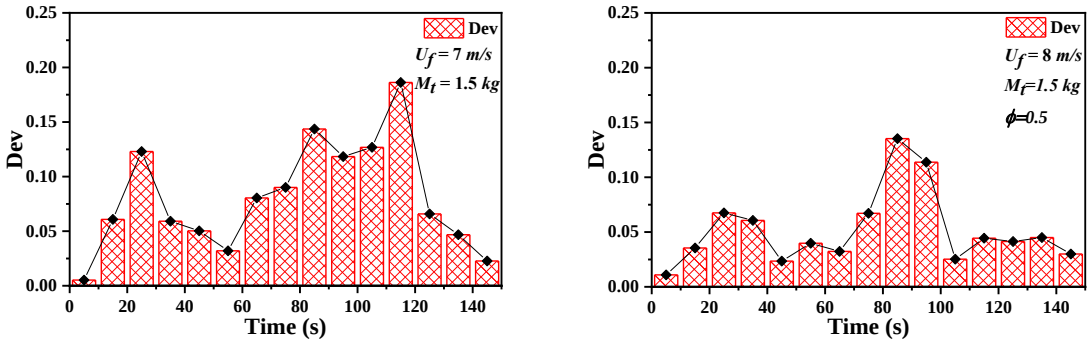

(a) (b)

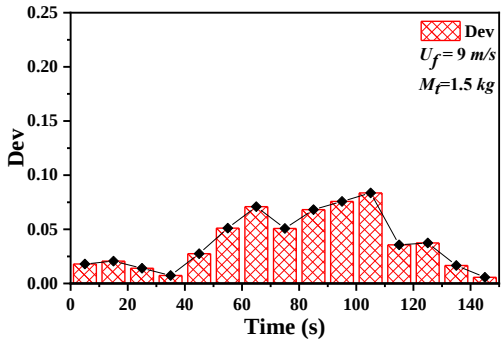

(c)

Fig 6.14. Relative deviation (Dev) of bed inventory between left and right external loops at different gas inlet velocities: U_f = 7 m/s (a); U_f = 8 m/s (b); U_f = 9 m/s (c).

Effect of solid inventory

Fig. 6.15 shows the time-evolution profiles of bed inventory in two external loops and riser with the gas inlet velocity and wall roughness fixed. It can be found that the bed inventory in the riser is relatively stable (around 0.7 ~ 0.9 kg) without significant deviations as the total solid inventory increases. The difference in mass distribution is mainly on both external loops. Enlarging the total solid inventory increases the packed bed inventory in both standpipes.

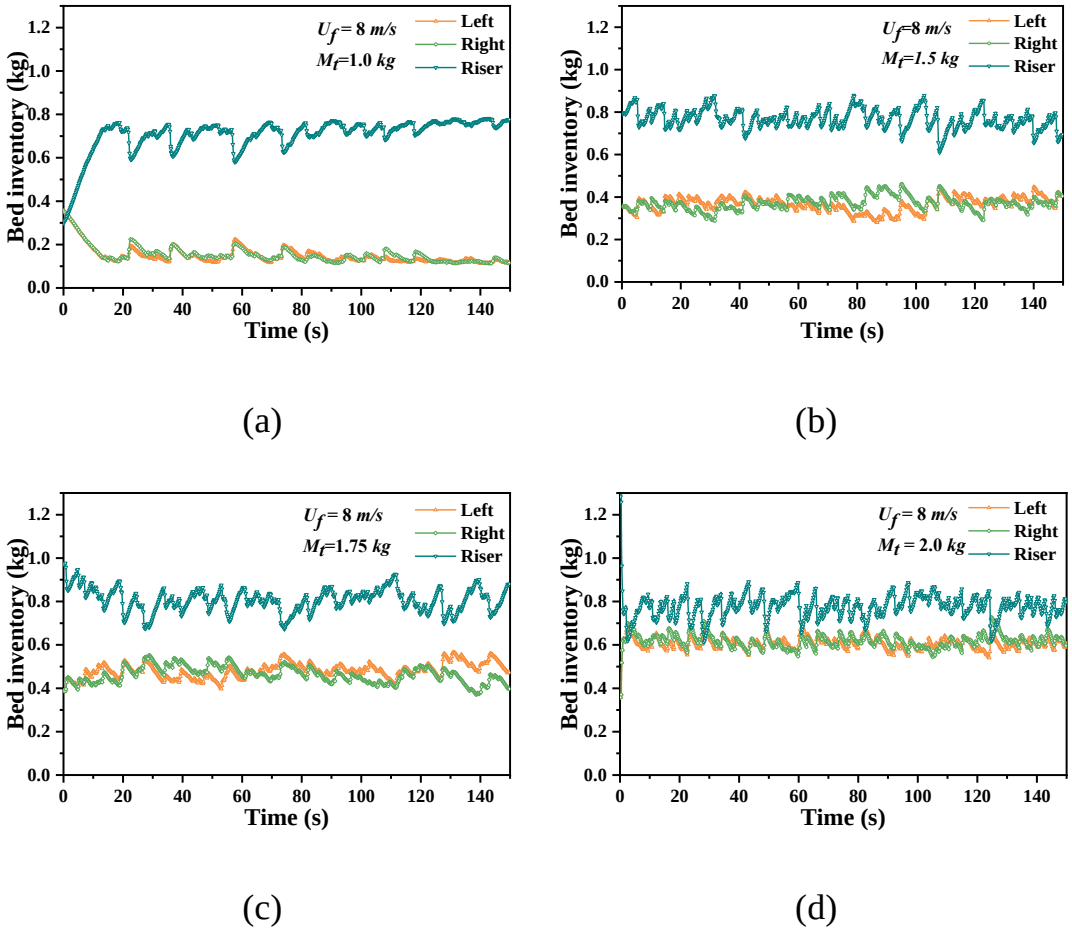

Fig 6.15. Time-evolution profiles of bed inventory in external loops and riser at different total solid inventories: M_t = 1.0 kg (a); M_t = 1.5 kg (b); M_t = 1.75 kg (c); M_t = 2.0 kg (d).

Fig. 6.16 shows the time-evolution profiles of solid mass fluxes at the cyclone inlet and L-valve outlet. It is noted that the solid flux increases at both the cyclone inlet and the L-valve outlet with the increase of total solid inventory. When the total solid inventory is 1 kg, the bed inventories in both external loops are approximately 0.1~0.2 kg. The solid flow has a different behaviour comparing with other cases at the outlet of the L-valve. This is because the solid inventory is not enough to form a seal at the structure of the L-valve which leads to the fluidizing gas entered from the riser inlet flowing into the external loops, causing the gas leakage. The gas leakage, if sufficient, affects the stability and intensity of the inner vortex of the cyclone and re-entrains separated particles into the inner core vortex of the cyclone, thus reducing the separation performance and possibly increasing erosion in the cone area [304]. Therefore, it is necessary to avoid gas leakage during the operation of the DRCFB by keeping a certain bed height in the standpipe.

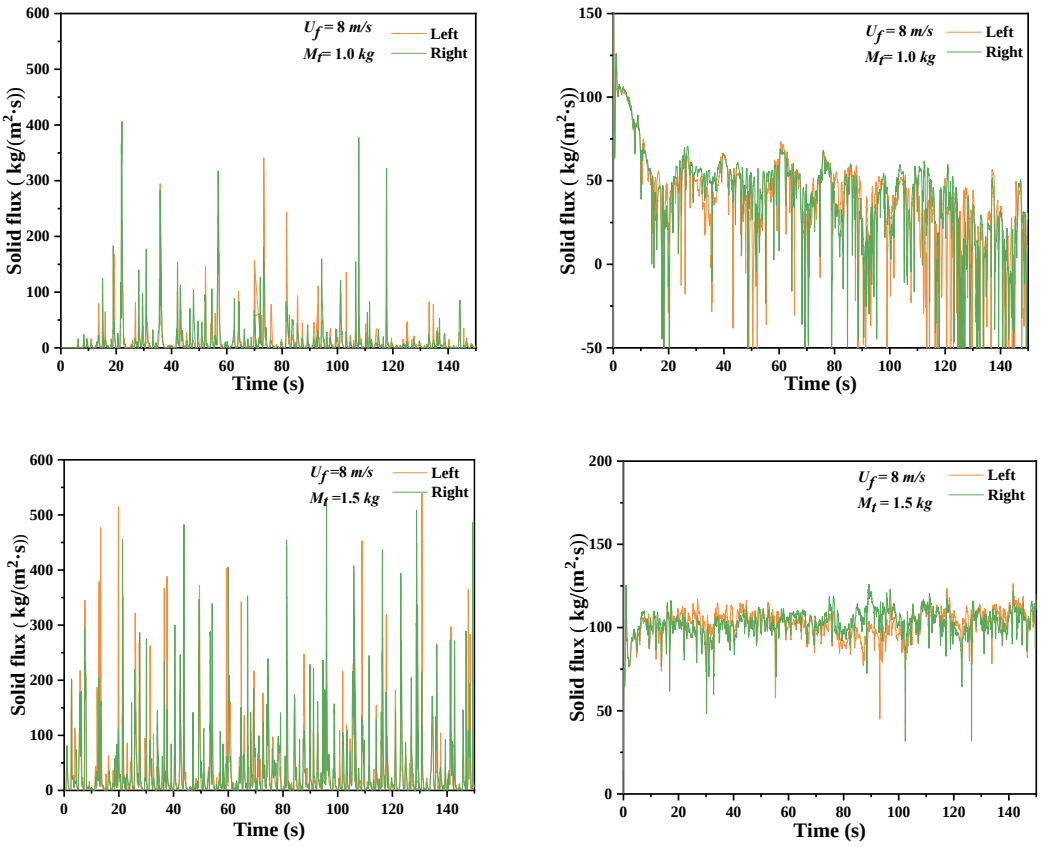

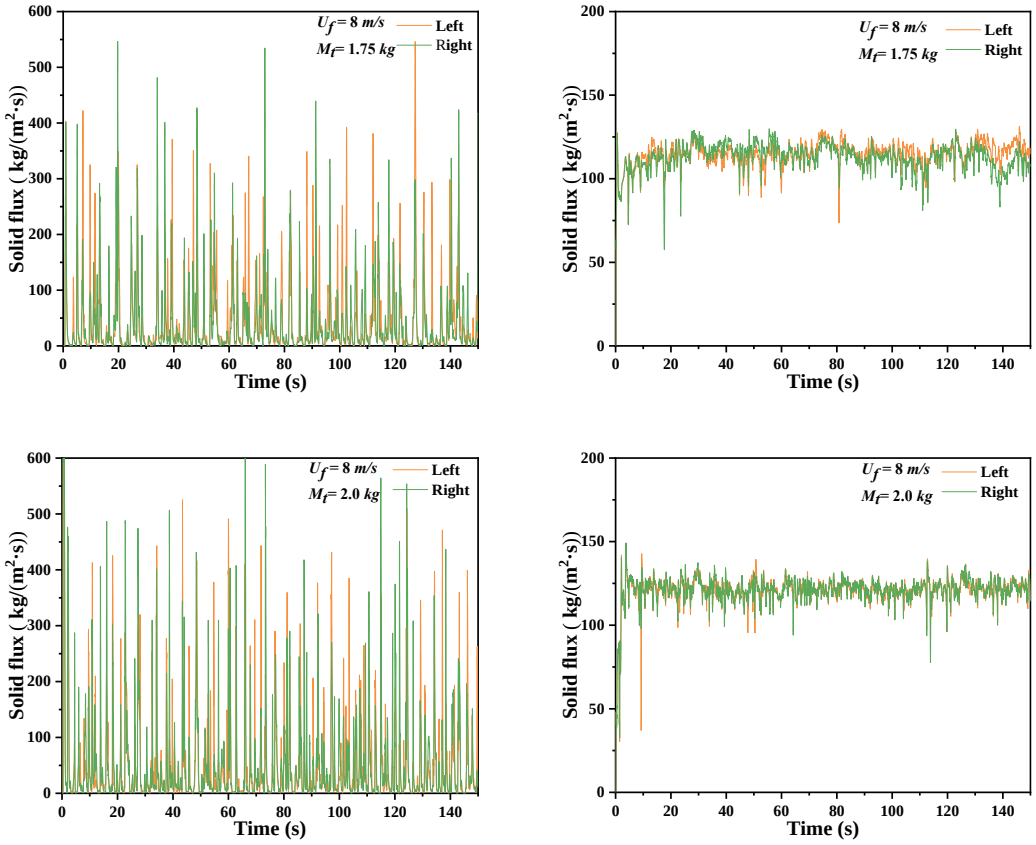

(a) (b)

Fig 6.16. Time-evolution profiles of solid flux at different total solid inventories: cyclone inlet (a); L-valve outlet (b).

As shown in Fig. 6.17, a high dominant frequency of pressure drop over the loop seal with less solid inventory (M_t = 1.0 kg) can be observed, which is caused by solid fluidization in the L-valve where the bed height is not enough to form a loop seal to avoid the gas leakage. When the total solid inventory is larger, there is only one dominant frequency can be observed. With the increase of total solid inventory, the dominant frequency is very similar, but the maximum amplitude of the fluctuation increases. Meanwhile, the amplitude of the relative deviation of the bed inventory in both sides decreases with the increase of total solid inventory (Fig. 6.18). A negative correlation is observed between the total solid inventory and solid balance distribution.

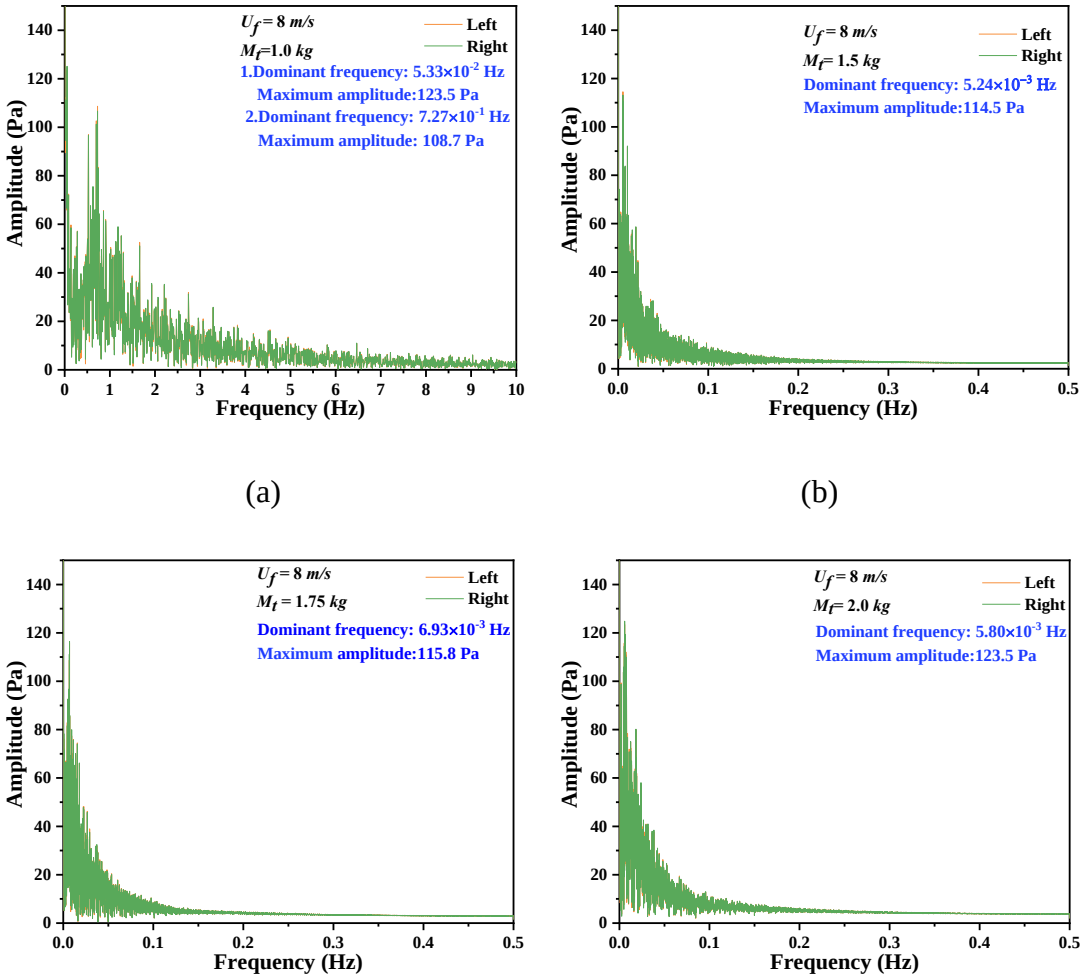

Fig 6.17. The Fourier spectral analysis of pressure drop in the loop seal at different total solid inventories: M_t = 1.0 kg (a); M_t = 1.5 kg (b); M_t = 1.75 kg (c); M_t = 2.0 kg (d).

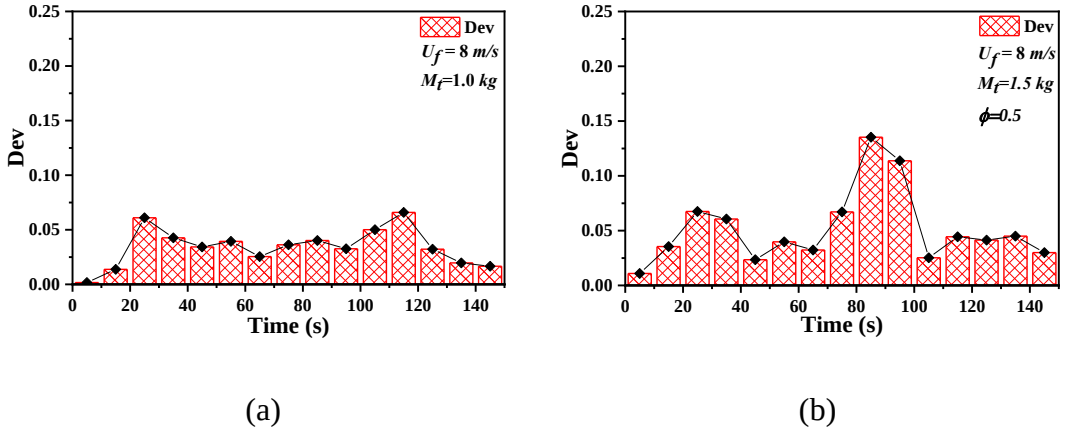

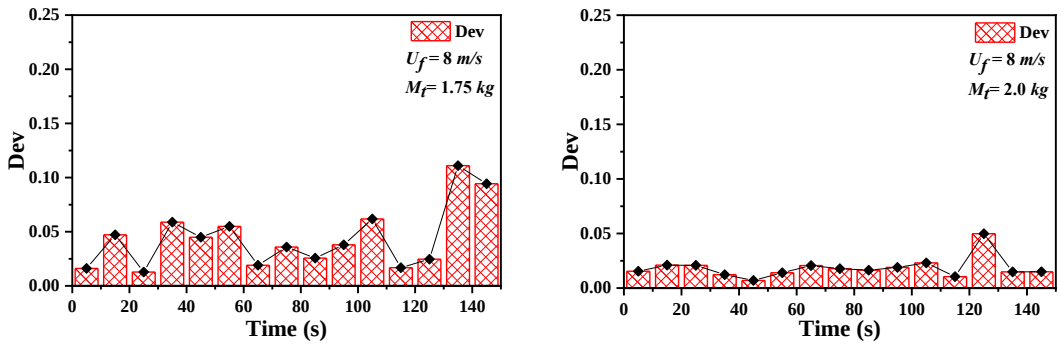

(c) (d)

Fig 6.18. The relative deviation (Dev) of bed inventory between left and right external loops at different total solid inventories: M_t = 1.0 kg (a); M_t = 1.5 kg (b); M_t = 1.75 kg (c); M_t = 2.0 kg (d).

Effect of wall function

The specularity coefficient (ϕ) is a critical parameter to describe the roughness of the reactor walls, which is difficult to determine. The value of the specularity coefficient commonly varies between 0 and 1. In this study, three values of 0, 0.5 and 1.0 are specified to account for different slip boundary conditions to compare the influence of different wall roughness on solid maldistribution.

Fig. 6.19 shows the time-evolution profiles of the bed inventories in two external loops and riser with the gas inlet velocity and total bed inventory fixed. It can be found that the solid carrying capacity in the riser increases with the specularity coefficient increases. More particles are carried from the riser to the cyclone and then to the standpipe, causing the packed bed inventory in both standpipes to increase.

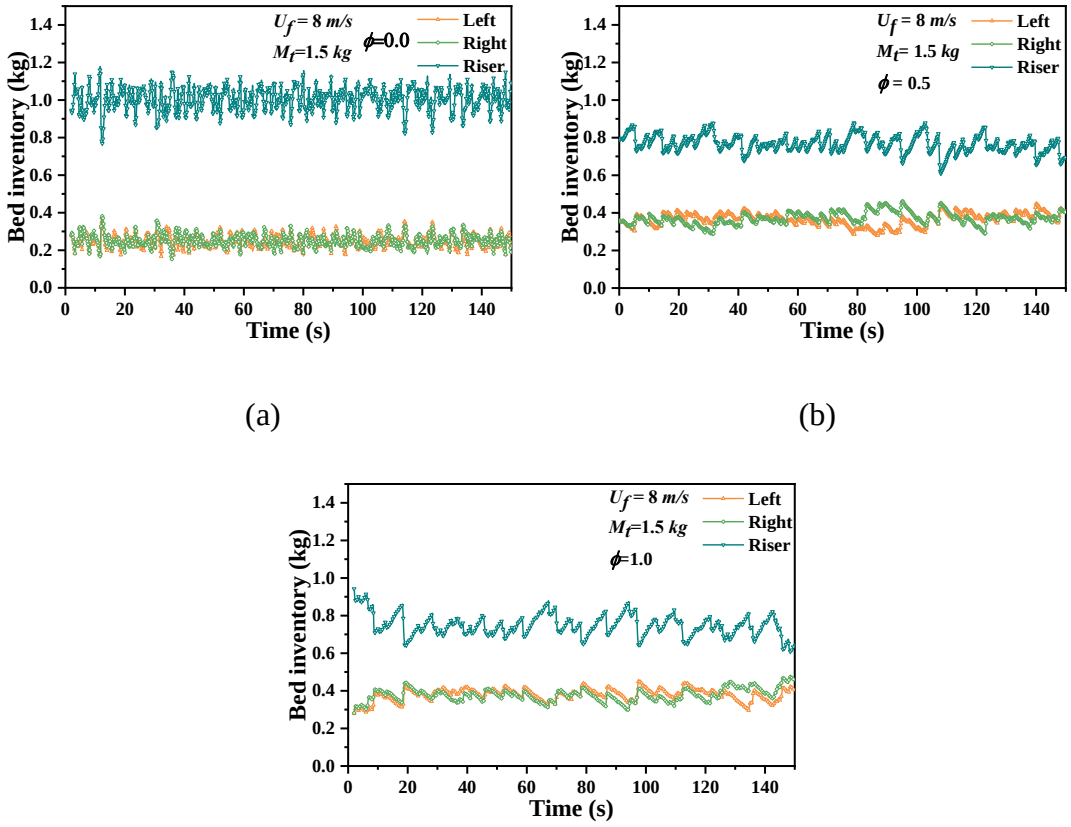

Fig 6.19. Time-evolution profiles of bed inventory in the loop seal and riser at wall roughness: ϕ = 0.0 (a); ϕ = 0.5 (b); ϕ = 1.0 (c).

Fig. 6.20 shows the time-evolution profiles of solid fluxes at the cyclone inlet and L-valve outlet. It shows that the solid flux decreases at the cyclone inlet and the L-valve with the increase of the specularity coefficient. The solid distribution under different operating conditions is caused by the comprehensive function of all parts of the system.

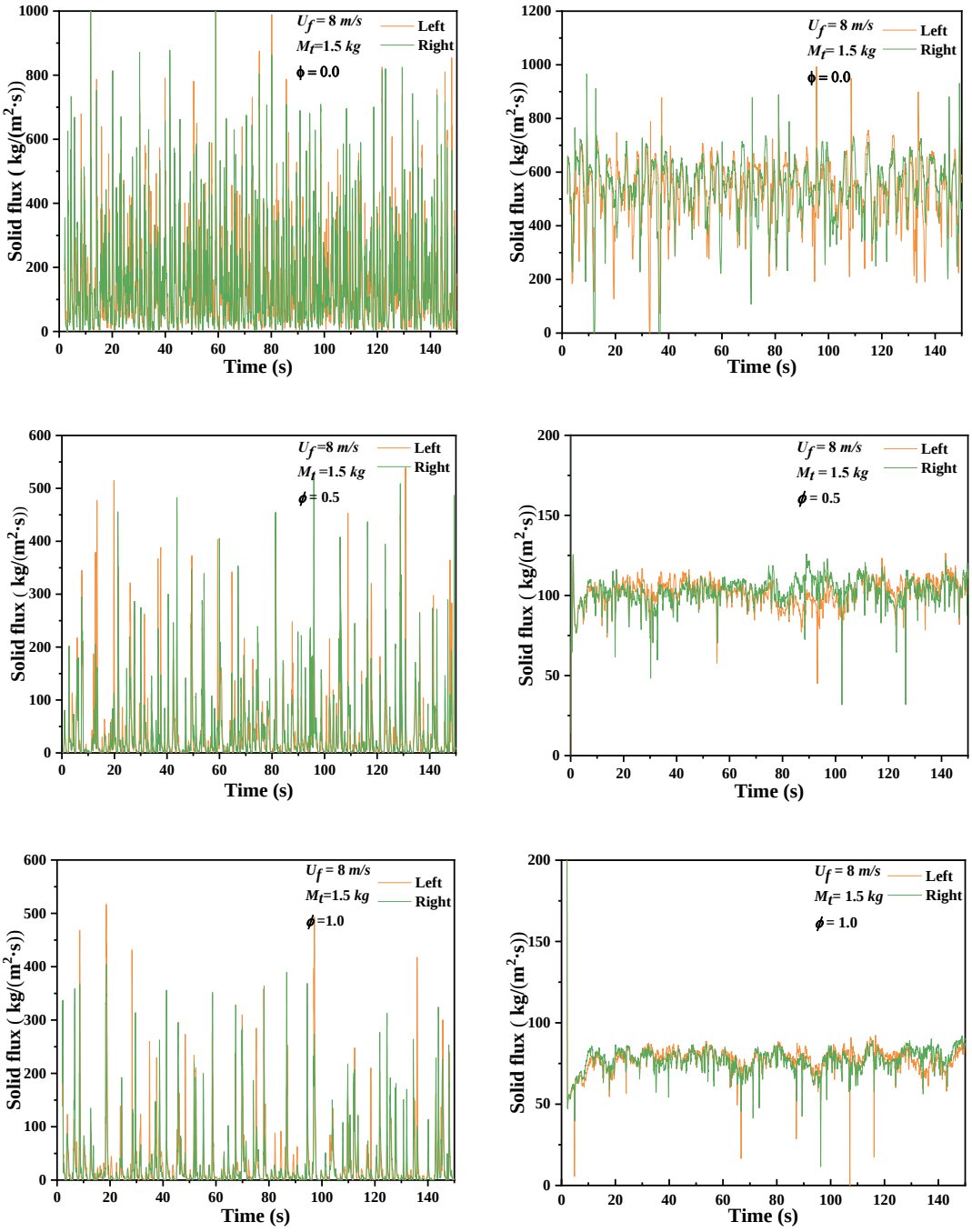

(a) (b)

Fig 6.20. Time-evolution profiles of solid mass flux at different wall roughness: cyclone inlet (a); L-valve outlet (b).

As shown in Fig. 6.21, it can be found that the dominant frequencies are very similar at different specularity coefficients and the maximum amplitude gradually increases. The relative deviations of bed inventory between two external loops are also very

approximated except for occasional high deviation (Fig. 6.22). It indicates the wall roughness greatly affects the solid flux in the full-loop DRCFB unit, but it has an insignificant impact on the degree of the mass maldistribution.

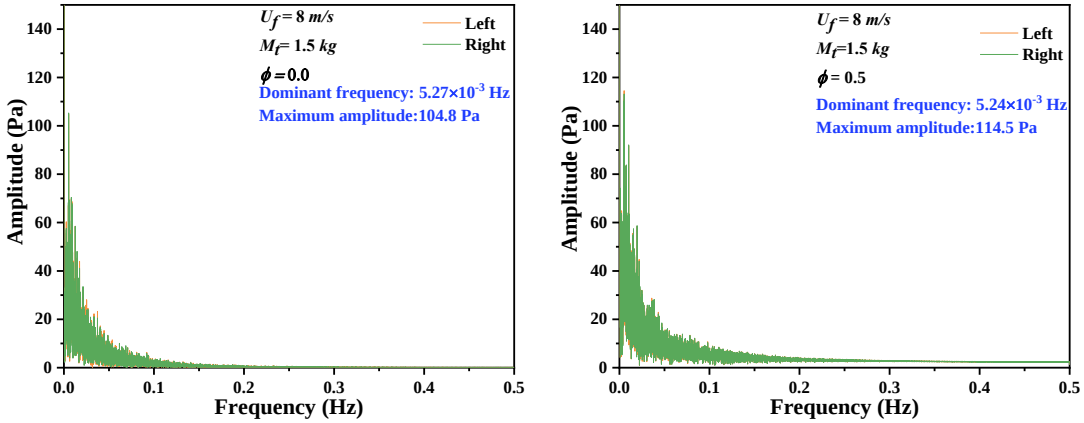

(a) (b)

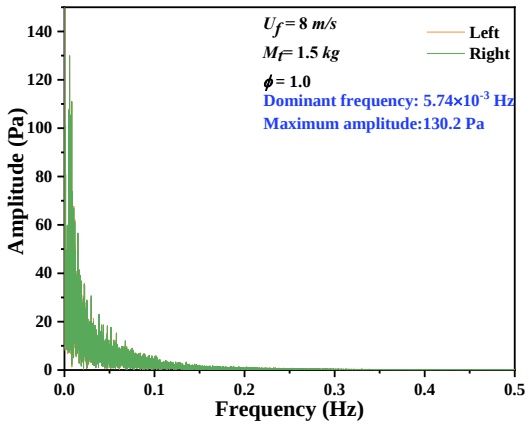

(c)

Fig 6.21. The Fourier spectral analysis of pressure drop in the external loops region at different wall roughness: ϕ = 0.0 (a); ϕ = 0.5 (b); ϕ = 1.0 (c).

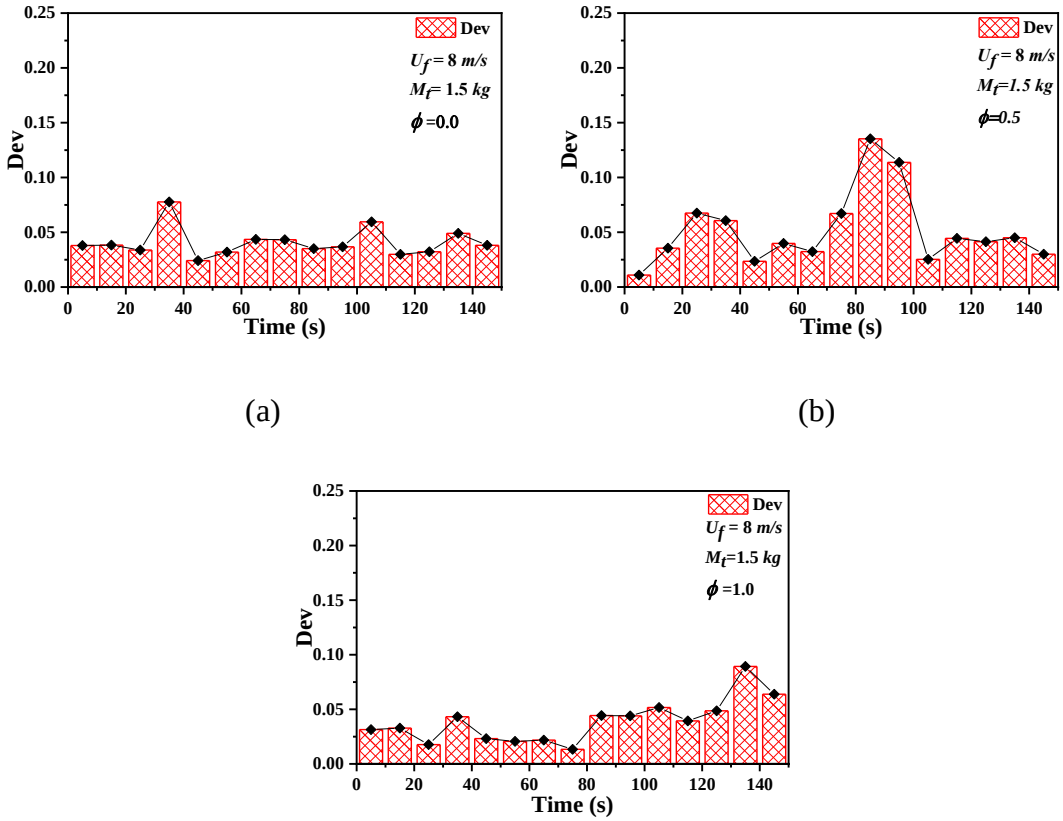

Fig 6.22. The relative deviation (Dev) of bed inventory between left and right external loops at different wall roughness: ϕ = 0.0 (a); ϕ = 0.5 (b); ϕ = 1.0 (c).

6.1.4 Conclusions

In this work, the characteristics of the maldistribution phenomenon in a symmetric dual-side refeed circulating fluidized bed (DRCFB) is numerically studied by a multi-fluid model based on the Eulerian-Eulerian framework. The influence of solid maldistribution on the performance of the cyclone, standpipe, L-valve, and riser in the DRCFB is discussed. Moreover, the effects of gas inlet velocity, solid inventory, and wall function on the degree of maldistribution are comprehensively explored. Based on the numerical results, the main conclusions can be drawn as follows:

(1) The solid maldistribution is an inevitable phenomenon in a DRCFB system with dual identical geometry configuration and operating parameters in each side.

(2) The maldistribution of solid mass in the DRCFB unit causes a deflection of the centre of gravity position of the device and the drastic difference of solid fluxes at the cyclones to lower the overall performance of cyclone.

(3) The solid mass flux at the L-valve outlet is proportional to the bed inventory in the standpipe. The standpipe and L-valve have an automatic control ability to some extent.

(4) This lateral pressure gradients in the riser and near the cyclone inlets are generally recognized as the main reason resulting in the maldistribution of the full-loop DRCFB system

(5) The relative deviation of the bed inventory in both external loops decreases with the increase of gas inlet velocity and total solid inventory. However, it is not sensitive to the wall roughness.

(6) The relative deviations of bed inventory in both external loops do not show a direct relationship with the transient changes of flow by analysing the pressure drop signal.

6.2 Investigation of the Non-uniformity in a Full-loop Circulating Fluidized Bed with Symmetrical Series Loops

6.2.1 Introduction

Multiple paths are usually connected to form circulating loops in many industrial applications, where the paths configuration can be identical or non-identical, and they may be connected in parallel or in series. The chemical looping combustion (CLC) system is regarded as one of the most promising clean combustion technologies because of the inherent CO_2 separation [305–308]. A typical CLC system consists of two fluidized bed reactors: an air reactor (AR) and a fuel reactor (FR). They are structurally interconnected but atmosphere isolated, enabling the clean combustion and inherent CO_2 separation.

Oxygen carriers continuously circulate between the two reactors to transport oxygen in the air from the AR to the fuel in the FR. Usually, the AR can be a fast fluidized bed reactor [152,163,309] due to the fast oxidation of reduced oxygen carriers, as the role to transfer the oxygen carriers back to the FR; the FR can generally be a bubbling fluidized bed reactor [152,163,310] or a moving bed reactor [102,310]. Generally, the geometry of AR and FR is non-identical. In recent years, many CLC units are established based on the symmetrical dual circulating fluidized bed (DCFB) where the AR and FR have identical configurations [198,311–313]. This structure effectively reduces the operating cost, and the circulation rate can be flexibly adjusted by altering superficial gas velocity and bed inventory. Therefore, it is important to understand the hydrodynamics of gas-solid flows in the symmetrical CLC units, where the identical paths can be connected in series.

Several experimental efforts have been made to explore the hydrodynamics of gas-solid flows in the symmetrical CLC units [198,312–314]. For example, IFP Energies Nouvelles [311,313] developed and studied the pilot-scale CLC consisting of two identical reactor configurations. The Cranfield Pilot-Scale Advanced CO_2 Capture Technology (PACT) chemical looping reactor comprising two identical interconnected CFB components was also developed and studied [312]. A dual circulating fluidized bed (DCFB) with symmetrical CFB components were experimentally studied by Geng et al. [198] for investigating particle behaviours between AR and FR. In these works, the boundary and operating conditions in the symmetrical CLC configuration are generally non-identical because of the different reactions taking place in the AR and FR. On the other hand, it is widely accepted that when multiphase flows travel through identical paths, a uniform distribution is commonly expected. However, the observations in the previous works that the flow distribution can be significantly non-uniform among the multiple paths even the boundary conditions are identical [292,294,309,315,316]. Such non-uniformity of gas-solid distribution is expected to deteriorate process units and cause various issues such as sub-optimal reactor performance, formation of differential erosion and fouling through

different paths, more frequent shutdowns, and unbalanced heat transfer [285–287,290]. It is proposed that the minor or slight asymmetry in geometry and operation conditions will possibly magnify the deviation caused by the non-uniformity compared with the completely symmetrical configuration [317]. Therefore, the asymmetry of this operation condition in the CLC unit will worsen the non-uniformity and further break the originally stable CLC operation, leading to great difficulties to control the flow and reaction of the system. Thus, it is necessary to study the gas-solid flow non-uniform phenomenon in detail.

Although the non-uniformity of mass distribution in CLC units can be studied by setting identical initial and boundary conditions for symmetrical paths, the experimental method shows some limits. This method is time-consuming and expensive; the reliability of experimental data may be affected by many factors and anomalies, including minor differences and fluctuation in two blower equipment. It is extremely hard to maintain exactly the same for each path in real experiments. A more high-fidelity method should be helpful for investigating the non-uniformity phenomenon in CLC units.

Computational fluid dynamics (CFD), as an alternative to the experimental method, has been increasingly used to unveil the intrinsic mechanism of gas-solid flows in the DCFB CLC units. Specifically, the CFD method can eliminate the influence of structure and external conditions on flow fields by ensuring the absolute and perfect symmetry of geometry, boundary and operating conditions in symmetrical paths.

In summary, the fundamental mechanism of the non-uniform distribution in the CFB system has been investigated through many theoretical and experimental studies [184,318,319]. However, to date, nearly all of these studies about the non-uniformity of bed inventory in DCFB system are based on parallel-connected paths, such as pant-leg structure [320,321] or multi-cyclone arrangements [286,289], because of their extensive applications in industries. The comprehensive study about the non-uniformity of bed inventory in the symmetrical CLC unit, which is a series circulation system, has not been

reported, although they were developed and practised widely [28,307,308,322]. Moreover, the simulation studies about the non-uniformity of gas-solid flow through the symmetrical CLC system which consists of two series paths have not been reported yet; and the relationship between non-uniform gas-solid distribution and the performance of the symmetrical CLC are yet being understood.

To overcome this deficiency, in the present work, the non-uniformity phenomenon of gas-solid distribution in a DCFB CLC unit with two identical paths connected in series is numerically studied, where the two paths are perfect symmetrical in terms of geometries, grids, and operating conditions. An index for assessing the degree of solid non-uniform distribution is proposed, and the influences of several key parameters are explored. The paper is organised as follows: In section 2, governing equations of the multifluid model are formulated including drag model. In section 3, geometry configuration and computational grids are given for studying the non-uniformity phenomenon. In section 4, the proposed model is validated against the experimental data, and the symmetry setting in terms of geometry, grid and operation conditions is verified. Then, the non-uniformity phenomenon is discussed, and the effects of several key operating parameters (*i.e.*, gas inlet velocity, total solid inventory, and wall roughness) on the degree of maldistribution are thoroughly investigated.

6.2.2 Mathematical model

In this work, the Eulerian-Eulerian two-fluid model (TFM) framework with the standard kinetic theory of granular flow (KTGF) is used to simulate the hydrodynamic behaviour in a symmetrical DCFB CLC unit [106,182]. The model has been well established and outlined below for completeness.

Governing equations

The gas phase and solid phase are both mathematically regarded as an interpenetrating continuum. The continuity equations for gas and particle phases are given by Ding and Gidaspow [323]. A detailed description of the governing equations and KTGF can be found in sections 3.2.1 and 3.2.2.

Drag force model

The energy-minimisation multi-scale (EMMS) drag model is adopted to describe drag force between the gas-solid phases, which is expressed by:

$$\beta=\frac{3}{4}\frac{\alpha_s\alpha_g\rho_g|\vec{u_s}-\vec{u_g}|}{d_p}C_D\alpha_g^{-2.65}H_D \tag{6-7}$$

where H_D is defined as β/β_0 to account for the hydrodynamic disparity between homogeneous and heterogeneous fluidisation.C_D represents the standard drag coefficient for particle phase:

$$C_D=\begin{cases}\frac{24}{Re_s}(1+0.15Re_s^{0.687}), & Re_s<1000\\ 0.44\ , & Re_s\geq 1000\end{cases} \tag{6-8}$$

$$Re_s=\frac{\rho_g|\vec{u_s}-\vec{u_g}|}{\mu_g}d_p \tag{6-9}$$

In this work, the EMMS model built by Lu et al. [197] for full-loop CFB is used. Table 6-2 summarises the formulas of H_D for CFB structure.

Table 6-2. Summary of formulas of H_D in EMMS model for the DCFB CLC unit.

Model parameters	**Range**
($H_D=a(\mathrm{Re_s}+b)^c, 0.001\leq \mathrm{Re_s}\leq 1000$)	($\alpha_{mf}<\alpha_g\leq 1$)

$$\begin{cases} a = 0.12621 + 0.51327\exp\left(-0.5\left(\dfrac{\alpha_g - 0.51738}{0.05325}\right)^2\right) \\ c = 0 \end{cases} \quad 0.4 \le \alpha_g \le 0.51228$$

$$\begin{cases} a = 0.06022 + \dfrac{0.64769}{1 + (\alpha_g / 0.54069)^{38.95056}} \\ b = 1.26148 - \dfrac{1.25109}{(1 + \exp(-(\alpha_g - 0.49842) / 0.00835))}\left(1 - \dfrac{1}{(1 + \exp(-(\alpha_g - 0.68685) / 0.03593))}\right) \\ c = 0.27298 - \dfrac{0.298}{1 + (\alpha_g / 0.55363)^{29.78427}} \end{cases} \quad 0.51228 < \alpha_g \le 0.60826$$

$$\begin{cases} a = 1/(15.09342 - 13.31486\alpha_g^{6.02771}) \\ b = -52.05197 + 346.18273\alpha_g - 914.53136\alpha_g^2 + 1202.33087\alpha_g^3 - 786.52213\alpha_g^4 + 204.82611\alpha_g^5 \\ c = 1/(3.51503 + 3.1596\alpha_g^{4.34314}) \end{cases} \quad 0.60826 < \alpha_g \le 0.9904$$

$$\begin{cases} a = 0.52193 + \dfrac{0.8812}{1 + \exp(-(\alpha_g - 0.99662) / 0.00112)}\left(1 - \dfrac{1}{1 + \exp(-(\alpha_g - 0.99752) / 0.00006)}\right) \\ b = 0.47595 - \dfrac{0.22085}{1 + (\alpha_g / 0.99594)^{2170.31695}} \\ c = 0.13788 - 0.07951\exp\left(-0.5\left(\dfrac{\alpha_g - 0.99841}{0.00142}\right)^2\right) \end{cases} \quad 0.9904 < \alpha_g \le 0.9997$$

$$a = 1,\ c = 0 \quad 0.9997 < \alpha_g \le 1$$

6.2.3 Simulation conditions

The geometry of the symmetrical CLC unit studied in this work is established according to a pilot-scale apparatus designed by Geng et al. [198], as shown in Fig. 6.23. The whole test rig includes two identical unit A and B which are connected in series, forming the symmetrical DCFB unit. Each of unit A and B consists of a riser with an inner diameter of 0.1 m and a height of 3 m, a cyclone separator, a downcomer with 0.1 m inner diameter and 1.73 m height, and a loop seal. The solid materials are sand with an average diameter of 140 μm and an apparent density of 2600 kg/m^3. The total amount of solid mass loading in the experiments is approximately 70 kg. One gas inlet is installed at the bottom of the riser to transport particles with massive gas velocity and two aeration inlets are located at

the bottom of loop seal to stabilise the gas-solid flows with a relatively small air flow rate. Fig 6.23 also shows the 3D geometry and grids of the CFB. The computational domain, including riser, cyclones, downcomers and loop seals, are meshed with 466,028 hexahedron elements. The geometry and also distribution of the grids of both units are identical, guaranteeing the comparison criteria.

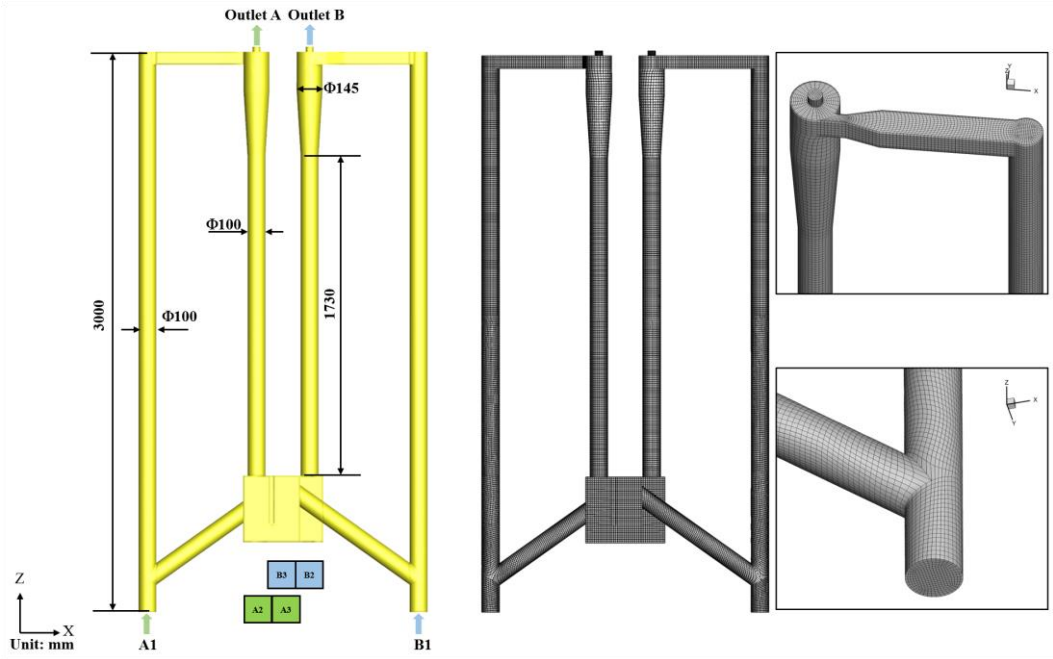

(a) (b) (c)

Fig 6.23. Schematic geometry [198] and grids of the investigated three-dimensional DCFB CLC unit: geometry (a); grids of the whole bed (b); grids of local regions (c).

Initially, the solid loadings are packed in the lower part of the CFB symmetrically with an initial solid volume fraction of 0.5. The velocity inlet boundary conditions are set for the inlet of the riser and loop seal in both units. The pressure outlet condition is adopted for the cyclone outlets. The frictional model of Schaeffer for the particle phase and the Johnson and Jackson's model [200] for wall boundary conditions of the solid phase are

used. The no-slip boundary condition is set for the gas phase. Different discretisation schemes for convection terms of each governing equation are employed: the second-order upwind scheme is chosen for the momentum equation; the Quadratic Upwind Interpolation of Convective Kinematics (QUICK) scheme is chosen for the volume fraction of gas and solid phases; the first-order upwind scheme is chosen for the turbulent kinetic energy and turbulent dissipation rate. The phase coupled Semi-Implicit Method for Pressure Linked Equations (SIMPLE) algorithm is used to deal with pressure-velocity coupling. The time step is assigned as 0.0001 s in this study. The mathematical model is solved using commercial software ANSYS Fluent v19.2. The total simulation time for each case is 120 s. Other material properties and simulation parameters are listed in Table 6-3.

Table 6-3. Gas-solid properties and computational settings.

Solid Properties		**Values**
Density (ρ_s)		2600 kg/m^3
Average particle size (d_p)		140 μm
Restitution coefficient of particles (e_{ss})		0.95
Restitution coefficient of particles (e_{sw})		0.95
Specularity coefficient (ϕ)		0.01
Angle of internal friction		30°
Friction packing limit		0.60
Gas Properties		**Values**
Aeration rate	A1	80/120/160 m^3/h
	B1	80/120/160 m^3/h

	A2	3 m^3/h
	B2	3 m^3/h
	A3	30 m^3/h
	B3	30 m^3/h
Gas density (ρ_g)		1.225 kg/m^3
Gas viscosity (μ_g)		1.837×10^{-5} pa·s
Computational Settings		**Values**
Pressure-velocity coupling		Phase coupled SIMPLE
Time step		1×10^{-4} s
Max. number of iterations per time step		50
Convergence criteria		10^{-4}

6.2.4 Results and discussion

Grid independence test

A grid-sensitivity analysis is conducted to determine the optimal number of grids. Three groups of grids, 127310, 334358 and 466028, are tested using the same case. Fig. 6.24 shows the time-averaged pressure profile along the riser height is significantly different in the coarse-grid case from that of the other two cases. Meanwhile, the pressures of the 334359 and 466028 grids show a similar trend with a slight deviation. In this work, the fine grids are used in order to obtain more accurate numerical results.

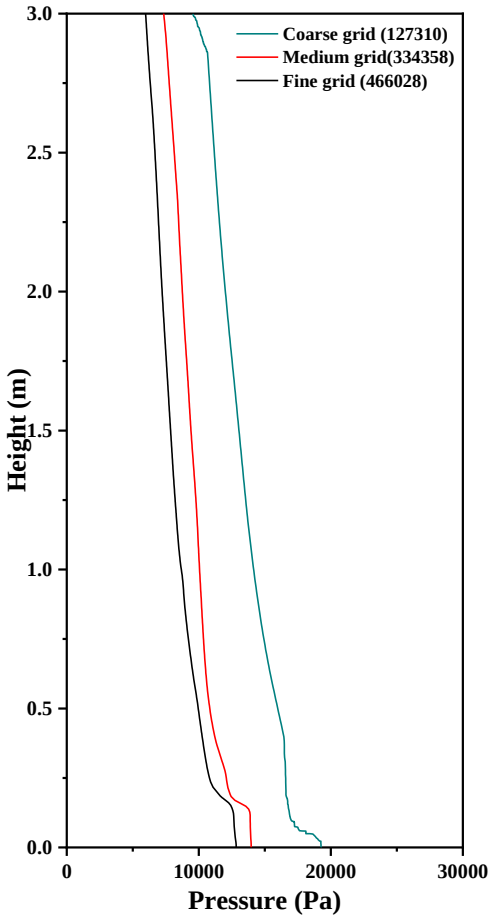

Fig 6.24. Time-averaged pressure profiles along the riser of unit A with different grid numbers.

Verification of computational domain symmetry

In this work, one obvious concern is to ensure identical geometry and grids of unit A and unit B in the full-loop CLC system and avoid the difference of non-negligible effects on flow patterns. For verifying the system symmetry, a gas stream is introduced into the empty CLC unit and the gas flow behaviour is monitored inside the symmetrical system. It is widely accepted that when a single-phase gas flow passes identical paths, the flow distributes itself uniformly among the multiple paths [285,287].

Fig. 6.25(a) shows the time-averaged gas velocity distribution in the full-loop CLC system with the air introduced. The identical distribution of gas velocity in the corresponding section of Unit A and Unit B can be observed. Fig. 6.25 (b) and (c) show the time-averaged air velocity and pressure distributions along the central lines of the riser A and riser B, respectively. The comparison shows that both the velocity and pressure distributions are nearly identical at most altitudes of unit A and unit B. Therefore, based on the discussion of the results above, the geometry and grid in unit A and unit B can be regarded as numerically identical.

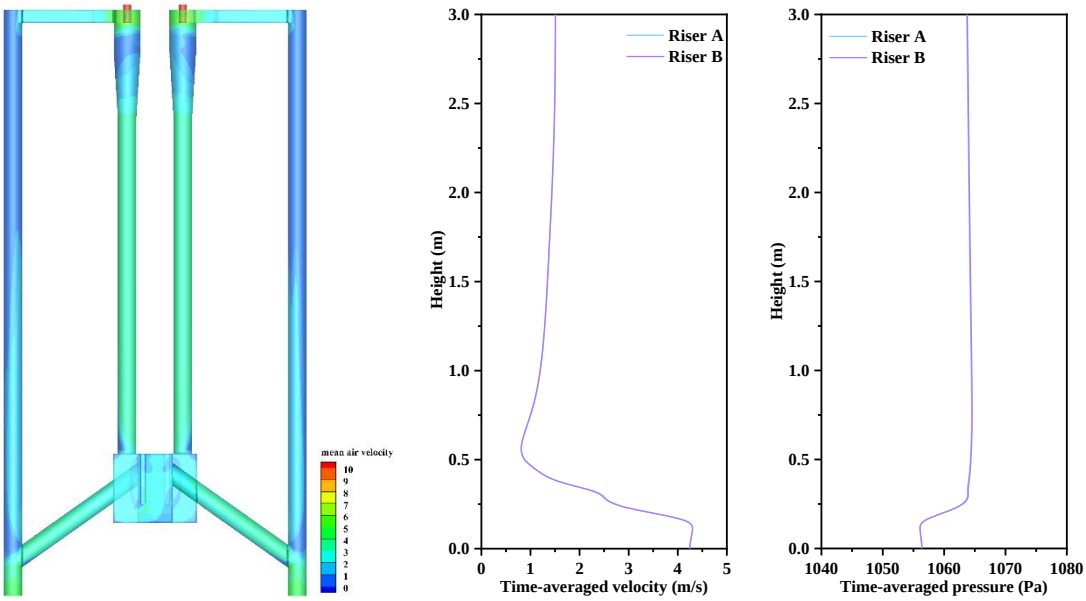

(a) (b) (c)

Fig 6.25. Contours of the time-averaged gas velocity distribution in the full-loop system (a); time-averaged air velocity profiles along the central lines of the riser (b); time-averaged pressure profiles along the central lines of the riser (c).

Model validation

In this section, the model validation is conducted by applying the model to the case by Geng et al. [198] and then comparing the simulation results with the measurements. Fig. 6.26(a) shows the profiles of the solid mass flow rates of riser A and riser B, respectively, where the solid mass flow rates are sampled from a horizontal cross-section set in the riser. The intense fluctuations of solid mass flow rates between 0 and 30 s can be observed, which is commonly regarded as the start-up process. Afterwards, the solid mass flow rates fluctuate around a constant value, which generally is regarded as the quasi-stable state. The instantaneous values of solid mass flow rates are averaged during the quasi-steady state. Fig. 6.26(b) shows that the time-averaged values predicted at the same height of the riser A and riser B show reasonable agreement with experimental data with a slight overestimation.

From Fig. 6.26(a), the system reaching a quasi-steady state means the flow characteristics will remain approximately stable for a long time. However, it can be seen in Fig. 6.26(b) that there is a difference of time-averaged solid mass flow rates between unit A and unit B although the identical geometry and boundary conditions are implemented. It is known that the components of the CLC unit are connected in series and there will be inevitable interactions between the intersecting sections. Therefore, whether the system stability can be judged by local variables changes only will require further research.

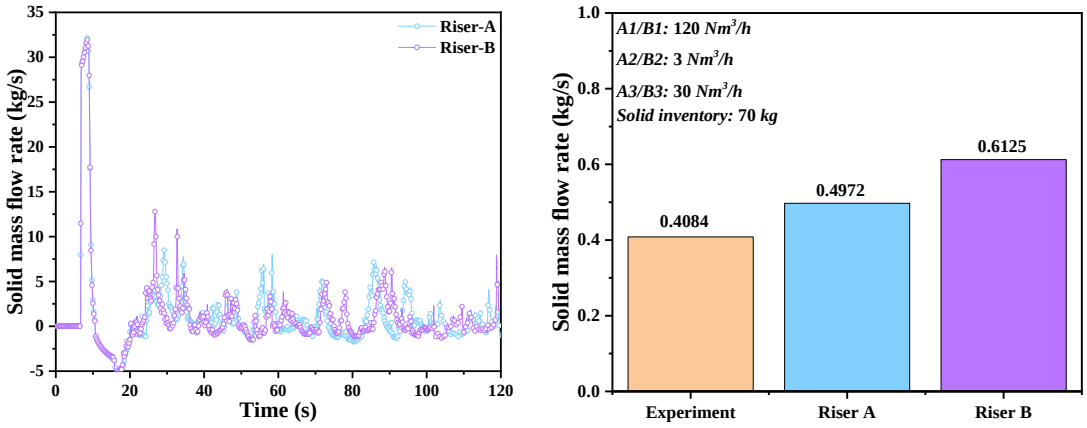

(a) (b)

Fig 6.26. Profile of the solid mass flow rate with different drag models: time-evolution solid mass flow rate (a) and time-averaged solid mass flow rates (b).

Typical phenomena of non-uniformity in a symmetrical CLC unit

Fig. 6.27 shows the instantaneous distribution of solid volume fraction in the CLC unit. The simulation results show that initially, all particles are symmetrically packed on the bottom of the riser and two loop seals. Meanwhile, the gas flow is introduced from inlets at the bottom of riser and loop seals to circulate particles. From the initial time to 10 s, no significant difference is observed between the distribution of solid volume fraction in both unit A and B. This is because the system has not established a complete solid circulation. At around 30 s, a slightly asymmetrical can be observed in the section of the downcomer which indicates the non-uniform gas-solid flow in the system has appeared. After this, an asymmetrical solid volume fraction distribution continuously exists, as shown in Fig 6.27. The results indicate that the non-uniform solid distribution indeed exists even in a symmetrical CLC system.

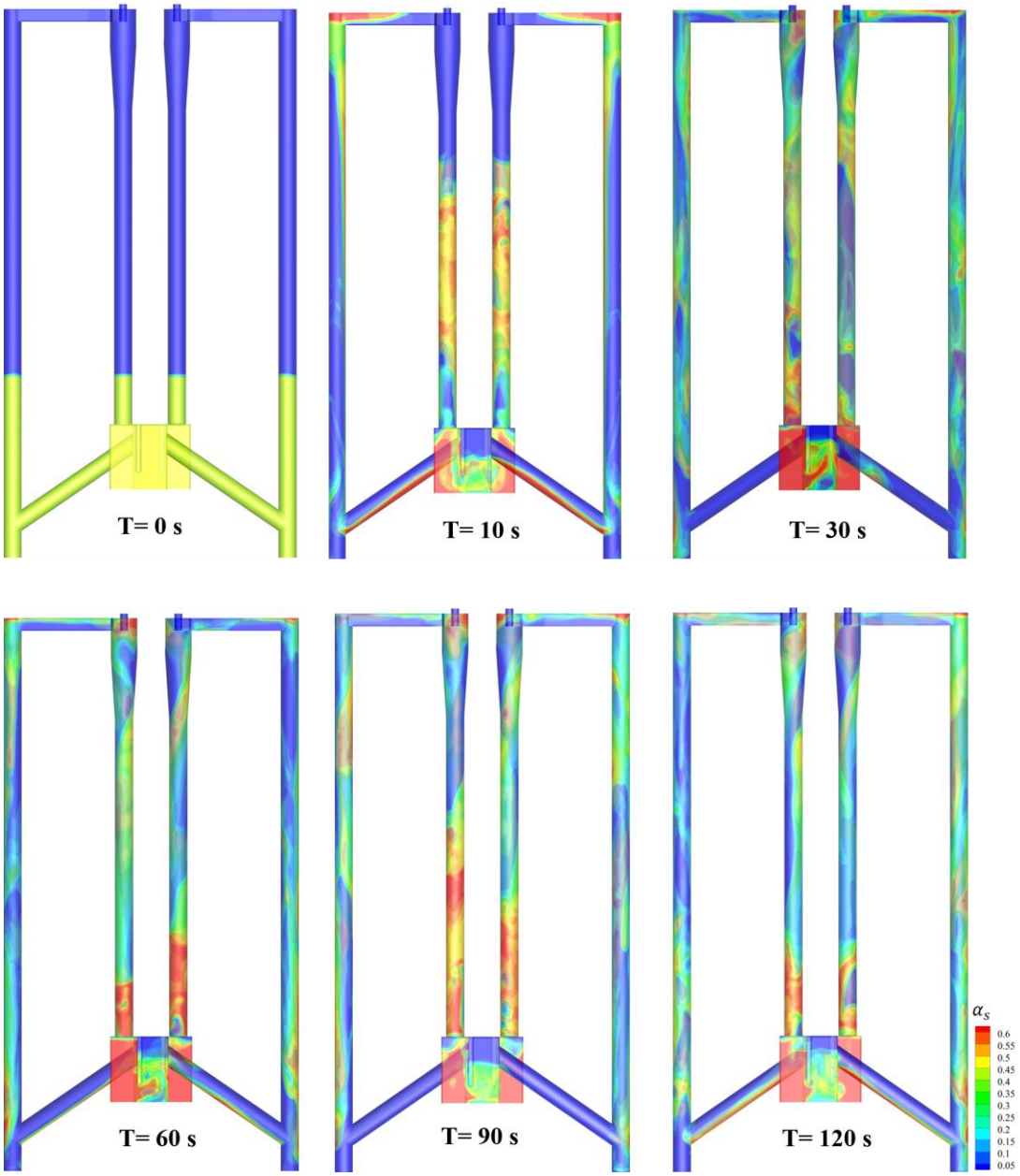

Fig 6.27. Instantaneous distributions of solid volume fraction (α_s) in the DCFB CLC unit.

For further comparison, the profiles of time series of bed inventory in unit A and unit B are plotted and compared. Fig. 6.28(a) shows the time series of bed inventories in the two identical series units. For both units, the non-uniformity of bed inventories exists in most of the simulation time. Besides, the difference in non-uniformity of mass distribution gradually increases over time. In order to quantitatively discuss the non-uniformity

between two identical units, the relative deviation (Dev) of bed inventory is adopted to define the degree of non-uniformity, which is defined as:

$$Dev = \frac{|m_A - m_B|}{m_A + m_B} \tag{6-10}$$

where m_A and m_B are the solid mass in unit A and unit B, respectively. *Dev* is a number between 0 and 1. The value of 0 represents an ideal situation that the solid mass is same in both units while the value of 1 represents the worst situation that all solid particles are transported into a specific unit and another unit is empty. Fig. 6.28(b) describes the relative deviation of bed inventory between unit A and B, which is averaged in every 5 s. It can be seen that the degree of deviation increases with time and the maximum bed inventory alternately occurs in the following time. The process, as described above, indicates that this symmetrical CLC system shows a significant non-uniform solid distribution and the amplitude of the *Dev* gradually increases along time, as shown in Fig. 6.28(b).

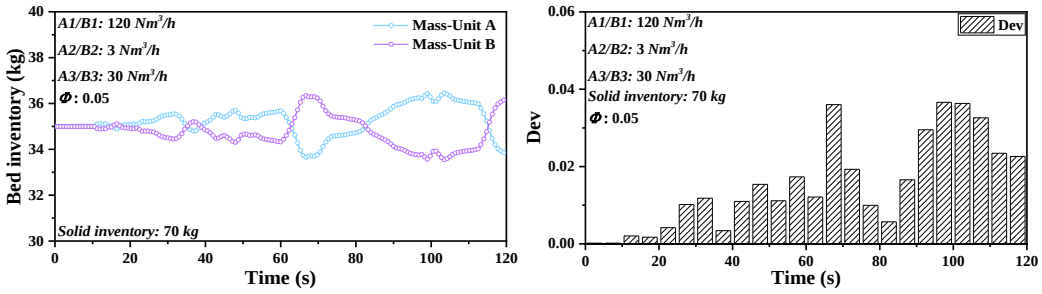

Fig 6.28. Time series of bed inventory in unit A and unit B (a); and relative deviation (Dev) of bed inventory between unit A and unit B (b).

Fig. 6.29 shows contours of time-averaged solid volume fraction in the symmetrical CLC unit, and the solid volume fraction and axial particle velocity at cross-sections of the riser. The core-annulus flow structure is clearly observed in both risers A and riser B, where

the wall region of the high solid concentration surrounds a region of low solid concentration at the centre of the riser. In the comparisons in terms of solid volume fraction and velocity distribution, it can be seen that the flow patterns in Unit A and Unit B are asymmetric. Moreover, the pressure balance closely relates to the fluidisation state (*e.g.*, bed inventory and solid circulation). On the other hand, the specific initial solid arrangement, as well as the operational conditions, will determine the pressure balance in turn. The pressure profiles of the system are used to compare the difference in flow behaviours. The time-averaged static pressure profiles along the axial direction in the full-loop system are presented in Fig. 6.30. It can be seen that the pressure drop in the expansion section of unit A and unit B is respectively 14525 Pa and 15263 Pa, which highly depends on the bed inventory in the unit A and Unit B. For the whole unit, the pressure gradient of unit B is higher than that of unit A. The pressure drop of each part can be further compared in riser, cyclone, downcomer and loop seal, respectively. It can be seen the pressure drop has a different value, indicating the different fluidisation states of the corresponding section between the two units. For the risers, the pressure of the riser A is larger than that of riser B. However, for the section of downcomer and loop seal, the pressure in unit B is larger than A. This difference is a result of the different allocations of solid bed inventory in different sections of the whole loop.

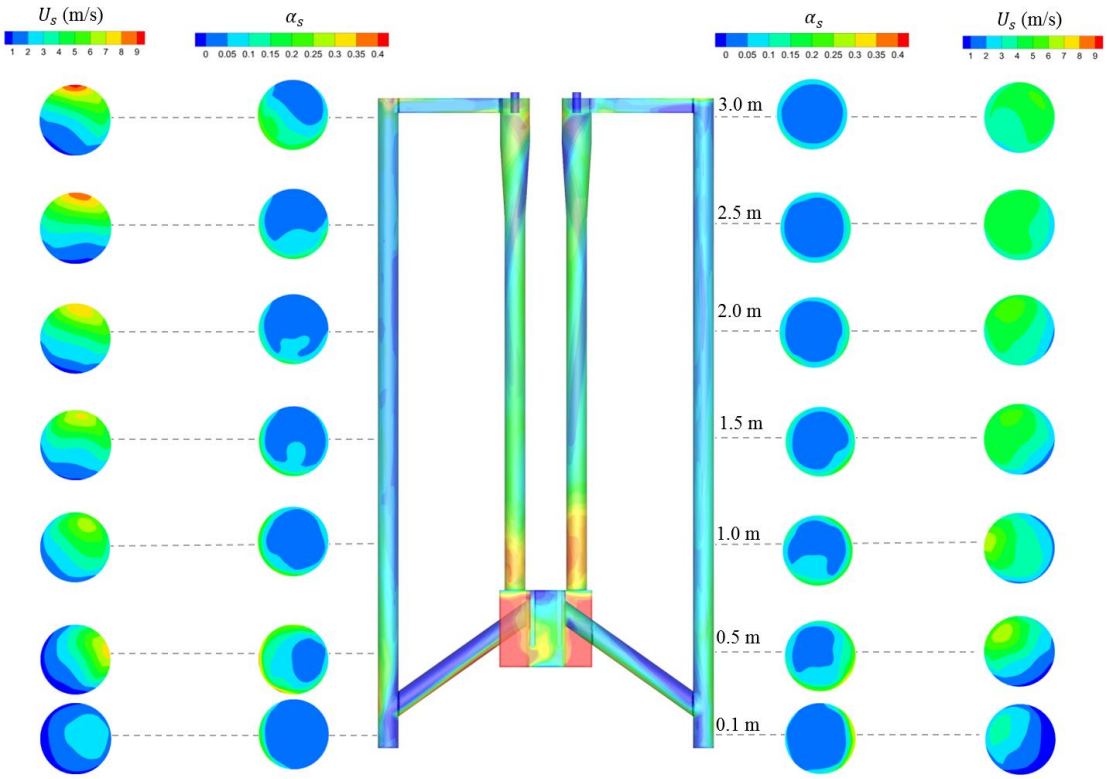

Fig 6.29. Time-averaged solid volume fraction and velocity distribution in the full-loop system with several horizontal cross sections at different heights of the riser.

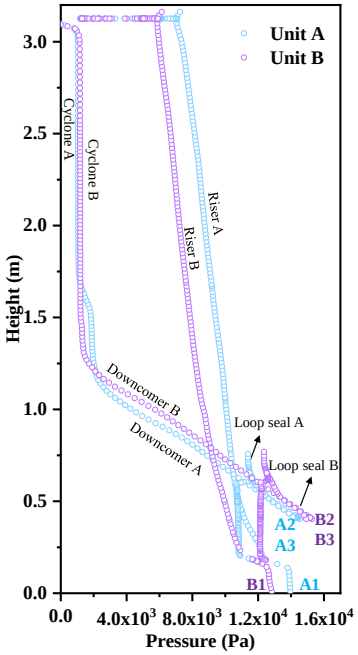

Fig 6.30. Time-averaged static pressure profile along the central line in the full-loop system.

The pressure balance plays an important role in the stable operation of the CLC system. The pressure difference between different units drives the solids circulation in the whole loop. The pressure balance established in the CLC system is important for assessing the overall system performance, and one of pressure balances established in this CLC unit can be written as:

$$\Delta P_1 = \Delta P_{riser} + \Delta P_{cyclone-inlet} + \Delta P_{cyclone-outlet} \quad (6\text{-}11)$$

where the ΔP_1 can reflect the flow characteristics in the riser in both unit A and unit B.

Fig.6.31 demonstrates the time-evolution of ΔP_1 in unit A and unit B, respectively. At the initial stage, the pressure drop increases as the solids inventory builds up. It then levels off, indicating that the solids circulating pattern has been fully developed and a statistically steady state has been achieved. To avoid the start-up effect, the first 40 s simulation is discarded for postprocessing. From Fig. 6.31(a), it can be seen although two pressure drops reach the quasi-stable state after 40 s, the difference still exists between the identical paths, which results from the non-uniformity of the instantaneous mass distribution.

To further investigate the slight difference of fluidisation state between unit A and unit B in the system, the Fourier spectral analysis of two pressure drops is compared, as shown in Fig. 6.31(b). It can be obtained by analysing that the dominant frequency of pressure drops $\Delta P_1$with identical conditions are 6.25e-5 Hz and 3.12e-4 Hz in unit A and unit B, respectively. The low frequency indicates the dilute regime flow pattern in both units. Meanwhile, the amplitudes of pressure drop have a discrepancy where the amplitude of pressure fluctuation is 2439 and 2646 Pa respectively for two units, indicating the difference of flow behaviours between two units.

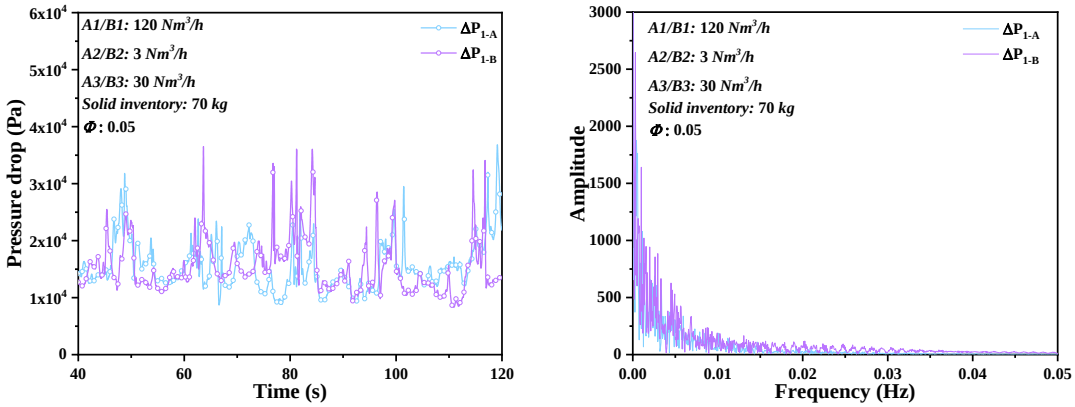

(a) (b)

Fig 6.31. Profiles of the time-evolution profiles of ΔP_1 (a); the Fourier spectral analysis of ΔP_1 (b).

Re-scaled range analysis, also named *R*/*S* analysis, was first used for the analysis of pressure fluctuations in fluidized beds by Fan et al. [324]. The *R*/*S* analysis can characterise correlations of signal series via the Hurst exponent. That is, the Hurst exponent indirectly reflects the dynamic behaviours of gas-solid flows in CFBs [325,326]. In the R/S analysis, the equation can be shown as follows:

$$R(t,\tau) = \max_{0\le u\le\tau}\left\{X^*(t+u) - X^*(t) - \frac{u}{t}[X^*(t+u) - X^*(t)]\right\} - \min_{0\le u\le\tau}\left\{X^*(t+u) - X^*(t) - \frac{u}{t}[X^*(t+u) - X^*(t)]\right\} \quad (6\text{-}12)$$

where X and R denote the discrete series of signal and the corresponding extreme difference, respectively. With τ being time intervals, X^* can be defined as:

$$X^*(t) = \sum_{u=1}^{t} x(u) \qquad (u = 1, 2, \cdots, t) \tag{6-13}$$

The standard deviation of time series pressure signal sequence $S(t, \tau)$ is demonstrated as follows:

$$S^2(t, \tau) = \frac{1}{\tau} \sum_{u=t+1}^{t+\tau} P^2(u) - \left[\sum_{u=t+1}^{t+\tau} P(u) \right]^2 \tag{6-14}$$

An empirical power law between the expectation of *R*/*S* and time lag τ is applied to determine the Hurst exponent:

$$\frac{R(t, \tau)}{S(t, \tau)} \propto \tau^h \tag{6-15}$$

where H is the Hurst exponent, the Hurst exponent for the curve of the interval can be obtained through the slopes of log(*R*/*S*) and log(τ). Each slope of this curve is equal to a Hurst exponent. Moreover, if the Hurst exponent equals 0.5, the time series is random. If it is larger than 0.5, the time series is persistent. It implies that if the trend in the time series increases or decreases, it has the chance of continuous increase or decrease in the future. Moreover, the strength of trend-reinforcing behaviour, or persistence, increases as the Hurst exponent approaches 1.0. Conversely, if the Hurst exponent is smaller than 0.5, the time series is anti-persistent. This means that whenever the trend in the time series increases, it will be more likely to decrease in a short time period. The strength of anti-persistence increases as the Hurst exponent approaches zero. A decrease in the value of the Hurst exponent indicates that higher disorder exists in the time-series data and higher pulsations occur in the flow. In contrast, an increase in the value of the Hurst exponent indicates the lower disorder for the time-series data and the decrease of turbulence or pressure fluctuations.

The R/S analysis is shown in Fig 6.32 through estimating the pressure signal ΔP_{1-A} and ΔP_{1-B} for various subperiod lengths. The slope of this logarithmic plot gives the Hurst exponent of the signal. It can be seen that the rescaled range estimated from the riser of unit A and unit B correlates linearly with the subperiod length. Both of the Hurst exponents exceed 0.9 for two pressure balances which means the motion of the solid is strong 'persistent' in both units and it highly depends on gas/bubble motion. The Hurst exponent in unit A is slightly larger than it in unit B, which implies a stronger persistence to repeat an increasing or decreasing trend of the signal itself. The difference of Hurst exponents also can reflect that the non-uniformity in the two units will be further intensified.

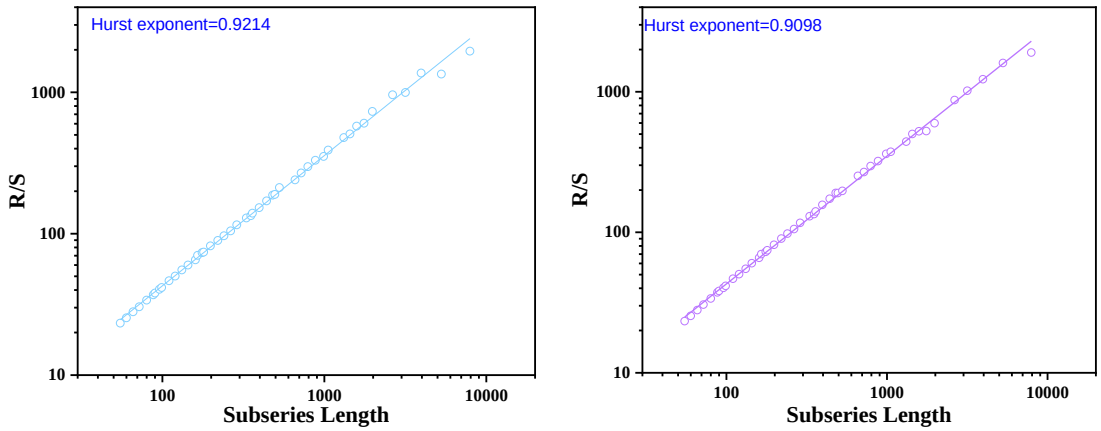

(a) (b)

Fig 6.32. Variation of the rescaled range estimated from the signals shown in Fig.7. 9 for various subperiod length: ΔP_{1-A} (a); ΔP_{1-B} (b).

Effects of key variables on non-uniformity

In the actual process, the operational parameters of CFB may vary over a wide range. A clear understanding of the effects of different operating parameters is of great significance for maintaining a stable and balanced system. In this section, the effects of total bed inventory, aeration rate and wall roughness on the degree of non-uniformity are discussed.

Effect of total bed inventory

Fig. 6.33(a) shows the time-evolution profiles of bed inventory in unit A and unit B, respectively, with other variables fixed. It is found that increasing total bed inventory increases the fluctuation amplitude of bed inventory difference and increases the maximum amplitude and frequency of the relative deviation of bed inventory via comparing the value of Dev (Fig. 6.33(b)), which means the system becomes more unstable.

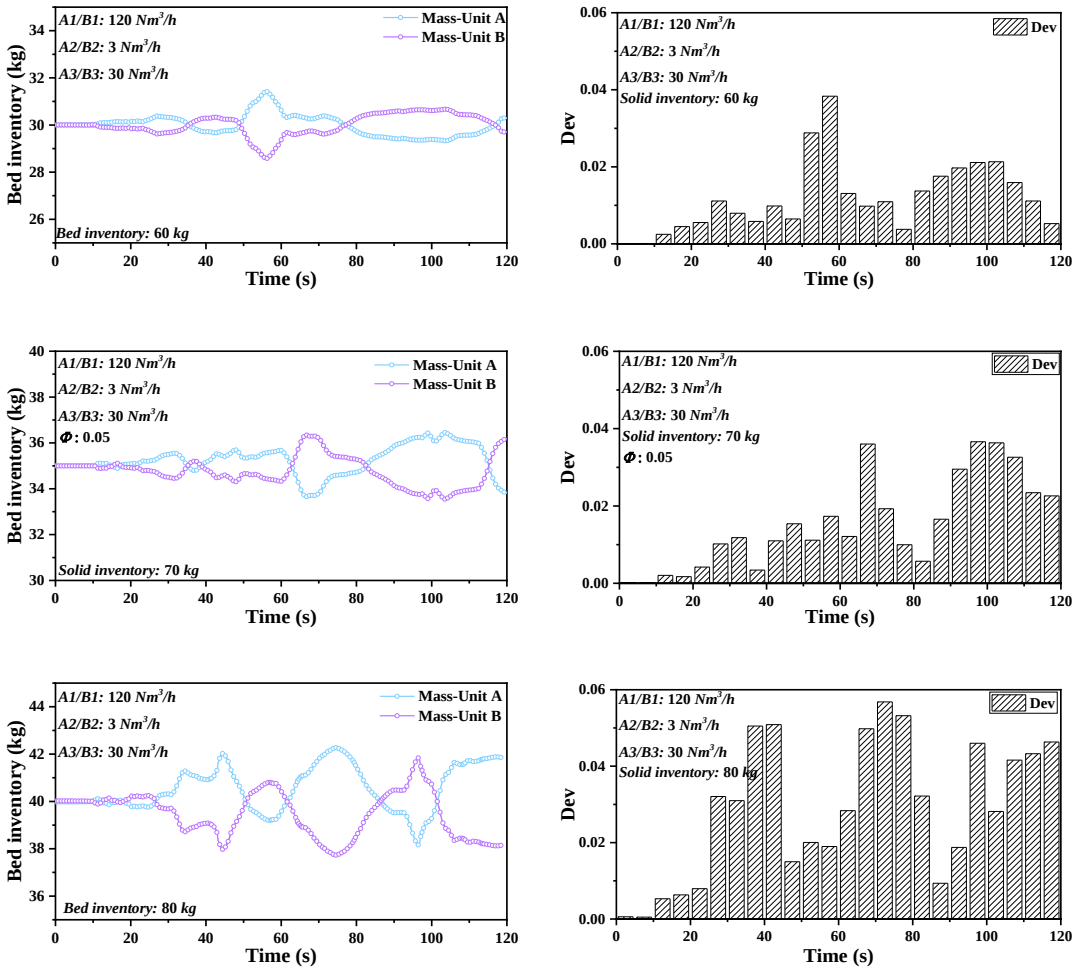

Fig 6.33. Time-evolution profiles of bed inventory (a); relative deviation (Dev) of bed inventory (b) in unit A and unit B at different total solid inventory.

Fig. 6.34(a) compares the pressure drop ΔP_1 in the two units. When the total bed inventory increases from 60 kg to 80 kg, it is found that the pressure drops for both ΔP_1 of unit A and unit B are increased significantly due to more energy dissipation from particle-particle/wall interactions. The fluctuation frequency of ΔP_1 of unit A and unit B for three different solid inventories are very close within the range of 10^{-5}~10^{-4} Hz due to the dilute flow pattern. However, the amplitude of the dominant frequency shows a significant rising tendency with the increase of solid inventory, indicating that the stronger intensity of the signal and the flow structure at the corresponding scale. As shown in Fig. 6.34(b), the frequency and amplitude of pressure fluctuations are different in units A and B for all cases, indicating the non-uniformity of flow patterns is not an accidental phenomenon in CFBs. Moreover, the solid inventory increases from 60 kg to 80 kg, with the amplitude of pressure fluctuation correspondingly increasing from around 1500 to 4000 Pa for both units A and unit B, indicating the gas-solid flow pattern becomes more unstable with the increase of total solid inventory.

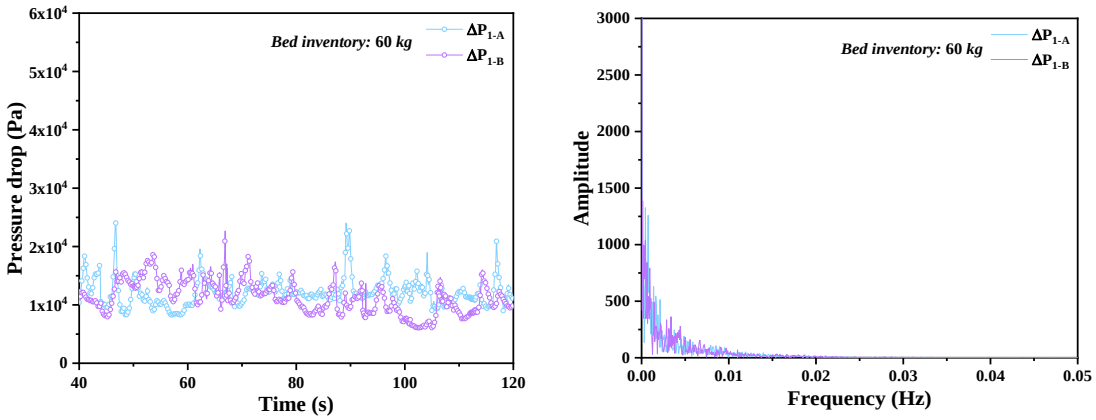

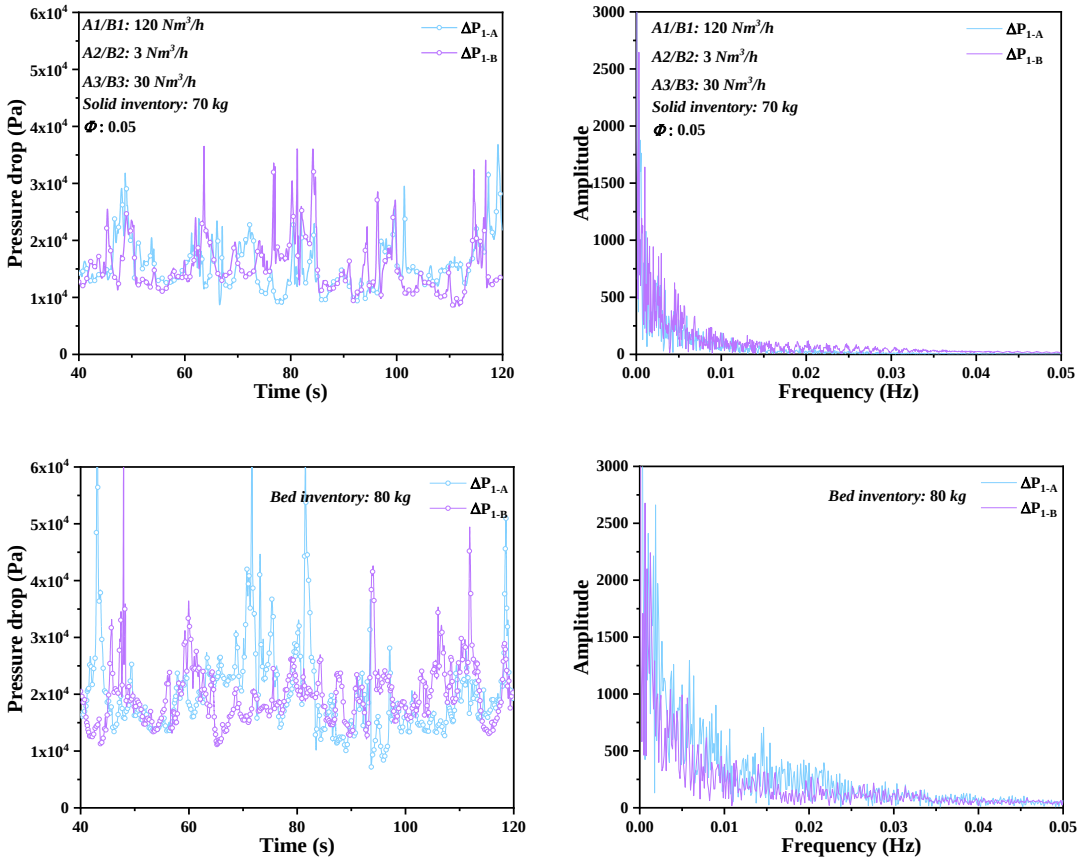

Fig 6.34. Profiles of the time evolution profiles of ΔP_1 (a) ; the Fourier spectral analysis of ΔP_1 (b) at different bed inventory.

Fig. 6.35 shows the Hurst exponents estimated from the logarithmic plot of the rescaled range at different solid inventories. The estimations of the Hurst exponent are close to 1.0 for all pressure drops, indicating that gas-solid flow behaviours in the CFB display strong persistent features under the conditions examined. The comparison shows that, increasing total bed inventory slightly decreases the Hurst exponent. This demonstrates that the fluctuations of the time series become more significant and more unstable. The difference of Hurst exponent between unit A and unit B gradually enhances from 60 kg to 80 kg, which also indicates the degree of non-uniformity will be intensified in the predictable short-term future with the increase of total solid bed inventory.

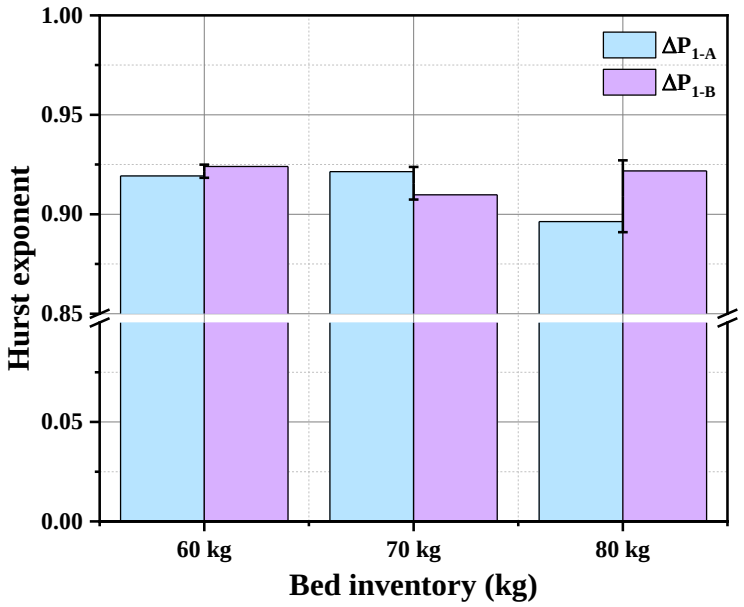

Fig 6.35. Comparison of Hurst exponent estimated at different solid inventory.

Effect of aeration rate

Fig.6.36(a) shows the time-evolution profiles of bed inventory for different aeration rates in unit A and unit B, respectively, with other variables fixed. It can be found that increasing the gas fluidisation rate increases the fluctuation amplitude of bed inventory. Meanwhile, with the increase of gas fluidisation rate, the maximum amplitude and frequency of the relative deviation of bed inventory increases by comparing the value of Dev (Fig 6.36(b)), which means the system becomes more unstable.

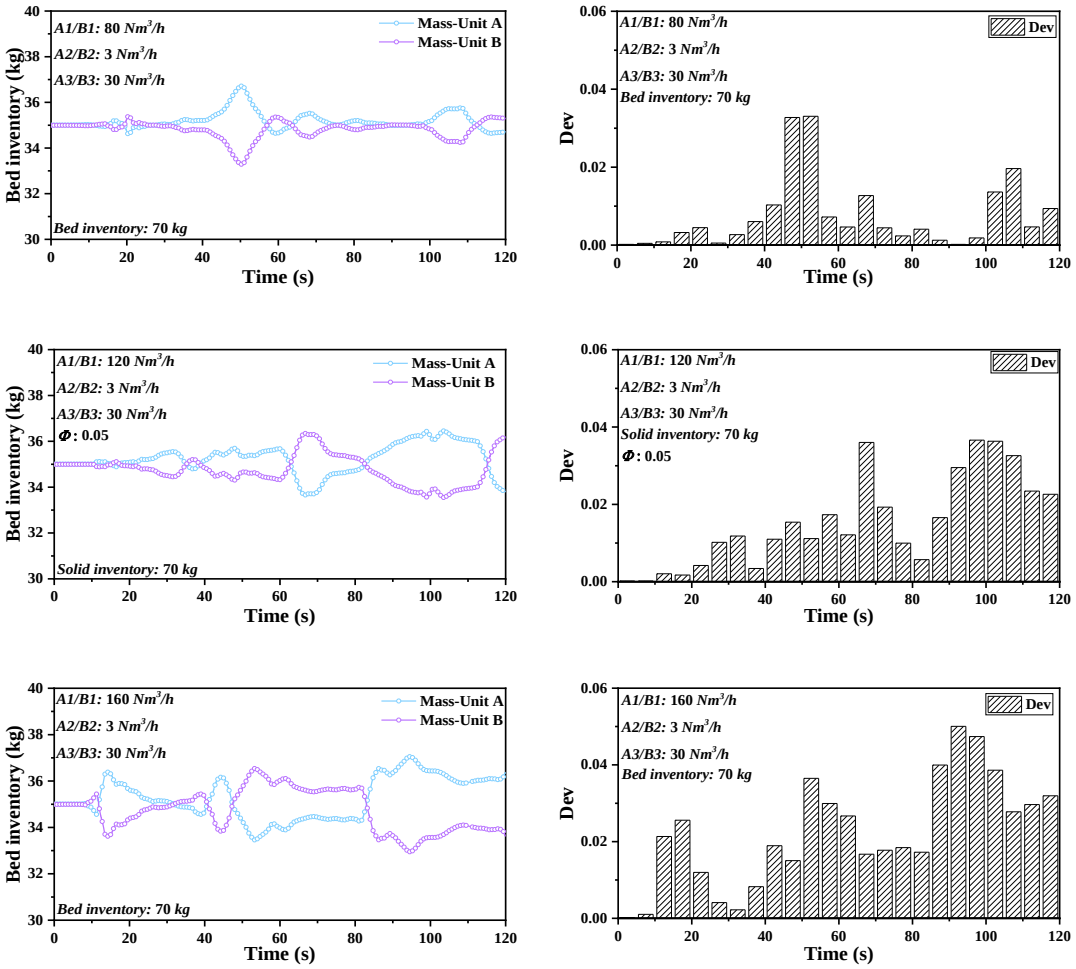

(a) (b)

Fig 6.36. Time-evolution profiles of bed inventory (a); relative deviation (Dev) of bed inventory (b) in unit A and unit B at different gas aeration rates.

To investigate the influence of gas aeration rates on gas-solid hydrodynamics in the symmetrical CLC unit, Fig. 6.37 shows the time series of pressure fluctuations of ΔP_1 of unit A and unit B at different aeration rates of 80, 120 and 160 Nm^3/h. As can be observed, by increasing the gas aeration rate, the amplitude of time series fluctuations increases owing to the increase of gas-solid interactions. As shown in Fig. 6.37(a), the dominant frequency of ΔP_1 of unit A and unit B for three different aeration rates are very close within the range of 10^{-5}~10^{-4} Hz due to the dilute flow pattern. However, as the gas aeration rate increases, the amplitude of the fluctuation steps up gradually, indicating a more unstable gas-solid flow pattern. Meantime, both the frequency and amplitude of

pressure drop are non-identical between unit A and unit B and the degree of non-uniformity further aggravates.

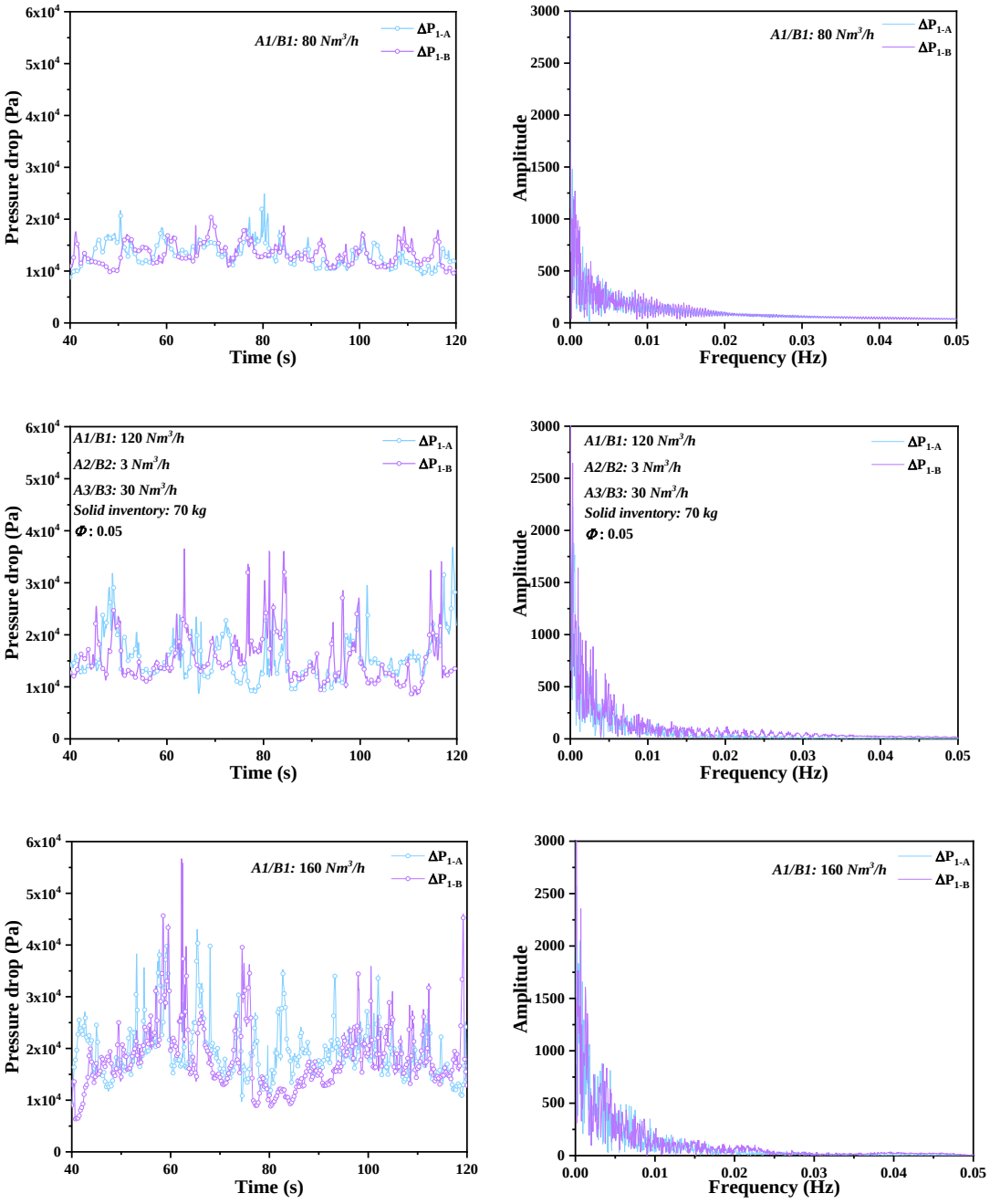

(a) (b)

Fig 6.37. Profiles of the time evolution profiles of ΔP_1 (a); the Fourier spectral analysis of ΔP_1 (b) at different gas aeration rates.

The Hurst exponent diagram of pressure fluctuations of ΔP_1 in unit A and unit B at the gas aeration rate of 80, 120 and 160 Nm^3/h are demonstrated in Fig. 6.38 Increasing the gas aeration rate decreases the value of Hurst exponent. A decrease in value of Hurst exponent indicates that higher disorder exists in the time-series data and higher pulsations occur in the gas-solid flows. Meantime, the difference of Hurst exponent between unit A and unit B is gradually enhanced from 80 to 160 Nm^3/h, indicating that the degree of non-uniformity will be intensified in the predictable short-term future.

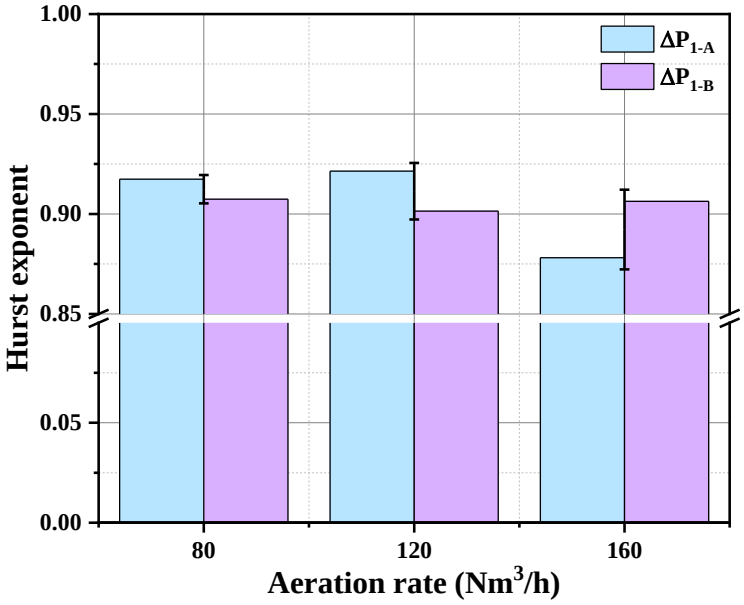

Fig 6.38.Comparison of the Hurst exponent estimated for various subperiod lengths at different gas aeration rates.

Effect of wall roughness

The value of specularity coefficient representing the roughness of the reactor walls varies between 0 and 1. In practice, it represents different materials and manufacturing processes used for reactors. In this study, five values of 0.05, 0.3, 0.5, 0.7 and 1.0 are adopted to account for different slip boundary conditions to examine the influence of different wall roughness on solid maldistribution.

Fig. 6.39 shows the time-evolution profiles of the bed inventories for different wall roughness in unit A and unit B, with the gas inlet velocity and total bed inventory fixed. The distribution and relative deviations of bed inventory between two identical units are very random, and there is not a clear tendency. One possibility is that the influence of wall-particle collisions has a more complicated mechanism and more comprehensive factors need to be considered in future studies.

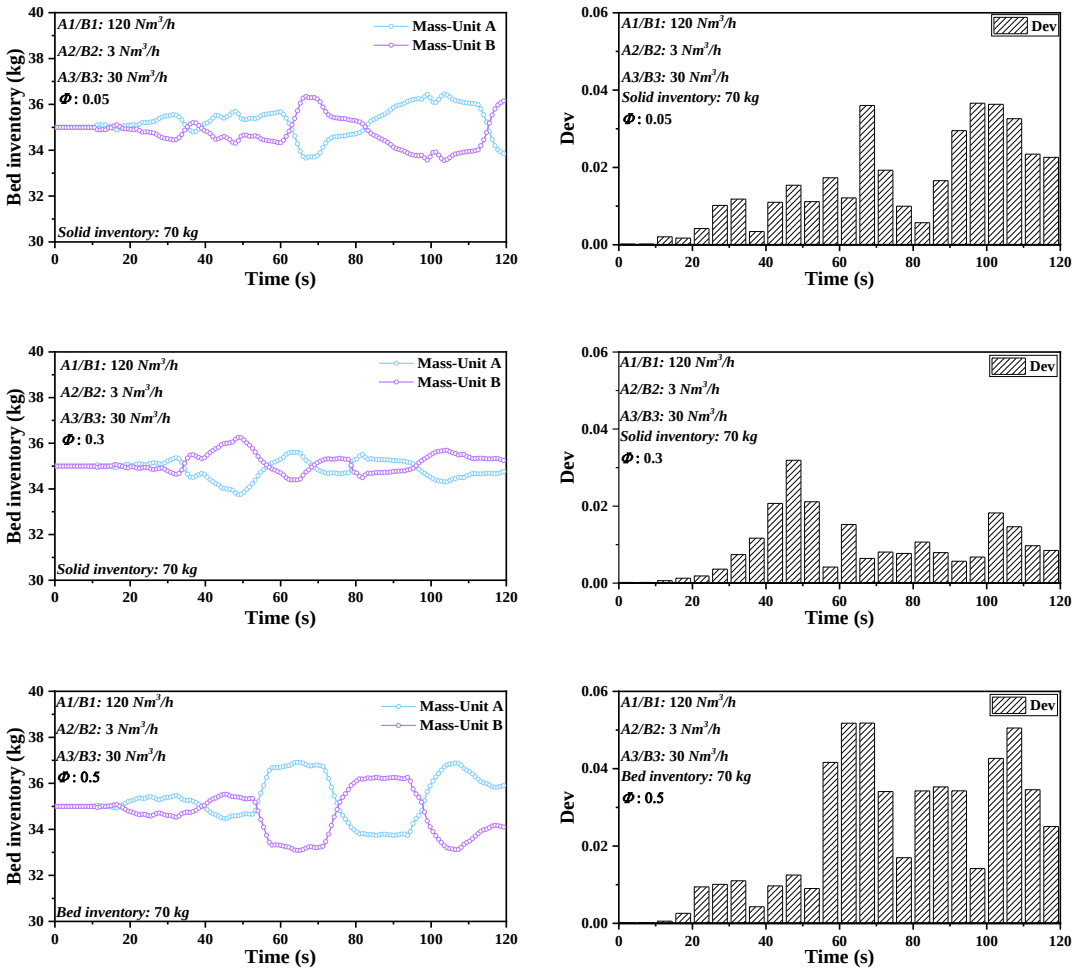

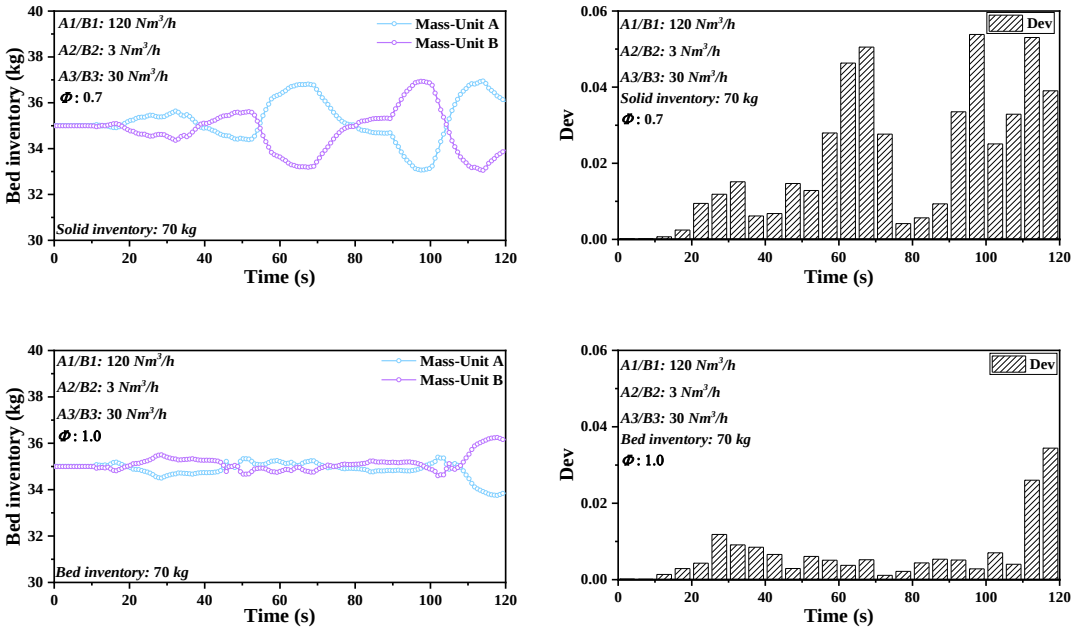

(a) (b)

Fig 6.39. Time-evolution profiles of bed inventory (a); relative deviation (Dev) of bed inventory (b) in unit A and unit B at different wall roughness.

Fig. 6.40 shows the time series of pressure fluctuations of ΔP_1 in unit A and unit B at different specularity coefficients of 0.05, 0.3, 0.5, 0.7 and 1.0. It can be seen there is no significant change in pressure drop with increasing the specularity coefficient. Meanwhile, the frequency of ΔP_1 shows a very similar behaviour without a significant difference at different wall roughness and the fluctuation amplitude of ΔP_1 shows an irregular change. The Hurst exponent diagram of pressure fluctuations of ΔP_1 in unit A and unit B at different wall roughness are compared in Fig. 6.41 With the increase of wall roughness, both the value of Hurst exponent and the difference between two units have no definite tendency, although the significant difference can be observed among different results. One possibility is that the influence of wall-particle collision has a more complicated mechanism and more comprehensive factors need to be considered.

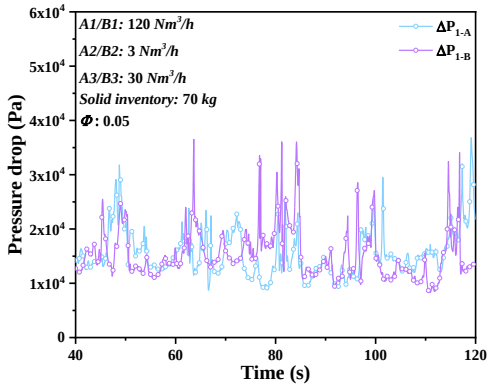
A1/B1: 120 Nm³/h
A2/B2: 3 Nm³/h
A3/B3: 30 Nm³/h
Solid inventory: 70 kg
Φ: 0.05
ΔP1-A
ΔP1-B
Pressure drop (Pa)
Time (s)

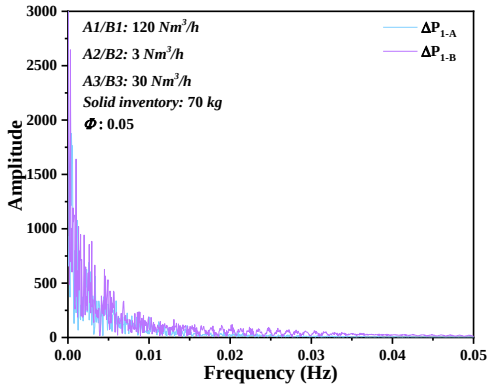
A1/B1: 120 Nm³/h
A2/B2: 3 Nm³/h
A3/B3: 30 Nm³/h
Solid inventory: 70 kg
Φ: 0.05
ΔP1-A
ΔP1-B
Amplitude
Frequency (Hz)

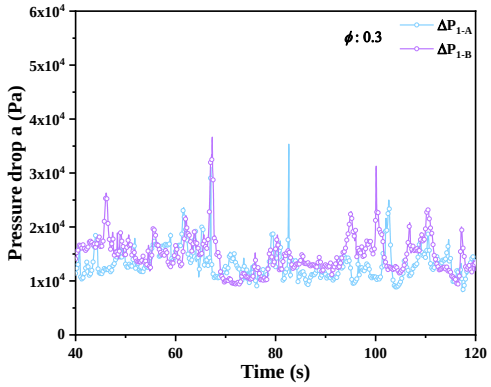
ϕ: 0.3
ΔP1-A
ΔP1-B
Pressure drop a (Pa)
Time (s)

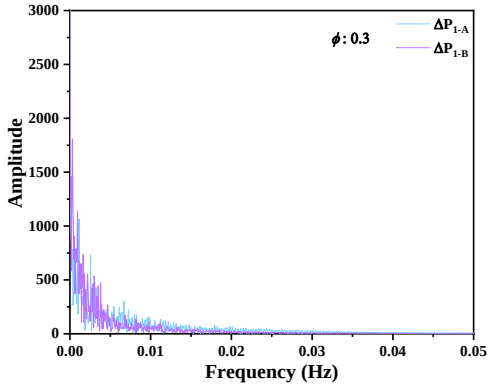
ϕ: 0.3
ΔP1-A
ΔP1-B
Amplitude
Frequency (Hz)

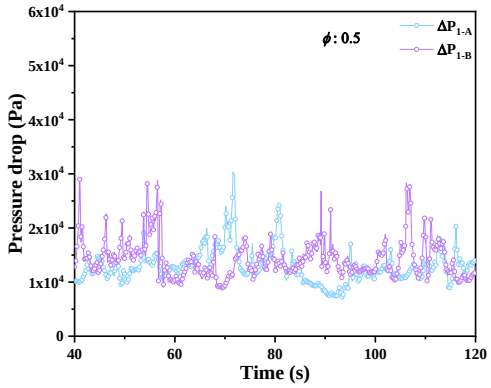
ϕ: 0.5
ΔP1-A
ΔP1-B
Pressure drop (Pa)
Time (s)

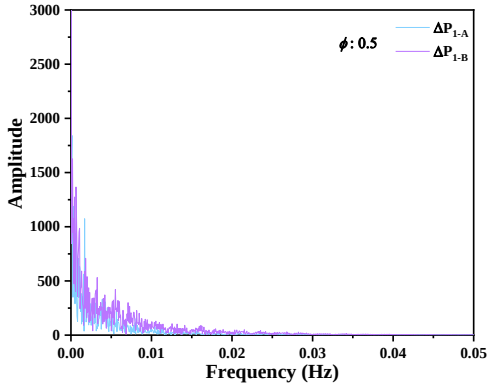
ϕ: 0.5
ΔP1-A
ΔP1-B
Amplitude
Frequency (Hz)

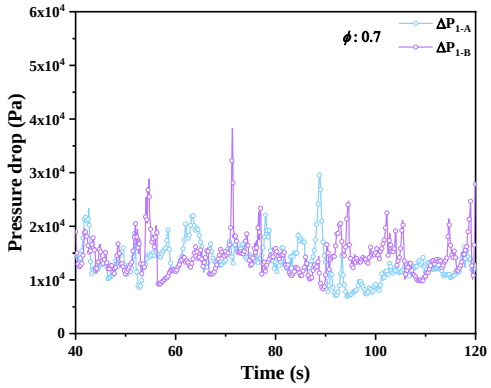
ϕ: 0.7
ΔP1-A
ΔP1-B
Pressure drop (Pa)
Time (s)

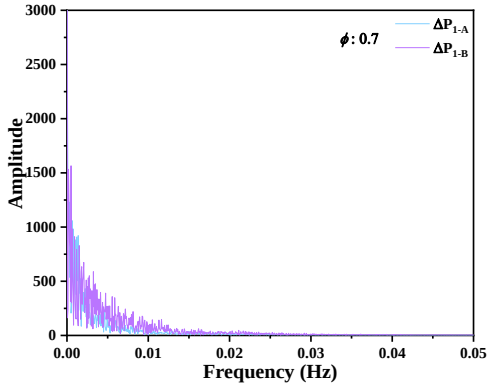
ϕ: 0.7
ΔP1-A
ΔP1-B
Amplitude
Frequency (Hz)

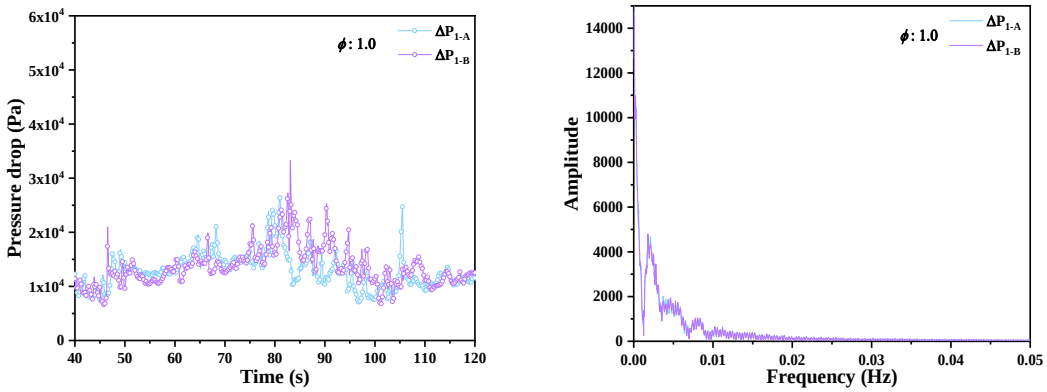

(a) (b)

Fig 6.40. Profiles of the time evolution profiles of ΔP_1(a); the Fourier spectral analysis of ΔP_1 (b) at different wall roughness.

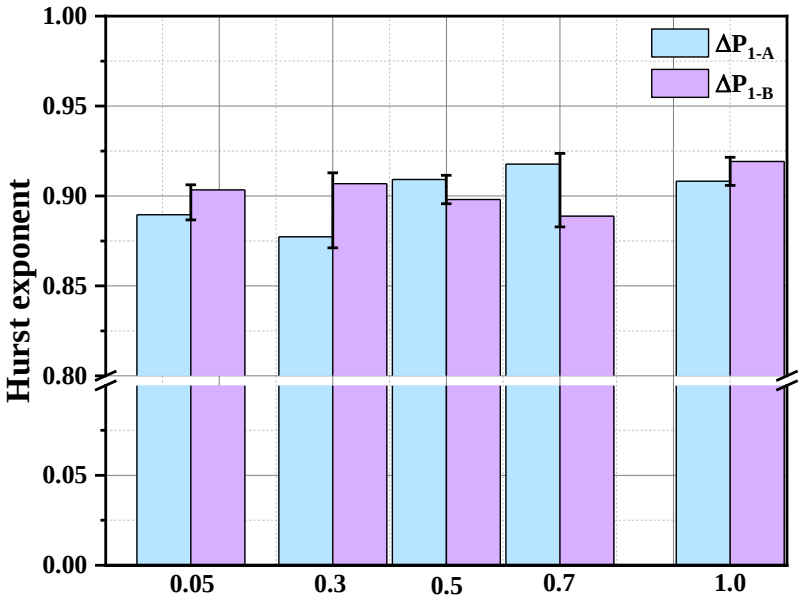

Fig 6.41. Comparison of the Hurst exponent estimated for various subperiod lengths at different wall roughness.

6.2.5 Conclusions

In this work, the non-uniformity of the gas-solid distribution in a symmetrical DCFB CLC unit is numerically studied using a multifluid CFD model based on Eulerian-Eulerian framework. The phenomenon of non-uniformity is discussed by comparing the deviation of bed inventory and flow patterns in unit A and unit B, respectively. Moreover, the effects of total solid inventory, gas aeration rate, and wall roughness on the degree of non-uniformity are comprehensively explored. Based on the numerical results, conclusions can be drawn as follows:

(1) The non-uniformity of gas-solid distribution can be observed in terms of solid mass distribution and local flow patterns in a symmetrical DCFB CLC system with an identical geometry configuration and operating parameters.
(2) Enlarging the total bed inventory increases the relative deviation of non-uniformity (Dev), the pressure fluctuation and the deviation of Hurst exponent, demonstrating the system becomes more unstable.
(3) Elevating the gas aeration rate increases the relative deviation of non-uniformity (Dev), the pressure fluctuation, and the deviation of Hurst exponent, indicating demonstrating the system becomes more unstable.
(4) The specularity coefficient has an uncertain influence on the degree of non-uniformity.

To summarise, the non-uniformity phenomenon is revealed by simulation results, and the influences of several critical operating variables on the degree of non-uniformity are studied. These fundamental mechanism of non-uniformity phenomenon should be helpful for the design and optimisation of CLC processes.

CHAPTER.7 Online Regulation of Maldistribution in a Full-loop CFB by Combining CFD and Process Simulation

Complex CFB units in industries require continuous monitoring and effective control to maintain product specifications and meet safety criteria. In this chapter, an integrated simulation method is firstly established by combining the CFD model and process simulation based on Ansys-Fluent and MATLAB platform. The detail coupling scheme of the Ansys-Fluent and MATLAB platform is described. To fulfill the availability of this method, an example is conducted based on this method to reduce the degree of maldistribution in one symmetrical DRCFB system (chapter 6) through online regulation of L-valve aeration rate and the better operating performance after coupling with the process controller is discussed. This work provides a new numerical method to test and optimise practical industrial CFB processes.

The paper “Online Regulation of Maldistribution in a Full-loop CFB by Combining CFD and Process Simulation” is under revision based on the content of this chapter.

Graphical abstract for this chapter

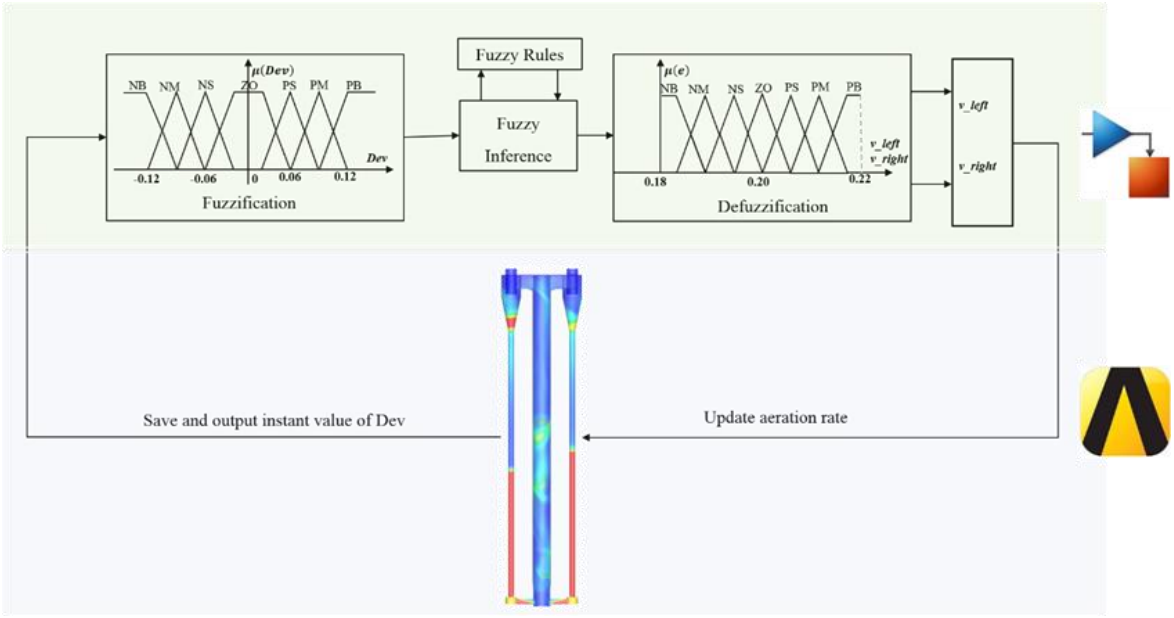

ABSTRACT

Complex CFB units in industries require continuous monitoring and effective control to maintain product specifications and meet safety criteria. In this work, an integrated simulation method is firstly established by combining the CFD model and process simulation based on Ansys-Fluent and MATLAB. An example is conducted based on this method to reduce the degree of maldistribution in one symmetrical DRCFB system through online regulation of L-valve aeration rate and the better operating performance after coupling with the process controller is discussed. This work provides a new numerical method to test and optimise practical industrial CFB processes.

7.1 Introduction

Circulating fluidized bed (CFB) has been widely applied to many chemical engineering processes, such as fluid catalytic cracking [327], coal combustion [328] and gasification [329] due to its good gas-solid mixing, wide fuel flexibility, and excellent heat and mass transfer performance. The critical point for CFB technology is to ensure long-term operational stability. However, some threats (e.g., bed agglomeration, material leakage, even unexplained shutdowns and fire explosion) significantly deteriorate the stability and efficiency of the CFB system. Therefore, to maintain product specifications and meet safety criteria, continuous monitoring and effective control of CFB processes are in urgent need.

Industrial control and automation technologies have benefited many large industrial plants for a long time [330,331]. They receive inputs from sensors, meters and so on, provide control functions, and deliver output control signals to controlled devices in plants. Despite the improvement in automation and information technology, the majority (i.e. 85-95%) of the feedback control loops in the process industries are based on the proportional-integral (PI) and proportional-integral-derivative (PID) control techniques [332–335]. These methods provide a quick control signal to guarantee system stability. However, this kind of simple logic or constraint-based control is commonly limited to simple linear systems [336,337]. Meantime, it is challenging to obtain a well-tunning PID controller for practical industrial chemical engineering processes which are integrated, nonlinear and multivariable systems [338,339]. In recent years, some advanced control algorithms (e.g. fuzzy control, neural networks, genetic algorithms, and expert systems) also have been proposed and applied in various CFB apparatuses from lab-scale to

industrial-scale [340–342]. However, the performance of most advanced control strategies has not been thoroughly tested in the experimental plants because of large lags in current measurement technologies. Due to the lack of comprehensive validation of efficiency, most of the advanced controllers cannot be finely implemented, leading to the difficulty of CFB apparatuses operating at healthy states in the industrial plants [343].

To overcome the above disadvantages of experimental methods, two numerical technologies (e.g. process simulation and CFD) have attracted increasing attention, with the rapid development of computer science [344,345]. Process simulation has been widely used to study individual unit operations as well as multiple interconnected units or even entire plants [5]. Nowadays, many process simulations are available for industrial plants, which offer a variety of solution algorithms, numerical models and component libraries. For example, Sun et al. (2011) [346] established a dynamic model of the Shell gasifier to explore the system performance via changing the oxygen-to-coal and steam-to-coal ratios in integrated coal gasification combined cycle (IGCC). The critical outlet variables, including the gas temperature, slag mass flow rate, thicknesses of slag layer and volume percentages of syngas, were dynamically obtained. Jin et al. [347] established a steady-state model and control system for a 600 MWe oxy-combustion pulverised-coal-fired boiler. The control system, aiming to regulate O_2 concentration in flue gas automatically, was integrated into the boiler model. The designed controller in this model gave a robust performance for different dynamic cases.

To accurately monitor and control the system, the precise flow characteristics and state changes in the CFB system should be well obtained. However, most of the mathematical models in process simulations either ignore all spatial field variations within each unit or

are constrained to simple geometries. Besides, process models include many empirical formulas, which describe physical processes incompletely. Another method to build accurate mathematical models in process simulations is the artificial neural network (ANN) [348–350]. However, its training process may be influenced by indeterministic factors, such as random noise. Besides, to obtain detailed flow and reactions, a considerable dataset is required for the training procedure, which is expensive and time-consuming [351,352]. Therefore, it is challenging to build comprehensive and accurate mathematical models in process simulations.

As another important computer-aided technology, the CFD simulation has become a cost-effective technique for overcoming the disadvantages of experimental methods and process simulations regarding instantaneous multiphase hydrodynamics and reactions in CFB systems. Over the last two decades, CFD simulations have been extensively conducted to unveil thermophysical behaviours in various CFB systems. Li and Shen (2020) [353] numerically modelled the full-loop CFB system using the Eulerian-Eulerian CFD method and the non-uniform distribution of solid holdup were well captured. Zhang et al. (2015) [354] implemented a CFD model based on the Eulerian–Eulerian multiphase framework to simulate the coal gasification processes in a CFB gasifier and the effects of many parameters were explored. To summarise, most of CFD simulations on CFB systems only revealed microscale phenomena based on separate reactor components, and the boundary and operating conditions were fixed during the simulation process without the external adjustment and environment change considered.

In the past many years, these two virtual simulation methods individually grow towards their maturity only in their field. Although the subjects, methods and purposes of the two

virtual technologies are different, the research objects of them are coordinated to improve the performance of chemical engineering processes in the actual industries. They can complement each other in function: the CFD can provide more accurate results than conventional, lumped-parameter unit operation models used in process simulations; and the process simulation can dynamically regulate the CFD boundary and operation conditions according to production demand and environmental change. More information can be obtained, including not only response characteristics of dynamic system performance at macroscale but also the transient in-furnace flow and reaction details at the microscale.

In recent years, a few attempts have been made to combine CFD modelling with process simulation. The most common method is to embed the control algorithm of process simulation into CFD simulation process through user-defined function (UDF), which is a specific tool for ANSYS Fluent [355,356]. The UDF can be dynamically loaded to extend the functionality of the standard solver. However, all previous studies using UDFs adopted simple control logic algorithms due to the problematic implementation of advanced and complex control algorithms (ANSYS Fluent Theory Guide, 2013). Besides, UDF is usually called on a per-cell basis every iteration, which dramatically slows the calculation of the CFD process. Therefore, the interaction of CFD modelling and process control based on UDFs is not an ideal coupling method. Moreover, some coupling methods between CFD packages (e.g., Fluent, CFX) and process platforms (e.g., Aspen Plus, gPROMS, HYSYS) also have been proposed based on some third interfaces such as CAPE-OPEN standards [358], USER3 protocol [359] or TCP/IP protocol [360]. However, the stability and accuracy of third interfaces to transfer data between CFD and process simulation software limits its further application.

To fulfil the knowledge gap, effectively realising the closed-loop modelling of chemical engineering processes by combining CFD and process simulation is an urgent need. In this work, an integrated online regulation method is firstly established to realize the collaborative simulation of the transient CFD model and process control algorithm based on Ansys-Fluent and MATLAB platforms. Then, an attempt to realise the online regulation of the CFB system through collaborative simulation is carried out, and the better operating performance of CFD results after coupling process controller is discussed.

7.2 Computational details

7.2.1 CFD model

Mathematical model

The CFD simulation is performed using ANSYS Fluent 19.2, in which the multiphase Eulerian granular model is used. The drag coefficient is closed by Syamlal-O'Brien drag model [181], which has been validated in our previous simulations of the same model [353], which can be found in section 3.2.3. The governing equations with the standard kinetic theory of granular flow (KTGF) are given in Sections 3.2.1 and 3.2.2.

Geometry, boundary condition and mesh

As shown in Fig. 7.1(a), a lab-scale DRCFB designed by Luo et al. (2017) is used in this work to show the maldistribution phenomenon of the parallel system in the separate CFB device, and as the target device to couple the process control unit. The symmetrical DRCFB consists of a riser and two external loops (consist of a cyclone, standpipe, and L-valve). The riser usually is used as the main reaction regime. The cyclone has a function

of gas-solid separation and collects solid material. The standpipe located below the cyclone is used for material storage. The non-mechanical L-valve can control solid flow circulation. Detailed size of geometry can be seen in Fig. 7.1(a). Particles exit the riser through two symmetric rectangular side ports 0.06 m in height, 0.022 m in width about 1.17 m above the gas distributor and enter the riser from two symmetrically rectangular side ports 0.017 m in edge length and 0.029 m above the gas distributor (from the centre line of the L-valve). The solid particles are sand with a mean diameter of 1.5 mm and a density of 2500 kg/m^3. The total amount of solid inventory in the computational domain is 1.5 kg. The gas inlet is assigned at the bottom of the riser to transport solid materials and two aeration inlets are located at the side of L-valves to recirculate particles to the bottom of the riser with a relatively low aeration rate.

Fig. 7.1(b, c) shows the grids of the DRCFB generated by ICEM to discrete the calculation domain. All the computational domains used in this situation have meshed with structured hexahedron elements. The distribution of grids in two external loops are totally symmetric, which is generated by mirroring.

For the setting of boundary conditions, the velocity inlet boundary conditions are set for aeration inlets at the bottom of the riser and the side of L-valves. The pressure outlet boundary condition is selected for two outlets of the cyclone vortex finder. The Schaeffer frictional model for particle phase and Johnson and Jackson's model [200] for wall boundary conditions of the solid phase is used. The no-slip boundary condition is specified for the gas phase. Different discretisation schemes for convection terms of each governing equation are employed: the second-order upwind scheme is chosen for the momentum equation; the Quadratic Upwind Interpolation of Convective Kinematics (QUICK) scheme is chosen for the volume fraction of gas and solid phases, and the first-

order upwind scheme is chosen for the turbulent kinetic energy and turbulent dissipation rate. The Semi-Implicit Method for Pressure Linked Equations (SIMPLE) algorithm is used to deal with pressure-velocity coupling. The material properties and simulation parameters are listed in Table 7-2.

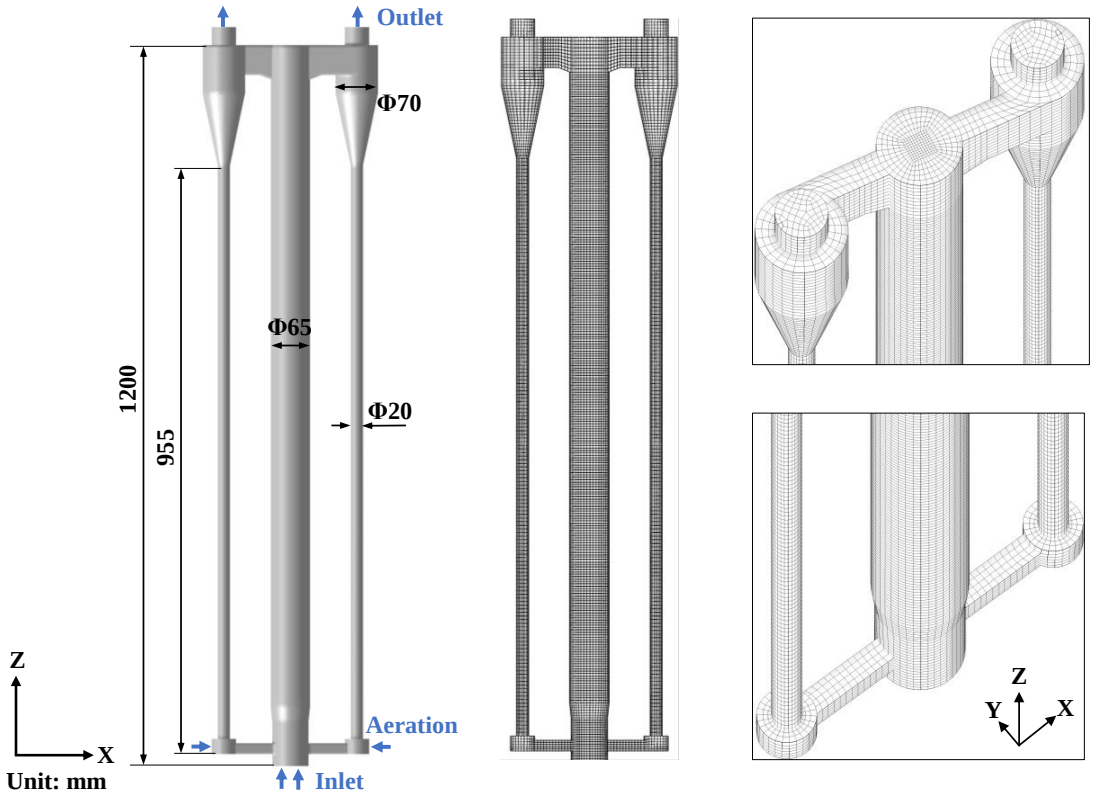

(a) (b) (c)

Fig 7.1. Schematic geometry [295] and grids of the investigated three-dimensional DRCFB: geometry (a); grids of the whole bed (b); grids of local regions (c).

Table 7-1. Gas-solid properties and computational settings for the base case.

Solid Properties	**Values**

Particle density	2500 kg/m^3
Particle size	1.5 mm
Minimum fluidization velocity	1.12 m/s
Restitution coefficient of particles	0.95
Restitution coefficient of particle and wall	0.95
Specularity coefficient	0.5
Angle of internal friction	30°
Friction packing limit	0.60
Packing limit of particles	0.63
Gas Properties	
Gas inlet velocity	8 m/s
Aeration gas velocity	0.2 m/s
Gas density	1.225 kg/m^3
Gas viscosity	1.837×10^{-5} Pa·s
Computational Settings	
Pressure-velocity coupling	SIMPLE
Drag model	Syamlal and O'Brien
Time step	1×10^{-4} s
Max. number of iterations per time step	50
Convergence criteria	10^{-4}

Problem description

Multiple identical paths are usually connected to form circulating loops in industrial reactors. The equal allocation generally is expected among multiple identical paths.

However, the flow pattern has been proven highly non-uniform in these identical paths, compromising the stability. In our previous work [353], the characteristics of the gas-solid distribution in a symmetrical DRCFB is numerically studied by a CFD multifluid model based on the Eulerian-Eulerian framework. The results demonstrate that even in a symmetrical DRCFB system, the unbalance solid distribution inevitably appears, as shown in Fig 7.2. This non-uniformity phenomenon is commonly termed as maldistribution [298,299]. In steady operation, chemical reactions will be affected by the disturbances in the feed-rate of the fuel and by the incomplete mixing of the fuel in the bed, which may cause changes in the burning rate, oxygen level and increase CO emissions. Moreover, the mass imbalance causes a deflection of the centre of gravity position of the device, which is unfavourable and unsafe for the long-time running of CFB systems. Therefore, it is necessary and urgent to reduce the maldistribution phenomenon in large chemical CFB systems by coupling with the online regulation.

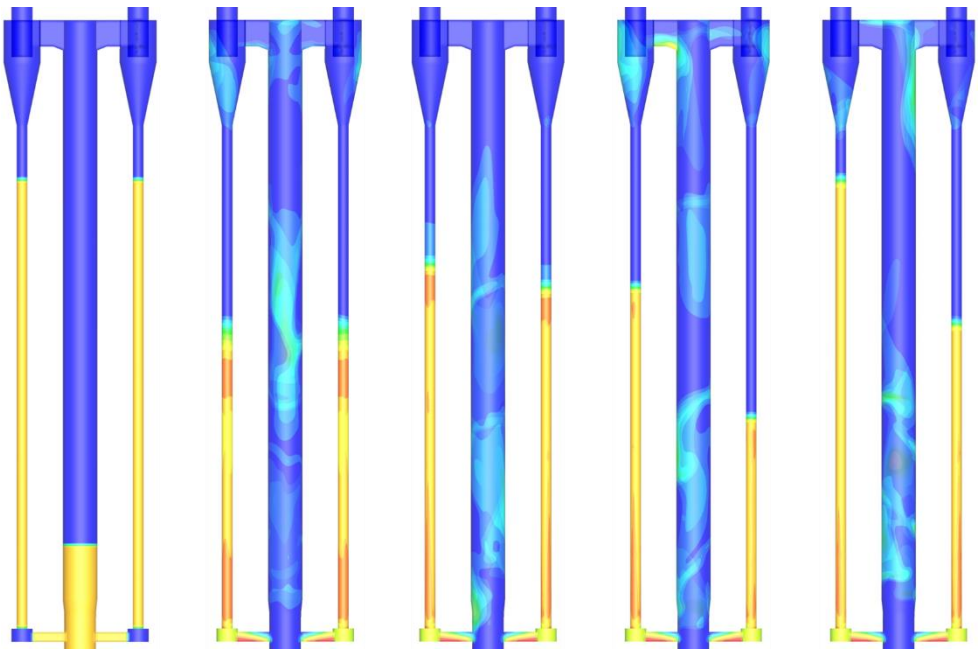

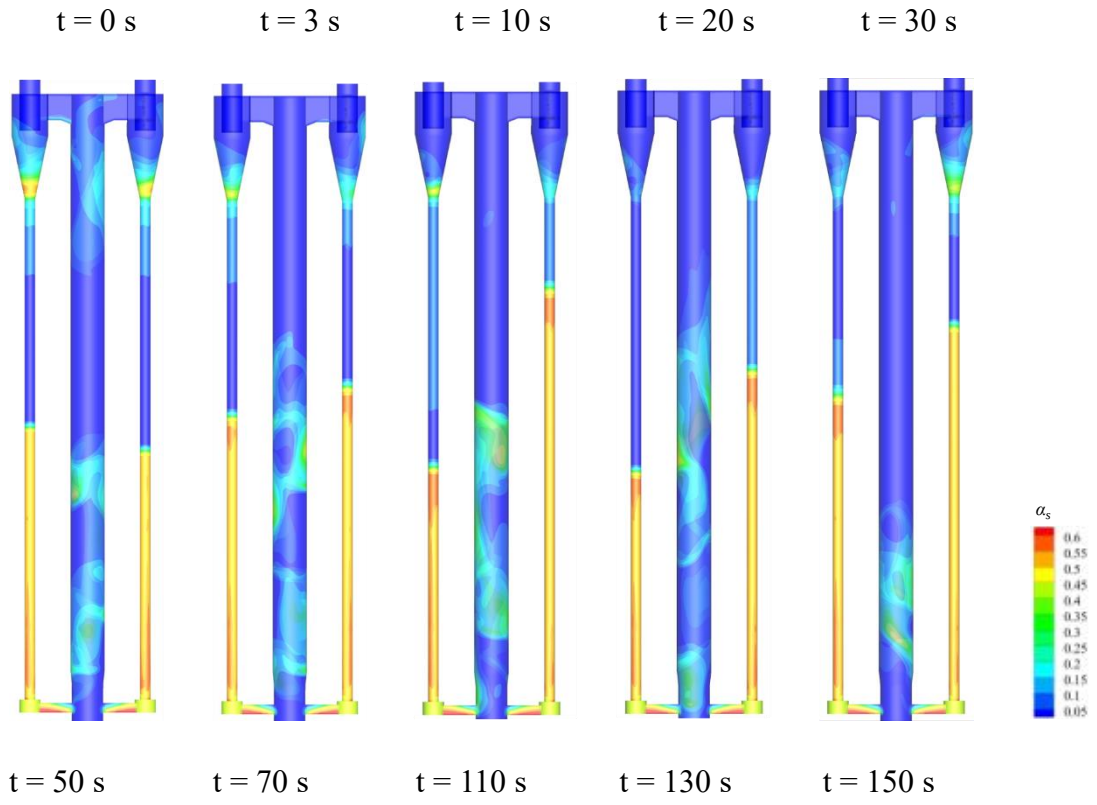

Fig 7.2. Contours of instantaneous solid volume fraction in the DRCFB.

To quantitatively quantify the maldistribution between two external loops in the CFD simulation, the relative deviation (Dev) of bed inventory is proposed to define the degree of maldistribution:

$$\mathrm{Dev} = \frac{m_l - m_r}{m_l + m_r} \tag{7-1}$$

where m_l and m_r are the mass in the left and right external loops, respectively. The magnitude of Dev is a number between 0 and 1. The value of 0 represents the solid mass is same in both external loops, which is an ideal distribution. The value of 1 represents all particles transported into one external loop and the other one is empty, which is the worst situation. And the sign of the Dev represents the position: when it is positive, it means the left side has more bed inventory. Conversely, when it is negative, it represents

the right side has more bed inventory. According to the magnitude and sign of Dev, the aeration rates at the side of L-valves are controlled to adjust the mass distribution in two external loops. Therefore, the objective of this work is to reduce the magnitude of Dev through the online regulation of the L-valve aeration rate by coupling Ansys-Fluent and MATLAB.

The grid independence test, the symmetry of the computational domain and the model validation have been done in our previous CFD work [353].

7.2.2 Control algorithm

MATLAB is an integrated and technical computing environment that combines numeric computation, advanced graphics and visualisation, and a high-level programming language. In industry, it is the tool of choice for high-productivity research, development, and analysis, used in control system design. Therefore, the MATLAB platform is chosen in this work to design the part of process simulation.

Simple logic controller

For verifying the feasibility of collaborative simulation, a simple logic controller written by M file in MATLAB is used to dynamically regulate the CFB system to imitate the manual adjustment during experiments at first. This controller emulates the manual control in experiments to make the *Dev* below a set value and the L-valve aeration rate increases or decreases with a fixed increment according to the transient value of the *Dev* output defined in eq (7-1). The flow chart of the simple logic controller is shown in Fig 7.3. It can be seen that the set value in this work is 0.03: it means when the magnitude of

Dev is less than 0.03, the system is regarded as a balanced distribution; when the magnitude of transient Dev is out of range, the controller will respond and change the L-valve aeration rate according to rules. Besides, to maintain stable operating conditions, the change range of the L-valve aeration rate is limited to [0.18, 0.22].

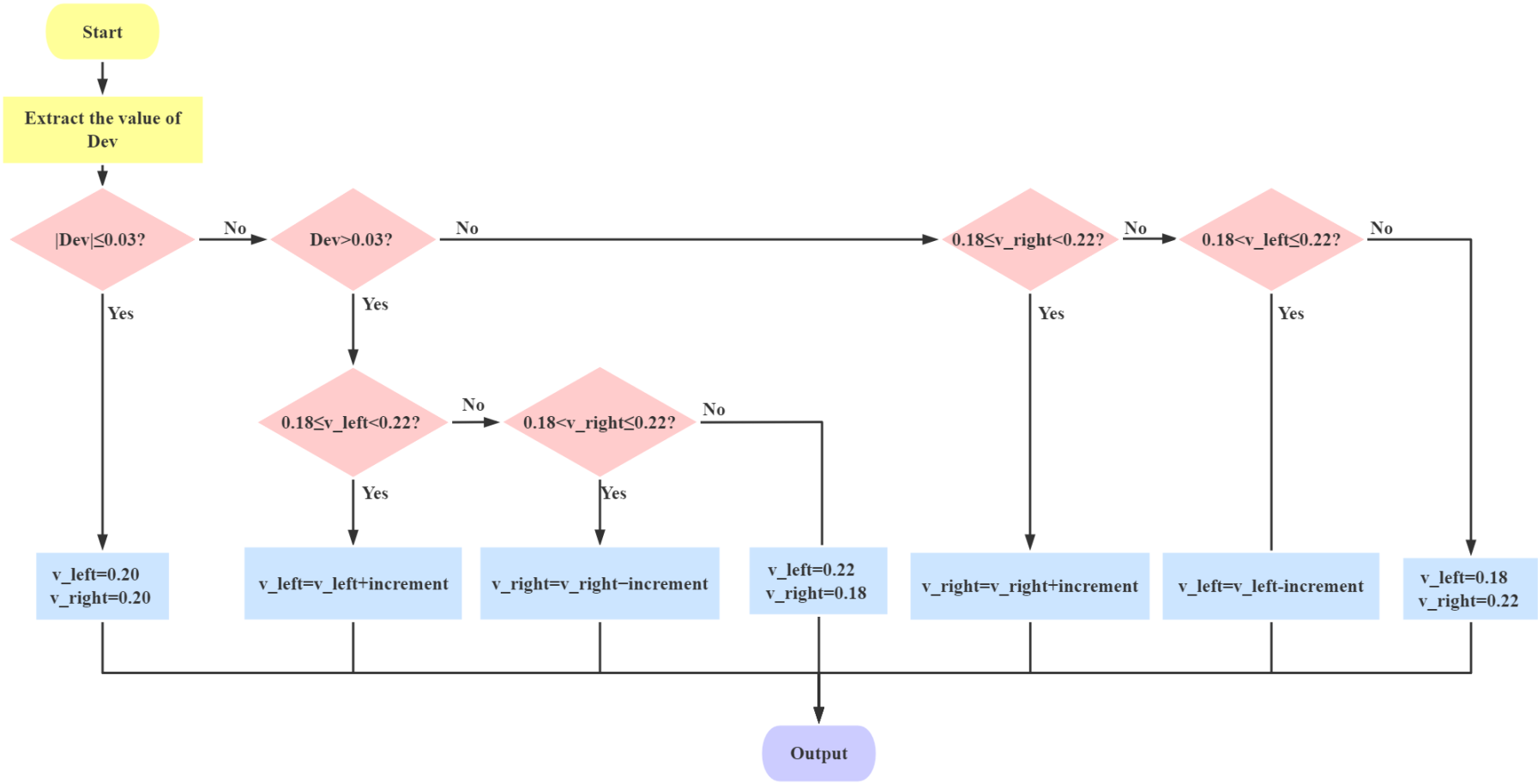

Fig 7.3. Flow chart of the simple logic controller.

Artificial intelligence control system design

Artificial Intelligence (AI) algorithms are becoming beneficial as substitute methods to conventional approaches or as components of incorporated systems. They have been utilised for solving complex applied problems in different fields and are becoming more and more popular at present [361,362]. Fuzzy logic control (FLC) is one of the useful intelligent control schemes for plants having difficulties in deriving mathematical models or having performance limitations with conventional linear control methods [363,364].

In this work, the Fuzzy Logic Toolbox in MATLAB/Simulink is utilised to a single-input and multiple-output (SIMO) Mamdani's Fuzzy Inference System [365] for the DRCFB system. The closed-loop framework of CFD model and FLC used in this work is depicted in Fig 7.4. Firstly, the CFD model dynamically outputs the instantaneous values of maldistribution degree *Dev*, which is the user-defined variable by Eqn (8-1). Then, the fuzzifier maps the crisp input (*Dev*) to fuzzy input sets (*e)* with the membership functions, that is, $e = f(Dev)$. The f is a nonlinerar function that is formed by fuzzy logic operations and mathematics of fuzzy sets. The membership functions are presented in the form of trapezoid, triangle, S-shape and Z-shape. Similarly, the linguistic variables *v1* and *v2* are chosen to describe the time variation of the two manipulated variables: the aeration rate at the left and right side in this work, respectively. The inference engine uses 7 IF-THEN fuzzy rules to generate fuzzy outputs according to the fuzzy input signal, which is set by summarising the real experimental experience, as shown in Table 7-2. And the change range of the L-valve aeration rate is limited to [0.18, 0.22] to avoid changing the flow pattern in standpipes.

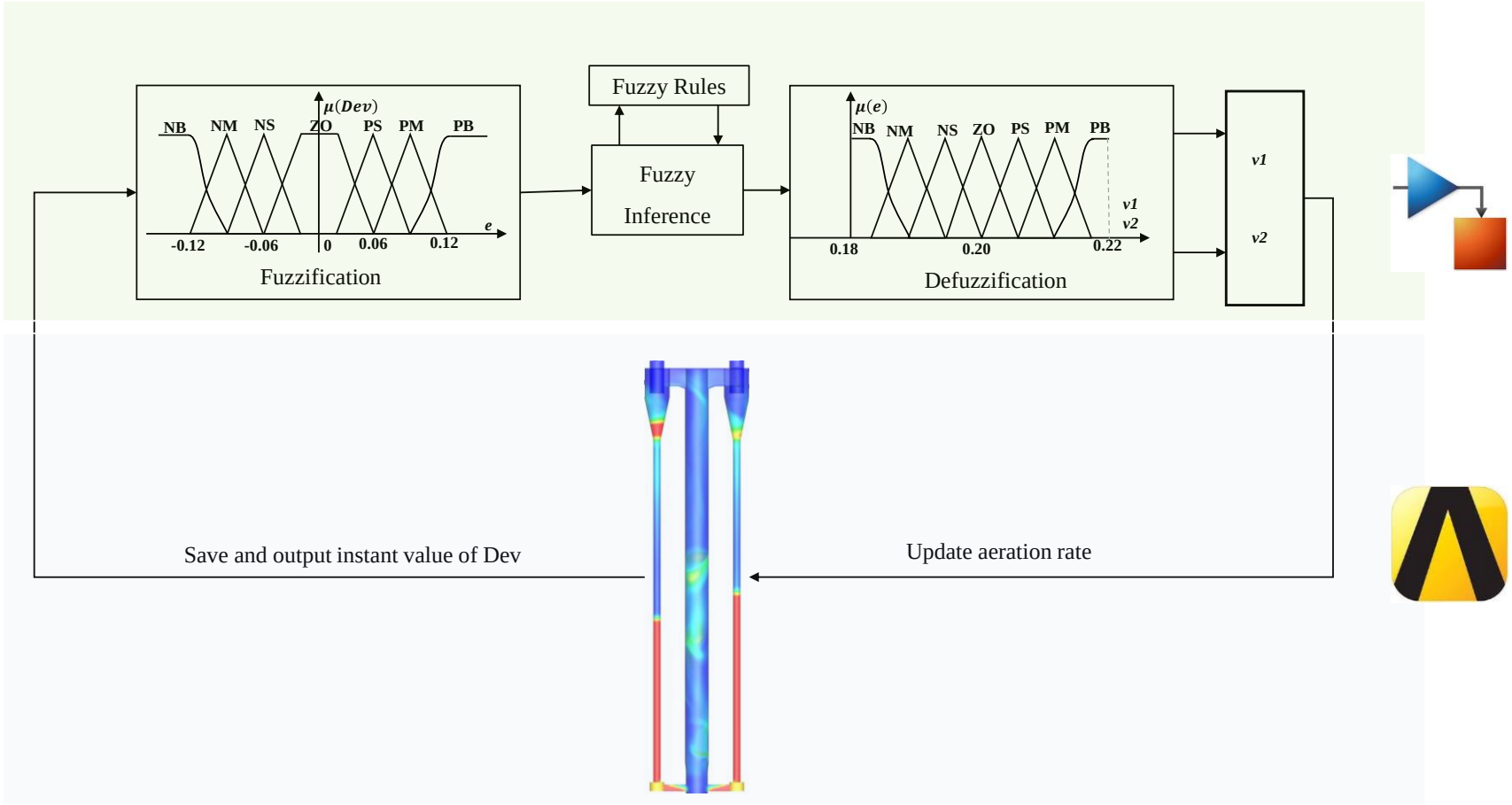

Fig 7.4. The scheme of the close loop composed by FLC framework and CFD model in this work.

Table 7-2. IF-THEN fuzzy rules

*IF (**Dev is NB**) THEN (**v1 is NB**) (**v2 is PB**)*
*IF (**Dev is NM**) THEN (**v1 is NM**) (**v2 is PM**)*
*IF (**Dev is NS**) THEN (**v1 is NS**) (**v2 is PS**)*
*IF (**Dev is ZO**) THEN (**v1 is ZO**) (**v2 is ZO**)*
*IF (**Dev is PS**) THEN (**v1 is PS**) (**v2 is NS**)*
*IF (**Dev is PM**) THEN (**v1 is PM**) (**v2 is NM**)*
*IF (Dev **is PB**) THEN (**v1 is PB**) (**v2 is NB**)*

7.2.3 Coupling method

There are two direct ways that can be used to realise the collaborative simulation of the CFD model and process controller. The first method is hooking a UDF in ANSYS Fluent along with the relevant control algorithm, and the UDF can be dynamically loaded by the ANSYS Fluent solver to call instantaneous simulation results and modify modelling setting according to control code. The second method is using the ANSYS Fluent as a Server (aaS) toolbox which establishes a connection between ANSYS Workbench and MATLAB directly. All the design variable or boundary conditions here can be established or changed using a MATLAB script. Two direct coupling methods are compared from different aspects, discussed in Table 7-3.

Table 7-3. Comparison of two direct coupling method

Coupled method	**UDF**[a]	**MATLAB**[b]
Specific users	Only used by ANSYS Fluent users	• Widely used in various disciplines. • A common tool for process control
Functionality	• Customisation of boundary conditions. • Material property definitions. • Surface and volume reaction rates. • Source terms in transport equations. • Source terms in user-defined scalar (UDS) Transport equations. • Diffusivity functions etc. *Not all solution variables or ANSYS-FLUENT models can be accessed by UDFs.	Local or remote client applications to access the full power of the ANSYS Fluent solver.
Operation mode	UDFs are called on a once-per-iteration basis.	Fluent and MATLAB work Alternatively.
Implementation of control algorithms	• Suitable for simple control algorithm. • Difficult to transplant a complex control algorithm to UDF format. • Complex algorithms can seriously slow down the computational efficiency.	• There are professional control system toolbox and Simulink. • Operation efficiency is relatively high.

[a.] The characters of UDF coupling method are summarised from ANSYS Fluent UDF manual [366].

[b] The characters of MATLAB coupling method are summarised from ANSYS Fluent as a Server User's Guide [366].

As summarised in Table 7-3, realising the collaborative simulation of ANSYS Fluent and MATLAB is of great significance for both disciplines. MATLAB is used to perform an interactive simulation with ANSYS Fluent working as a server. These two software packages communicate with one another through aaS toolbox, which is a set of tools and functionality used to access the full power of the ANSYS Fluent Solver. The interface, named ANSYS_aaS MATLAB toolbox, is developed and officially supported by ANSYS. Details of the approach are provided in Table 7-4 and Fig 7.5.

Table 7-4. Description of the coupling approach between ANSYS Fluent and MATLAB

Tools	• ANSYS Fluent • MATLAB
Interface	• ANSYS Fluent output file • Fluent journal file • ANSYS_aaS MATLAB toolbox
Fluent Functionality	• CFD solver: provide detailed dynamic flow information. • Execute remote commands from MATLAB to update simulation setup, modelling parameters and boundary values • Save simulation results and output parameter values being monitored and analysed by MATLAB codes
MATLAB Functionality	• Check and analyse simulation results from Fluent • Refresh the simulation setup, modelling parameters and boundary values according to the control algorithm • Send TUI commands to Fluent to modify simulation conditions

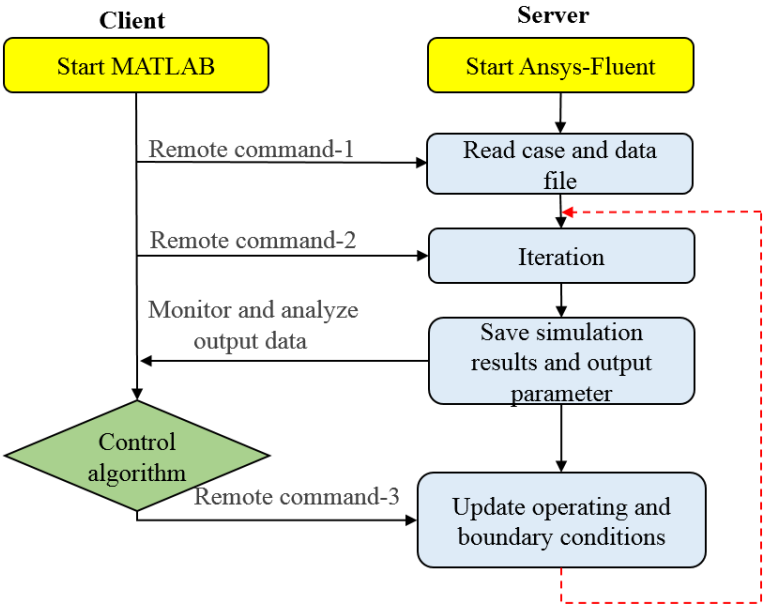

Fig 7.5. Flow chart for the MATLAB-Fluent coupling method.

7.3 Results and discussions

To illuminate the feasibility of this coupling method for CFB operating system, the collaborative simulation system is built by coupling CFD model with the online controller of the L-valve aeration rate to reduce the degree of maldistribution. In this section, the control effects of two control schemes set in Section 7.2 are discussed and compared with original CFD results without external control. Before the controller is added, the individual DRCFB model will run 20 s to build the circulation loop.

7.3.1 Simple logic controller

For complex full loop CFB systems, there is a large time-delay responding to the operation and boundary regulation. Therefore, a suitable sampling time should be selected to achieve the optimal control effect. In this simple control scheme, three different sample times of 5 s, 10 s, 15 s are chosen in the controller to retrieve and analyze simulation results from Ansys Fluent and send commands to modify the transient aeration rates in

CFD model. It can be seen from Fig 7.6(a) that L-valve aeration rates are regulated dynamically according to the degree of maldistribution Dev in the system during the collaborative simulation process. The transient values of Dev have been suppressed to a certain extent for all sampling times after coupling the process control unit compared with the original CFD results, as shown in Fig 7.6(b). In order to better consider the long-lasting effect of the controller on the DRCFB unit, the instantaneous value is averaged every 10s (Fig 7.6(c)). Through the time-average value of Dev, it can be found that when the sample time is 10s, the system can maintain the balance distribution without strong fluctuation in the whole simulation time which means the material distribution is more balanced across the entire system.

Meantime, it can be seen from Fig 7.6(a) that each time the only one aeration rate changes at a fixed increment for this simple logic controller design. It is more suitable for small and simple devices, but for some large complex devices, the system may cost a lot of time to achieve the optimal regulation state

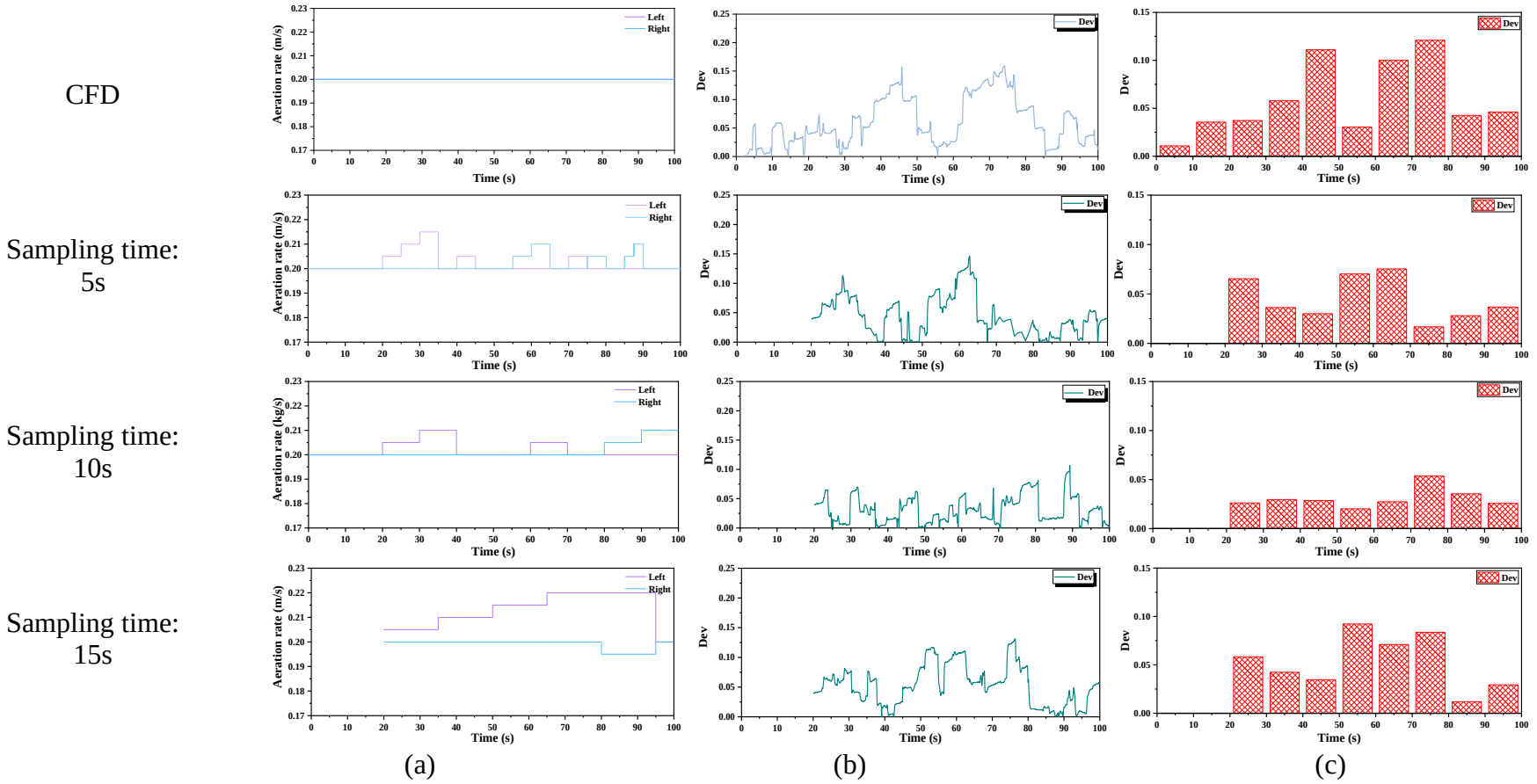

Fig 7.6. Time-evolution profiles of transient aeration rate at the left and right L-valve inlet (a); the transient value of *Dev* (b); Statistic Dev averaged every 10 seconds (c).

7.3.2 Fuzzy logic controller

As shown in Fig 7.7, the FLC regulates both aeration rates according to the real-time value of Dev and fuzzy rules designed in section 7.3.2. The transient values of Dev in the system are suppressed to a certain extent for all sample times compared with the original CFD results. When the sampling time is 10 s, the control effect is optimal along the whole simulation time where the material distribution is more balanced in the system. Therefore, the sampling time of 10 s is taken as an example to further analyze the improvement of system stability after the coupling control process.

To give an intuitive display of the effect of process controller on the degree of maldistribution Dev during simulation, Fig 7.8 illustrates the transient solid distribution in the 3D full-loop DRCFB at t= 40, 70, 100s. It is noted that the solid maldistribution phenomenon can be observed in the DRCFB external loops in most of the simulation time for both cases without and with the controller (Fig 7.8 (a)(b)). However, the addition of real-time controller into the system has a significant function to balance the distribution of the solid material in external loops. It makes, the solid volume fraction becomes more uniformly dispersed in two standpipes compared with the original CFD results at the same time shown above, in which the system is in a more stable state of operation

CFD

Sampling time: 5s

Sampling time: 10s

Sampling time: 15s

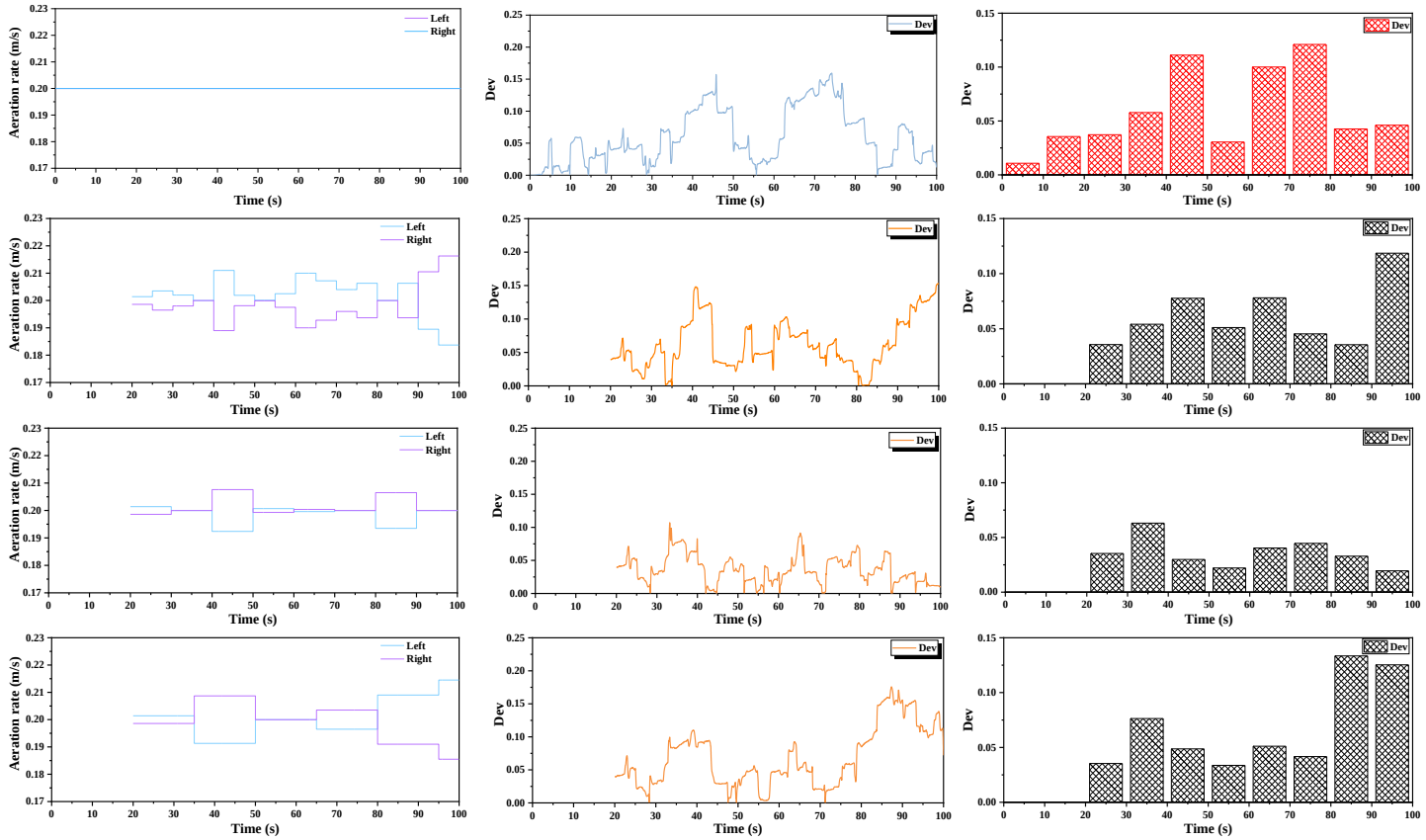

(a) (b) (c)

Fig 7.7. Time-evolution profiles of transient aeration rate at the left and right L-valve inlet (a); the transient value of Dev (b); Statistic Dev averaged every 10 seconds (c).

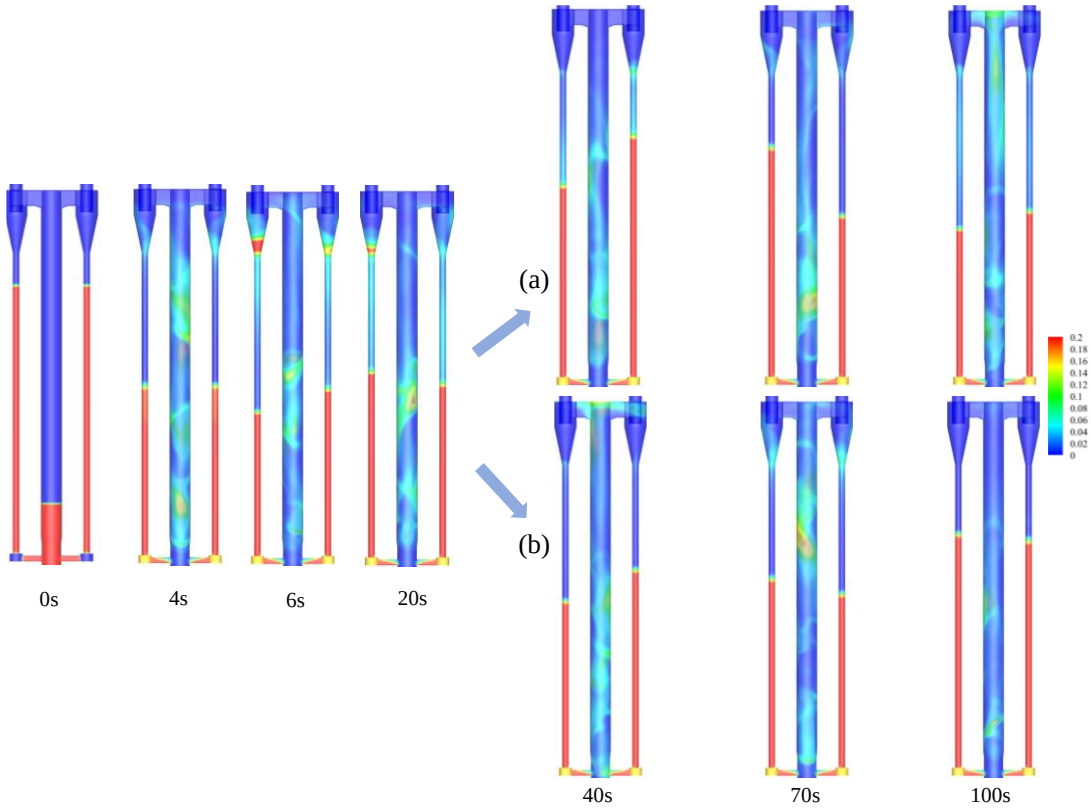

Fig 7.8. Contours of transient solid volume fraction in the DRCFB without controller (a) and with controller (b).

Fig 7.9 (a)(b) present the time-averaged distribution of the solid volume fraction of full-looping system without and with the process controller, respectively. The difference of time-averaged bed height decreases after adding the process controller comparing with the original DRCFB system. Although there is an instantaneous mass imbalance in the system during the operating process, the solid distribution is relatively balanced after coupling with the controller in a relatively long-term period, in which the statistic state is more valuable for the operation of industrial devices.

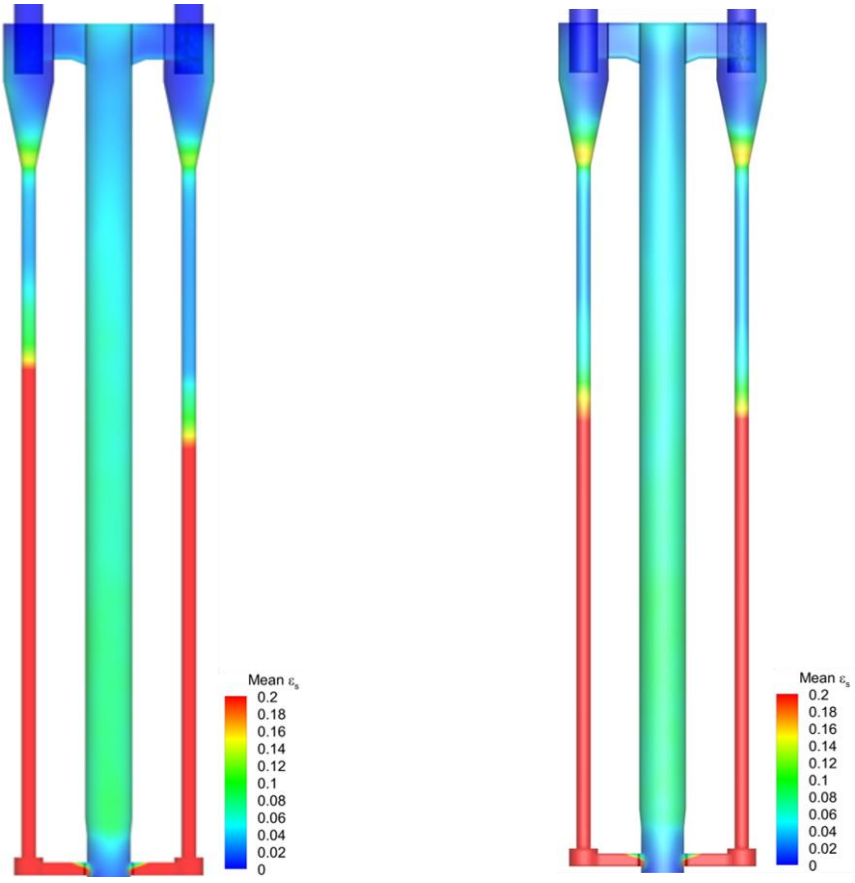

(a) (b)

Fig 7.9. Contours of time-averaged solid volume fraction in the DRCFB without controller (a) and with controller (b).

In addition to the solid volume fraction, the pressure fluctuation characteristics in CFBs is critical to be studied when the boundary conditions in the system are adjusted dynamically. For the DRCFB unit, the equilibrium pressure distribution is an essential factor to keep the system stable. Fig 7.10 shows the time-averaged pressure distribution of the full-looping DRCFB system without and with the process controller, respectively. Significantly, the pressure distribution in two standpipes is different in the original CFD results, where the inflection points of pressure distribution occur around 0.7 m at the left standpipe but 0.6 m at the right standpipe due to the transition from dilute phase to dense phase. It is a direct reflection of different bed heights. After coupling with the real-time controller, the bed height of two inflection points of pressure distribution is more symmetrical than original CFD results.

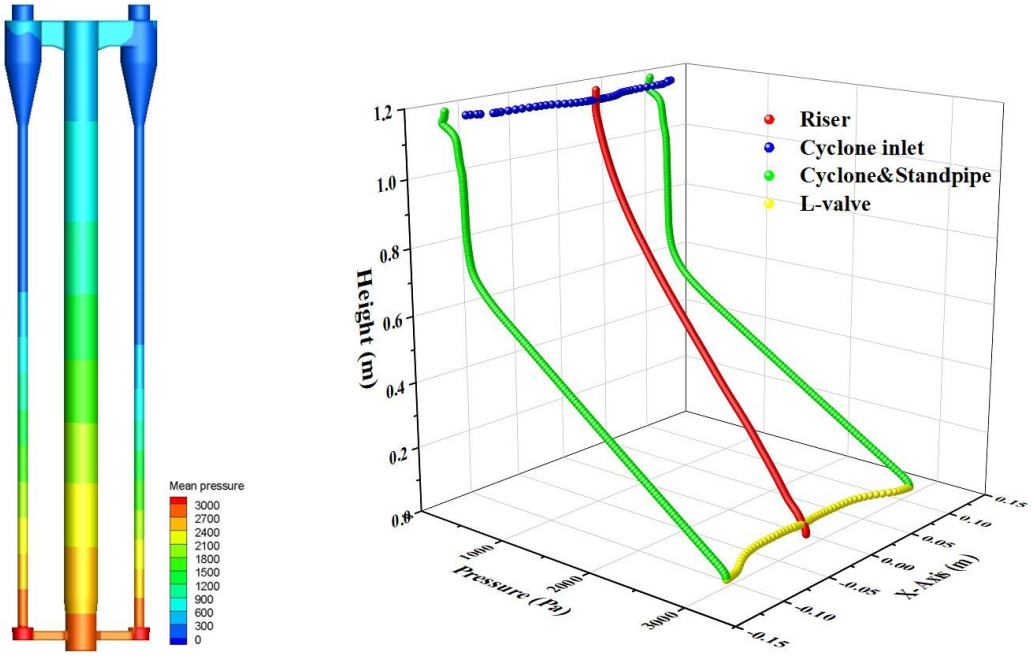

(a)

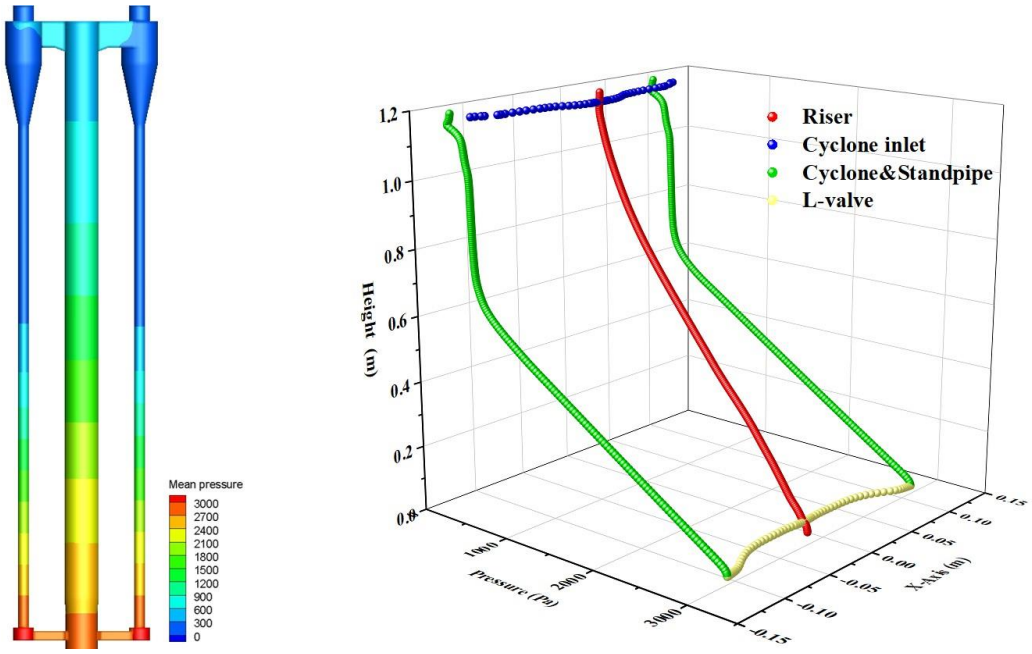

(b)

Fig 7.10. Full-loop distribution of the time-averaged pressure without controller (a) and with controller (b).

Fig 7.11 shows the fluctuations of pressure drop with time across the left and right external loops with and without process controller, respectively. Here, the pressure drop

of the external loop is computed as the pressure difference between the cyclone inlet surface and L-valve outlet surface of this symmetrical DRCFB unit. The time-evolution pressure drop of each case randomly oscillates around a fixed value. It is noted from Fig 7.11 (a) that the difference of pressure drop between left and right external loops increases slightly after coupling process controller because of the different aeration rates at the L-valve that are adjusted according to the transient value of Dev. However, because standpipe can balance the pressure drop automatically, the difference between left and right pressure drop is very limited, which shows that the dynamic change of boundary conditions will not cause an obvious pressure imbalance. To further compare the difference of pressure fluctuation between systems without and with process controller, the Fourier spectral analysis of two pressure drops is reached, as shown in Fig 7.11 (b). It can be seen that the values of dominant frequency and magnitude over left and right external loops show apparent differences. After coupling with the real-time controller, both the dominant frequency and magnitude of pressure fluctuation over two external loops decrease, demonstrating the improvement of solid uniformity and stability.

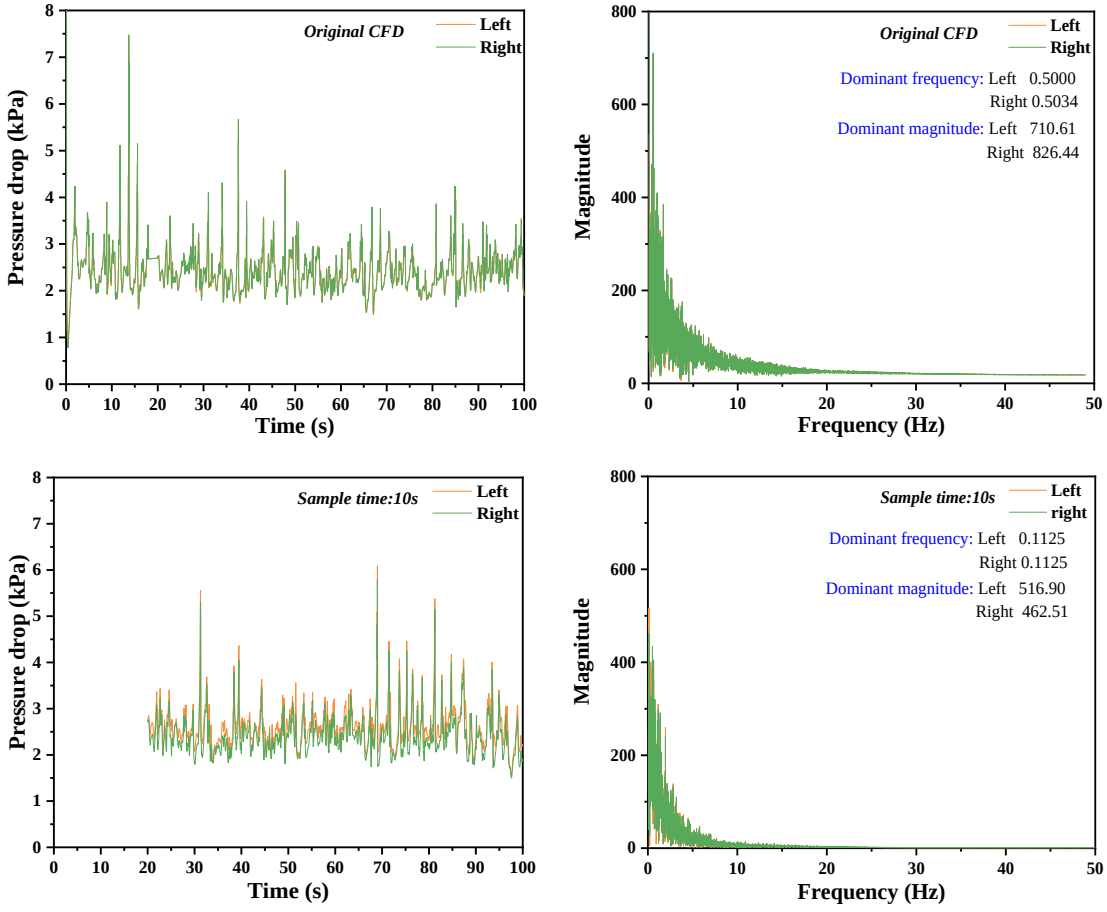

(a) (b)

Fig 7.11.Time-evolution profiles of pressure drop (a) and Fourier spectral analysis of pressure drop (b) in the external loops.

Fig 7.12 (a)(b) shows the time-evolution profiles of solid mass flux monitored at the left and right cyclone inlets. It can be seen that the solid flux has drastic fluctuations over the entire simulation time and the peak of transient value alternates between two cyclone inlets. In order to compare the difference better, the transient deviation of solid flux between the left and right cyclone inlet is calculated, as shown in Fig 7.12 (c). It shows that during the whole calculation time, the fluctuation range of standard deviation of solid flux has limited difference for two cases, all below 1.0. And the time-averaged deviation of the case with process controller slightly decreases, as shown in Fig 7.12 (d), which means a more balanced operating condition between two cyclones after adding the controller. The scale of the DRCFB unit in this work is small, resulting in a slight flow difference. In the actual industrial CFB units with hundreds of tons of solid material, the deviation will be larger.

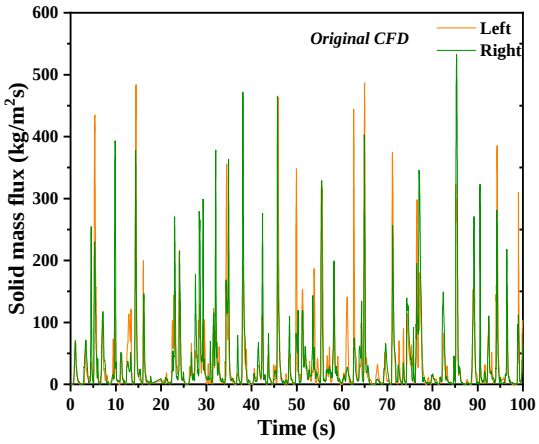

(a)

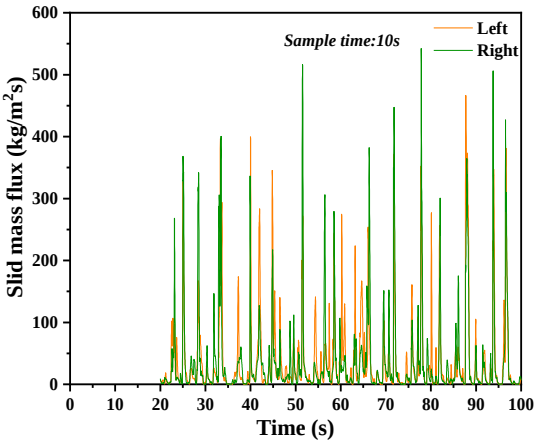

(b)

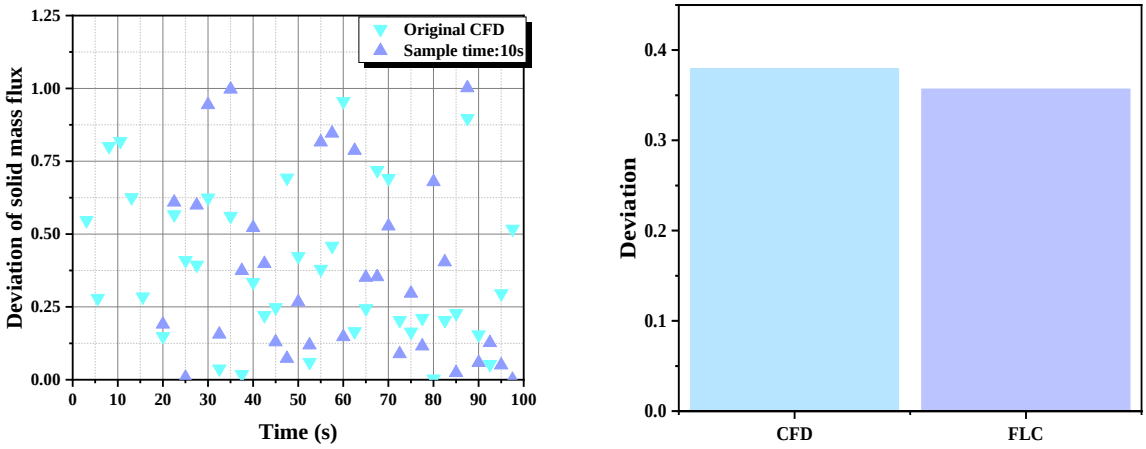

(c) (d)

Fig 7.12. Time-evolution profiles of solid flux without the process controller (a) and with the process controller (b); transient deviation of solid flux (c); time-averaged deviation of solid flux (d) at the inlet of cyclones.

Fig 7.13(a) shows the time-evolution profiles of the solid flux at the L-valve outlet, which represents the amount of material returned to the bottom of the riser. The solid flux is more stable over time compared with the changing of solid fluxes at the cyclone inlet (Fig 7.13). In order to illustrate the difference, the transient deviation of solid flux between the left and right L-valve outlet is calculated, as shown in Fig 7.13(c). It shows that during the whole calculation time, the fluctuation range of standard deviation of solid flux is narrow, most of them below 0.08. And the time-averaged deviation of the case with the process controller is significantly lower than the original CFD result, which means a more uniform feeding at the bottom of the reactor.

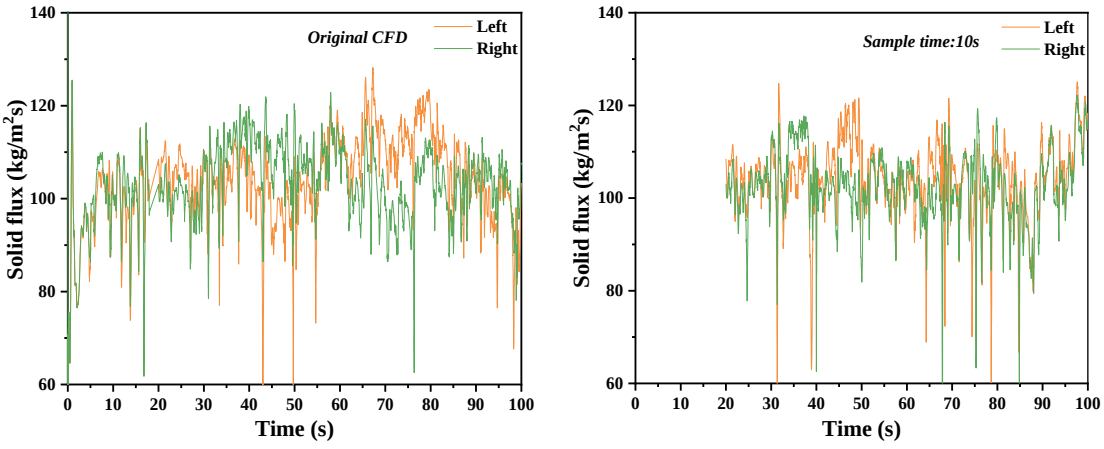

(a) (b)

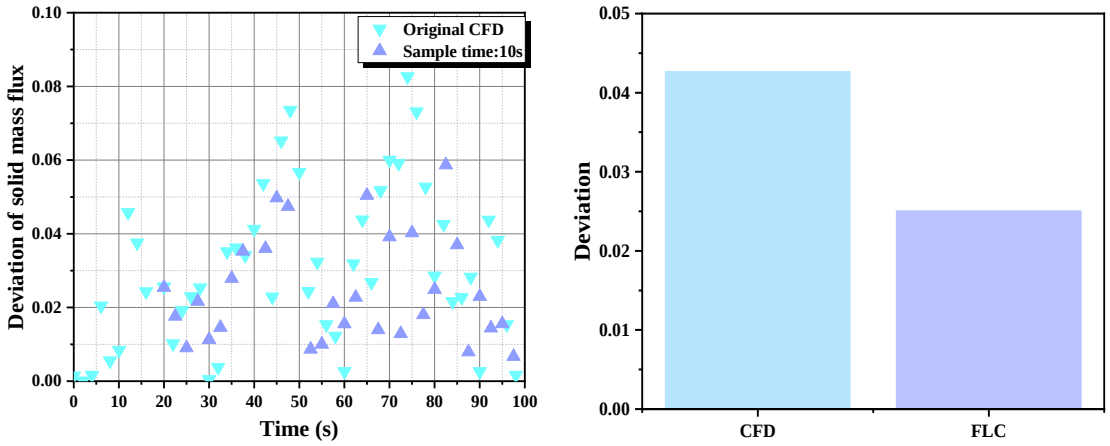

(c) (d)

Fig 7.13. Time-evolution profiles of solid flux without the process controller (a) and with the process controller (b); transient deviation of solid flux (c); time-averaged deviation of solid flux (d) at the outlet of L-valve.

Fig 7.14 shows the time-averaged distributions of solid volume fractions at different heights in the riser. It is worth noting that the values of solids volume fraction are higher at the centre comparing with the wall which is a special phenomenon of Geldart D type particles at high superficial gas velocity-high solids flux conditions called the anti-core-annulus structure [297,367]. By comparing the distribution of solid volume fraction from both radial and axial directions of the riser (Fig 7.14 (a)(b)), it can be seen that the particle holdup distribution in the riser has changed little after adding the controller, which is because the dimension of the DRCFB unit used in this work is too small to show the significant difference. According to practical and theoretical experience, the more balanced bottom-feed rate will make the material distribution more uniform in the reactor with a larger cross-section area. This characteristic is beneficial for more efficient energy and product output.

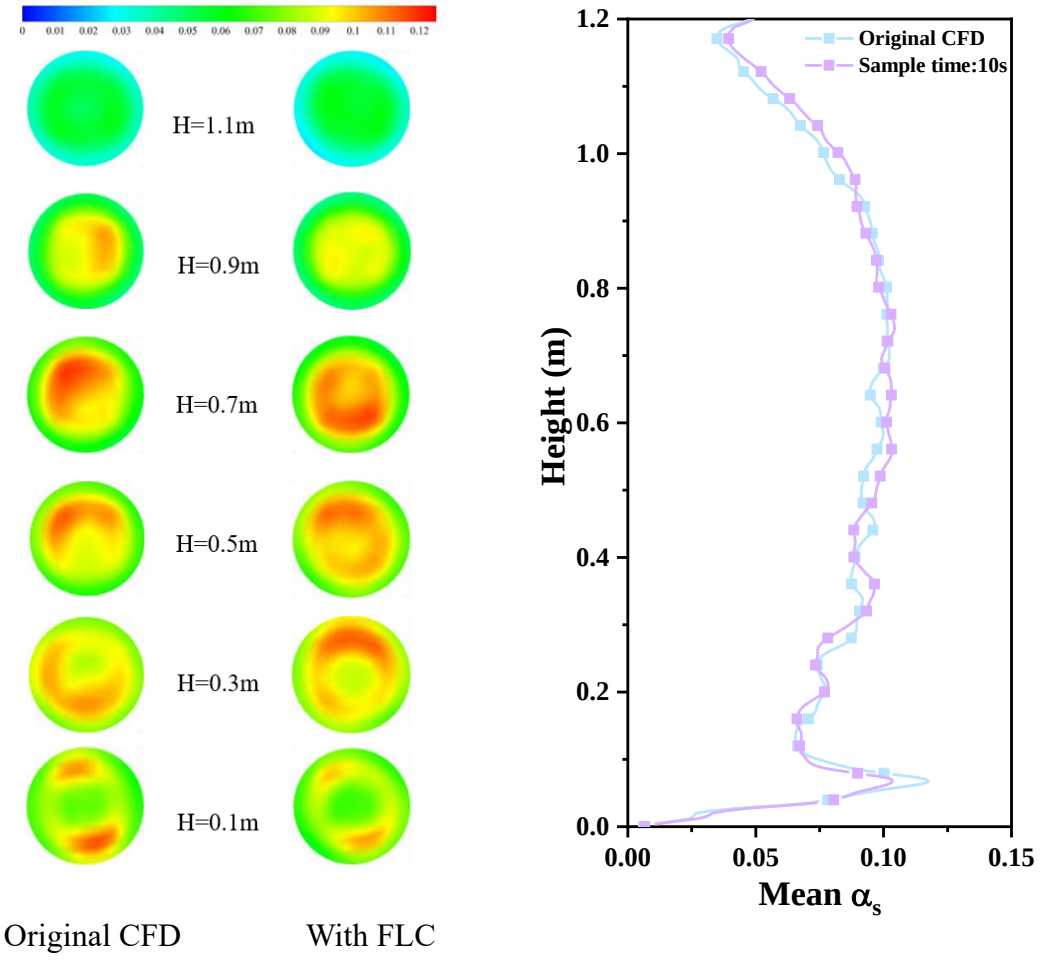

Fig 7.14. Contour of time-averaged solid volume fraction with several horizontal cross sections at different heights of the riser (a); profiles of time-averaged solid volume fraction along the central line of the riser (b).

Fig 7.15 illustrates the time-averaged solid vertical velocity at different heights of the riser. It indicates that the range of solid back-mixing is narrowed after coupling with the process controller, where particles move downward with negative velocities in the centre at the range of 0.3965 m< Z < 1.0697 m for the original CFD case but 0.5368 m< Z < 1.0817 m for the case with the process controller. The back-mixing behaviour of solids affects both the reaction rate and reaction time which is generally a reflection of poor gas distribution in the riser and strongly decreases the chemical reaction conversion and selectivity [368,369].

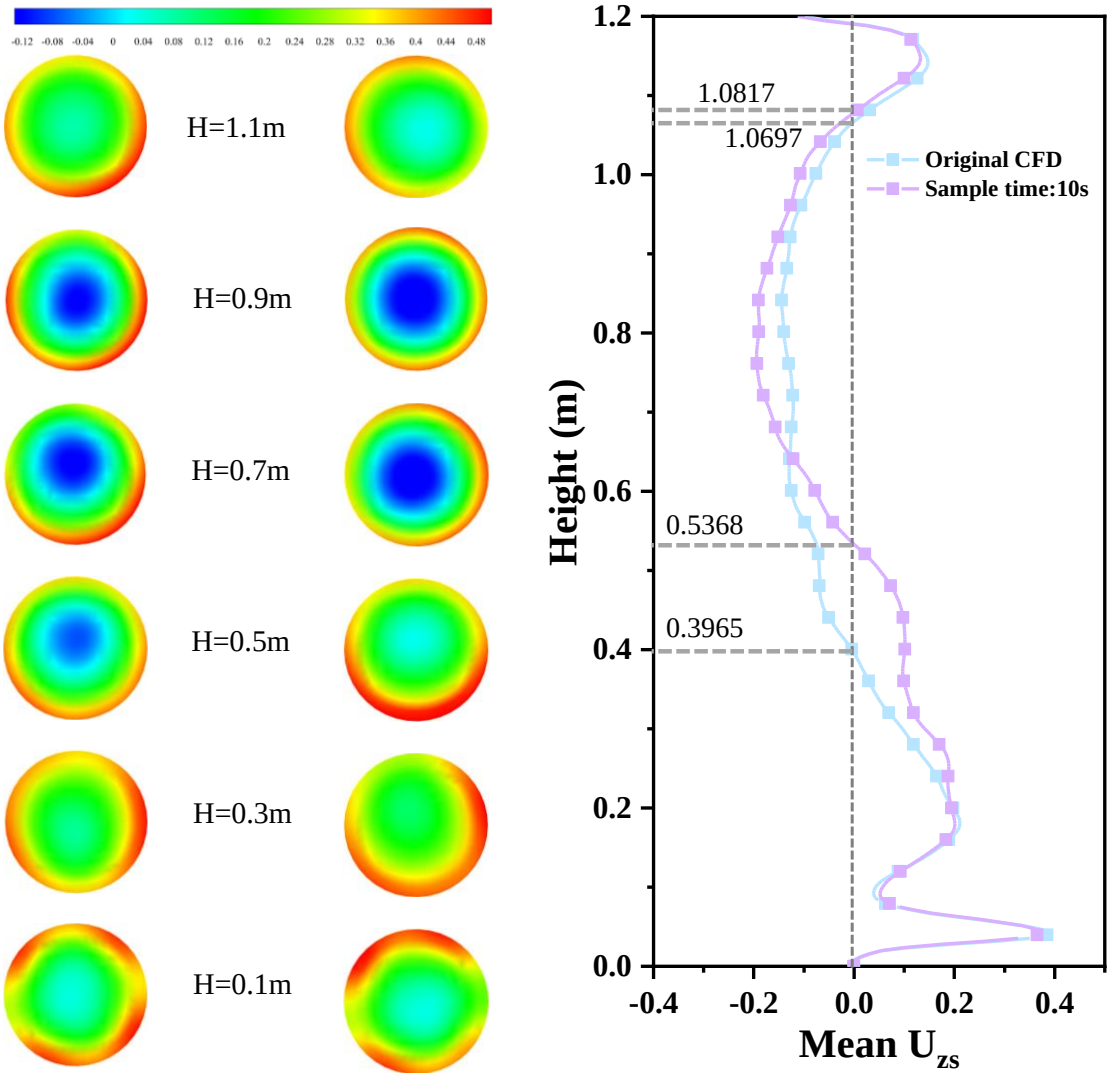

(a) (b)

Fig 7.15. Contour of time-averaged solid vertical velocity with several horizontal cross sections at different heights of the riser (a); profiles of time-averaged solid volume fraction along the central line of the riser (b).

In summary, various result analyses have shown that the addition of a real-time controller has effectively suppressed the maldistribution phenomenon and improved the performance of the DRCFB in this work to a certain extent.

7.4 Conclusions

This work utilises a novel direct coupling method to interact CFD modelling and process simulation dynamically and realises the real-time regulation of boundary and operating

conditions of reactors in chemical engineering processes according to the CFD outputs and control algorithm.

To illustrate the feasibility of this method, a collaborative simulation is conducted in this work to reduce the degree of maldistribution in one symmetrical DRCFB system through online regulation of L-valve aeration rate based on Ansys-Fluent and MATLAB. The example presented in this work illustrates the benefits of the collaborative simulation of the CFD modelling and process control in giving an effective way to obtain not only response characteristics of dynamic system performance at macroscale but also the transient in-furnace flow and reaction details at the microscale.

In future work, more advanced and complex control algorithms can be coupled and tested with CFD models of extensive individual unit operations as well as multiple interconnected units or even entire plants to improve the design and optimisation of chemical engineering processes in economical and safe manners.

CHAPTER.8 Conclusions and Recommendations

In this section, the main conclusions of the present work are summarized, and recommendations for further work are outlined.

8.1 Summary and conclusions

CFBs have been widely applied to many chemical engineering processes, due to its good gas-solid mixing, wide fuel flexibility, and excellent heat and mass transfer performance. Among various CFB chemical systems, the CLC system is regarded as one of the most promising clean combustion technologies because of the inherent CO_2 separation. Although significant developments have been made in solid fuel combustion using the CLC technology during the last decades, as introduced in Chapter 2, the detailed inner information cannot be obtained by experiments because of complicated flow pattern in the system and backward measuring equipment. The present knowledge, understanding, and experience of the CLC process mainly come from a limited number of research groups operating small CLC plants. Meantime, the lab- or pilot-scale results cannot safely be translated to an industrial scale, the performance of the actual industrial CLC unit is still uncertain. With the development of computer technology and parallel computing, numerical simulation has become the primary method to accelerate the development of the CLC technology, reduce the cost of design and operating time, as well as reduce the technical risks. However, present simulations are still very limited for the full-loop CLC system, especially the reactions in some complex configurations. Besides, the simulation work of the hydrodynamic and reaction behaviours of the moving-bed CDCL process has not been done yet and details of the flow and reaction have not been revealed and fully understood. Besides, the maldistribution phenomena in symmetrical CFB systems have not been comprehensively investigated. For non-identical CFB configurations, the effect of maldistribution on the system stability will intensify. Therefore, it is important to get a deep understanding of the maldistribution phenomenon. Moreover, most CFD simulations on complex CFB systems only revealed microscale phenomena based on separate reactor components. The boundary and operating conditions were fixed during the simulation process without the external adjustment and environment change considered. For fulfilling the knowledge gap, an integrated online regulation method is firstly established to realize the collaborative simulation of the transient CFD model and process control algorithm based on Ansys-Fluent and MATLAB platforms. This thesis aims to provide more detailed in-furnace phenomena of CLC units, including the hydrodynamic behaviours and chemical reactions based on the numerical simulation method. Meanwhile, the optimisation of boundary conditions and the model set is thoroughly investigated in these CLC processes.

- In chapter 3, a multi-fluid model (TFM) based on the Eulerian-Eulerian framework is used to study the gas-solid hydrodynamics, such as solid distribution, particle motion and solid velocity, in a three-dimensional (3D) CLC unit with the configuration of dual circulating fluidized bed (DCFB). The influence of four different drag force models, including two classic models, i.e. Gidaspow, EMMS drag model and two recent drag models, i.e. Rong and Tang drag model, on hydrodynamics in DCFB are assessed. The overall assessment confirms that the drag model selection has a significant influence on simulations of gas-solid flows in DCFBs for chemical looping combustion. For qualitative analysis, all the drag models can predict a reasonable radial solid distribution and pressure distribution, but only the EMMS, Rong and Tang drag models can capture the phenomenon of dense state in the low part of the riser. For quantitative analysis, the solid circulating rate predicted by the EMMS drag model is the closest to the experimental measurements. In contrast, the results predicted by the Gidaspow drag model show the most significant deviation. In summary, in the system and conditions investigated, the EMMS drag model gives the best results for simulating dense gas-solid flows in DCFB, followed by Rong and Tang drag models. The Gidaspow drag model shows the most significant deviation. The results shed lights on the drag force model sections and the optimization of DCFBs.

- In chapter 4, a comprehensive 3-D numerical simulation has been carried out to simulate the gas-solid flow characteristics in a two-staged air reactor and full-loop unit of a moving-bed CDCL unit using TFM. The gas-solid flow behaviors, solid axial velocity and solid circulating characteristics are investigated. Moreover, the effects of gas inlet velocity, specularity coefficient, and drag model is explored in detail. The following conclusions can be drawn for single AR, in the combustor, the solid material shows a dense solids slug movement where the particles move upward in the central region and drop down near the wall, which is beneficial to increase solid residence time for oxidation. In the riser, the solid phase distribution is dilute because of high gas velocity. The particles move upward in the whole radial positions and shows an anti-core-annulus flow pattern, which is beneficial for solid transportation. In the combustor, increasing the gas inlet velocity can reduce the solid concentration, meaning the amount of solid material and solid

residence time decrease in this section. In the riser, the solid concentration increases with the increase of gas inlet velocity, meaning the transport efficiency increases. The specularity coefficient of zero and Syamlal-O'Brien drag model are found suitable for the 3-D air reactor model to reasonably predict gas-solid flow behaviors. In the full-loop system, different fluidization regimes can be observed in the system: slugging fluidization in the bottom combustor, fast fluidization in the riser, and moving bed fluidization in the L-valve and reducer, which corresponds to their functions. Compared with dual fluidized bed CLC unit, the pressure drops in the whole CDCL unit and moving-bed reducer are low which means the system is more stable. The SCR is controlled by the flow rate of aeration gas on the standpipe of L-valve.

- In chapter 5, a 3D Eulerian-Eulerian-Lagrangian (E-E-L) hybrid model is used to study the gas-solid flow and reaction characteristics of the 25 kWh sub-pilot CDCL process with the unique moving bed FR developed at OSU. The flow behaviours of both oxygen carrier and powder coal are investigated under cold and hot conditions. And the reaction characteristics are also detailed discussed. Based on the numerical results, conclusions can be drawn as follows: The mixing and separation process of the coarse oxygen carrier and fine coal powder is captured by simulation, and the mechanism is further explained by numerical results. A severe gas leakage phenomenon can be observed by simulation in the system, where the O_2 and N_2 from the AR and N_2 from the L-valve gas leak into the FR and dilute the CO_2 at the outlet of the FR. The high temperatures in the CLC system are seen in the AR riser and in the cyclone, whereas the low temperatures are present in the bottom of the fuel reactor and the L-valve. The reaction rates and reactants distribution of all reactions considered in this chapter are reasonably predicted by simulation, showing the applicability of the hybrid model to investigate the CDCL unit.

- In chapter 6, the characteristics of the maldistribution phenomenon in a symmetric dual-side refeed circulating fluidized bed (DRCFB) is numerically studied by a multi-fluid model based on the Eulerian-Eulerian framework. The influence of solid maldistribution on the performance of the cyclone, standpipe, L-valve, and riser in the DRCFB is discussed. Moreover, the effects of gas inlet velocity, solid

inventory, and wall function on the degree of maldistribution are comprehensively explored. Based on the numerical results, the main conclusions can be drawn as follows: The solid maldistribution is an inevitable phenomenon in a DRCFB system with dual identical geometry configuration and operating parameters in each side. The maldistribution of solid mass in the DRCFB unit causes a deflection of the centre of gravity position of the device and the drastic difference of solid fluxes at the cyclones to lower the overall performance of cyclone. The solid mass flux at the L-valve outlet is proportional to the bed inventory in the standpipe. The standpipe and L-valve have an automatic control ability to some extent. This lateral pressure gradients in the riser and near the cyclone inlets are generally recognized as the main reason resulting in the maldistribution of the full-loop DRCFB system. The relative deviation of the bed inventory in both external loops decrease with the increase of gas inlet velocity and total solid inventory. However, it is not sensitive to the wall roughness. The relative deviations of bed inventory in both external loops do not show a direct relationship with the transient changes of flow by analysing the pressure drop signal. In section 2, the non-uniformity of the gas-solid distribution in a symmetrical DCFB CLC unit is numerically studied using a multifluid CFD model based on Eulerian-Eulerian framework. The phenomenon of non-uniformity is discussed by comparing the deviation of bed inventory and flow patterns in unit A and unit B, respectively. Moreover, the effects of total solid inventory, gas aeration rate, and wall roughness on the degree of non-uniformity are comprehensively explored. Based on the numerical results, conclusions can be drawn as follows: The non-uniformity of gas-solid distribution can be observed in terms of solid mass distribution and local flow patterns in a symmetrical DCFB CLC system with an identical geometry configuration and operating parameters. Enlarging the total bed inventory increases the relative deviation of non-uniformity (Dev), the pressure fluctuation and the deviation of Hurst exponent, demonstrating the system becomes more unstable. Elevating the gas aeration rate increases the relative deviation of non-uniformity (Dev), the pressure fluctuation, and the deviation of Hurst exponent, indicating demonstrating the system becomes more unstable. The specularity coefficient has an uncertain influence on the degree of non-uniformity. To summarise, the non-uniformity phenomenon is revealed by simulation results, and the influences of several critical operating

variables on the degree of non-uniformity are studied. These fundamental mechanism of non-uniformity phenomenon should be helpful for the design and optimisation of CLC processes.

- The chapter 8 utilises a novel direct coupling method to interact CFD modelling and process simulation dynamically and realises the real-time regulation of boundary and operating conditions of reactors in chemical engineering processes according to the CFD outputs and control algorithm. To illustrate the feasibility of this method, a collaborative simulation is conducted in this work to reduce the degree of maldistribution in one symmetrical DRCFB system through online regulation of L-valve aeration rate based on Ansys-Fluent and MATLAB. The example presented in this work illustrates the benefits of the collaborative simulation of the CFD modelling and process control in giving an effective way to obtain not only response characteristics of dynamic system performance at macroscale but also the transient in-furnace flow and reaction details at the microscale.

8.2 Recommended future work

In this final section, some weaknesses and suggestions on current research directions are proposed.

- More accurate and efficient numerical method should be used to simulate the hydrodynamic and thermodynamic behaviours of CLC processes with complex CFB configurations. The current assumption and simplification of multi-fluid models based on the Eulerian-Eulerian or Eulerian-Eulerian-Lagrangian framework cannot provide all solid information at particle level during simulation, resulting the deviation when simulating flow and thermochemical related behaviours. With the development of novel numerical methods, more accurate and efficient numerical method (such as CPFD) may be applied in large scale and long-time reaction modelling.

- The characteristics of the reactive flow in the 25 kWh sub-pilot CDCL process with the unique moving bed FR, discussed in chapter 4 and 5 should be further investigated. The influence of multiple parameters, including variable gas inlet

velocity, total solid inventory, solids circulation rate, coal feeding rate, temperature and so on, on the performance of system operation should be detailed investigated. Besides, the optimization of operation condition and design should be further explored to minimize the gas leakage and improve the system efficiency. For the reaction kinetics, more accurate chemistry should be adopted to simulate the multi-reduction step of the iron-based oxygen carrier in the CDCL process used in this thesis.

- The impact of asymmetrical difference in dual CFBs on the maldistribution degree is an interesting topic and worthy of further study, such as slight differences of boundary conditions and geometries.

- In future work, more advanced and complex control algorithms can be coupled and tested with CFD models of extensive individual unit operations as well as multiple interconnected units or even entire plants to improve the design and optimisation of chemical engineering processes in economical and safe manners.

Bibliography

[1] S.K. Sansaniwal, K. Pal, M.A. Rosen, S.K. Tyagi, Recent advances in the development of biomass gasification technology: A comprehensive review, Renew. Sustain. Energy Rev. 72 (2017) 363–384.

[2] A.D. Nikitin, N.A. Abaimov, E.B. Butakov, A.P. Burdukov, A.F. Ryzhkov, Investigation of multistage air-steam-blown entrained-flow coal gasification, in: J. Phys. Conf. Ser., IOP Publishing, 2020: p. 12043.

[3] X. Guo, Z. Dai, X. Gong, X. Chen, H. Liu, F. Wang, Z. Yu, Performance of an entrained-flow gasification technology of pulverized coal in pilot-scale plant, Fuel Process. Technol. 88 (2007) 451–459.

[4] X. Wang, X. Wang, Y. Shao, B. Jin, Three-dimensional modelling of the multiphase hydrodynamics in a separated-gasification chemical looping combustion unit during full-loop operation, J. Clean. Prod. 275 (2020) 122782.

[5] A.J. Minchener, Coal gasification for advanced power generation, Fuel. 84 (2005) 2222–2235.

[6] A. V Bridgwater, Review of fast pyrolysis of biomass and product upgrading, Biomass and Bioenergy. 38 (2012) 68–94.

[7] S. Czernik, A. V Bridgwater, Overview of applications of biomass fast pyrolysis oil, Energy & Fuels. 18 (2004) 590–598.

[8] T.R. Anderson, E. Hawkins, P.D. Jones, CO2, the greenhouse effect and global warming: from the pioneering work of Arrhenius and Callendar to today's Earth System Models, Endeavour. 40 (2016) 178–187.

[9] C. Karakosta, C. Pappas, V. Marinakis, J. Psarras, Renewable energy and nuclear power towards sustainable development: Characteristics and prospects, Renew. Sustain. Energy Rev. 22 (2013) 187–197.

[10] S.M. Benson, F.M. Orr, Carbon dioxide capture and storage, MRS Bull. 33 (2008) 303–305.

[11] J. Gibbins, H. Chalmers, Preparing for global rollout: A ‘developed country first’demonstration programme for rapid CCS deployment, Energy Policy. 36 (2008) 501–507.

[12] P.H.M. Feron, C.A. Hendriks, CO2 capture process principles and costs, Oil Gas Sci. Technol. 60 (2005) 451–459.

[13] J. Gibbins, H. Chalmers, Carbon capture and storage, Energy Policy. 36 (2008) 4317–4322.

[14] T. Mattisson, A. Lyngfelt, Applications of chemical-looping combustion with capture of CO2, Second Nord. Minisymp. CO2 Capture Storage, Göteborg, Sweden. (2001).

[15] G. Tang, A.K. Silaen, B. Wu, D. Fu, D. Agnello-Dean, J. Wilson, Q. Meng, S. Khanna, C.Q. Zhou, Numerical simulation and optimization of an industrial fluid catalytic cracking regenerator, Appl. Therm. Eng. 112 (2017) 750–760.

[16] J.M. Matsen, Design and scale-up of CFB catalytic reactors, in: Circ. Fluid. Beds, Springer, 1997: pp. 489–503.

[17] A.P. Steynberg, R.L. Espinoza, B. Jager, A.C. Vosloo, High temperature Fischer–Tropsch synthesis in commercial practice, Appl. Catal. A Gen. 186 (1999) 41–54.

[18] H. Boerrigter, H. Den Uil, H.-P. Calis, Green diesel from biomass via Fischer-Tropsch synthesis: new insights in gas cleaning and process design, Pyrolysis Gasif. Biomass Waste. 1 (2003).

[19] J.R. Grace, T.M. Knowlton, A.A. Avidan, Circulating fluidized beds, Springer Science & Business Media, 2012.

[20] A. Marafi, H. Albazzaz, M.S. Rana, Hydroprocessing of heavy residual oil: Opportunities and challenges, Catal. Today. 329 (2019) 125–134.

[21] M. Huang, Y. Zheng, S. Li, S. Xu, Enhancing Transient Event Trigger Real-Time Optimization for Fluid Catalytic Cracking Unit Operation with Varying Feedstock, Ind. Eng. Chem. Res. 58 (2019) 20340–20356.

[22] Y. Du, L. Sun, A.S. Berrouk, C. Zhang, X. Chen, D. Fang, W. Ren, Novel integrated reactor-regenerator model for the fluidized catalytic cracking unit based on an equivalent reactor network, Energy & Fuels. 33 (2019) 7265–7275.

[23] Y. Zhang, M. Yao, G. Sun, S. Gao, G. Xu, Characteristics and kinetics of coked catalyst regeneration via steam gasification in a micro fluidized bed, Ind. Eng. Chem. Res. 53 (2014) 6316–6324.

[24] R. Wang, X. Luo, F. Xu, Economic and control performance of a fluid catalytic cracking unit: Interactions between combustion air and CO promoters, Ind. Eng. Chem. Res. 53 (2014) 287–304.

[25] J. Rezaiyan, N.P. Cheremisinoff, Gasification technologies: a primer for engineers and scientists, CRC press, 2005.

[26] B.S. Hoffmann, A. Szklo, Integrated gasification combined cycle and carbon capture: a risky option to mitigate CO2 emissions of coal-fired power plants, Appl. Energy. 88 (2011) 3917–3929.

[27] M.A. Duchesne, A.Y. Ilyushechkin, R.W. Hughes, D.Y. Lu, D.J. McCalden, A. Macchi, E.J. Anthony, Flow behaviour of slags from coal and petroleum coke blends, Fuel. 97 (2012) 321–328.

[28] J. Adanez, A. Abad, F. Garcia-Labiano, P. Gayan, F. Luis, Progress in chemical-looping combustion and reforming technologies, Prog. Energy Combust. Sci. 38 (2012) 215–282.

[29] N. Berguerand, A. Lyngfelt, Design and operation of a 10 kWth chemical-looping combustor for solid fuels–Testing with South African coal, Fuel. 87 (2008) 2713–2726.

[30] N. Berguerand, A. Lyngfelt, The use of petroleum coke as fuel in a 10 kWth chemical-looping combustor, Int. J. Greenh. Gas Control. 2 (2008) 169–179.

[31] N. Berguerand, A. Lyngfelt, Chemical-looping combustion of petroleum coke using ilmenite in a 10 kWth unit− high-temperature operation, Energy & Fuels. 23 (2009) 5257–5268.

[32] T. Mattisson, A. Lyngfelt, H. Leion, Chemical-looping with oxygen uncoupling for combustion of solid fuels, Int. J. Greenh. Gas Control. 3 (2009) 11–19.

[33] A. Cuadrat, C. Linderholm, A. Abad, A. Lyngfelt, J. Adánez, Influence of limestone addition in a 10 kWth chemical-looping combustion unit operated with petcoke, Energy & Fuels. 25 (2011) 4818–4828.

[34] C. Linderholm, A. Lyngfelt, A. Cuadrat, E. Jerndal, Chemical-looping combustion of solid fuels–Operation in a 10 kW unit with two fuels, above-bed and in-bed fuel feed and two oxygen carriers, manganese ore and ilmenite, Fuel. 102 (2012) 808–822.

[35] C. Linderholm, A. Lyngfelt, C. Dueso, Chemical-looping combustion of solid fuels in a 10 kW reactor system using natural minerals as oxygen carrier, Energy Procedia. 37 (2013) 598–607.

[36] M. Schmitz, C. Linderholm, A. Lyngfelt, Chemical looping combustion of sulphurous solid fuels using spray-dried calcium manganate particles as oxygen carrier, Energy Procedia. 63 (2014) 140–152.

[37] M. Schmitz, C. Linderholm, P. Hallberg, S. Sundqvist, A. Lyngfelt, Chemical-looping combustion of solid fuels using manganese ores as oxygen carriers, Energy & Fuels. 30 (2016) 1204–1216.

[38] M. Schmitz, C.J. Linderholm, A. Lyngfelt, Chemical looping combustion of four different solid fuels using a manganese-silicon-titanium oxygen carrier, Int. J. Greenh. Gas Control. 70 (2018) 88–96.

[39] I. Gogolev, A.H. Soleimanisalim, C. Linderholm, A. Lyngfelt, Commissioning, performance benchmarking, and investigation of alkali emissions in a 10 kWth solid fuel chemical looping combustion pilot, Fuel. (2020) 119530.

[40] P. Markström, A. Lyngfelt, Designing and operating a cold-flow model of a 100 kW chemical-looping combustor, Powder Technol. 222 (2012) 182–192.

[41] P. Markström, A. Lyngfelt, C. Linderholm, Chemical-looping combustion in a 100 kW unit for solid fuels, in: 21st Int. Conf. Fluid. Bed Combust., 2012: pp. 3–6.

[42] P. Markström, C. Linderholm, A. Lyngfelt, Chemical-looping combustion of solid fuels--design and operation of a 100 kW unit with bituminous coal, Int. J. Greenh. Gas Control. 15 (2013) 150–162.

[43] P. Markström, C. Linderholm, A. Lyngfelt, Operation of a 100 kW chemical-looping combustor with Mexican petroleum coke and Cerrejón coal, Appl. Energy. 113 (2014) 1830–1835.

[44] C. Linderholm, M. Schmitz, P. Knutsson, M. Källén, A. Lyngfelt, Use of low-volatile solid fuels in a 100 kW chemical-looping combustor, Energy & Fuels. 28 (2014) 5942–5952.

[45] C. Linderholm, P. Knutsson, M. Schmitz, P. Markström, A. Lyngfelt, Material balances of carbon, sulfur, nitrogen and ilmenite in a 100 kW CLC reactor system, Int. J. Greenh. Gas Control. 27 (2014) 188–202.

[46] C. Linderholm, M. Schmitz, P. Knutsson, A. Lyngfelt, Chemical-looping combustion in a 100-kW unit using a mixture of ilmenite and manganese ore as oxygen carrier, Fuel. 166 (2016) 533–542.

[47] C. Linderholm, M. Schmitz, M. Biermann, M. Hanning, A. Lyngfelt, Chemical-looping combustion of solid fuel in a 100 kW unit using sintered manganese ore as oxygen carrier, Int. J. Greenh. Gas Control. 65 (2017) 170–181.

[48] I. Gogolev, C. Linderholm, D. Gall, M. Schmitz, T. Mattisson, J.B.C. Pettersson, A. Lyngfelt, Chemical-looping combustion in a 100 kW unit using a mixture of synthetic and natural oxygen carriers–Operational results and fate of biomass fuel alkali, Int. J. Greenh. Gas Control. 88 (2019) 371–382.

[49] L. Shen, J. Wu, J. Xiao, Experiments on chemical looping combustion of coal with a NiO based oxygen carrier, Combust. Flame. 156 (2009) 721–728.

[50] L. Shen, J. Wu, J. Xiao, Q. Song, R. Xiao, Chemical-looping combustion of biomass in a 10 kWth reactor with iron oxide as an oxygen carrier, Energy & Fuels. 23 (2009) 2498–2505.

[51] L. Shen, J. Wu, Z. Gao, J. Xiao, Characterization of chemical looping combustion of coal in a 1 kWth reactor with a nickel-based oxygen carrier, Combust. Flame. 157 (2010) 934–942.

[52] H. Gu, L. Shen, J. Xiao, S. Zhang, T. Song, Chemical looping combustion of biomass/coal with natural iron ore as oxygen carrier in a continuous reactor, Energy & Fuels. 25 (2011) 446–455.

[53] T. Song, L. Shen, J. Xiao, D. Chen, H. Gu, S. Zhang, Nitrogen transfer of fuel-N in chemical looping combustion, Combust. Flame. 159 (2012) 1286–1295.

[54] T. Song, T. Shen, L. Shen, J. Xiao, H. Gu, S. Zhang, Evaluation of hematite oxygen carrier in chemical-looping combustion of coal, Fuel. 104 (2013) 244–252.

[55] H. Gu, L. Shen, Z. Zhong, X. Niu, H. Ge, Y. Zhou, S. Xiao, Potassium-modified iron ore as oxygen carrier for coal chemical looping combustion: continuous test in 1 kW reactor, Ind. Eng. Chem. Res. 53 (2014) 13006–13015.

[56] H. Gu, L. Shen, Z. Zhong, X. Niu, H. Ge, Y. Zhou, S. Xiao, S. Jiang, NO release during chemical looping combustion with iron ore as an oxygen carrier, Chem. Eng. J. 264 (2015) 211–220.

[57] H. Gu, L. Shen, Z. Zhong, X. Niu, W. Liu, H. Ge, S. Jiang, L. Wang, Cement/CaO-modified iron ore as oxygen carrier for chemical looping combustion of coal, Appl. Energy. 157 (2015) 314–322.

[58] H. Ge, L. Shen, H. Gu, T. Song, S. Jiang, Combustion performance and sodium transformation of high-sodium ZhunDong coal during chemical looping combustion with hematite as oxygen carrier, Fuel. 159 (2015) 107–117.

[59] S. Jiang, L. Shen, X. Niu, H. Ge, H. Gu, Chemical looping co-combustion of sewage sludge and zhundong coal with natural hematite as the oxygen carrier, Energy & Fuels. 30 (2016) 1720–1729.

[60] S. Zhang, H. Gu, J. Zhao, L. Shen, L. Wang, Development of iron ore oxygen carrier modified with biomass ash for chemical looping combustion, Energy. 186 (2019) 115893.

[61] L. Shen, J. Wu, Z. Gao, J. Xiao, Reactivity deterioration of NiO/Al2O3 oxygen carrier for chemical looping combustion of coal in a 10kWth reactor, Combust. Flame. 156 (2009) 1377–1385.

[62] A. Cuadrat, A. Abad Secades, F. García Labiano, P. Gayán Sanz, L.F. de Diego Poza, J. Adánez Elorza, Ilmenite as oxygen carrier in a chemical looping combustion system with coal, (2011).

[63] J. Adánez, A. Abad, R. Perez-Vega, F. Luis, F. García-Labiano, P. Gayán, Design and operation of a coal-fired 50 kWth chemical looping combustor, Energy Procedia. 63 (2014) 63–72.

[64] A. Cuadrat, A. Abad, F. Garc ia-Labiano, P. Gayán, L.F. De Diego, J. Adánez, The use of ilmenite as oxygen-carrier in a 500 Wth chemical-looping coal combustion unit, Int. J. Greenh. Gas Control. 5 (2011) 1630–1642.

[65] A. Abad, I. Adánez-Rubio, P. Gayán, F. Garc ia-Labiano, F. Luis, J. Adánez, Demonstration of chemical-looping with oxygen uncoupling (CLOU) process in a 1.5 kWth continuously operating unit using a Cu-based oxygen-carrier, Int. J. Greenh. Gas Control. 6 (2012) 189–200.

[66] A. Cuadrat, A. Abad, F. García-Labiano, P. Gayán, L.F. de Diego, J. Adánez, Effect of operating conditions in Chemical-Looping Combustion of coal in a 500 Wth unit, Int. J. Greenh. Gas Control. 6 (2012) 153–163.

[67] I. Adánez-Rubio, A. Abad, P. Gayán, L.F. De Diego, F. García-Labiano, J. Adánez, Performance of CLOU process in the combustion of different types of coal with CO2 capture, Int. J. Greenh. Gas Control. 12 (2013) 430–440.

[68] J. Adánez, P. Gayán, I. Adánez-Rubio, A. Cuadrat, T. Mendiara, A. Abad, F. García-Labiano, L.F. De Diego, Use of Chemical-Looping processes for coal combustion with CO2 capture, Energy Procedia. 37 (2013) 540–549.

[69] T. Mendiara, L.F. de Diego, F. García-Labiano, P. Gayán, A. Abad, J. Adánez, Behaviour of a bauxite waste material as oxygen carrier in a 500 Wth CLC unit with coal, Int. J. Greenh. Gas Control. 17 (2013) 170–182.

[70] T. Mendiara, A. Abad, L.F. De Diego, F. García-Labiano, P. Gayán, J. Adánez, Biomass combustion in a CLC system using an iron ore as an oxygen carrier, Int. J. Greenh. Gas Control. 19 (2013) 322–330.

[71] I. Adánez-Rubio, A. Abad, P. Gayán, F. García-Labiano, F. Luis, J. Adánez, The fate of sulphur in the Cu-based Chemical Looping with Oxygen Uncoupling (CLOU) Process, Appl. Energy. 113 (2014) 1855–1862.

[72] T. Mendiara, M.T. Izquierdo, A. Abad, L.F. De Diego, F. García-Labiano, P. Gayán, J. Adánez, Release of pollutant components in CLC of lignite, Int. J. Greenh. Gas Control. 22 (2014) 15–24.

[73] T. Mendiara, L.F. De Diego, F. García-Labiano, P. Gayán, A. Abad, J. Adánez, On the use of a highly reactive iron ore in Chemical Looping Combustion of different coals, Fuel. 126 (2014) 239–249.

[74] I. Adánez-Rubio, A. Abad, P. Gayán, L.F. De Diego, F. García-Labiano, J. Adánez, Biomass combustion with CO2 capture by chemical looping with oxygen uncoupling (CLOU), Fuel Process. Technol. 124 (2014) 104–114.

[75] R. Pérez-Vega, I. Adánez-Rubio, P. Gayán, M.T. Izquierdo, A. Abad, F. García-Labiano, F. Luis, J. Adánez, Sulphur, nitrogen and mercury emissions from coal combustion with CO2 capture in chemical looping with oxygen uncoupling (CLOU), Int. J. Greenh. Gas Control. 46 (2016) 28–38.

[76] T. Mendiara, I. Adánez-Rubio, P. Gayán, A. Abad, L.F. De Diego, F. García-Labiano, J. Adánez, Process Comparison for Biomass Combustion: In Situ Gasification-Chemical Looping Combustion (iG-CLC) versus Chemical Looping with Oxygen Uncoupling (CLOU), Energy Technol. 4 (2016) 1130–1136.

[77] A. Abad, T. Mendiara, P. Gayán, F. García-Labiano, L.F. De Diego, J.A. Bueno, R. Pérez-Vega, J. Adánez, Comparative evaluation of the performance of coal combustion in 0.5 and 50 kWth chemical looping combustion units with ilmenite, redmud or iron ore as oxygen carrier, Energy Procedia. 114 (2017) 285–301.

[78] T. Mendiara, P. Gayán, F. García-Labiano, L.F. De Diego, A. Pérez-Astray, M.T. Izquierdo, A. Abad, J. Adánez, Chemical looping combustion of biomass: an approach to BECCS, Energy Procedia. 114 (2017) 6021–6029.

[79] I. Adánez-Rubio, A. Abad, P. Gayán, F. García-Labiano, F. Luis, J. Adánez, Coal combustion with a spray granulated Cu-Mn mixed oxide for the Chemical Looping with Oxygen Uncoupling (CLOU) process, Appl. Energy. 208 (2017) 561–570.

[80] T. Mendiara, A. Pérez-Astray, M.T. Izquierdo, A. Abad, L.F. De Diego, F. García-Labiano, P. Gayán, J. Adánez, Chemical looping combustion of different types of biomass in a 0.5 kWth unit, Fuel. 211 (2018) 868–875.

[81] I. Adánez-Rubio, A. Pérez-Astray, A. Abad, P. Gayán, L. de Diego, J. Adánez, Biomass combustion by chemical looping with oxygen uncoupling process: experiments with Cu-based and Cu-Mn mixed oxide as oxygen carriers, in: Int. Conf. Negat. CO2 Emiss., 2018.

[82] I. Adánez-Rubio, A. Abad, P. Gayán, F. Luis, J. Adánez, CLOU process performance with a Cu-Mn oxygen carrier in the combustion of different types of coal with CO2 capture, Fuel. 212 (2018) 605–612.

[83] R. Pérez-Vega, A. Abad, F. García-Labiano, P. Gayán, F. Luis, M.T. Izquierdo, J. Adánez, Chemical Looping Combustion of gaseous and solid fuels with manganese-iron mixed oxide as oxygen carrier, Energy Convers. Manag. 159 (2018) 221–231.

[84] I. Adánez-Rubio, A. Pérez-Astray, T. Mendiara, M.T. Izquierdo, A. Abad, P. Gayán, F. Luis, F. García-Labiano, J. Adánez, Chemical looping combustion of biomass: CLOU experiments with a Cu-Mn mixed oxide, Fuel Process. Technol. 172 (2018) 179–186.

[85] A. Abad, P. Gayán, T. Mendiara, J.A. Bueno, F. Garcia-Labiano, F. Luis, J. Adanez, Assessment of the improvement of chemical looping combustion of coal by using a manganese ore as oxygen carrier, Fuel Process. Technol. 176 (2018) 107–118.

[86] A. Pérez-Astray, I. Adánez-Rubio, T. Mendiara, M.T. Izquierdo, A. Abad, P. Gayán, L.F. de Diego, F. García-Labiano, J. Adánez, Comparative study of fuel-N and tar evolution in chemical looping combustion of biomass under both iG-CLC and CLOU modes, Fuel. 236 (2019) 598–607.

[87] I. Adánez-Rubio, A. Pérez-Astray, A. Abad, P. Gayán, F. Luis, J. Adánez, Chemical looping with oxygen uncoupling: an advanced biomass combustion technology to avoid CO 2 emissions, Mitig. Adapt. Strateg. Glob. Chang. 24 (2019) 1293–1306.

[88] A. Pérez-Astray, T. Mendiara, L.F. de Diego, A. Abad, F. García-Labiano, M.T. Izquierdo, J. Adánez, Improving the oxygen demand in biomass CLC using manganese ores, Fuel. 274 (2020) 117803.

[89] R. Pérez-Vega, A. Abad, P. Gayán, F. García-Labiano, M.T. Izquierdo, F. Luis, J. Adánez, Coal combustion via Chemical Looping assisted by Oxygen Uncoupling with a manganese-iron mixed oxide doped with titanium, Fuel Process. Technol. 197 (2020) 106184.

[90] I. Samprón, F. Luis, F. García-Labiano, M.T. Izquierdo, A. Abad, J. Adánez, Biomass Chemical Looping Gasification of pine wood using a synthetic Fe2O3/Al2O3 oxygen carrier in a continuous unit, Bioresour. Technol. 316 (2020) 123908.

[91] O. Condori, F. García-Labiano, F. Luis, M.T. Izquierdo, A. Abad, J. Adánez, Biomass chemical looping gasification for syngas production using ilmenite as oxygen carrier in a 1.5 kWth unit, Chem. Eng. J. 405 (2020) 126679.

[92] A. Abad, R. Pérez-Vega, F. Luis, F. García-Labiano, P. Gayán, J. Adánez, Design and operation of a 50 kWth Chemical Looping Combustion (CLC) unit for solid fuels, Appl. Energy. 157 (2015) 295–303.

[93] R. Pérez-Vega, A. Abad, F. García-Labiano, P. Gayán, F. Luis, J. Adánez, Coal combustion in a 50 kWth Chemical Looping Combustion unit: Seeking operating conditions to maximize CO2 capture and combustion efficiency, Int. J. Greenh. Gas Control. 50 (2016) 80–92.

[94] A. Abad, P. Gayán, R. Pérez-Vega, F. García-Labiano, L.F. de Diego, T. Mendiara, M.T. Izquierdo, J. Adánez, Evaluation of different strategies to improve the efficiency of coal conversion in a 50 kWth Chemical Looping combustion unit, Fuel. 271 (2020) 117514.

[95] J. Ma, H. Zhao, X. Tian, Y. Wei, S. Rajendran, Y. Zhang, S. Bhattacharya, C. Zheng, Chemical looping combustion of coal in a 5 kWth interconnected fluidized bed reactor using hematite as oxygen carrier, Appl. Energy. 157 (2015) 304–313.

[96] J. Ma, X. Tian, C. Wang, X. Chen, H. Zhao, Performance of a 50 kWth coal-fuelled chemical looping combustor, Int. J. Greenh. Gas Control. 75 (2018) 98–106.

[97] Y. Shao, Y. Zhang, X. Wang, X. Wang, B. Jin, H. Liu, Three-dimensional full loop modeling and optimization of an in situ gasification chemical looping combustion system, Energy & Fuels. 31 (2017) 13859–13870.

[98] X. Liu, C. Zhang, J. Zhan, Quantitative comparison of image analysis methods for particle mixing in rotary drums, Powder Technol. 282 (2015) 32–36.

[99] L. Zeng, Z. Cheng, J.A. Fan, L.-S. Fan, J. Gong, Metal oxide redox chemistry for chemical looping processes, Nat. Rev. Chem. 2 (2018) 349–364.

[100] V. Shah, R. Joshi, L.-S. Fan, Thermodynamic Investigation of Process Enhancement in Chemical Looping Reforming of Methane through Modified Ca–Fe Oxygen Carrier Utilization, Ind. Eng. Chem. Res. 59 (2020) 15531–15541.

[101] Y. Liu, L. Qin, Z. Cheng, J.W. Goetze, F. Kong, J.A. Fan, L.-S. Fan, Near 100% CO selectivity in nanoscaled iron-based oxygen carriers for chemical looping methane partial oxidation, Nat. Commun. 10 (2019) 1–6.

[102] H.R. Kim, D. Wang, L. Zeng, S. Bayham, A. Tong, E. Chung, M. V Kathe, S. Luo, O. McGiveron, A. Wang, others, Coal direct chemical looping combustion process: Design and operation of a 25-kWth sub-pilot unit, Fuel. 108 (2013) 370–384.

[103] S.C. Bayham, H.R. Kim, D. Wang, A. Tong, L. Zeng, O. McGiveron, M. V Kathe, E. Chung, W. Wang, A. Wang, Iron-based coal direct chemical looping combustion process: 200-h continuous operation of a 25-kWth subpilot unit, Energy & Fuels. 27 (2013) 1347–1356.

[104] S. Bayham, O. McGiveron, A. Tong, E. Chung, M. Kathe, D. Wang, L. Zeng, L.-S. Fan, Parametric and dynamic studies of an iron-based 25-kWth coal direct chemical looping unit using sub-bituminous coal, Appl. Energy. 145 (2015) 354–363.

[105] T. Knowlton, S.B. Reddy Karri, J.S. Smith, Hydrodynamic scale-up of circulating fluidized beds, (2007).

[106] J.L. Sinclair, R. Jackson, Gas-particle flow in a vertical pipe with particle-particle interactions, AIChE J. 35 (1989) 1473–1486.

[107] M.A. Hamilton, K.J. Whitty, J.S. Lighty, Incorporating oxygen uncoupling kinetics into computational fluid dynamic simulations of a chemical looping system, Energy Technol. 4 (2016) 1237–1246.

[108] Y. Guan, J. Chang, K. Zhang, B. Wang, Q. Sun, D. Wen, Three-dimensional full loop simulation of solids circulation in an interconnected fluidized bed, Powder Technol. 289 (2016) 118–125.

[109] S. Banerjee, X. Zhang, R.K. Agarwal, CFD Simulations of Complete Circulating Dual Fluidized Bed Systems for Chemical Looping Combustion, (2016).

[110] R.W. Breault, E.R. Monazam, Modeling of the reduction of hematite in the chemical looping combustion of methane using barracuda, Energy Technol. 4 (2016) 1221–1229.

[111] A.B. Harichandan, S. Pande, M.M. Sheth, CFD MODELING OF FUEL REACTOR FOR A CHEMICAL LOOPING COMBUSTION PROCESS, (n.d.).

[112] S. Banerjee, R.K. Agarwal, Characterization of scaling laws in computational fluid dynamics simulations of spouted fluidized beds for chemical looping combustion, Energy & Fuels. 30 (2016) 8638–8647.

[113] M.A. Hamilton, K.J. Whitty, J.S. Lighty, Numerical simulation comparison of two reactor configurations for chemical looping combustion and chemical looping with oxygen uncoupling, J. Energy Resour. Technol. 138 (2016).

[114] S. Banerjee, R.K. Agarwal, An Eulerian approach to computational fluid dynamics simulation of a chemical-looping combustion reactor with chemical reactions, J. Energy Resour. Technol. 138 (2016).

[115] Y. Zhang, Z. Chao, H.A. Jakobsen, Modelling and simulation of hydrodynamics in double loop circulating fluidizedbed reactor for chemical looping combustion process, Powder Technol. 310 (2017) 35–45.

[116] Y. Zhang, Z. Chao, H.A. Jakobsen, Modelling and simulation of chemical looping combustion process in a double loop circulating fluidized bed reactor, Chem. Eng. J. 320 (2017) 271–282.

[117] R.W. Breault, J. Weber, D. Straub, S. Bayham, Computational Fluid Dynamics Modeling of the Fuel Reactor in NETL's 50 kWth Chemical Looping Facility, J. Energy Resour. Technol. 139 (2017).

[118] R. Sharma, J. May, F. Alobaid, P. Ohlemueller, J. Stroehle, B. Epple, Euler-Euler CFD simulation of the fuel reactor of a 1 MWth chemical-looping pilot plant: Influence of the drag models and specularity coefficient, Fuel. 200 (2017) 435–446.

[119] R. Sornumpol, W. Uraisakul, P. Kuchonthara, B. Chalermsinsuwan, P. Piumsomboon, CFD simulation of fuel reactor in chemical looping combustion, Energy Procedia. 138 (2017) 979–984.

[120] L. Chen, X. Yang, G. Li, X. Li, C. Snape, Prediction of bubble fluidisation during chemical looping combustion using CFD simulation, Comput. Chem. Eng. 99 (2017) 82–95.

[121] K.G. Menon, V.S. Patnaikuni, CFD simulation of fuel reactor for chemical looping combustion of Indian coal, Fuel. 203 (2017) 90–101.

[122] C. Luo, Z. Peng, E. Doroodchi, B. Moghtaderi, A three-dimensional hot flow model for simulating the alumina encapsulated NI-NIO methane-air CLC system based on the computational fluid dynamics-discrete element method, Fuel. 224 (2018) 388–400.

[123] R. Ben-Mansour, H. Li, M.A. Habib, M.M. Hossain, Numerical study of radiative heat transfer and effects of thermal boundary conditions on CLC fuel reactor, Heat Mass Transf. 54 (2018) 571–590.

[124] X. Feng, L. Shen, L. Wang, Effect of baffle on hydrodynamics in the air reactor of dual circulating fluidized bed for chemical looping process, Powder Technol. 340 (2018) 88–98.

[125] M. Sheth, A. Roy, A. Harichandan, Performance of fuel reactor in a chemical looping combustion system with different oxygen carriers, Therm. Sci. Eng. Prog. 5 (2018) 303–308.

[126] S. Wang, W. Yin, Z. Li, X. Yang, K. Zhang, Numerical investigation of chemical looping gasification process using solid fuels for syngas production, Energy Convers. Manag. 173 (2018) 296–302.

[127] X. Wang, B. Jin, H. Liu, B. Zhang, Y. Zhang, Prediction of In-Situ Gasification Chemical Looping Combustion Effects of Operating Conditions, Catalysts. 8 (2018) 526.

[128] M. Yang, S. Banerjee, R.K. Agarwal, Transient Cold Flow Simulation of Fast Fluidized Bed Fuel Reactors for Chemical-Looping Combustion, J. Energy Resour. Technol. 140 (2018).

[129] J. May, F. Alobaid, P. Ohlemueller, A. Stroh, J. Stroehle, B. Epple, Reactive two–fluid model for chemical–looping combustion–Simulation of fuel and air reactors, Int. J. Greenh. Gas Control. 76 (2018) 175–192.

[130] Z. Reinking, H.-S. Shim, K.J. Whitty, J.S. Lighty, Computational simulation of a 100 kW dual circulating fluidized bed reactor processing coal by chemical looping with oxygen uncoupling, Int. J. Greenh. Gas Control. 90 (2019) 102795.

[131] J. Lin, K. Luo, L. Sun, S. Wang, C. Hu, J. Fan, Numerical Investigation of Nickel–Copper Oxygen Carriers in Chemical-Looping Combustion Process with Zero Emission of CO and H2, Energy & Fuels. 33 (2019) 12096–12105.

[132] X. Wang, X. Liu, Y. Zhang, B. Zhang, B. Jin, Numerical Investigation of Solid-Fueled Chemical Looping Combustion Process Utilizing Char for Carbon Capture, Processes. 7 (2019) 603.

[133] X. Chen, J. Ma, X. Tian, Z. Xu, H. Zhao, Numerical investigation on the improvement of carbon conversion in a dual circulating fluidized bed reactor for chemical looping combustion of coal, Energy & Fuels. 33 (2019) 12801–12813.

[134] X. Chen, J. Ma, X. Tian, J. Wan, H. Zhao, CPFD simulation and optimization of a 50 kWth dual circulating fluidized bed reactor for chemical looping combustion of coal, Int. J. Greenh. Gas Control. 90 (2019) 102800.

[135] Z. Li, H. Xu, W. Yang, A. Zhou, M. Xu, CFD simulation of a fluidized bed reactor for biomass chemical looping gasification with continuous feedstock, Energy Convers. Manag. 201 (2019) 112143.

[136] Z. Hamidouche, E. Masi, P. Fede, O. Simonin, K. Mayer, S. Penthor, Unsteady three-dimensional theoretical model and numerical simulation of a 120-kW chemical looping combustion pilot plant, Chem. Eng. Sci. 193 (2019) 102–119.

[137] Y. Shao, R.K. Agarwal, J. Li, X. Wang, B. Jin, Computational Fluid Dynamics–Discrete Element Model Simulation of Flow Characteristics and Solids' Residence Time Distribution in a Moving Bed Air Reactor for Chemical Looping Combustion, Ind. Eng. Chem. Res. 59 (2020) 18180–18192.

[138] J. Lin, K. Luo, L. Sun, S. Wang, C. Hu, J. Fan, Numerical investigation of a syngas-fueled chemical looping combustion system, Energy & Fuels. 34 (2020) 12800–12809.

[139] W. Yin, S. Wang, K. Zhang, Y. He, Numerical investigation of in situ gasification chemical looping combustion of biomass in a fluidized bed reactor, Renew. Energy. 151 (2020) 216–225.

[140] X. Wang, Y. Shao, B. Jin, Y. Zhang, Three-dimensional multiphase full-loop simulation of directional separation of binary particle mixtures in high-flux coal-direct chemical-looping combustion system, Particuology. 49 (2020) 179–190.

[141] Z. Hamidouche, X. Ku, J. Lin, J. Wang, Numerical simulation of a chemical looping combustion of biomass: Hydrodynamic investigation, Fuel Process. Technol. 207 (2020) 106486.

[142] X. Zhu, X. Feng, Y. Zou, L. Shen, Effect of baffles on bubble behavior in a bubbling fluidized bed for chemical looping processes, Particuology. (2020).

[143] Y. Shao, R.K. Agarwal, X. Wang, B. Jin, Numerical simulation of a 3D full loop iG-CLC system including a two-stage counter-flow moving bed air reactor, Chem. Eng. Sci. 217 (2020) 115502.

[144] S. Wang, J. Gao, H. Lu, G. Liu, P. Xu, L. Sun, Simulation of flow behavior of particles by cluster structure-dependent drag coefficient model for chemical

looping combustion process: Air reactor modeling, Fuel Process. Technol. 104 (2012) 219–233.

[145] W. Shuai, Y. Yunchao, L. Huilin, W. Jiaxing, X. Pengfei, L. Guodong, Hydrodynamic simulation of fuel-reactor in chemical looping combustion process, Chem. Eng. Res. Des. 89 (2011) 1501–1510.

[146] Z. Zhang, R. Agarwal, Transient simulations of spouted fluidized bed for coal-direct chemical looping combustion, in: ASME Power Conf., American Society of Mechanical Engineers, 2014: p. V001T01A018.

[147] X. Wang, B. Jin, Y. Zhang, Y. Zhang, X. Liu, Three dimensional modeling of a coal-fired chemical looping combustion process in the circulating fluidized bed fuel reactor, Energy & Fuels. 27 (2013) 2173–2184.

[148] Y. Guan, J. Chang, K. Zhang, B. Wang, Q. Sun, Three-dimensional CFD simulation of hydrodynamics in an interconnected fluidized bed for chemical looping combustion, Powder Technol. 268 (2014) 316–328.

[149] S. Banerjee, R. Agarwal, Transient reacting flow simulation of spouted fluidized bed for coal-direct chemical looping combustion with different Fe-based oxygen carriers, Appl. Energy. 160 (2015) 552–560.

[150] J.M. Parker, CFD model for the simulation of chemical looping combustion, Powder Technol. 265 (2014) 47–53.

[151] C. Geng, W. Zhong, Y. Shao, D. Chen, B. Jin, Computational study of solid circulation in chemical-looping combustion reactor model, Powder Technol. 276 (2015) 144–155.

[152] A. Lyngfelt, B. Leckner, T. Mattisson, A fluidized-bed combustion process with inherent CO2 separation; application of chemical-looping combustion, Chem. Eng. Sci. 56 (2001) 3101–3113.

[153] E.S. Rubin, C. Chen, A.B. Rao, Cost and performance of fossil fuel power plants with CO2 capture and storage, Energy Policy. 35 (2007) 4444–4454.

[154] H. Herzog, D. Golomb, Carbon Capture and Storage from Fossil Fuel Use, Encycl. Energy. 1 (2004) 277–287.

[155] J.C.M. Pires, F.G. Martins, M.C.M. Alvim-Ferraz, M. Simões, Recent developments on carbon capture and storage: An overview, Chem. Eng. Res. Des. 89 (2011) 1446–1460.

[156] P. Asiedu-Boateng, R. Legros, G.S. Patience, Attrition resistance of calcium oxide–copper oxide–cement sorbents for post-combustion carbon dioxide capture, Adv. Powder Technol. 27 (2016) 786–795.

[157] A. Abad, I. Adánez-Rubio, P. Gayán, F. García-Labiano, L.F. de Diego, J. Adánez, Demonstration of chemical-looping with oxygen uncoupling (CLOU) process in a 1.5kWth continuously operating unit using a Cu-based oxygen-carrier, Int. J. Greenh. Gas Control. 6 (2012) 189–200. https://doi.org/https://doi.org/10.1016/j.ijggc.2011.10.016.

[158] J. Ströhle, M. Orth, B. Epple, Design and operation of a 1 MWth chemical looping plant, Appl. Energy. 113 (2014) 1490–1495.

[159] N. Berguerand, A. Lyngfelt, Batch testing of solid fuels with ilmenite in a 10 kWth chemical-looping combustor, Fuel. 89 (2010) 1749–1762.

[160] A.K. Dubey, A. Samanta, P. Sarkar, M.K. Karmakar, A. Mukherjee, C. Loha, M. Kumar, S.G. Sahu, V.K. Saxena, P.K. Chatterjee, Hydrodynamic characteristics in a pilot-scale cold flow model for chemical looping combustion, Adv. Powder Technol. 29 (2018) 1499–1506.

[161] A. Tong, D. Sridhar, Z. Sun, H.R. Kim, L. Zeng, F. Wang, D. Wang, M. V Kathe, S. Luo, Y. Sun, Continuous high purity hydrogen generation from a syngas chemical looping 25 kWth sub-pilot unit with 100% carbon capture, Fuel. 103 (2013) 495–505.

[162] M. Rydén, A. Lyngfelt, Using steam reforming to produce hydrogen with carbon dioxide capture by chemical-looping combustion, Int. J. Hydrogen Energy. 31 (2006) 1271–1283.

[163] B. Kronberger, E. Johansson, G. Löffler, T. Mattisson, A. Lyngfelt, H. Hofbauer, A two-compartment fluidized bed reactor for CO2 capture by chemical-looping combustion, Chem. Eng. Technol. Ind. Chem. Equipment-Process Eng. 27 (2004) 1318–1326.

[164] B. Kronberger, A. Lyngfelt, G. Löffler, H. Hofbauer, Design and fluid dynamic analysis of a bench-scale combustion system with CO2 separation− chemical-looping combustion, Ind. Eng. Chem. Res. 44 (2005) 546–556.

[165] J. Adánez, P. Gayán, J. Celaya, L.F. De Diego, F. García-Labiano, A. Abad, Chemical looping combustion in a 10 kWth prototype using a CuO/Al2O3 oxygen carrier: Effect of operating conditions on methane combustion, Ind. Eng. Chem. Res. 45 (2006) 6075–6080.

[166] A. Thon, M. Kramp, E.-U. Hartge, S. Heinrich, J. Werther, Operational experience with a system of coupled fluidized beds for chemical looping combustion of solid fuels using ilmenite as oxygen carrier, Appl. Energy. 118 (2014) 309–317.

[167] P. Kolbitsch, J. Bolhàr-Nordenkampf, T. Pröll, H. Hofbauer, Operating experience with chemical looping combustion in a 120 kW dual circulating fluidized bed (DCFB) unit, Int. J. Greenh. Gas Control. 4 (2010) 180–185.

[168] M.W. Seo, T.D.B. Nguyen, Y. Il Lim, S.D. Kim, S. Park, B.H. Song, Y.J. Kim, Solid circulation and loop-seal characteristics of a dual circulating fluidized bed: experiments and CFD simulation, Chem. Eng. J. 168 (2011) 803–811.

[169] T. Pröll, P. Kolbitsch, J. Bolhàr-Nordenkampf, H. Hofbauer, A novel dual circulating fluidized bed system for chemical looping processes, AICHE J. 55 (2009) 3255–3266.

[170] P. Kolbitsch, T. Pröll, J. Bolhar-Nordenkampf, H. Hofbauer, Design of a chemical looping combustor using a dual circulating fluidized bed (DCFB) reactor system, Chem. Eng. Technol. Ind. Chem. Equipment-Process Eng. 32 (2009) 398–403.

[171] S. Wang, K. Luo, C. Hu, J. Fan, CFD-DEM study of the effect of cyclone arrangements on the gas-solid flow dynamics in the full-loop circulating fluidized bed, Chem. Eng. Sci. 172 (2017) 199–215.

[172] M.A. van der Hoef, M. van Sint Annaland, N.G. Deen, J.A.M. Kuipers, Numerical simulation of dense gas-solid fluidized beds: a multiscale modeling strategy, Annu. Rev. Fluid Mech. 40 (2008) 47–70.

[173] M.W. Baltussen, K.A. Buist, E.A.J.F. Peters, J.A.M. Kuipers, Multiscale Modelling of Dense Gas–Particle Flows, in: Adv. Chem. Eng., Elsevier, 2018: pp. 1–52.

[174] H.P. Zhu, Z.Y. Zhou, R.Y. Yang, A.B. Yu, Discrete particle simulation of particulate systems: a review of major applications and findings, Chem. Eng. Sci. 63 (2008) 5728–5770.

[175] Y. Cui, W. Zhong, J. Xiang, G. Liu, Simulation on coal-fired supercritical CO2 circulating fluidized bed boiler: Coupled combustion with heat transfer, Adv. Powder Technol. 30 (2019) 3028–3039.

[176] J. Gu, Y. Shao, X. Liu, W. Zhong, A. Yu, Modelling of particle flow in a dual circulation fluidized bed by a Eulerian-Lagrangian approach, Chem. Eng. Sci. 192 (2018) 619–633.

[177] S. Wang, H. Lu, F. Zhao, G. Liu, CFD studies of dual circulating fluidized bed reactors for chemical looping combustion processes, Chem. Eng. J. 236 (2014) 121–130.

[178] M. Su, H. Zhao, J. Ma, Computational fluid dynamics simulation for chemical looping combustion of coal in a dual circulation fluidized bed, Energy Convers. Manag. 105 (2015) 1–12.

[179] T. Li, S. Pannala, M. Shahnam, CFD simulations of circulating fluidized bed risers, part II, evaluation of differences between 2D and 3D simulations, Powder Technol. 254 (2014) 115–124.

[180] C.Y. Wen, Mechanics of fluidization, in: Chem. Eng. Prog., Symp. Ser., 1966: pp. 100–111.

[181] M. Syamlal, T.J. O'Brien, Computer simulation of bubbles in a fluidized bed, in: AIChE Symp. Ser, 1989: pp. 22–31.

[182] D. Gidaspow, Multiphase flow and fluidization: continuum and kinetic theory descriptions, Academic press, 1994.

[183] S. Ergun, Fluid flow through packed columns, Chem. Eng. Prog. 48 (1952) 89–94.

[184] J. Li, Particle-fluid two-phase flow: the energy-minimization multi-scale method, Metallurgical Industry Press, 1994.

[185] Y. Wu, D. Liu, J. Ma, X. Chen, Effects of gas-solid drag model on Eulerian-Eulerian CFD simulation of coal combustion in a circulating fluidized bed, Powder Technol. 324 (2018) 48–61.

[186] D.L. Koch, R.J. Hill, Inertial effects in suspension and porous-media flows, Annu. Rev. Fluid Mech. 33 (2001) 619–647.

[187] M.A. van der Hoef, R. Beetstra, J.A.M. Kuipers, Lattice-Boltzmann simulations of low-Reynolds-number flow past mono-and bidisperse arrays of spheres: results for the permeability and drag force, J. Fluid Mech. 528 (2005) 233–254.

[188] S. Benyahia, M. Syamlal, T.J. O'Brien, Extension of Hill–Koch–Ladd drag correlation over all ranges of Reynolds number and solids volume fraction, Powder Technol. 162 (2006) 166–174.

[189] R. Beetstra, M.A. van der Hoef, J.A.M. Kuipers, Drag force of intermediate Reynolds number flow past mono-and bidisperse arrays of spheres, AICHE J. 53 (2007) 489–501.

[190] W. Holloway, X. Yin, S. Sundaresan, Fluid-particle drag in inertial polydisperse gas–solid suspensions, AICHE J. 56 (2010) 1995–2004.

[191] F. Cello, A. Di Renzo, F.P. Di Maio, A semi-empirical model for the drag force and fluid–particle interaction in polydisperse suspensions, Chem. Eng. Sci. 65 (2010) 3128–3139.

[192] S. Tenneti, R. Garg, S. Subramaniam, Drag law for monodisperse gas--solid systems using particle-resolved direct numerical simulation of flow past fixed assemblies of spheres, Int. J. Multiph. Flow. 37 (2011) 1072–1092.

[193] Y. Tang, E. Peters, J.A.M. Kuipers, Direct numerical simulations of dynamic gas-solid suspensions, AIChE J. 62 (2016) 1958–1969.

[194] Y. Tang, E. Peters, J.A.M. Kuipers, S.H.L. Kriebitzsch, M.A. van der Hoef, A new drag correlation from fully resolved simulations of flow past monodisperse static arrays of spheres, AICHE J. 61 (2015) 688–698.

[195] L.W. Rong, K.J. Dong, A.B. Yu, Lattice-Boltzmann simulation of fluid flow through packed beds of uniform spheres: Effect of porosity, Chem. Eng. Sci. 99 (2013) 44–58.

[196] C.K.K. Lun, S.B. Savage, D.J. Jeffrey, N. Chepurniy, Kinetic theories for granular flow: inelastic particles in Couette flow and slightly inelastic particles in a general flowfield, J. Fluid Mech. 140 (1984) 223–256.

[197] B. Lu, N. Zhang, W. Wang, J. Li, J.H. Chiu, S.G. Kang, 3-D full-loop simulation of an industrial-scale circulating fluidized-bed boiler, AICHE J. 59 (2013) 1108–1117.

[198] C. Geng, Y. Shao, W. Zhong, A. Yu, Experiments on particles flow in a dual circulating fluidized bed with symmetrical structure, Powder Technol. 304 (2016) 81–88.

[199] J. Gu, W. Zhong, Y. Shao, X. Liu, Particle-Motion Behaviors in a Dual Circulating Fluidized Bed by a Multiphase Particle-in-Cell Method, Ind. Eng. Chem. Res. 57 (2018) 14809–14821.

[200] D.G. Schaeffer, Instability in the evolution equations describing incompressible granular flow, J. Differ. Equ. 66 (1987) 19–50.

[201] P.C. Johnson, R. Jackson, Frictional--collisional constitutive relations for granular materials, with application to plane shearing, J. Fluid Mech. 176 (1987) 67–93.

[202] X. Zhou, J. Gao, C. Xu, X. Lan, Effect of wall boundary condition on CFD simulation of CFB risers, Particuology. 11 (2013) 556–565.

[203] M.T. Shah, R.P. Utikar, V.K. Pareek, M.O. Tade, G.M. Evans, Effect of closure models on Eulerian–Eulerian gas–solid flow predictions in riser, Powder Technol. 269 (2015) 247–258.

[204] K. Hong, Y. Gao, A. Ullah, F. Xu, Q. Xiong, G. Lorenzini, Multi-scale CFD modeling of gas-solid bubbling fluidization accounting for sub-grid information, Adv. Powder Technol. 29 (2018) 488–498.

[205] N. Zhang, B. Lu, W. Wang, J. Li, Virtual experimentation through 3D full-loop simulation of a circulating fluidized bed, Particuology. 6 (2008) 529–539.

[206] C. Liu, M. Zhao, W. Wang, J. Li, 3D CFD simulation of a circulating fluidized bed with on-line adjustment of mechanical valve, Chem. Eng. Sci. 137 (2015) 646–655.

[207] S. Wang, K. Luo, S. Yang, C. Hu, J. Fan, Parallel LES-DEM simulation of dense flows in fluidized beds, Appl. Therm. Eng. 111 (2017) 1523–1535.

[208] Y. Xu, J. Musser, T. Li, B. Gopalan, R. Panday, J. Tucker, G. Breault, M.A. Clarke, W.A. Rogers, Numerical Simulation and Experimental Study of the Gas–Solid Flow Behavior Inside a Full-Loop Circulating Fluidized Bed: Evaluation of Different Drag Models, Ind. Eng. Chem. Res. 57 (2018) 740–750.

[209] S. Wang, K. Luo, C. Hu, J. Fan, CFD-DEM study of the effect of ring baffles on system performance of a full-loop circulating fluidized bed, Chem. Eng. Sci. 196 (2019) 130–144.

[210] N. Yang, W. Wang, W. Ge, J. Li, CFD simulation of concurrent-up gas–solid flow in circulating fluidized beds with structure-dependent drag coefficient, Chem. Eng. J. 96 (2003) 71–80.

[211] A. Nikolopoulos, N. Nikolopoulos, A. Charitos, P. Grammelis, E. Kakaras, A.R. Bidwe, G. Varela, High-resolution 3-D full-loop simulation of a CFB carbonator cold model, Chem. Eng. Sci. 90 (2013) 137–150.

[212] Y. Yao, Y.-J. He, Z.-H. Luo, L. Shi, 3D CFD-PBM modeling of the gas–solid flow field in a polydisperse polymerization FBR: The effect of drag model, Adv. Powder Technol. 25 (2014) 1474–1482.

[213] V. Jiradilok, D. Gidaspow, S. Damronglerd, W.J. Koves, R. Mostofi, Kinetic theory based CFD simulation of turbulent fluidization of FCC particles in a riser, Chem. Eng. Sci. 61 (2006) 5544–5559.

[214] H. Zhu, J. Zhu, Characterization of fluidization behavior in the bottom region of CFB risers, Chem. Eng. J. 141 (2008) 169–179.

[215] D. Bai, A.S. Issangya, J.R. Grace, Characteristics of gas-fluidized beds in different flow regimes, Ind. Eng. Chem. Res. 38 (1999) 803–811.

[216] S. Hu, X. Liu, N. Zhang, J. Li, W. Ge, W. Wang, Quantifying cluster dynamics to improve EMMS drag law and radial heterogeneity description in coupling with gas-solid two-fluid method, Chem. Eng. J. 307 (2017) 326–338.

[217] J. Wang, Flow structures inside a large-scale turbulent fluidized bed of FCC particles: Eulerian simulation with an EMMS-based sub-grid scale model, Particuology. 8 (2010) 176–185.

[218] M.S. Alagha, P. Szentannai, Analytical review of fluid-dynamic and thermal modeling aspects of fluidized beds for energy conversion devices, Int. J. Heat Mass Transf. 147 (2020) 118907.

[219] L. Zhou, Z.G. Qu, T. Ding, J.Y. Miao, Lattice Boltzmann simulation of the gas-solid adsorption process in reconstructed random porous media, Phys. Rev. E. 93 (2016) 43101.

[220] K. Hong, Z. Shi, A. Ullah, W. Wang, Extending the bubble-based EMMS model to CFB riser simulations, Powder Technol. 266 (2014) 424–432.

[221] H.T. Bi, J. Li, Multiscale analysis and modeling of multiphase chemical reactors, Adv. Powder Technol. 15 (2004) 607–627.

[222] M. Marek, Numerical simulation of a gas flow in a real geometry of random packed bed of Raschig rings, Chem. Eng. Sci. 161 (2017) 382–393.

[223] L.W. Rong, Z.Y. Zhou, A.B. Yu, Lattice–Boltzmann simulation of fluid flow through packed beds of uniform ellipsoids, Powder Technol. 285 (2015) 146–156.

[224] L.W. Rong, K.J. Dong, A.B. Yu, Lattice-Boltzmann simulation of fluid flow through packed beds of spheres: Effect of particle size distribution, Chem. Eng. Sci. 116 (2014) 508–523.

[225] C.C. Chueh, A. Bertei, J.G. Pharoah, C. Nicolella, Effective conductivity in random porous media with convex and non-convex porosity, Int. J. Heat Mass Transf. 71 (2014) 183–188.

[226] L. Wang, J. Mi, Z. Guo, A modified lattice Bhatnagar–Gross–Krook model for convection heat transfer in porous media, Int. J. Heat Mass Transf. 94 (2016) 269–291.

[227] R. Stanly, G. Shoev, Detailed analysis of recent drag models using multiple cases of mono-disperse fluidized beds with Geldart-B and Geldart-D particles, Chem. Eng. Sci. 188 (2018) 132–149.

[228] M.J. V Goldschmidt, R. Beetstra, J.A.M. Kuipers, Hydrodynamic modelling of dense gas-fluidised beds: comparison and validation of 3D discrete particle and continuum models, Powder Technol. 142 (2004) 23–47.

[229] W. Wang, B. Lu, N. Zhang, Z. Shi, J. Li, A review of multiscale CFD for gas–solid CFB modeling, Int. J. Multiph. Flow. 36 (2010) 109–118.

[230] S. Sundaresan, Instabilities in fluidized beds, Annu. Rev. Fluid Mech. 35 (2003) 63–88.

[231] X. Gao, L.-J. Wang, C. Wu, Y.-W. Cheng, X. Li, Novel bubble–emulsion hydrodynamic model for gas–solid bubbling fluidized beds, Ind. Eng. Chem. Res. 52 (2013) 10835–10844.

[232] H. Andrus, G. Burns, J. Chiu, G. Lijedahl, P. Stromberg, P. Thibeault, Hybrid Combustion-Gasification Chemical Looping, Alstom Power Inc, 2009.

[233] A. Tong, S. Bayham, M. V Kathe, L. Zeng, S. Luo, L.-S. Fan, Iron-based syngas chemical looping process and coal-direct chemical looping process development at Ohio State University, Appl. Energy. 113 (2014) 1836–1845.

[234] D. Xu, Y. Zhang, T.-L. Hsieh, M. Guo, L. Qin, C. Chung, L.-S. Fan, A. Tong, A novel chemical looping partial oxidation process for thermochemical conversion of biomass to syngas, Appl. Energy. 222 (2018) 119–131.

[235] Z. Miao, Z. Zhou, A.B. Yu, Y. Shen, CFD-DEM simulation of raceway formation in an ironmaking blast furnace, Powder Technol. 314 (2017) 542–549.

[236] Y. Shen, A. Yu, P. Zulli, CFD modelling and analysis of pulverized coal injection in blast furnace: an overview, Steel Res. Int. 82 (2011) 532–542.

[237] J. Liao, A.B. Yu, Y. Shen, Modelling the injection of upgraded brown coals in an ironmaking blast furnace, Powder Technol. 314 (2017) 550–556.

[238] X. Wang, B. Jin, W. Zhong, Y. Zhang, M. Song, Three-dimensional simulation of a coal gas fueled chemical looping combustion process, Int. J. Greenh. Gas Control. 5 (2011) 1498–1506.

[239] H. Liu, J. Li, Q. Wang, Simulation of gas--solid flow characteristics in a circulating fluidized bed based on a computational particle fluid dynamics model, Powder Technol. 321 (2017) 132–142.

[240] S. Wang, K. Luo, C. Hu, L. Sun, J. Fan, Effect of superficial gas velocity on solid behaviors in a full-loop CFB, Powder Technol. 333 (2018) 91–105.

[241] Y. Tang, S.H.L. Kriebitzsch, E. Peters, M.A. Van der Hoef, J.A.M. Kuipers, A methodology for highly accurate results of direct numerical simulations: drag force in dense gas–solid flows at intermediate Reynolds number, Int. J. Multiph. Flow. 62 (2014) 73–86.

[242] H.R. Kim, Coal-Direct Chemical Looping Combustion Process for In-Situ Carbon Dioxide Capture–Operational Experience of Integrated 25-kWth Sub-Pilot Scale Unit, (2012).

[243] X. Shi, Y. Wu, X. Lan, F. Liu, J. Gao, Effects of the riser exit geometries on the hydrodynamics and solids back-mixing in CFB risers: 3D simulation using CPFD approach, Powder Technol. 284 (2015) 130–142.

[244] Y. Zhang, Q. Ma, X. Xu, Y. Xiao, F. Lei, Numerical study of gas–solid flow behavior in a two-stage high-density riser using EMMS-based drag model, Chem. Eng. Process. Process Intensif. 98 (2015) 71–85.

[245] Q. Zhou, J. Wang, J. Li, Three-dimensional simulation of dense suspension upflow regime in high-density CFB risers with EMMS-based two-fluid model, Chem. Eng. Sci. 107 (2014) 206–217.

[246] M. Abdulkadir, V. Hernandez-Perez, S. Lo, I.S. Lowndes, B.J. Azzopardi, Comparison of experimental and Computational Fluid Dynamics (CFD) studies of slug flow in a vertical riser, Exp. Therm. Fluid Sci. 68 (2015) 468–483.

[247] D. Wang, M. Xu, Q. Marashdeh, B. Straiton, A. Tong, L.-S. Fan, Electrical Capacitance Volume Tomography for Characterization of Gas–Solid Slugging

Fluidization with Geldart Group D Particles under High Temperatures, Ind. Eng. Chem. Res. 57 (2018) 2687–2697. https://doi.org/10.1021/acs.iecr.7b04733.

[248] C. Amornsirirat, B. Chalermsinsuwan, L. Mekasut, P. Kuchonthara, P. Piumsomboon, Experiment and 3D simulation of slugging regime in a circulating fluidized bed, Korean J. Chem. Eng. 28 (2011) 686–696.

[249] F. Berruti, N. Kalogerakis, Modelling the internal flow structure of circulating fluidized beds, Can. J. Chem. Eng. 67 (1989) 1010–1014.

[250] H. Zhang, W. Huang, J. Zhu, Gas-solids flow behavior: CFB riser vs. downer, AIChE J. 47 (2001) 2000–2011.

[251] J. You, C. Zhu, B. Du, L. Fan, Heterogeneous structure in gas–solid riser flows, AIChE J. 54 (2008) 1459–1469.

[252] A. Anantharaman, A. Issangya, S.B.R. Karri, J. Findlay, C.M. Hrenya, R.A. Cocco, J.W. Chew, Annulus flow behavior of Geldart Group B particles in a pilot-scale CFB riser, Powder Technol. 305 (2017) 816–828.

[253] M. Kashyap, D. Gidaspow, W.J. Koves, Circulation of Geldart D type particles: Part I--High solids fluxes. Measurements and computation under solids slugging conditions, Chem. Eng. Sci. 66 (2011) 183–206.

[254] B. Lu, W. Wang, J. Li, Eulerian simulation of gas–solid flows with particles of Geldart groups A, B and D using EMMS-based meso-scale model, Chem. Eng. Sci. 66 (2011) 4624–4635.

[255] X. Lan, C. Xu, J. Gao, M. Al-Dahhan, Influence of solid-phase wall boundary condition on CFD simulation of spouted beds, Chem. Eng. Sci. 69 (2012) 419–430.

[256] Y.S. Won, A.-R. Jeong, J.-H. Choi, S.-H. Jo, H.-J. Ryu, C.-K. Yi, Temperature effects on riser pressure drop in a circulating fluidized bed, Korean J. Chem. Eng. 34 (2017) 913–920.

[257] W. Wang, B. Lu, W. Dong, J. Li, Multi-scale CFD simulation of operating diagram for gas–solid risers, Can. J. Chem. Eng. 86 (2008) 448–457.

[258] Z. Chen, L.G. Gibilaro, P.U. Foscolo, Fluid pressure loss in slugging fluidised beds, Chem. Eng. Sci. 52 (1997) 55–62.

[259] L. Zeng, F. Li, R. Kim, S. Bayham, O. McGiveron, A. Tong, D. Connell, S. Luo, D. Sridhar, F. Wang, Coal Direct Chemical Looping Retrofit to Pulverized Coal Power Plants for In-Situ CO2 Capture, Ohio State University Research Foundation, 2013.

[260] D.J. Gunn, Transfer of heat or mass to particles in fixed and fluidised beds, Int. J. Heat Mass Transf. 21 (1978) 467–476.

[261] P. Cheng, Two-dimensional radiating gas flow by a moment method, AIAA J. 2 (1964) 1662–1664.

[262] M. Lopez de Bertodano, Turbulent bubbly flow in a triangular duct, New York Rensselaer Polytech. Inst. (1991).

[263] F. Greifzu, C. Kratzsch, T. Forgber, F. Lindner, R. Schwarze, Assessment of particle-tracking models for dispersed particle-laden flows implemented in OpenFOAM and ANSYS FLUENT, Eng. Appl. Comput. Fluid Mech. 10 (2016) 30–43.

[264] A. Lyngfelt, B. Kronberger, J. Adanez, J.-X. Morin, P. Hurst, The grace project: Development of oxygen carrier particles for chemical-looping combustion. Design and operation of a 10 kW chemical-looping combustor, in: Greenh. Gas Control Technol. 7, Elsevier, 2005: pp. 115–123.

[265] K. Mahalatkar, J. Kuhlman, E.D. Huckaby, T. O'brien, Simulations of a circulating fluidized bed chemical looping combustion system utilizing gaseous fuel, Oil Gas Sci. Technol. d'IFP Energies Nouv. 66 (2011) 301–311.

[266] W. Shuai, L. Guodong, L. Huilin, C. Juhui, H. Yurong, W. Jiaxing, Fluid dynamic simulation in a chemical looping combustion with two interconnected fluidized beds, Fuel Process. Technol. 92 (2011) 385–393.

[267] D.. Bolthrunis, C.O., Silverman, R.W, Ferrari, Rocky Road to Commercialization: Breakthroughs and Challenges in the Commercialization of Fluidized Bed Reactors, Eng. Conf. Int. (2004) 547–554.

[268] G. Minor, X. Zhu, P. Oshkai, P.C. Sui, N. Djilali, Water transport dynamics in fuel cell micro-channels, in: Mini-Micro Fuel Cells, Springer, 2008: pp. 153–170.

[269] X. Wang, B. Zhou, Liquid water flooding process in proton exchange membrane fuel cell cathode with straight parallel channels and porous layer, J. Power Sources. 196 (2011) 1776–1794.

[270] R. Anderson, L. Zhang, Y. Ding, M. Blanco, X. Bi, D.P. Wilkinson, A critical review of two-phase flow in gas flow channels of proton exchange membrane fuel cells, J. Power Sources. 195 (2010) 4531–4553.

[271] F. Bonniol, C. Sierra, R. Occelli, L. Tadrist, Similarity in dense gas–solid fluidized bed, influence of the distributor and the air-plenum, Powder Technol. 189 (2009) 14–24.

[272] C. Sobrino, N. Ellis, M. de Vega, Distributor effects near the bottom region of turbulent fluidized beds, Powder Technol. 189 (2009) 25–33.

[273] Y. He, T.J. Evans, Y.S. Shen, A.B. Yu, R.Y. Yang, Discrete modelling of the compaction of non-spherical particles using a multi-sphere approach, Miner. Eng. 117 (2018) 108–116.

[274] H. Zhou, Z.-G. Luo, T. Zhang, Y. You, Z.-S. Zou, Y. Shen, DEM study of solid flow in COREX shaft furnace with areal gas distribution beams, ISIJ Int. 56 (2016) 245–254.

[275] Y. Zhuo, Y. Shen, Modelling of the pyrolysis of low-rank-coal briquettes in an industrial-scale gas heat carrier pyrolyzer, Powder Technol. 361 (2020) 52–61.

[276] A.A. Avidan, Fluid catalytic cracking, in: Circ. Fluid. Beds, Springer, 1997: pp. 466–488.

[277] G.X. Yue, H.R. Yang, J.F. Lu, H. Zhang, Latest development of CFB boilers in China, in: Proc. 20th Int. Conf. Fluid. Bed Combust., Springer, 2009: pp. 3–12.

[278] G. Yue, R. Cai, J. Lu, H. Zhang, From a CFB reactor to a CFB boiler–The review of R&D progress of CFB coal combustion technology in China, Powder Technol. 316 (2017) 18–28.

[279] F. Duan, B. Jin, Y. Huang, B. Li, Y. Wu, M. Zhang, Results of bituminous coal gasification upon exposure to a pressurized pilot-plant circulating fluidized-bed (CFB) reactor, Energy & Fuels. 24 (2010) 3150–3158.

[280] X.T. Bi, X. Liu, High density and high solids flux CFB risers for steam gasification of solids fuels, Fuel Process. Technol. 91 (2010) 915–920.

[281] S. Yang, H. Yang, H. Zhang, S. Li, G. Yue, A transient method to study the pressure drop characteristics of the cyclone in a CFB system, Powder Technol. 192 (2009) 105–109.

[282] S. De, P.K. Nag, Pressure drop and collection efficiency of cyclone and impact separators in a CFB, Int. J. Energy Res. 23 (1999) 51–60.

[283] L. Zhang, W. Du, H.T. Bi, D.P. Wilkinson, J. Stumper, H. Wang, Gas–liquid two-phase flow distributions in parallel channels for fuel cells, J. Power Sources. 189 (2009) 1023–1031.

[284] X. Zhou, L. Cheng, Q. Wang, Z. Luo, K. Cen, Non-uniform distribution of gas–solid flow through six parallel cyclones in a CFB system: An experimental study, Particuology. 10 (2012) 170–175.

[285] J.R. Grace, H. Cui, S.S.E.H. Elnashaie, Non-uniform distribution of two-phase flows through parallel identical paths, Can. J. Chem. Eng. 85 (2007) 662–668.

[286] M.S. Masnadi-Shirazi, Mal-distribution of gas-solid flow through identical parallel paths, (2009).

[287] M.S. Masnadi, J.R. Grace, S. Elyasi, X. Bi, Distribution of multi-phase gas–solid flow across identical parallel cyclones: Modeling and experimental study, Sep. Purif. Technol. 72 (2010) 48–55.

[288] L. Fan, J.R. Grace, N. Epstein, Investigation of nonuniformity in a liquid–solid fluidized bed with identical parallel channels, AIChE J. 56 (2010) 92–101.

[289] T.-W. Kim, J.-H. Choi, D.W. Shun, S.-S. Kim, S.D. Kim, J.R. Grace, Wear of water walls in a commercial circulating fluidized bed combustor with two gas exits, Powder Technol. 178 (2007) 143–150.

[290] C. Fushimi, K. Yato, M. Sakai, T. Kawano, T. Kita, Recent Progress in Efficient Gas–Solid Cyclone Separators with a High Solids Loading for Large-scale Fluidized Beds, KONA Powder Part. J. (2019) 2021001.

[291] W. Fei, R. Xing, Z. Rujin, L. Guohua, J. Yong, A dispersion model for fluid catalytic cracking riser and downer reactors, Ind. Eng. Chem. Res. 36 (1997) 5049–5053.

[292] G.X. Yue, H.R. Yang, L. Nie, Y. Wang, H. Zhang, Hydrodynamics of 300 MWe and 600 MWe CFB boilers with asymmetric cyclone layout, Circ. Fluid. Bed Technol. IX. (2008) 13–16.

[293] D. Shuai, X. Wang, Q. Lyu, Hydrodynamics in a circulating fluidized bed with annular furnace and six parallel cyclones, J. Therm. Sci. 26 (2017) 273–281.

[294] N. Zhang, B. Lu, W. Wang, J. Li, 3D CFD simulation of hydrodynamics of a 150 MWe circulating fluidized bed boiler, Chem. Eng. J. 162 (2010) 821–828.

[295] K. Luo, S. Wang, S. Yang, C. Hu, J. Fan, Computational Fluid Dynamics–Discrete Element Method Investigation of Pressure Signals and Solid Back-Mixing in a Full-Loop Circulating Fluidized Bed, Ind. Eng. Chem. Res. 56 (2017) 799–813.

[296] S. Wang, K. Luo, S. Yang, C. Hu, J. Fan, LES-DEM investigation of the time-related solid phase properties and improvements of flow uniformity in a dual-side refeed CFB, Chem. Eng. J. 313 (2017) 858–872.

[297] S. Li, Y. Shen, Numerical study of gas-solid flow behaviors in the air reactor of coal-direct chemical looping combustion with Geldart D particles, Powder Technol. 361 (2020) 74–86.

[298] J. Sánchez-Prieto, A. Soria-Verdugo, J. Gómez-Hernández, J. V Briongos, D. Santana, Maldistribution detection in bubbling fluidized beds, Chem. Eng. J. 270 (2015) 272–281.

[299] R.B. Thorpe, J.F. Davidson, M. Pollitt, J. Smith, Maldistribution in fluidized beds, Ind. Eng. Chem. Res. 41 (2002) 5878–5889.

[300] J. Chen, M. Shi, A universal model to calculate cyclone pressure drop, Powder Technol. 171 (2007) 184–191.

[301] L.X. Zhou, S.L. Soo, Gas-solid flow and collection of solids in a cyclone separator, Powder Technol. 63 (1990) 45–53.

[302] M.M. Yazdanpanah, A. Forret, T. Gauthier, A. Delebarre, An experimental investigation of L-valve operation in an interconnected circulating fluidized bed system, Powder Technol. 221 (2012) 236–244.

[303] Y. Zhang, M. Zhang, S. Zhu, Y. Huang, B. Deng, X. Gao, X. Jiang, J. Lyu, H. Yang, Mechanism analysis of gas solid flow non-uniformity problem of 330 MW CFB boiler, Chem. Eng. Res. Des. 145 (2019) 258–267.

[304] A.C. Hoffmann, L.E. Stein, Computational fluid dynamics, Springer, 2008.

[305] T. Song, L. Shen, Review of reactor for chemical looping combustion of solid fuels, Int. J. Greenh. Gas Control. 76 (2018) 92–110.

[306] B. Moghtaderi, Review of the recent chemical looping process developments for novel energy and fuel applications, Energy & Fuels. 26 (2012) 15–40.

[307] A. Lyngfelt, Chemical-looping combustion of solid fuels–status of development, Appl. Energy. 113 (2014) 1869–1873.

[308] M.M. Hossain, H.I. de Lasa, Chemical-looping combustion (CLC) for inherent CO2 separations—a review, Chem. Eng. Sci. 63 (2008) 4433–4451.

[309] W.R. Paterson, E.L. Berresford, D.L. Moppett, D.M. Scott, V.K. Simmons, R.B. Thorpe, Gas flow maldistribution in moving beds of monosized particles, Chem. Eng. Sci. 55 (2000) 3515–3527.

[310] A. Abad, J. Adánez, F. García-Labiano, F. Luis, P. Gayán, J. Celaya, Mapping of the range of operational conditions for Cu-, Fe-, and Ni-based oxygen carriers in chemical-looping combustion, Chem. Eng. Sci. 62 (2007) 533–549.

[311] M.M. Yazdanpanah, A. Hoteit, A. Forret, A. Delebarre, T. Gauthier, Experimental investigations on a novel chemical looping combustion configuration, Oil Gas Sci. Technol. d'IFP Energies Nouv. 66 (2011) 265–275.

[312] S.K. Haider, L. Duan, K. Patchigolla, E.J. Anthony, A Hydrodynamic Study of a Fast-Bed Dual Circulating Fluidized Bed for Chemical Looping Combustion, Energy Technol. 4 (2016) 1254–1262.

[313] M.M. Yazdanpanah, A. Forret, T. Gauthier, A. Delebarre, An experimental investigation of loop-seal operation in an interconnected circulating fluidized bed system, Powder Technol. 237 (2013) 266–275.

[314] S. Li, Y. Shen, Multi-fluid modelling of hydrodynamics in a dual circulating fluidized bed, Adv. Powder Technol. (2020).

[315] C. Zhang, Q. Wang, Z. Jia, U. Muhammad, W. Qian, F. Wei, Design of parallel cyclones based on stability analysis, AIChE J. 62 (2016) 4251–4258.

[316] S. Yang, H.R. Yang, Q. Liu, H. Zhang, Y.X. Wu, G.X. Yue, Y.Z. Wang, Research on flow non-uniformity in main circulation loop of a CFB boiler with multiple cyclones, in: Proc. 20th Int. Conf. Fluid. Bed Combust., Springer, 2009: pp. 341–344.

[317] C. Zhang, Q. Xu, A. Bourane, M. Ghrami, I. Abba, F. Wei, Stability Analysis of Gas–Solid Distribution through Nonidentical Parallel Paths, Ind. Eng. Chem. Res. 59 (2020) 6707–6715.

[318] J. Baeyens, D. Geldart, An investigation into slugging fluidized beds, Chem. Eng. Sci. 29 (1974) 255–265.

[319] C. Zhang, S. Li, Z. Wang, Y. Shen, F. Wei, Model and experimental study of relationship between solid fraction and back-mixing in a fluidized bed, Powder Technol. 363 (2020) 146–151.

[320] J. Li, H. Zhang, H. Yang, Q. Liu, G. Yue, The mechanism of lateral solid transfer in a CFB riser with pant-leg structure, Energy & Fuels. 24 (2010) 2628–2633.

[321] Z. Wang, J. Sun, Z. Yang, L. West, Z. Li, Bed-inventory overturn mechanism for pant-leg circulating fluidized bed boilers, Powder Technol. 214 (2011) 469–476.

[322] M. Ishida, H. Jin, A new advanced power-generation system using chemical-looping combustion, Energy. 19 (1994) 415–422.

[323] J. Ding, D. Gidaspow, A bubbling fluidization model using kinetic theory of granular flow, AIChE J. 36 (1990) 523–538.

[324] L.T. Fan, D. Neogi, M. Yashima, R. Nassar, Stochastic analysis of a three-phase fluidized bed: Fractal approach, AIChE J. 36 (1990) 1529–1535.

[325] F.J. Cabrejos, G.E. Klinzing, Characterization of dilute gas-solids flows using the rescaled range analysis, Powder Technol. 84 (1995) 139–156.

[326] N. Ellis, L.A. Briens, J.R. Grace, H.T. Bi, C.J. Lim, Characterization of dynamic behaviour in gas–solid turbulent fluidized bed using chaos and wavelet analyses, Chem. Eng. J. 96 (2003) 105–116.

[327] H. Zhang, R. Xiao, D. Wang, Z. Zhong, M. Song, Q. Pan, G. He, Catalytic fast pyrolysis of biomass in a fluidized bed with fresh and spent fluidized catalytic cracking (FCC) catalysts, Energy & Fuels. 23 (2009) 6199–6206.

[328] R. Cai, H. Zhang, M. Zhang, H. Yang, J. Lyu, G. Yue, Development and application of the design principle of fluidization state specification in CFB coal combustion, Fuel Process. Technol. 174 (2018) 41–52.

[329] J. Zhang, R. Wu, G. Zhang, C. Yao, Y. Zhang, Y. Wang, G. Xu, Recent studies on chemical engineering fundamentals for fuel pyrolysis and gasification in dual fluidized bed, Ind. Eng. Chem. Res. 52 (2013) 6283–6302.

[330] B. Galloway, G.P. Hancke, Introduction to industrial control networks, IEEE Commun. Surv. Tutorials. 15 (2012) 860–880.

[331] K. Stouffer, J. Falco, K. Scarfone, Guide to industrial control systems (ICS) security, NIST Spec. Publ. 800 (2011) 16.

[332] J.C. Basilio, S.R. Matos, Design of PI and PID controllers with transient performance specification, IEEE Trans. Educ. 45 (2002) 364–370.

[333] T.L. Blevins, PID advances in industrial control, IFAC Proc. Vol. 45 (2012) 23–28.

[334] P.D. Domański, Statistical measures for proportional–integral–derivative control quality: Simulations and industrial data, Proc. Inst. Mech. Eng. Part I J. Syst. Control Eng. 232 (2018) 428–441.

[335] A. Izadkhah, K. Nouri, A. Nikoobin, Proportional integral derivative control of fractional–order for a quarter–vehicle active suspension system, Rom. J. Phys. 65 (2020) 103.

[336] S. Akhyar, S. Omatu, Self-tuning PID control by neural-networks, in: Proc. 1993 Int. Conf. Neural Networks (IJCNN-93-Nagoya, Japan), IEEE, 1993: pp. 2749–2752.

[337] C. Zhao, L. Guo, PID controller design for second order nonlinear uncertain systems, Sci. China Inf. Sci. 60 (2017) 22201.

[338] D.P. Atherton, S. Majhi, Limitations of PID controllers, in: Proc. 1999 Am. Control Conf. (Cat. No. 99CH36251), IEEE, 1999: pp. 3843–3847.

[339] S.W. Sung, I.-B. Lee, Limitations and countermeasures of PID controllers, Ind. Eng. Chem. Res. 35 (1996) 2596–2610.

[340] P. Basu, S. Mitra, Application of an expert system to the design of furnace of a circulating fluidized bed boiler, (1994).

[341] J. Krzywanski, H. Fan, Y. Feng, A.R. Shaikh, M. Fang, Q. Wang, Genetic algorithms and neural networks in optimization of sorbent enhanced H2 production in FB and CFB gasifiers, Energy Convers. Manag. 171 (2018) 1651–1661.

[342] J. Krzywanski, M. Wesolowska, A. Blaszczuk, A. Majchrzak, M. Komorowski, W. Nowak, The non-iterative estimation of bed-to-wall heat transfer coefficient in a CFBC by fuzzy logic methods, Procedia Eng. 157 (2016) 66–71.

[343] L. Desborough, R. Miller, Increasing customer value of industrial control performance monitoring-Honeywell's experience, in: AIChE Symp. Ser., New York; American Institute of Chemical Engineers; 1998, 2002: pp. 169–189.

[344] J.D. Anderson, J. Wendt, Computational fluid dynamics, Springer, 1995.

[345] J. Mikleš, M. Fikar, Process modelling, identification, and control, (2007).

[346] B. Sun, Y. Liu, X. Chen, Q. Zhou, M. Su, Dynamic modeling and simulation of shell gasifier in IGCC, Fuel Process. Technol. 92 (2011) 1418–1425.

[347] B. Jin, H. Zhao, C. Zheng, Dynamic modeling and control for pulverized-coal-fired oxy-combustion boiler island, Int. J. Greenh. Gas Control. 30 (2014) 97–117.

[348] D.C. Psichogios, L.H. Ungar, Direct and indirect model based control using artificial neural networks, Ind. Eng. Chem. Res. 30 (1991) 2564–2573.

[349] M.J. Willis, C. Di Massimo, G.A. Montague, M.T. Tham, A.J. Morris, Artificial neural networks in process engineering, in: IEE Proc. D (Control Theory Appl., IET, 1991: pp. 256–266.

[350] M.J. Willis, G.A. Montague, C. Di Massimo, M.T. Tham, A.J. Morris, Artificial neural networks in process estimation and control, Automatica. 28 (1992) 1181–1187.

[351] S. SN, Introduction to artificial neural networks, (2003).

[352] A.D. Dongare, R.R. Kharde, A.D. Kachare, Introduction to artificial neural network, Int. J. Eng. Innov. Technol. 2 (2012) 189–194.

[353] S. Li, Y. Shen, CFD investigation of maldistribution in a full-loop circulating fluidized bed with double parallel cyclones, Powder Technol. (2020).

[354] Y. Zhang, F. Lei, Y. Xiao, Computational fluid dynamics simulation and parametric study of coal gasification in a circulating fluidized bed reactor, Asia-Pacific J. Chem. Eng. 10 (2015) 307–317.

[355] S.-Y. Wong, W. Zhou, J. Hua, Designing process controller for a continuous bread baking process based on CFD modelling, J. Food Eng. 81 (2007) 523–534.

[356] S. Afshar, H. Jubaer, L. Metzger, H. Patel, C. Selomulya, M.W. Woo, Implementation of P-Controller in Computational Fluid Dynamics (CFD) Simulation of a Pilot Scale Outlet Temperature Controlled Spray Dryer, in: IDS 2018. 21st Int. Dry. Symp. Proc., Editorial Universitat Politècnica de València, 2018: pp. 155–162.

[357] ANSYS Fluent Theory Guide, ANSYS Fluent Theory Guide, ANSYS Inc., USA. 15317 (2013) 724–746. http://www.afs.enea.it/project/neptunius/docs/fluent/html/th/main_pre.htm.

[358] F. Bezzo, S. Macchietto, C.C. Pantelides, A general framework for the integration of computational fluid dynamics and process simulation, Comput. Chem. Eng. 24 (2000) 653–658.

[359] Y. Lang, S.E. Zitney, L.T. Biegler, Optimization of IGCC processes with reduced order CFD models, Comput. Chem. Eng. 35 (2011) 1705–1717.

[360] Y. Liu, Q. Xiao, A. Incecik, C. Peyrard, Aeroelastic analysis of a floating offshore wind turbine in platform-induced surge motion using a fully coupled CFD-MBD method, Wind Energy. 22 (2019) 1–20.

[361] B.A.A. Yousef, H. Rezk, M.A. Abdelkareem, A.G. Olabi, A.M. Nassef, Fuzzy modeling and particle swarm optimization for determining the optimal operating parameters to enhance the bio-methanol production from sugar cane bagasse, Int. J. Energy Res. 44 (2020) 8964–8973.

[362] D. Adams, D.-H. Oh, D.-W. Kim, C.-H. Lee, M. Oh, Prediction of SOx–NOx emission from a coal-fired CFB power plant with machine learning: Plant data learned by deep neural network and least square support vector machine, J. Clean. Prod. 270 (2020) 122310.

[363] R. Beigzadeh, S. Eiamsa-ard, Fuzzy logic to thermal and friction characteristics of turbulent air-flow over diamond-shaped turbulators, Int. Commun. Heat Mass Transf. (2020) 105001.

[364] J. Krzywanski, D. Urbaniak, H. Otwinowski, T. Wylecial, M. Sosnowski, Fluidized Bed Jet Milling Process Optimized for Mass and Particle Size with a Fuzzy Logic Approach, Materials (Basel). 13 (2020) 3303.

[365] E.H. Mamdani, S. Assilian, An experiment in linguistic synthesis with a fuzzy logic controller, Int. J. Man. Mach. Stud. 7 (1975) 1–13.

[366] A. Fluent, ANSYS fluent UDF manual, ANSYS Inc., USA. (2015).

[367] Y. Shao, R.K. Agarwal, X. Wang, B. Jin, Review of CFD Studies on Chemical Looping Combustion, J. Energy Resour. Technol. (2020) 1–37.

[368] W. Namkung, S.D. Kim, Gas backmixing in a circulating fluidized bed, Powder Technol. 99 (1998) 70–78.

[369] M. Van de Velden, J. Baeyens, K. Smolders, Solids mixing in the riser of a circulating fluidized bed, Chem. Eng. Sci. 62 (2007) 2139–2153.